Nanoparticles and nanoimaging for organic solar cells

Pedersen, Emil Bøje Lind

Publication date:
2015

Document Version
Publisher's PDF, also known as Version of record

Ph.D. Thesis

DTU Energy
Department of Energy Conversion and Storage

*Nano*particles and *nano*imaging

for organic solar cells

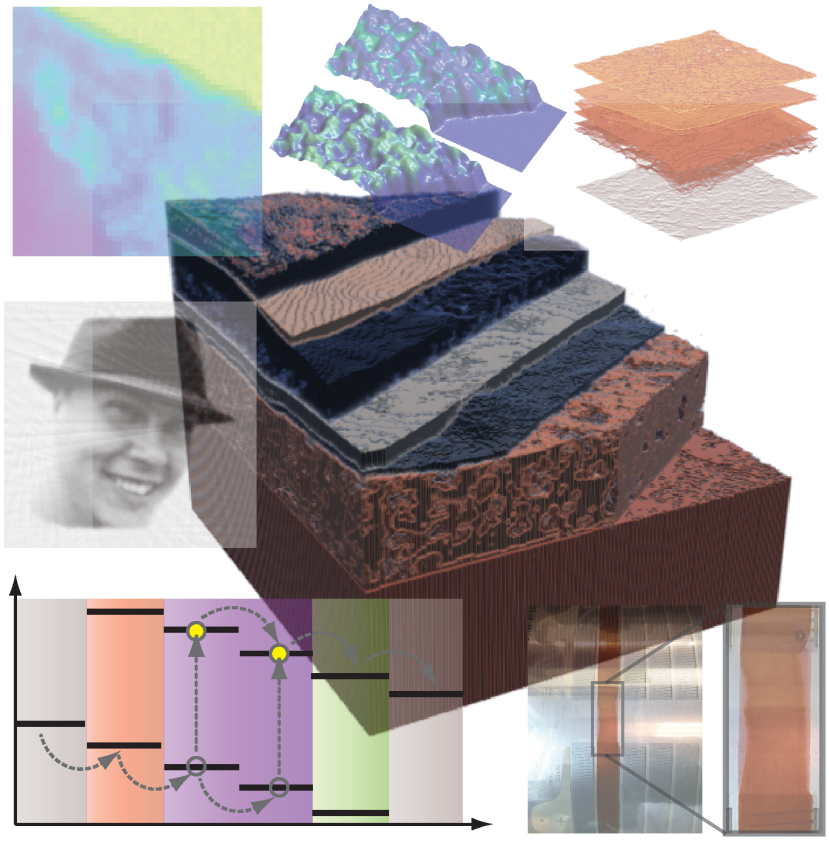

Emil Bøje Lind Pedersen (EBLPE)

DTU Risø Campus 2015
ECS-Ph.D.-2015

DTU

Department of Energy Conversion and Storage
Technical University of Denmark
Frederiksborgvej 399, Building 775
4000 Roskilde
Phone (+45) 46 77 58 00
info@ecs.dtu.dk
www.ecs.dtu.dk
Ph.D. 2015

Preface

This PhD thesis was prepared at the department of Energy Conversion and Energy Storage at the Technical University of Denmark. The work was carried out in the period 1. Juni 2012 until 29. May 2015 in fulfilment of the requirements for acquiring the PhD degree. The project was funded by The Danish Council for Strategic Research through WAPART - Water-based particulate approach to organic photovoltaics with controlled morphology (DSF China-grant), 0603-00493B. I was supervised by senior researcher Jens Wenzel Andreasen with Henrik Aanæs as co-supervisor. Articles produced in relation to the project are listed in the appendix.

I would like to thank my supervisor Jens Wenzel Andreasen for introducing me to the world of X-ray characterization, large scale X-ray facilites and a number of outstanding scientific collaborators. I have greatly valued our collaboration where he have provided me the freedom to operate and at the same time always had a sincere interest in my work.

The collaboration with Jakob Sauer Jørgensen has been most enjoyable, and I would like to thank him for sharing his knowledge in a friendly atmosphere. I would also like to thank both the SOL and the ISA group for making my time at Risø campus most enjoyable.

During the project I spent half a year in Changchun, China and I would like to thank Prof. Zhiyuan Xie and Prof. Yanhou Geng for hosting me. I would also like to thanks Wu Jiang, Liu Jian and Yunfeng Deng for going out of their way to make my stay enjoyable and Rasmus Guldbæk Brandt for joining me in this Chinese adventure.

I would like to thank Jens Wenzel Andreasen, Mikkel Schou Nielsen, Amalie Christensen, Kim Georg Lind Pedersen, Jacob Larsen and especially Kjertan Lyster for proofreading my dissemination. I would also like to thank Kjertan for providing sufficient board game distractions during thesis writing to keep my mood high.

At last I would like to thank my family and my lovely girlfriend, Maria Cavallius, for their endless support.

DTU Risø Campus, May 29, 2015

Emil Bøje Lind Pedersen (EBLPE)

Short contents

Abstract

Solar energy is one of the few energy sources with the potential to power humanity in a future scenario where fossil fuels are not attractive due to their effect on the global climate or fossil fuels have been depleted all together. Organic photovoltaics is a promising technology for solar harvesting due to its potential for scalable roll-to-roll production and low manufacturing cost. However, the technology is faced with several obstacles which have to be overcome such as low efficiency and stability. Some of the issues are related to nano structures and device morphology.

This dissertation is devoted to studying organic photovolatics on the micro to nanometer scale, in particular photoactive Landfester particles. The ultimate goal is to increase the performance of Landfester particle layers so they can become a viable alternative to photoactive layers cast from organic solvent. Transition to a water based ink would provide a production environment without toxic fumes from organic solvents and the nanoparticle structure would provide additional morphological control.

The first part of the dissertation maps photodegradation in active layers cast from organic solvents. Reduction in degradation rates is quantified for mixed electron donor and acceptor material. The spatial distribution of photodegradation in an electron donor material is mapped and the degradation is found to be homogeneous at the sub-micron length scale.

The second and third part is devoted to studying the nano structures in photoactive Landfester nanoparticles. The dispersed particles are characterized by size, internal structure and crystallinity. Crystal orientation and spatial distribution of materials are quantified for cast layers of Landfester particles. A layer of particles is also investigated in a tandem solar cell and compared to other layers in the structure using Tomographic 3D mapping.

The fourth part presents a projection alignment algorithm for tomographic methods. It works by estimating projection movement through iterative logic using projection distance minimization. It is tested on simulated datasets and results in decreased angular displacements and increased spatial resolution. Further development of the algorithm could therefore be used to increase spatial resolution for characterization of organic photovoltaics and computed tomography in general.

Dansk resume

Solenergi er en af de få energikilder med potentiale til at levere energi til menneskeheden i et fremtidsscenarie hvor fossile brændstoffer ikke er attraktive grundet deres effekt på det globale klima eller hvor fossile brændstoffer er blevet fuldstændig opbrugt. Organiske solceller er en lovende teknologi til at høste solenergi grundet dets potentiale for skalerbar rulle til rulle produktion og lave produktions omkostninger. Teknologien står imidlertid over for udfordringer i forhold til energikonverterings effektivitet og stabilitet. Mange af de udfordringer er relateret til nanostrukturer og morfologi i solcellerne.

Afhandlingens fokus er på at studere organiske solceller fra mikro til nanometerskala, i særdeleshed fotoaktive Landfester partikler. Det endelige mål er at øge effektiviteten af Landfester partikellag, så de kan blive et alternativ til fotoaktive lag lavet fra organiske opløsningsmidler. Overgangen til en vandbaseret blæk vil give et produktionsmiljø uden giftige dampe fra organiske opløsningsmidler, og nanopartikelstrukturen vil give mulighed for at kontrollere morfologien i det fotoaktive lag.

Første del af afhandlingen kortlægger lysnedbrydning i aktive lag lavet fra organiske opløsningsmidler. Reduktionen i nedbrydningshastigheder kvantificeres for blandede elektrondonor og acceptor materialer. Den rumlige fordeling af lysnedbrygning kortlægges endvidere for et elektrondonor materiale og nedbrydning er homogen på en sub-micrometer længdeskala.

Anden og tredje del er afsat til studiet af nanostrukturer i fotoaktive Landfester nanopartikler. Partiklen i dispersion bliver karakteriseret ud fra størrelse, intern struktur og krystallinitet. Krystalorienteringer og den rumlige fordeling af materialer bliver kvantificeret for lag af Landfester partikler. Et lag af partikler bliver også undersøgt i en tandem solcelle og sammenlignet med andre lag i strukturen via tomografisk 3D kortlægning.

Fjerde del fremlægger en projektions-justerings-algoritme til tomografiske metoder. Den virker ved at vurdere projektions forskydninger via iterativ logik og brug af projektion-afstands minimering. Algoritmen er testet på simulerede datasæt, hvor vinkelforskydninger reduceres og den rumlig opløsning øges. Videreudvikling af algoritmen kan derfor bruges til at øge rumlig opløsning i karakteriseringen af organiske solceller og i computertomografi generelt.

List of abbreviations

2D	2 dimensional
3D	3 dimensional
AFM	Atomic Force Microscopy
ART	Algebraic Reconstruction Technique
BHJ	Bulk hetero junction
C60	Buckminsterfullerene
CT	Computed Tomography
DLS	Dynamic Light Scattering
EMIL	Estimated Movement by Iterative Logic
EPBT	Energy payback time
FIB	Focused Ion Beam
FIB-SEM	Focused Ion Beam - Scanning Electron Microscopy
FT	Fourier Transform
GIWAXS	Grazing Incidence Wide Angle X-ray Scattering
IFT	Inverse Fourier Transform
IO	Input output
ITO	Indium Tin Oxide
NEXAFS	Near Edge X-ray Absorption Fine Structure
NP	Nanoparticles
OD	Optical Density
OPV	Organic photovoltaics
OSA	Order Sorting Aperture
P3HT	Poly(3-hexylthiophene)
PCBM	Phenyl-C61-butyric acid methyl ester
PDM	Ptychographic Difference Map
PEDOT:PSS	Poly(3,4-ethylenedioxythiophene):Polystyrene sulfonate
PET	Polyethylene terephthalate
PIE	Ptychographic Iterative Engine
PXCT	Ptychographic X-ray Computed Tomography
RAM	Random Access Memory
rpm	Rounds per minute
SART	Simultaneous Algebraic Reconstruction Technique
SAXS	Small Angle X-ray Scattering
SDS	Sodium Dodecyl Sulfate
SNR	Signal to Noise Ratio
STXM	Scanning Transmission X-ray Microscopy
TEM	Transmission Electron Microscopy
TOF-SIMS	Time-of-flight Secondary Ion Mass Spectroscopy

TV	Total Variation
ZnO	Zinc oxide

Contents

CHAPTER 1

Introduction

1.1 Energy production

In human society there is a need for energy resources. This need is primarily (87%) satisfied by the consumption of coal, oil and natural gas[1]. These resources have been created by biological and geological processes that are orders of magnitudes slower than the current consumption, which will lead to depletion in the long term. We therefore have a motivation to seek alternative energy sources. Another concern is the release of CO_2 gas into the atmosphere which is predicted to change Earth's climate[2, 3] calling for imminent change in energy sources. The following section will very briefly introduce current and future energy sources and the role of plastic solar cells also known as organic photovoltaics (OPV).

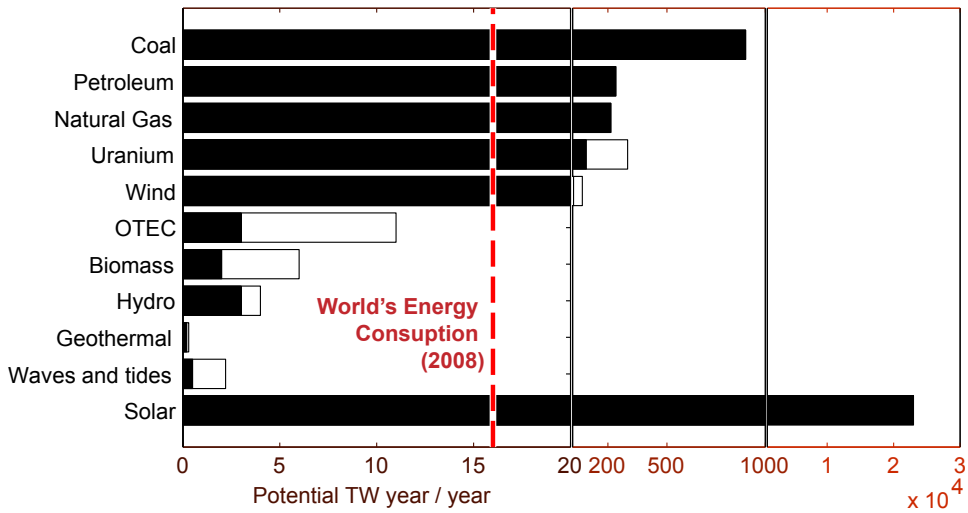

Figure 1.1: Potential power output from different energy sources based on data presented by Perez et al.[4]. Ocean Thermal Energy Conversion is abbrivated as OTEC. The white bars indicate an interval due to different estimates. The only renewable resources with sufficient potential to meet the world's energy demand is wind and solar. Even with increasing energy demand solar energy have a vast potential about 14000 times the world's 2008 energy demand.

There is a range of energy sources available listed in figure 1.1. Upcoming technologies such as Thorium fission or nuclear fusion have not been included.

With the exception of solar energy, all these energy sources uses energy extraction by pressure driven turbines. Solar energy is fundamentally different and uses the direct conversion of photons into an electric potential i.e. photoelectric effect. There exist niche technologies such as direct thermal-electric and mechanical-electric conversion which might play a role in the future but currently have not demonstrated large scale production.

For an immediate reduction in CO_2 emission all alternatives to fossil fuels are feasible. The main barriers for application of alternative energy sources are higher energy prices and limited availability. Now, in 2015, only hydro, geo-thermal and nuclear fission energy can compete directly with the price point of fossil fuels. Due to fluctuations in the worlds' economies, cost is not a rigorous scientific measure when quantifying development of energy technologies. The more scientific term of energy payback time will therefore be used rather than cost when discussing the feasibility of OPV. In essence, it is necessary to develop alternative energy sources so they can compete with and replace fossil fuels.

Another challenge is energy availability when balancing a power grid with intermittent energy sources, that is sources that are not constantly available nor within our control. Energy supply and consumption must be equal at all times within certain tolerances. Oversupply will cause damage to the energy grid and devices, whereas an overconsumption will cause device failures. Therefore it is essential to have energy sources that can be regulated to fit consumption, which is possible with sources such as fossil fuels, nuclear and hydro energy. Sources such as wind, wave and solar energy can not match consumption due to their intermittence. There are great costs associated with ramping energy production up and down and also limits in the ramping rates. To facilitate energy sources with fluctuating production, it is necessary to develop energy storage, more adaptive consumption and energy distribution, i.e. smart devices and smart grids.

The previous sections have focused on the short term goal of reducing CO_2 emission, whereas the longterm goal of humankind is to completely replace fossil fuels with renewable energy sources. Human energy consumption is increasing – from 1990 to 2008 it increased by 40% from 11.4 terawatts to 16 terawatts[5]. Therefore, it is essential to find energy sources with a potential of tens of TW, which can only be achieved by wind (25-70 TW) and solar energy (23000 TW)[4]. Another potential source is fusion reactors and in 2014 an experimental power plant achieved a short period where power output was greater than consumption[6]. The first commercial fusion reactor is estimated to be operational in 2050[7] assuming challenges with unstable plasma can be addressed.

The ultimate goal of our energy sources should be not only to support current existence but to carry human development forward. Beyond Earth, the main source of energy is photons originating from fusion inside stars. Therefore the ultimate fate of humanity seems to lie in either controlling the fusion process or harvesting the vast amount of fusion reactors scattered throughout the universe using photovoltaics. The next section will introduce the role of photovoltaics with an emphasis on OPV.

Niche of organic solar cells

Photovoltaics are a quite different energy technology compared to conventional energy technologies i.e. fossil and nuclear energy solutions. In terms of producing the power plant, solar cells require a large amount of small units with controlled nanostructure whereas fossil and nuclear plants require one big central unit with macroscopic machinery. In terms of maintenance, conventional power plants require a steady supply of fuel and supervision

whereas solar plants generate power on their own until the end of their lifetime. The feasibility of photovoltaics as an energy source therefore mainly depends on the production cost, the energy conversion efficiency and the lifetime. Compared to conventional power plants photovoltaics take up much larger areas, that could otherwise be used for other purposes. Unlike fossil fuels the power generation can not be controlled. Energy production relying mainly on solar cells demands large energy storage capability coupled with the solar plants to guarantee reliable power.

In the realm of solar power, organic photovoltaics are a niche of its own. Compared to the industry standard, silicon photovoltaics, OPV have a series of advantages and disadvantages. OPV have lower energy conversion efficiencies (module: 1.5-8.7% versus 22.9% for silicon[8, 9]), lower lifetimes (approaching years versus 25 years for silicon[10, 11]), but also lower production cost. If the lower performance can be matched by a sufficiently low production and deployment cost, OPV cells are a very attractive option. A way of measuring this is energy payback time (EPBT), i.e. how long time should the solar cell operate to pay for its own energy consumption. For silicon the EPBT is $\sim$1.5 years[12], whereas organic solar cells have EPBTs of $\sim$100 days with the possibility of bringing it down to 1 day[13]. That gives organic solar cells an advantage in scalability. What makes organic solar cells truly scalable is the fast production speed of 60 meters per minute that allows the technology to meet the world's future energy demand[14].

The low energy conversion efficiency of organic photovoltaics compared to silicon means larger areas of land are needed to produce the same amount of energy. Another contester for land area is farming. Deploying OPV on fields will reduce agricultural production, which is already predicted to be insufficient to feed the world's population by 2050[15]. It might become possible to develop methods for coexistence of solar panels and agriculture as demonstrated by Harinarayana et al.[16]. Even if it is not feasible to put organic solar cells in our fields, there are plenty of unused area e.g. roofs, mountains and deserts where it is advantageous to place organic solar cells. The deployment is even easier than for conventional solar cells due to the low weight and flexibility of the organic solar cells. Hence, until we have filled all our roofs, deserts, mountains and coasts with solar cells, there is a niche for organic solar cells as a scalable way to meet the world's energy demand.

Using OPV panels means we depend on the sun for power. Furthermore, unless a global power grid is implemented where electricity can be transported halfway around the Earth, we are limited to power during the day. Cloudy days mean little solar power to be harvested, giving us a need for short term energy storage (days/weeks). On a longer time scale, the seasonal change provides less sun light and thereby less power during the winter which also gives us a need for long term energy storage (a year). Energy storage is inherently wasteful. One must convert power to a storable form and back to electrical power, with both processes operating at less than 100% efficiency. The most efficient solution today is water pumps and turbines (pumped hydroelectricity storage) which have a total efficiency of about 70-80%[17]. The short term power demand is therefore better solved by chiefly relying on flexible energy consumption (smart grids and adaptable industrial production)[18]. Technological improvements will likely increase the energy storage efficiency but switching to renewable resources will result in a larger demand on future energy production, since 20-30% will be lost in the storage process. The fate of the organic solar cell is therefore also dependent on improvements in other technologies, which enable flexible energy consumption and energy storage.

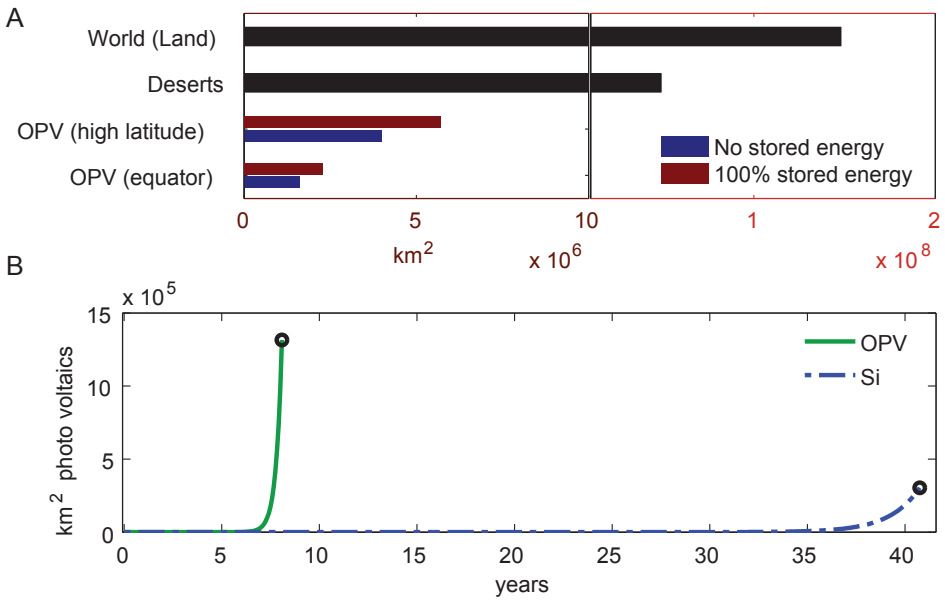

Figure 1.2: A) Required OPV land use to meet the world's 2008 energy demand depending on location and need for energy storage (estimated 70% energy loss). Along is shown Earth's total landmass and desert area. B) Time scale for bootstrapping energy production with photovoltaics starting from 1 m^2 of solar cell and reinvesting all energy production into more solar cells until the world's 2008 energy demand is met. In these calculations only energy going into the solar panels have been considered i.g. no energy is deducted for making production facilities and there is no limit on fabrication speed. The energy production is based on equatorial placement with no deduction for energy storage.

Back of the envelope calculations for OPV

Predicting the future of global energy systems faces several challenges in using oversimplified scenarios where the magnitude of crude approximations and systematic errors are hard to estimate. However, quantifying critical parameters such as land use and deployment time scale is necessary to estimate the feasibility of OPV and justify further development of the technology. I will for these estimates use the rough approximation of an OPV module efficiency of 4%, life time of 4 years and EPBT of 100 days (0.27 year). For silicon solar cells I assume module efficiency of 20%, life time of 25 years and EPBT of 1.5 years.

Estimating the land area required to supply the world with energy, $A_{W.E.}$, can be done based on the world's yearly energy need, E_W, average effect of solar radiation per area of the surface of the earth, P_{Sun}/A, the efficiency of the photovoltaic cell, η_{Cell} and an intermittency factor denoting energy loss due to storage, ρ:

$$A_{W.E.} = \frac{E_W}{\eta_{Cell} \cdot \rho \cdot (P_{Sun}/A)} \tag{1.1}$$

E_W was in 2008 16 TW year = $5{\cdot}10^{40}$J. P_{Sun}/A varies depending on latitude and range from about 100 W/m^2 in Scandinavia to 250 W/m^2 near Equator taking into account night time, clouds and seasons[19, 20]. ρ depends on how well a grid with solely OPV can be constructed. If no energy needs to be stored it is 1, but if all energy needs to be stored at 70% efficiency it is 0.7. Land use for different scenarios is presented in figure 1.2. Even in the worst case with high latitude placement and total use of energy storage the land demand is only 3.9% of world's land area.

Another concern is the scalability. The growth potential can be considered by how fast the technology is able to bootstrap itself energy wise. Assuming there exists a given area of solar devices, A_D, at a time, t, their potential production capacity of new device area can be calculated for the time step, Δt, by the EPBT and device lifetime, T_L:

$$A_D(t + \Delta t) = A_D(t) + A_D(t)\frac{\Delta t}{EPBT} - A_D(t - T_L) \tag{1.2}$$

The equation assumes the energy payback is distributed over the lifetime of the device. Starting from 1 m^2 of photovoltaic device, the area development is simulated for OPV and silicon until the 2008 energy demand of the world is reached. This is showed in figure 1.2. OPV can meet the worlds energy demand in less than 10 years, whereas silicon needs 40 years despite having higher efficiency and using less land area. Note that concerns regarding production and deployment limits have not been considered, so it is a very optimistic back of the envelope calculation. However, OPV as a technology have clear advantages when it comes to large scale production and deployment, and therefore appears as an attractive photovoltaic technology able to meet the world's energy need.

1.2 Organic solar cells

An indepth understanding of the material science behind solar cells in general and organic photovoltaics in particular is required to understand the scope of this project. Furthermore, an understanding of the engineering challenges associated with the construction of successful organic photovoltaic devices is also important as outlined in the following sections.

Solar cell overview

Photovoltaics rely on the process in which photons are converted to power in the form of an electric potential difference. Photons are electromagnetic discrete packages of energy, and they can transfer their energy to matter by exciting a bound electron to a higher energy state. This is known as the photoelectric effect. However, the photons can also transfer energy in the form of lattice vibrations (phonons) and similar processes, resulting in dissipation of heat. The photoelectric effect can only take place if the available energy gaps in the absorber materials match the photon's energy. After a photoelectric excitation, the system has an electron in a higher state (than before) and an electron vacancy in the lower state – this is commonly denoted an electron-hole pair or an exciton.

Unless the exciton is separated it will decay, and the energy will either be re-emitted as a photon or dissipate as heat. In regular materials, dissociation of the electron and hole is unlikely. However, by combining different materials or doping a material with different elements, one can facilitate this disassociation of the electron-hole pair. An electric potential

will be generated by collecting the electrons and holes at two different positions. In practice, the solar cell is a multilayer sandwich structure with a top and bottom electrode surrounding the absorber/separator materials in the middle (see figure 1.3). There is a preferred flow of electrons and holes in the separator materials. The device thereby effectively functions as a diode allowing current to flow in only one direction.

Silicon and organic photovoltaics are quite different. Traditional silicon devices use crystalline silicon doped with various other atoms from group III and group V of the periodic table to form n- and p-type silicon respectively (n-type is conductive due to extra electrons, whereas p-type is conductive due to extra holes). Silicon itself absorbs visible light, primarily in the range of wavelengths 400-1100 nm[21]. The separation of the electron-hole and transportation to the electrode are ensured by having a p- and n-doped layer as illustrated in figure 1.3. Doped crystalline silicon is a good conductor that allows for easy electron-hole separation and transport to the electrodes.

Organic photovoltaics are made up of "p- and n- types" molecules or more commonly denoted acceptor and donor molecules (see figure 1.3). These molecules are semi-crystalline at best and often rely on conjugated carbon bonds for charge transport. The conductivity is low, and the exciton diffusion length is only about 10 nm[22] as opposed to about 0.1 mm in doped silicon[23]. An exciton physically has to be at an interface for the charges to separate and with the limited exciton diffusion length the donor and acceptor molecules have to be mixed. Ideally, there should be less than 10 nm to any interface between the two materials and at the same time a continuous pathway from the donor/acceptor to the appropriate electrode. This mixture of donor and acceptor material is commonly denoted a bulk hetero junction (BHJ). Since donors and acceptors are mixed we need additional layers to make sure the electrons and holes are collected at separate electrodes. If no interface layers were present, the electron and hole could go to the same electrode, where they will recombine and no potential difference would be generated. The active BHJ is therefore placed between other p and n type materials, which do not absorb light, but allow either mainly holes or electrons to pass through due to their energy levels. These materials are therefore often referred to as electron- or hole-blocking layers.

Device design & characterization

When designing an organic solar cell there are two basic designs (see figure 1.4). Either the electrons go to the top electrode (where the light enters) or to the back electrode. These structures switch the electron- and hole- blocking layers and are referred to as inverted and normal geometry respectively and shown in figure 1.4. I will briefly list the structures of figure 1.4 with common material choices (for full names see list of abbreviations and for the structure of P3HT and PCBM, see figure 1.6).

- transparent top electrode, e.g. Indium Tin Oxide (ITO)
- hole blocking layer, e.g. Zinc oxide (ZnO)
- active donor / acceptor material e.g. Poly(3-hexylthiophene) (P3HT) / Phenyl-C61-butyric acid methyl ester (PCBM)
- electron blocking layer, e.g. Poly(3,4-ethylenedioxythiophene):Polystyrene sulfonate (PEDOT:PSS)

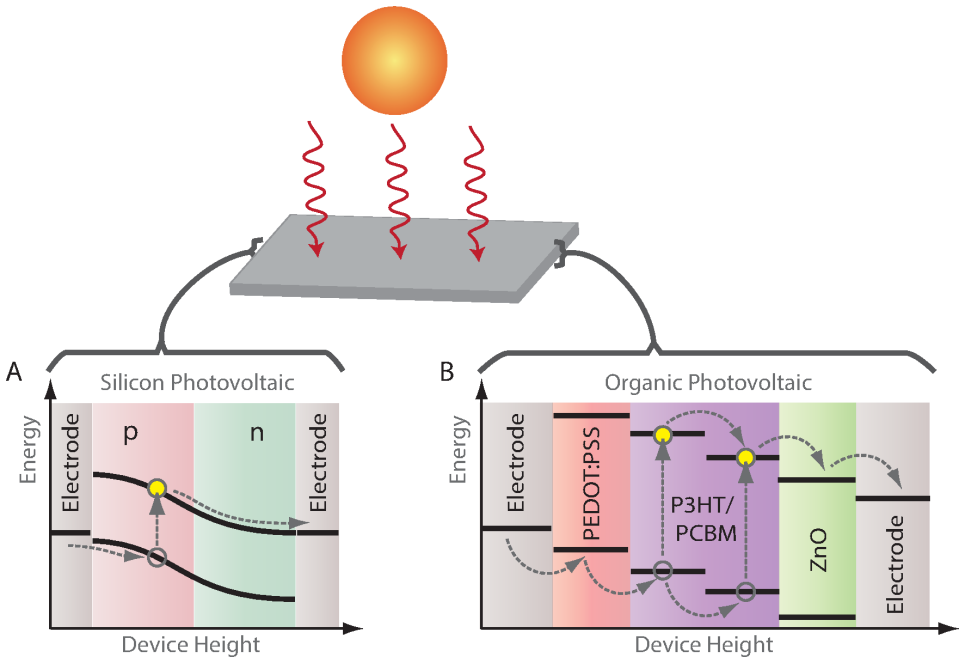

Figure 1.3: Model of a single junction solar cell showing the path of the electrons through the solar cell (vertical arrows are photo excitation). In both type of devices the basic principle is: light excites an electron in a photo active layer, and the electron is transported to the anode while the hole is transported to the cathode - creating an electric potential across the solar cell. A) Crystalline silicon with p- and n- type doping with continuous energy levels. B) Organic solar cell with discrete energy levels of different type of materials.

- bottom electrode, e.g. Silver (Ag)

In addition to to these it is also possible to combine more organic solar cells into a single structure, e.g. two cells into a tandem structure. The tandem structure makes it possible to capture more of the solar spectrum by combining polymers tuned to absorb both high and low energy parts of the solar radiation. Basic device characterization aim at finding four parameters: Short circuit current (J_{sc}), open circuit voltage (V_{oc}), fill factor (FF) and power conversion efficiency (PCE). These parameters are extracted by applying a bias voltage across an illuminated solar cell while measuring the current. This procedure produces an JV-curve characteristic for the diode, see figure 1.5. J_{sc} is found as the intersection with the current axis at zero electric potential. A potential of zero effectively short circuits the system and the maximum current is drawn from the device. V_{oc} is found at the intersection with the electric potential axis at zero current. In the limit where the potential is so large that only an infinitesimal current is drawn the circuit approach an open circuit. The power, P, is the product of the current, J, and electric potential, V

$$P = JV. \tag{1.3}$$

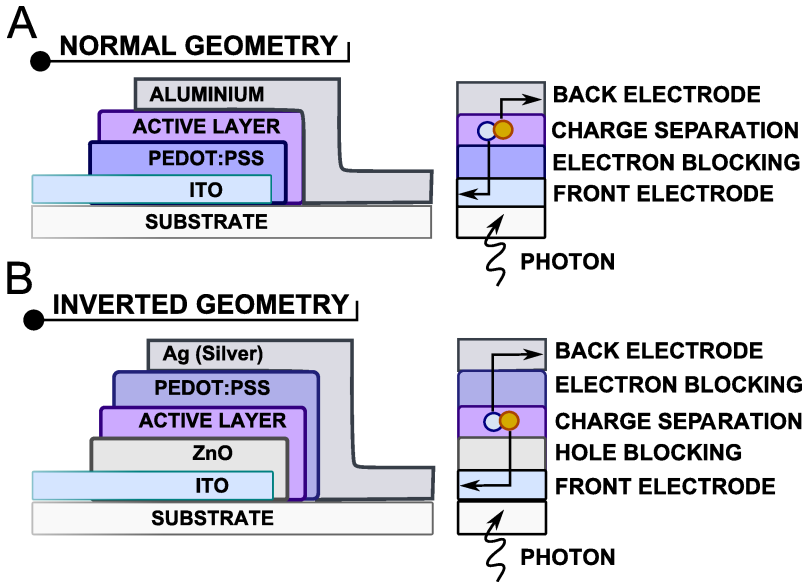

Figure 1.4: Model of normal geometry, A), and inverted geometry, B). In both cases the devices are made on a glass substrate with ITO (a transparent conductor) as top electrode. Scalable production would use a flexible substrate and a more complex layer structure. As observed in A) the electron blocking layer is sufficient to create a diode effect and enable a potential build-up across the solar cell. Different electrode materials are used in the normal and inverted geometry to match the work functions. This results in smaller potential "jumps" for electrons between materials.

Organic solar cells are not perfect diodes which means the maximum power output P_{out} is lower than the product of J_{sc} and V_{oc}. The fraction between the highest theoretical power and the highest actual power output is denoted the fill factor (FF) and normally expressed in percent. FF expresses how ideal a diode the system is

$$P_{out} = J_{sc} \cdot V_{oc} \cdot FF. \tag{1.4}$$

PCE is defined as P_{out} divided with incoming power, P_{in} (solar irradiation).

$$PCE = \frac{P_{out}}{P_{in}} = \frac{J_{sc} \cdot V_{oc} \cdot FF}{P_{in}} \tag{1.5}$$

Standard testing of solar cells uses a calibrated solar simulator with known spectrum and power output. The V_{oc} depends on the materials used, whereas J_{sc} and FF, depends on the device structure and the efficiency at which it generates and extracts electrons.

Spatial challenges for organic photovoltaics

As mentioned previously there are some challenges for organic photovoltaics, in particular the low power conversion efficiency. Charge generation and extraction needs to be optimized

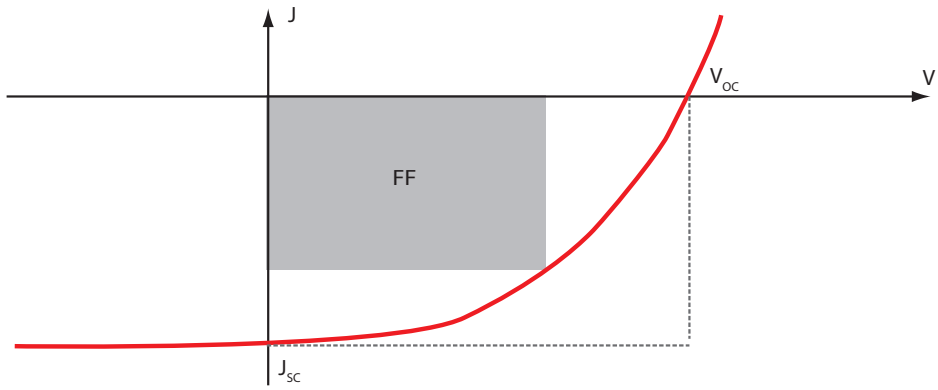

Figure 1.5: Schematic view of electric characterization of an organic photovoltaic device performed by applying a potential, V, across an illuminated device while measuring the current, J. J_{SC} is indicated at the intersection with the J-axis, V_{OC} is indicated at the intersection with the V-axis, the maximum power output of a perfect diode is indicated with gray dashed lines, and the FF is shown in solid gray.

to achieve a high PCE. The first step towards optimizing charge generation is to maximize the number of incident photons absorbed by the active layer. The ideal materials have a high absorption coefficient and sufficient active layer thickness (50-500 nm) to absorb most photons[24]. After absorption, the electron-hole pair needs to separate, which requires the donor and acceptor molecules to be well-mixed. Well-mixed means that at any point in the layer, the distance to an acceptor-donor interface is less than the exciton diffusion length ($\sim$10 nm)[22]. After charge separation, the electron (and hole) needs to be transported to the appropriate hole (or electron) blocking layer, which requires a connected network of acceptor (and donor) molecules across the the active layer of about 50-500 nm[24]. At the boundary of the active layer, the hole (and electron) blocking layer needs to fully cover the active layer interface and have a sufficient thickness to selectively allow the correct charge through. The blocking layers have ideally low resistance to allow for easy charge transport.

The active layer has a set of spatial requirements in the nanometer scale, e.g. interface distances ($<$10 nm) and connected networks to top and bottom through the active layer ($>$100 nm). Leveraging the main advantage of organic solar cells, large scale production, the nano design has to be achieved by a scalable self-assembly processes. Currently, this is achieved by casting a highly intermixed bulk hetero junction, and afterwards using temperature or solvent annealing to increase the domain size to form an optimal morphology. The structures of the active layer and entire photovoltaic device will primarily be investigated by a number of X-ray based techniques.

1.3 Photoactive nanoparticles

Alternatives to self-assembled bulk hetero junctions need to use other self-assembly processes to control the mixture and network of donor and acceptor molecules. One way is to treat the

ink before casting and shape it into nanoparticles. It is possible to control nano morphology in large scale layer formation by tuning the particle fabrication parameters. One way is to ensure sufficient mixing of donor acceptor materials by forming small particles with sizes in the range of the exciton diffusion length (radius 10 nm). It might also be possible to control the internal structure of the particles and thereby affect the charge transport networks formed as the nanoparticles are cast into films. Preprocessing of the donor and acceptor materials into nanoparticles also allows to access solvents like alcohols and water. These solvents are more suitable for large scale production than organic solvents.

Motivation for water based inks

Water based inks are an alternative to organic solvents which form toxic and flammable fumes due to their low boiling point. Large scale production using organic solvents is difficult mainly due to safety requirements associated with limiting human exposure to the harmful solvents. Presently, full body suits are required to protect against respiratory exposure. The established printing industry has limited the use of organic solvents since their harmful effects became evident in the 1980's[25]. Organic solvents act as market barrier, since the technology cannot fully utilize the established printing industries' development and production capabilities. Instead, it is necessary to develop customized production lines and printing setups for organic photovoltaics. The vision of large scale production of organic solar cells will also require large amounts of organic solvents. E.g. to make 1 GW production capacity of processOne solar cells[26] 16 million liters of chlorobenzene would be needed[27]. Even with a recollection scheme it would be more suited for closed loop ink preparation, where a limited amount of organic solvent could be reused to produce large quantities of water based inks.

Landfester nanoparticles

One route to stable organic nanoparticles (NP) is Landfester particles[28, 29]. The process is illustrated in figure 1.6 with P3HT and PCBM as the donor- and acceptor-molecules respectively. The nanoparticles are made by dissolving the donor and acceptor materials in an organic solvent. It is then mixed with water containing a high concentration of surfactant, typically Sodium Dodecyl Sulfate (SDS), and ultra sound is used to ensure sufficient mixing forming a miniemulsion. The organic solvent is evaporated (a condenser could be applied to reuse of the solvent), and the donor- and acceptor-molecules are left behind, mixed inside stable nanoparticles suspended in water. Excess SDS is removed by dialysis, and the suspension is upconcentrated by centrifugation.

1.4 Introduction to X-rays and X-ray based techniques

The following sections will briefly introduce some of the methods used to characterize organic nanoparticles, active layers and whole solar cell stacks. The section focuses on key ideas and basic concepts e.g. phase versus absorption contrast, whereas later chapters will provide a more mathematical and in depth explanation of the techniques.

X-rays are electro-magnetic waves with wavelengths ranging from 0.01 – 10 nm. They were first discovered by Wilhelm Röntgen in 1895. X-rays quickly became a hot topic in the scientific community and in 1900 a whole 9% of all papers were on X-rays at an international

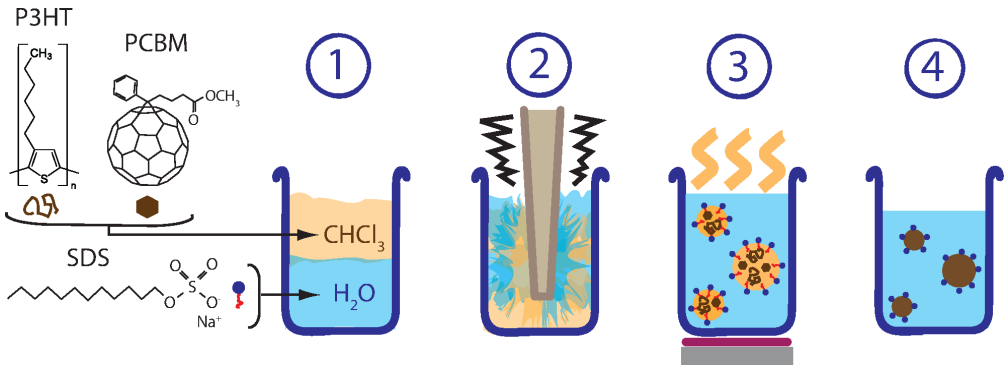

Figure 1.6: The Landfester method for nano particle fabrication: 1) Organic materials (P3HT & PCBM) are dissolved in an organic solvent and a surfactant (SDS) is dissolved in water. 2) The two phases are mixed with ultrasound leading to formation of a mini emulsion. 3) Organic solvent is evaporated. 4) Final dispersion of organic nano particles in water.

physics conference held in Paris[30]. The first application of X-ray imaging was the now famous absorption images of Anna Röntgen's hand (figure 1.7)

Figure 1.7: X-ray absorption image of Anne Röntgen's hand. Early X-ray imaging that demonstrates absorption contrast between light elements (carbon, oxygen and hydrogen in organic tissue) and heavier elements (calcium in bone, and metal in the ring).

The field of medicine quickly adopted X-ray absorption having the first clinical trial within the year of the X-ray discovery[31]. Since, the X-ray imaging has continued to play a role in medicine through the use of more advanced methods such as the computerized axial tomography invented by Hounsfield in 1972[31].

In the field of material sciences, crystallography was one of the early adopters of X-rays. In 1912, Max von Laue did the first X-ray diffraction on copper sulphate[32]. The following year, Bragg determined the atomic crystal structure of NaCl[33]. Since then,

crystallography has been used to map the atomic structures of any crystalline material and can now be used to automatically find the structure of complex protein molecules[34].

Small Angle X-ray Scattering (SAXS) is useful to measure material distribution at the nano scale. Wide Angle X-ray Scattering (WAXS) is used to characterize crystalline texture and strain. SAXS was first observed by Krishnamurty in 1930[35]. It was initially used on powders and fibres and in 1937 Guinier formulated particle scattering to determine the particle size of diluted systems[36]. Later it was shown by Kratky and Porod, that SAXS could be used to determine the size of macromolecules such as hemoglobin[37]. Recently, scattering was used to complement crystallography when determining protein structures [38] and distances related to domain formation in new nano materials[39].

The initial use of X-rays in material science employed signal amplification from either diffraction from multiple unit cells in crystals or scattering from multiple particles or domains. In contrast to these bulk measurements, X-ray tomography produces detailed 3D images of all individual features of an object. The aggregation of multiple 2D images requires computation power, which made this technique available much later than the other techniques. A decade after medical tomography was invented by Hounsfield[31], Elliott performed the first X-ray microtomography in 1982[40]. With the introduction of microtomography, Elliott sparked interest in using X-rays for high resolution imaging by demonstrating 19 micron spatial resolution[40]. With the focus on nanometer scale materials, new X-ray imaging methods seek the highest possible resolution. High resolution X-ray tomography tries to overcome challenges with low contrast and accessing high magnification with very limited access to optical solutions. As the samples get smaller, the volume of each voxel in a tomogram decreases. Less volume means, less material to penetrate and thereby lower constrast. This lead to the exploration of phase contrast as an alternative to traditional absorption contrast. It is difficult to detect X-rays with spatial nanometer resolution, especially since X-ray optics are more challenging than traditional optics for visible light. This is due to the difference in refractive index of the materials, which for visible light can be much greater than 1 but is always slightly less than 1 for X-rays. This makes it attractive to develop lensless methods where the diffraction patterns are detected and the conversion to real space is done computationally. These methods are known as coherent diffractive imaging (CDI).

The idea of CDI originated in the crystallography community, where Sayers proposed phase retrieval by oversampling in 1952[41]. In the 1970's, algorithms for efficient phase retrieval was proposed by Gerchberg and Saxton[42] and further developed by Fienup[43, 44]. At the same time, Hoppe and Rodenburg pioneered theory and application of coherent imaging in electron microscopes[45, 46]. In the late 1990's the idea of X-ray phase imaging was popularized by a demonstration by Miao (and Sayers)[47], and in 2010 Dierolf et al. demonstrated CDI tomography with 100 nm resolution[48]. The late application of X-ray CDI tomography is due to high demands in computational power and, more importantly, a need for highly coherent X-ray sources (first available with third generation synchrotrons and afterwards with X-ray electron free lasers). Currently, X-ray CDI imaging approaches the nanometer regime as illustrated by an obtained isotropic spatial resolution of 16 nm in a 6 micron thick sample[49]. It is speculated that in the future (with the use of X-ray free electron lasers) a spatial resolution below 1 nm could be reached[50].

X-ray phase versus absorption

How is X-ray phase contrast different from absorption contrast? A convenient way to look at the difference is through the refractive index which can be written as a complex number:

$$n = 1 - \delta + i\beta \tag{1.6}$$

The electric field of a photon interacting with matter is[51]:

$$E(r) = E_0 \exp(in\bar{k} \cdot \bar{r}) = E_0 \exp(i\bar{k} \cdot \bar{r}) \cdot \exp(-i\delta\bar{k} \cdot \bar{r}) \cdot \exp(-\beta\bar{k} \cdot \bar{r}) \tag{1.7}$$

It is apparent that the contribution from δ is complex (phase), while the contribution from β is real (absorption). By relating them to the atomic number, Z, and energy using the wave vector, $\bar{k}$, the relative interaction strength can be estimated.

$$\delta = \frac{2\pi\rho_E r_0}{|\bar{k}|^2} \sim \frac{Z}{k^2} \tag{1.8}$$

Where $\rho_E \sim Z$ is the electron density and r_0 is the classic electron radius.

$$\beta = \frac{\rho_A \sigma_A}{2|k|} \sim \frac{Z^4}{k^4} \tag{1.9}$$

Where ρ_A is the atomic number density, and σ_A is the absorption cross section – for high energy X-rays $\sigma_A \sim Z^4/k^3$[51]. From these rough scaling laws it is apparent that as the X-ray energy increases, absorption contrast decreases faster than phase contrast. High energy also means high penetration which is desirable for tomography. Looking at the atomic number Z we see that absorption increases faster for heavy elements. Phase contrast has proven itself useful for imaging low density materials, such as organic tissue or polymers[52, 53, 54].

Key ideas used in X-ray based techniques

I have used Near Edge X-ray Absorption Fine Structure (NEXAFS) and Scanning Transmission X-ray Microscopy (STXM) to map photo degradation in photoactive materials. NEXAFS is an X-ray spectroscopy method based on the basic principle that the X-ray absorption cross sections vary with photon energy depending on the element and their conformation e.g. bonds to other elements. Therefore, spectroscopy provides chemical fingerprint of molecules and their oxidation state and can access elemental/chemical contrast. NEXAFS is also known as X-ray Absorption Near Edge Structure (XANES). Today the term NEXAFS is typically used for soft X-ray whereas XANES are used for hard X-ray[55], so in this dissertation the technique will referred to as NEXAFS as it is used with soft X-rays. X-ray absorption spectroscopy can be extended spatially by a focused beam and mechanically scanning the sample, i.e. STXM. X-rays provide a high spatial resolution compared to optical methods and a high penetration depth compared to transmission electron microscopy. For more information see chapter 2.

Small Angle X-ray Scattering (SAXS) has been used on particles in suspension. X-ray scattering happens when X-ray photons are deflected by the electrons and thereby change paths. The different distribution of electron densities will give scattered X-rays different angular dependences. In general, far from the scattering object (far field) the spatial distribution of scattered rays are the Fourier transform of the real space object. In particular

small objects or other contrasts giving small distances in the object will translate to large scattering angles. Small distances are therefore intrinsically easier to measure than large distances. This is directly opposed to real space methods like absorption contrast. The niche of scattering is thus to measure small distances. For more information see chapter 3.

Grazing Incidence Wide Angle X-ray Scattering (GIWAXS) has been used on cast layers, to measure relative crystallinity, crystal domain sizes and crystal orientation. Ordered crystal structures have a large number of unit cells with the same distance and orientation. Scattering signals will therefore be very strong for certain distances and orientations resulting in Bragg peaks corresponding to the crystal lattice structure. Bragg peaks can be used to map the crystal structure and distance and typically have good signal to noise. Furthermore, an infinite crystal will form a single Bragg point, whereas a crystal of smaller size will result in a broaden the Bragg peaks as described by the Scherrer equation[56, 57]. Diffraction can therefore also be used to determine crystal sizes as described in chapter 3.

Ptychographic X-ray Computed Tomography (PXCT) has been used to study complete stacks of organic solar cells. The key idea behind ptychographic 2D projection is to use a coherent beam to oversample an object with regular intensity measurements and use the extra intensity constraints to restrict the phase solution so it can be determined uniquely. It is a phase contrast method with an arbitrary field of view, as it is a scanning method with overlapping measurements, and a high spatial contrast. It is ideal for high resolution, especially for elements which have little difference in absorption contrast, since the increased contrast by phase imaging enabler segmentation otherwise not possible. More detailed explanations can be found in chapter 4.

Tomography is a general method to convert 2D projections to 3D maps, and has been used to extend the ptychographic 2D phase contrast projections to 3D electron density tomograms. The key idea behind tomography is to construct a 3D model of an object by imaging it with penetrating rays from multiple angles. The data can either be analytically transformed from a sinogram to a real space object, or be found algebraically by minimization using the constraints from the multiple angles. It can be used together with any 2D imaging method to extend it into 3D by multiple exposures from different directions, see also chapter 5.

1.5 Summary

We are facing growing energy needs, which has to be met without further forcing of climate change. The only sources with suitable potential are wind, solar and nuclear (in particular fusion energy). Among solar technologies, organic photovoltaics, are promising due to a low production cost and fast, scalable production methods. Although their efficiencies and lifetimes are lower than other technologies, a low energy payback time makes organic photovoltaics competitive. Regardless of the solar energy technology that is used its success and wide commercial use depends on flexible energy consumption and efficient energy storage.

Organic solar cells are a nano technology in the sense that most layer thicknesses' are on the order of 100's of nm and key processes, such as electron-hole separation, are on the order of 10 nm. The two component active layer can be processed into water dispersible nano particles, which provides the possibility of doing scalable engineering of morphology and facilitate the transition of the organic photovoltaic technology from labs to industrial production. We investigate model systems and whole solar cells in the nm scale using X-ray

based methods to understand the challenges associated with the photoactive nanoparticles. The techniques used are:

- Spectroscopy techniques to map chemical composition and degradation state.
- Small angle scattering to measure particle and domain size distributions.
- Wide angle scattering to measure domain size and orientation of crystalline regions.
- Ptychographic tomography to map 3D electron density distributions.

CHAPTER 2

Degradation in PBCM and P3HT studied by X-ray absorption

Introduction

The OPV technology can compete with silicon solar cells on EPBT despite lower efficiency of OPV compared to silicon solar cells as mentioned in chapter 1. A central part of the energy pay back is lifetime. Improving device lifetime means understanding and preventing degradation processes. Some of the main degradation pathways are water and oxygen reacting with the active layer materials and degrading them to materials with reduced or no photovoltaic efficiency[58]. The degradation is accelerated by heat and photons – essentially when the organic solar cells are exposed to sun light[59]. Two ways to prevent degradation are better barrier layers, which block out oxygen and water, and more stable material compositions.

A thorough understanding of the degradation process is needed in order to achieve stable material composition. This chapter is focused on quantifying degradation in the active layer materials P3HT and PCBM using X-ray absorption. The first section introduces the current knowledge of degradation in P3HT and PCBM, as well as the NEXAFS and STXM method. The last sections deal with a specific experiment, data treatment and results. The STXM technique is also used to study nanoparticle films in chapter 3.

2.1 Degradation in P3HT and PCBM

Degradation studies with P3HT, PCBM and similar materials have mainly aimed at improving device durability[60]. The photodegradation in P3HT has been found to be caused by oxidation of the sulfur atoms and the side chains[61][62]. Photodegradation in PCBM is caused by oxidation of the fullerene cage[63]. In general there has not been many investigations of spatial degradation, but studies above the nanometer scale exist. An experiment by Feron et al. has mapped photocurrent and quantum efficiency for whole structures on the millimeter scale[64]. Time-of-flight Secondary Ion Mass Spectrometry (TOF-SIMS) has also been used to map OPV devices achieving nanometer depth resolution[65]. TOF-SIMS studies with oxygen-18 show formation of pinhole structures on the micron scale in Buckminsterfullerene (C60)[66]. TOF-SIMS excels at elemental analysis and is best used to map infiltration of exotic elements, but can not image disintegration of existing materials. Photo degradation of the active layer has to our knowledge not been investigated on the nanometer scale but it can be done by combining NEXAFS and STXM.

2.2 Principle of NEXAFS and STXM

NEXAFS is a technique to indirectly measure electron energy levels of specific elements, e.g. chemical bonds by X-ray absorption[55]. X-ray absorption depends mainly on electron density, i.e. elements and density. It is therefore impossible to distinguish between two elements with different chemical bonds using multichromatic X-ray absorption. However, with sufficient energy resolution it is possible to scan energies near an absorption edge and detect the difference in chemical bonds as illustrated in figure 2.1.

The technique is partly explained by the photo electric effect where X-ray photons can only transfer their energy to an electron if the photon energy is sufficient to reach a higher energy state. The fraction of X-rays that is absorbed depends mostly on which atomic energy levels are available which is modified by chemical bonds. The bond orientation and X-ray polarization also affects the absorption cross section, because bonds absorb stronger when they are oriented parallel with the polarization direction. This effect is more pronounced if the probed molecules are highly ordered.

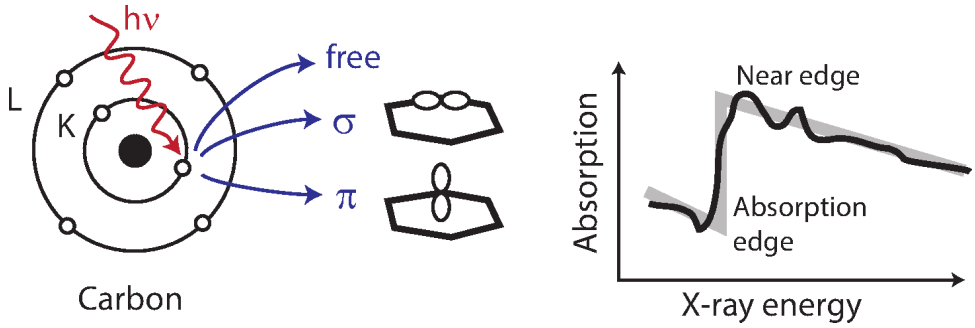

Figure 2.1: NEXAFS principle: An X-ray photon is absorbed if it can move a core electron to a higher energy state, and the available energy depends on chemical bonds e.g. σ orbital or π orbitals. Overall X-ray absorption increases sharply when the energy becomes sufficient to excite new electrons in an atom, which is known as an absorption edge e.g. carbon k-edge. In general the X-ray absorption depends mainly on the number of electrons, but near an absorption edge the available states cause significant perturbations in the absorption making it possible to distinguish molecules with similar elements but different chemical bonds.

The effect of chemical bonds on X-ray absorption is stronger when the X-ray photon just has enough energy to transfer an electron to a higher energy state, i.e. near an absorption edge. The near edge regions denote the energies around an absorption edge, which is named after the origin of the excited electron, e.g. the carbon-K edge tells us the electron originates from the inner shell of the carbon atom. Because the absorption edges are element dependent, it is possible to map elements by selecting energies corresponding to an edge. Different molecules with similar elements can be distinguished by perturbations in the X-ray absorption caused by the chemical bonds that modify the electron energy levels[55]. This way NEXAFS provide a way to study even small chemical changes - like photo degradation

in materials relevant for organic photovoltaics.

Chemical information from NEXAFS scans can be resolved spatially by systematically scanning an area, i.e. STXM. Fresnel lenses and an order sorting aperture (OSA) focus the soft X-rays down to nanometer spot sizes making it possible to scan chemical changes with nanometer resolution. X-rays need to penetrate the sample, thus the sample thickness is limited to a few hundred nanometer for soft X-rays. Thicker samples can have there surface investigated by total electron yield but the probed area is limited to a few nanometers[55]. Samples are normally prepared similar to transmission electron microscopy (TEM) on copper grids or silicon nitride membranes. In practice, when measuring absorption, one needs a proper measurement of the incoming X-rays to deduce the percentage absorbed by the material. Furthermore, spectra are normalized to an energy far from an absorption edge (no near edge features) to correct for sample thickness. The energy scale also needs to be calibrated between measurements to enable comparison. For more corrections and normalizations associated with NEXAFS measurements see Collins and Ade[67].

NEXAFS work on materials for P3HT and PCBM

NEXAFS spectra of pristine P3HT and PCBM show that only the first P3HT π^* peak is slightly perturbed by polarization[68, 69]. Polarization is thus not a major concern for degradation mapping. Blend measurements also show it is possible to make composition fits to P3HT-PCBM[69]. Degradation in blends can therefore also be tracked. Spatial NEXAFS maps have been used to follow domain formation in P3HT-PCBM blends during annealing[**?**, 70]. In fact Burke et al. has mapped nano structures of P3HT and PCBM down to a 10 nm resolution using STXM and model fits[71].

2.3 Degradation in OPV materials

The aim of the experiment is to spatially map the degradation states of OPV materials using systematic NEXAFS scans over an area (effectively STXM scans at multiple energies). The samples are thin films of OPV material where different samples are degraded to different levels. For each sample, a NEXAFS spectrum is obtained and for a limited number of samples multiple energy STXM maps. Degradation is mapped using least square fitting of measured reference spectra. Before showing the results, the sample preparation and materials will be discussed.

Methods

The experimental setup has two main steps.

1. Sample preparation: Produce thin homogeneous films of active layer materials with known degree of degradation.

2. NEXAFS measurements: Acquire comparable spectra with sufficient features to map degradation, without inflicting additional degradation from X-ray exposure (beam damage).

Sample preparation

Pure material (see table 2.2) or material blends in chloroform solution were spin coated (material dropped on a spinning substrate) on 100 nm thick silicon nitride membranes. Silicon nitride is a good sample substrate as it is commercially available as thin membranes (<100 nm) and therefore absorb a low fraction of the X-rays. P3HT samples were degraded on glass substrates with PEDOT:PSS and floated onto copper grids afterwards. This preparation method carried problems with film wrinkling and disintegration and was not pursued for the other materials. However, when P3HT was spin coated on silicon nitride membranes it formed small aggregates instead of homogeneous films unsuitable for X-ray absorption experiments. Thus, P3HT data from samples on copper grids were used.

Name	Formula	Molecular weight (g/mol) per monomer
P3HT	$C_{10}H_{14}S$	166.28
PCBM	$C_{72}H_{14}O_2$	910.88
PC70BM	$C_{82}H_{14}O_2$	1030.99
bis PCBM	$C_{84}H_{28}O_4$	1101.12
C60	C_{60}	720.64
C70	C_{70}	840.78
ICBA	$C_{78}H_{16}$	952.96

Table 2.2: Materials used for degradation studies using energy resolved X-ray absorption.

Sample degradation

Absorption was measured in the ultraviolet-visible spectrum and the state was determined based on integrated absorption (wave-lengths of 400-600 nm). The initial absorption of pristine films was denoted T100. Degraded samples were exposed to 1 SUN in an AM 1.5 solar simulator until only a fraction of the initial absorption was left (if 80% of pristine absorption was left, it was denoted T80). The degradation times are shown in table 2.3 where it can be noted that the degradation rate of is reduced for the bend.

Material	Optical density	Degradation rate[72] (%/h)	T80 (h)	T60 (h)	T40 (h)	T20 (h)
P3HT	0.47	2.5	8	16	-	34
PCBM	1.0	0.36	60	120	-	-
P3HT-PCBM	0.69	0.36	60	120	180	-

Table 2.3: Degradation rates and times to reach certain degradation states. Missing states were either not prepared, or no X-ray data were successfully obtained for the sample. Note state names are rounded to nearest 10 for a clearer presentation.

X-ray measurements

X-ray absorption was measured for soft x-rays at the carbon k-edge (energies 282-292 eV, step size of 0.1 eV) at the synchrotron beamline (experimental station) UE46-PGM2-STXM at Bessy II, Berlin. The settings were chosen, such that no beam damage was visible in subsequent scans. The scan types point, line and image used 10 μm focus and 500 ms dwell time, 300 nm focus and 20 ms dwell time and 30 nm focus and 10 ms dwell time respectively.

All data were converted to optical density (OD) and normalized. X-ray absorption follow Lambert-Beers law, where the initial x-ray intensity, I_0, is reduced to the intensity, I, after penetrating a material of thickness, x with absorption coefficient μ

$$I = I_0 \exp(-\mu x) \tag{2.1}$$

As we measured on spin coated films it was not possible to obtain I_0 with each measurement, and this was done separately on areas without film. In equation 2.1 only the absorption coefficient, μ, depends on the X-ray energy. Because the X-ray spectra are normalized the thickness, x, can be absorbed into a unitless measure for absorption: Optical Density, OD.

$$OD = \ln\left(\frac{I_0}{I}\right). \tag{2.2}$$

The error of the measured intensity, δI, is given by the Poisson error on the photon count.

$$\delta I = \sqrt{I}. \tag{2.3}$$

From error propagation the error of the optical density, δOD, is:

$$\delta OD = \left|\frac{\partial OD(I)}{\partial I}\right| \delta I = I^{-1}\sqrt{I} = \frac{1}{\sqrt{I}} \tag{2.4}$$

Energy calibration

Between different NEXAFS experiments there is a need for energy calibration to be able to compare spectra, which is necessary for compositional mapping. There were two experiments with P3HT, one measurement on TEM-grid and one on a silicon nitride membrane (where only P3HT T100 was successfully measured). One of the differences were the detector setup with a photo avalanche diode for the TEM-grid experiments and a photo multiplier for the silicon nitride experiments. The difference in energy is caused by the difference in detector and beamline calibration. As the P3HT T100 spectrum was obtained for both experiments, it was used for calibration as shown in figure 2.4

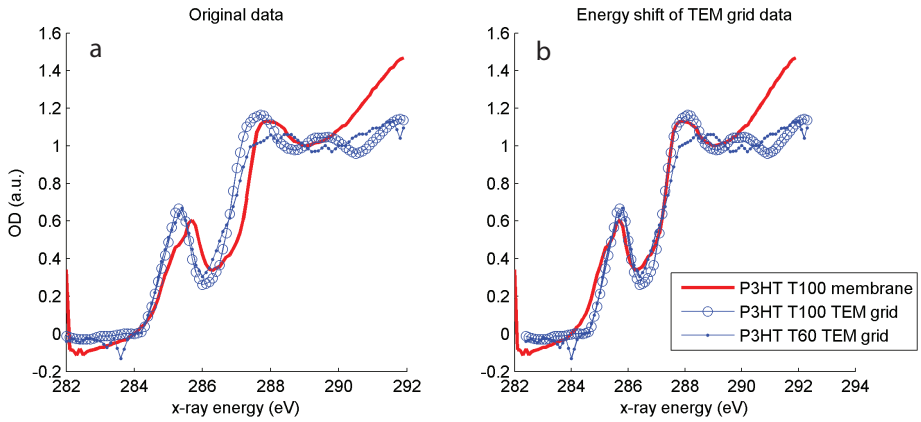

Figure 2.4: Calibration of NEXAFS spectra for P3HT on TEM grids to P3HT on silicon nitride membranes by an energy shift of 0.4 eV. This ensures the degraded spectra later can be fitted to blend spectra (measured on silicon nitride).

Data and analysis

With the basic sample preparation and data treatment covered, the experimental section will cover:

Raw data

- Degraded P3HT, PCBM and P3HT:PCBM 1:1 blend
- Analogues to P3HT and PCBM (for comparing degradation products).

Fitting linear combinations

- Introducing fitting and interpretation
- P3HT:fullerenes tests of
  - compositional mapping (mass fraction)
  - state mapping (chemical state).
- Degradation mapping of components in P3HT-PCBM blends.
- Spatial degradation mapping in P3HT films.

Photo degradation of P3HT and PCBM

Understanding the chemical changes is the first step in understanding the degradation process. Thus we will interpret the NEXAFS spectra of phtotodegraded P3HT, PCBM and 1:1 blend shown in figure 2.5. The difference in chemical composition gives rise to different spectra. In the chosen energy range we see two peaks in P3HT and 3 peaks in PCBM marked in figure 2.5. The blend appears to be a linear combination of the two spectra at least in the pristine state.

Consider the chemical meaning of the photo degradation. As P3HT degrades it keeps much of its structure until the final degradation step. Previous studies conjectured that

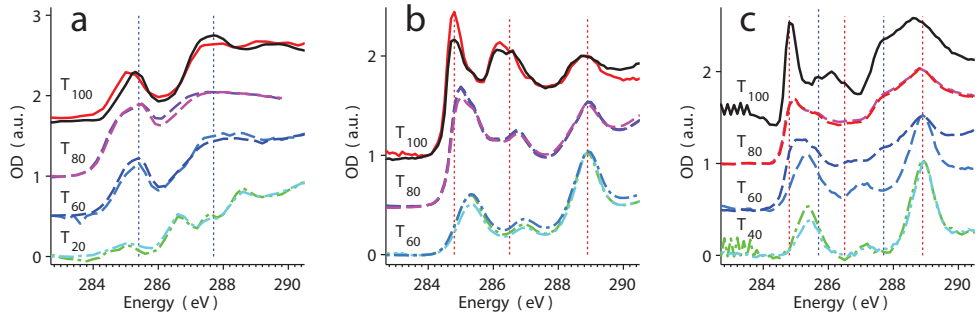

Figure 2.5: NEXAFS spectra of optically degraded a) P3HT, b) PCBM and c) P3HT and PCBM blend. Multiple spectra in the same state indicate multiple measurements. The spectra suggest the blend spectra can be found as a linear combination of the pure materials at various degradation steps.

the first two carbon peaks correspond to σ bonds in the P3HT molecule, whereas peaks at higher energies constitute the π bonds[69]. Part of the chemical changes in P3HT might take place outside the measured energy interval, and can therefore not be investigated in this study. The changes from P3HT T100 to T60 are too subtle to interpret directly. The final degradation step to T20 shows a drastic change in the spectrum with an overall increase in energies indicating broken bonds and disintegration of the molecule.

The PCBM spectra exhibit some interesting changes. The first and second peak shifts to higher energies, and the relative height between the first and third peak changes (initially the first peak is highest where the third peak is highest for the degraded sample). Density functional theory calculations for PCBM estimated the individual carbon atoms contribution to the full PCBM spectrum[74]. It indicated fullerene cage atoms contribute mainly to the first peak (284.8 eV), whereas the side chain contributes to the third peak (288.9 eV). This indicates that fullerene cage atoms are oxidized, causing a peak shift, whereas the side chain remains unchanged. That would also cause a change in relative peak intensity. The interpretation is consistent with another study which found PCBM photo-degradation to be caused by oxidation of the fullerene cage[63].

Pristine P3HT-PCBM blends have peaks from both P3HT and PCBM indicating two degradation processes taking place independently. The rate of degradation is greater for P3HT than for PCBM e.g. see table 2.3. This becomes very clear when comparing T60 of the pure PCBM with T40 of the blend as P3HT signal is lost whereas PCBM remains. An independent degradation means that the blend spectra can be expressed as a linear combination of the spectra of the pure materials.

PCBM and P3HT analogues

Studying NEXAFS spectra of different materials similar to P3HT and PCBM is another source of chemical information i.e. a subset of analogues might both share a feature in their NEXAFS spectra and chemistry. A number of PCBM and P3HT analogues are shown in figure 2.6. The peak positions of the analogues are similar to P3HT and PCBM, but show additional peaks, perturbed peak positions and different peak heights. For instance, P3HT

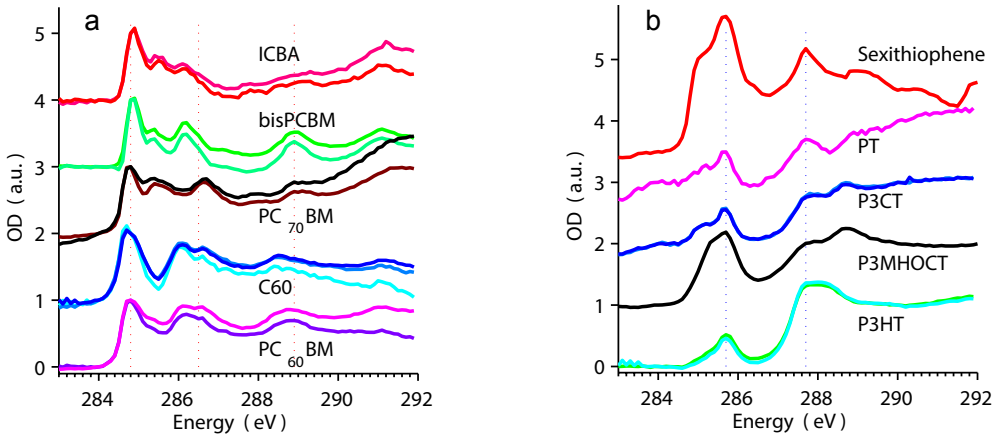

Figure 2.6: NEXAFS spectra of the carbon K-edge for a) PC60BM and PC60BM-analogous and b) P3HT and P3HT-analogues. More than one curve for a material indicates different measurements.

analogues with simpler or no side chains (Sexithiophene and PT) have a more pronounced shoulder for low energies (285 eV). As seen on the degradation spectra (Fig. 2.5) none of the analogues resemble steps in the degradation pathway of P3HT and PCBM. For P3HT it is an indirect indicator that the side chains do not change during degradation and the conjugation length does not decrease (they do not acquire a shoulder resembling sexithiophene). For the PCBM degradation pathway it indicates that the oxidation is not happening at the side chains but on the fullerene cage which supports our previous hypothesis.

Introducing linear combination

The main aim is to track degradation, and P3HT-PCBM blend is most relevant as it is deployed in the OPV devices as active layer. To extract the degradation of each component in the blend signal, it is necessary to develop a method to decompose the signal into the signal of the two pure materials. It was noticed that the blend had peaks from both materials. This could be achieved if the blend spectrum was a linear combination of the pure spectra. We will now pursue the path of linear combinations more rigorously with a theoretical derivation using Lambert-Beers law, test on various P3HT-fullerenes blends and lastly apply to the P3HT-PCBM blend material.

Linear combinations from Lambert Beers law

Assuming that the materials do not interact chemically, the X-ray absorption in a blend of two materials, a and b, can be expressed by the thickness x and the absorption coefficient μ

$$I = I_0 \exp(-\mu_a x_a) \exp(-\mu_b x_b) = I_0 \exp(-\mu_a x_a - \mu_b x_b). \tag{2.5}$$

The optical density of the blend material can be written as a linear combination of the pure optical densities (see equation 2.2), by reformulating the thickness, x_a and x_b, into the

scaling parameters, α and β;

$$OD_{blend} = \mu_a x_a + \mu_b x_b = \alpha OD_a + \beta OD_b$$

Our data is fitted by a linear combination of, OD_{P3HT}, and the used fullerene $OD_{Fullerene}$, to the blend spectrum, OD_{Blend}. A constant, γ_i, is used to correct for any offset. The fitting is performed by minimizing residuals squared, r^2:

$$\min(r^2) = \min((OD_{i\_Blend} - OD_{i\_Fit})^2)$$

$$OD_{i\_Fit} = \alpha\, OD_{i\_P3HT} + \beta\, OD_{i\_Fullerene} + \gamma_i$$

The goodness of fit is evaluated by the reduced chi square, χ^2_{red}. χ^2_{red} is based on the residuals, r, and the variance σ, and the degrees of freedom, ν

$$\chi^2_{red} = \frac{1}{\nu} \sum_i \frac{r_i^2}{\sigma_i^2}, \tag{2.6}$$

where the degrees of freedom is given by the number of data points minus fit parameters in our case 3. The obtained parameters, α and β, will be used to check mass composition. Whereas the goodness of fit χ^2_{red} will be used to estimate chemical state.

Mass ratio from NEXAFS spectra

Mass ratio is interesting to map the heterogeneities in blend materials, and for instance correlate with degradation rate. The NEXAFS signal is largely affected by the bonds of the carbon atoms near the carbon edge. At higher energies (further from the carbon edge) absorption becomes independent of the local bonds and depends only on the number of carbon atoms. NEXAFS spectra are normalized to 1 at the highest energies, because the average signal at these energies depends on the elements and not the molecular structure (one have to ensure not get affected by an extended X-ray absorption fine structure signal). The scale parameters α and β can be linked to mass ratio through carbon density. A number for the theoretical ratios between α and β can be calculated based on the number of carbon atoms, C, carbon atoms per molecule, N_C, the molecular weight, M, and the mass ratio m_α/m_β.

$$\frac{\alpha}{\beta} = \frac{C_\alpha}{C_\beta} = \frac{m_\alpha}{m_\beta} \frac{N_{C\_\alpha}/M_\alpha}{N_{C\_\beta}/M_\beta} = \frac{N_{C\_\alpha}/M_\alpha}{N_{C\_\beta}/M_\beta} \tag{2.7}$$

$m_a/m_b = 1$ for mass ratio of 1:1. The ratio α/β for blends of P3HT and various fullerenes is calculated with P3HT as α and fullerene as β and, shown in table 2.7 (for a mass ratio of 1:1). The calculations are based on data shown in table 2.2. The predicted ratios do not match the obtained fitting ratios very well as seen on Fig. 2.8. It therefore seems the method is not suited for determining the mass ratio in blends without further corrections. However, the method has in general been shown to work[75, 67], but observed problems arise due to our limited range of energies. The absence of higher energies means our normalization values still are the in the near edge region, and is therefore not an adequate representation of the number of carbon atoms. It would therefore be ideal to include higher energies in the spectra for future experiments, as at least a few measurements at higher energies (above 340 eV) [67] would provide proper normalization and not compromise the experiment with an increased exposure time. Because mass ratios cannot be extracted reliably from our current dataset, no further discussion will be forthcoming.

Combination	ratio α / β
P3HT / PCBM	0.76
P3HT / PC70BM	0.76
P3HT / bis PCBM	0.79
P3HT / C60	0.72
P3HT / C70	0.72
P3HT / ICBA	0.73

Table 2.7: Material blends and their predicted contribution ratio to a blend NEXAFS spectrum for a mass ratio of 1:1. The weight ratio used is α/β = (P3HT weight / fullerene weight).

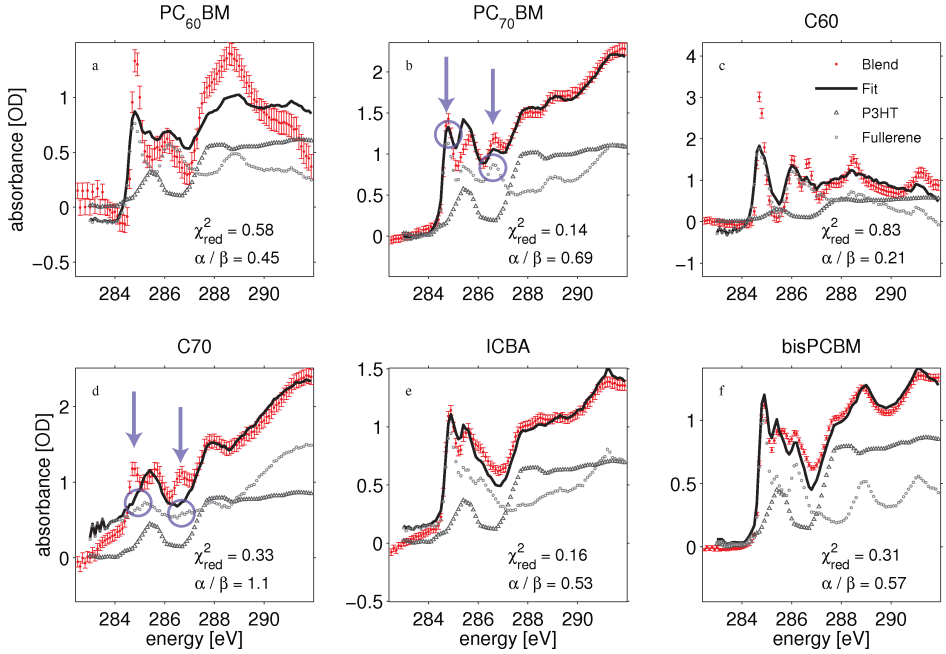

Figure 2.8: NEXAFS spectra of P3HT-fullerene blends (with the fullerene stated in the headline of each plot): In each sub-figure the blend data (red), The P3HT (dark grey) and the fullerene (light grey) are shown along with the linear combination of the pure NEXAFS spectra (Black). At the bottom of each fit is stated the found mass ratio, α/β = (P3HT weight / fullerene weight) and goodness of fit χ^2_{red}. The arrows in figure d) indicate C70 is spectrum is incorrect, as it is missing two peaks that are present it similar samples i.e. P3HT-C70 blend, the P3HT-PC70BM blend and pure PC70BM. [73] - Adapted by permission of The Royal Society of Chemistry.

State mapping using NEXAFS signal

Chemical state mapping in blend materials are important to map the degradation state in P3HT and PCBM. To test the robustness of method initial test experiments with known

state is performed. In general the chemical state of a material in terms of bonds is determined by the overall shape of its NEXAFS spectrum. The most likely state of individual components in a blend can be selected from a set of possible reference states or "state catalogue". This is performed by fitting all possible linear combinations of relevant reference states to the blend spectra. The best fit is chosen based on reduced χ^2). The method is inspired by model testing often employed in astronomy[76, 77] and has to our knowledge not been applied to NEXAFS data before. We employ a simple data driven scheme where we estimate the uncertainty of the χ^2 through a test experiment with blends of P3HT and various fullerenes. The test is designed to determine the fullerene component in known P3HT-fullerene blends using measured NEXAFS spectra of the pure P3HT and fullerene materials. In table 2.9 we show the reduced χ^2 values for all linear combinations.

χ^2_{red}	PC60BM	PC70BM	C60	C70	ICBA	BisPCBM
P3HT-PC60BM	***0.58***	0.97	**0.54**	1.00	0.97	0.76
P3HT-PC70BM	0.68	***0.14***	0.92	1.13	0.57	0.62
P3HT-C60	1.01	1.63	***0.83***	2.82	2.12	1.63
P3HT-C70	0.63	**0.21**	0.70	*0.33*	0.35	0.53
P3HT-ICBA	0.34	**0.15**	0.58	1.01	***0.16***	**0.13**
P3HT-BisPCBM	0.59	0.72	1.33	3.14	0.95	***0.31***

Table 2.9: Reduced χ^2 obtained from fitting linear combination of NEXAFS spectra of P3HT and various fullerenes (ordered horizontally) to blend spectra (shown vertically). Bold denotes the lowest reduced chi square value and values within 0.1 of this optimum. The exception is P3HT-C70 (discussed in the main text), otherwise the reduced chi square determines the correct fullerene spectra within a precision of 0.1.

Test experiments for PC70BM, C60 and bisPCBM unambiguously identified the correct fullerenes using this method. These cases indicate the method can work but cannot be used to estimate uncertainty. However, in two cases (PC60BM and ICBA) the correct fullerenes did not have the lowest reduced χ^2, but values close to the lowest reduced χ^2. A rough estimate of the uncertainty of the reduced χ^2 is found to be 0.1, as this range allow the correct fullerenes to be selected within uncertainty. Using similar experimental setup and data treatment for later data, we will use an uncertainty of 0.1. Alternative ways to estimate χ^2 more mathematically can be found in reference[76, 77].

The five cases that has meaningful reduced χ^2 results has been discussed. One dataset, C70, did not pinpoint the correct component within the uncertainty. A closer examination of the data revealed problems with the pure C70 sample. In particular, the primary carbon absorption peak near 285 eV is missing, which is present in the PC70BM and the blend P3HT-C70 (as well as all the other fullerenes). Overall the NEXAFS spectrum of pure PC70 bears little resemblance to the other fullerenes and is most likely a product of a contaminated sample. As such it is not meaningful for our test case for state mapping.

In conclusion, the method seems adequate at determining the right component of a blend material with an uncertainty of 0.1 in the reduced χ^2 in the test experiment. The more interesting case of degradation in P3HT-PCBM can now be discussed.

2.4 Degradation in P3HT-PCBM blends

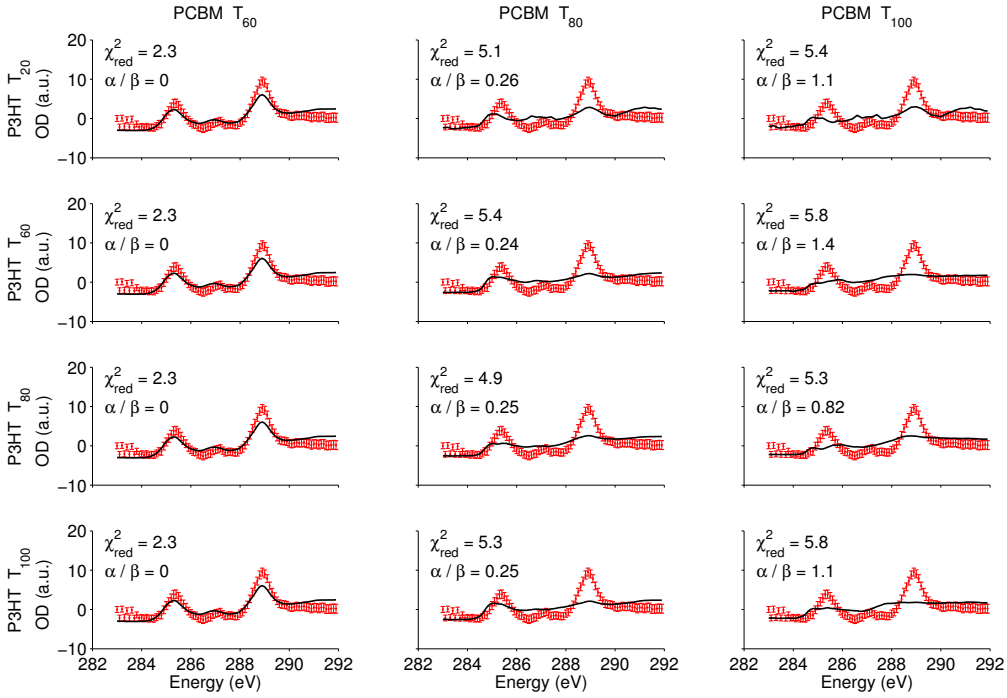

Figure 2.10: Linear fits of degraded PCBM and P3HT to a blend T40 spectrum. The data (red) is the same in each plot, and the linear combination (black) is indicated by the column (PCBM, labelled top) and row (P3HT, labelled left). The chi-squares along with the weighted ratio are displayed for each fit. In this case the lowest reduced χ^2 are for PCBM T60, all of which have a zero weight of P3HT ie. no P3HT signal as $\alpha/\beta = 0$. [73] - Reproduced by permission of The Royal Society of Chemistry.

Determining the degradation states in P3HT-PCBM blend is interesting because it allows us to quantify the reduction in degradation rate we observed based on table 2.3 and figure 2.5. The goal is determine the individual degradation state of the P3HT and PCBM material using a state catalogue of the 4 P3HT and 3 PCBM degradation states shown in figure 2.5. For each photodegraded state of P3HT-PCBM we test all possible linear combinations (12 fits) and based on the reduced chi-square estimate the most likely composition. As an example the fits for blend T40 is shown in figure 2.10. The lowest reduced χ^2 are found in combinations of PCBM T60 and any P3HT for T40. When the ratio α/β equals 0 ($\Rightarrow \alpha = 0$), the only signal contribution comes from PCBM. This could be due to phase segregation (so only PCBM was measured) but similar results are obtained from different measurements, indicating that the P3HT is degraded to a point where it does not contribute to the NEXAFS spectra of the blend material.

The remaining blend materials are investigated using the same procedure. The degra-

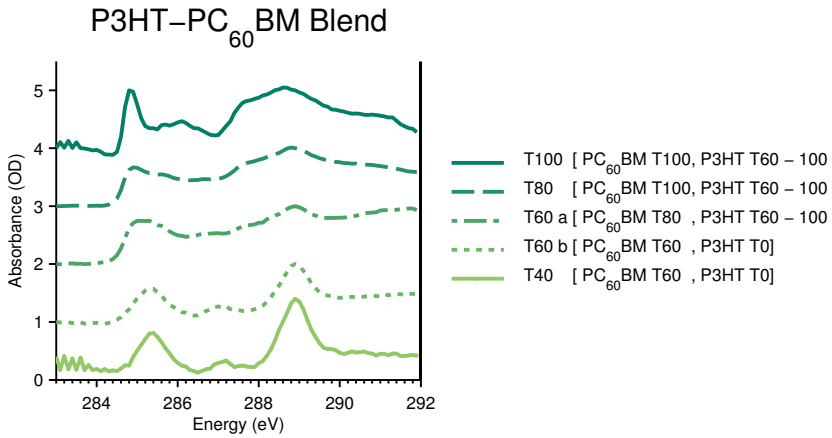

Figure 2.11: NEXAFS spectra of optically degraded P3HT-PCBM blends. The denoted degradation steps to the right are the assessment of the component degradation using the spectra shown in figure 2.5 as state catalogue. The clear difference in the PCBM NEXAFS spectra provides more accurate values for PCBM degradation as compared to P3HT. [73] - Reproduced by permission of The Royal Society of Chemistry.

dation states found are indicated in figure 2.11, whereas a more detailed view of the reduced chi squares is found in table 2.12. Due to the uncertainty in the reduced χ^2 there is several cases of ambiguity in the state of P3HT. The overall result is that P3HT is faster degraded than PCBM, also in the blend material, to the point of complete degradation at blend T40. It seems feasible, to track small changes caused by photodegradation especially in PCBM. It is possible more significant results could be obtained for P3HT if measuring at a greater energy interval as discussed previously.

Besides an increased understanding of the degradation process, the results can also be used to estimate the quantitative difference in degradation rates between pure materials and material blends. The degradation rate of pure P3HT and PCBM are known from previous experiments[72]. The degradation rates in the blend are found from degradation time and the fitting results (see table 2.3 for degradation times). The earliest point for P3HT to reach T0 (complete degradation) is in a T60 blend sample. This would mean a change in degradation rate from 2.5% / hour to 0.82% / hour (the percent refer to number of percent point loss of original absorption). That means a decrease in degradation by a factor of 3 due to contact with PCBM. This estimate is conservative as there is both T60 blend samples with and without P3HT signal, so the decrease in degradation could be larger, but is found to be at least a factor of 3.

The T60 blend is either PCBM T60 or T80. It corresponds to a degradation rate going from 0.36% / h for pure PCBM to 0.16-0.33 % / h for PCBM mixed with P3HT. The reduction in PCBM degradation rate is less pronounced than in P3HT with a decrease between 1.1 and 2.3. The fact that degradation rate in PCBM decreases shows that the reduced degradation in P3HT is not transferred to PCBM as a result of the charge transfer, but that the contact between P3HT and PCBM cause both to degrade slower.

The reduced degradation of P3HT and PCBM blends have been observed previously[72], but to our knowledge the degradation rates of the individual components within a blend have not been quantified before.

We conjecture the overall mechanics for the reduced degradation rates can be explained by charge transfer from P3HT to PCBM. The reduction in P3HT degradation could be caused by PCBM quenching of the excited state of P3HT[63]. The reduction in PCBM degradation could be caused by excess electrons (from P3HT) filling vacancies in the PCBM homo level and thereby reducing the degradation.

Blend T100	PC60BM T60	PC60BM T80	PC60BM T100
P3HT T20	1	1.1	0.81
P3HT T60	0.86	0.86	**0.63**
P3HT T80	0.91	0.86	**0.58**
P3HT T100	0.89	0.88	**0.58**
BLEND T80	PC60BM T60	PC60BM T80	PC60BM T100
P3HT T20	1.5	1.4	1.1
P3HT T60	0.87	0.72	**0.4**
P3HT T80	1.2	0.79	**0.41**
P3HT T100	1.1	0.84	**0.37**
BLEND T60a	PC60BM T60	PC60BM T80	PC60BM T100
P3HT T20	2	0.73	1.4
P3HT T60	1.1	**0.1**	0.77
P3HT T80	1.8	**0.16**	0.98
P3HT T100	1.3	**0.098**	0.59
BLEND T60b	PC60BM T60	PC60BM T80	PC60BM T100
P3HT T20	**0.048**	0.59	0.74
P3HT T60	**0.048**	0.64	0.87
P3HT T80	**0.048**	0.53	0.74
P3HT T100	**0.048**	0.63	0.86
BLEND T40	PC60BM T60	PC60BM T80	PC60BM T100
P3HT T20	**2.3**	5.1	5.4
P3HT T60	**2.3**	5.4	5.8
P3HT T80	**2.3**	4.9	5.3
P3HT T100	**2.3**	5.3	5.8

Table 2.12: Reduced χ^2 obtained from fitting linear combination of NEXAFS spectra of degraded P3HT and PCBM. Bold denotes the lowest reduced chi square value and values within 0.1 of this optimum. When multiple fits are within the χ^2_{red} uncertainty it leaves some ambiguity i.e. PCBM state is determined in each case, but the P3HT state is denoted by an interval. Blend T60a and blend T60b denotes measurements at two different positions of the T60 blend.

2.5 Spatial degradation in P3HT films

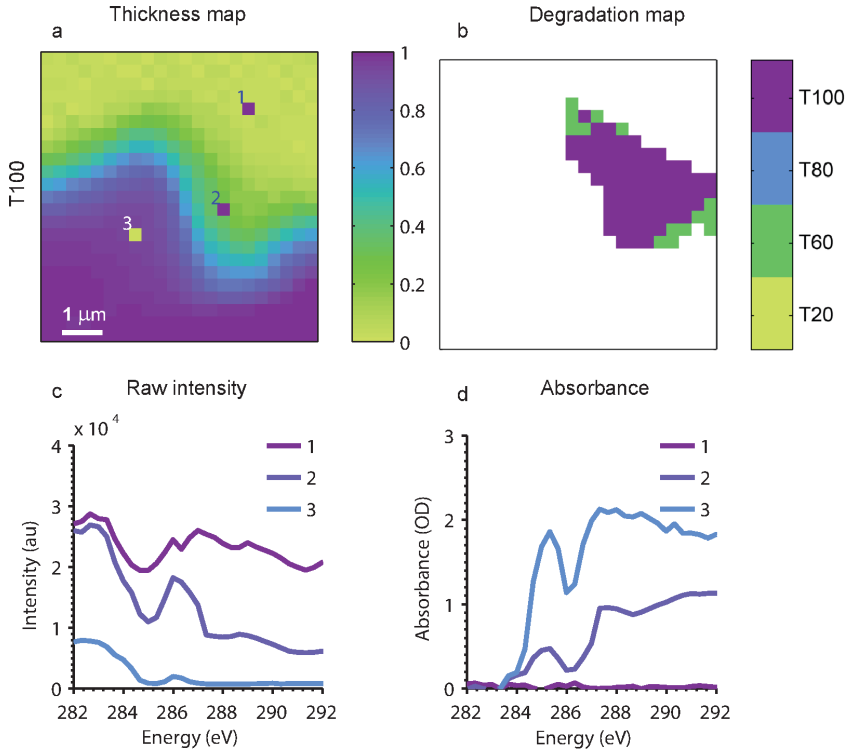

Figure 2.13: a) Thickness map of P3HT T100 film obtained from STXM map at 286 eV. 3 positions have been marked and their raw intensity profiles are shown in figure c, and their optical densities are shown in figure d. b) Degradation state maps of areas with appropriate thickness, obtained from fitting reference spectra. Point interpretation: 1) shows intensity from an area without a film (seen by plenty of raw intensity and a constant optical density of zero). 2) shows an area with appropriate thickness for obtaining a P3HT NEXAFS spectrum (never total absorption, but sufficient absorption to form an optical density profile). 3) shows an area with too high material thickness (seen by total absorption in part of the raw intensity profile, resulting in distorted optical densities). [73] - Reproduced by permission of The Royal Society of Chemistry.

The difference between the two T60 blends from figure 2.11 indicates that spatial differences in degradation might be present. A scanning variation of the NEXAFS technique known as energy resolved STXM is well suited for investigating spatial heterogeneities. Combined with modelling, resolution down to 10 nm has been demonstrated[71]. As P3HT is the fastest degrading component, it is the most critical for device lifetime. To demonstrate the 2D capacity of the developed method, we investigate spatial degradation in pure P3HT

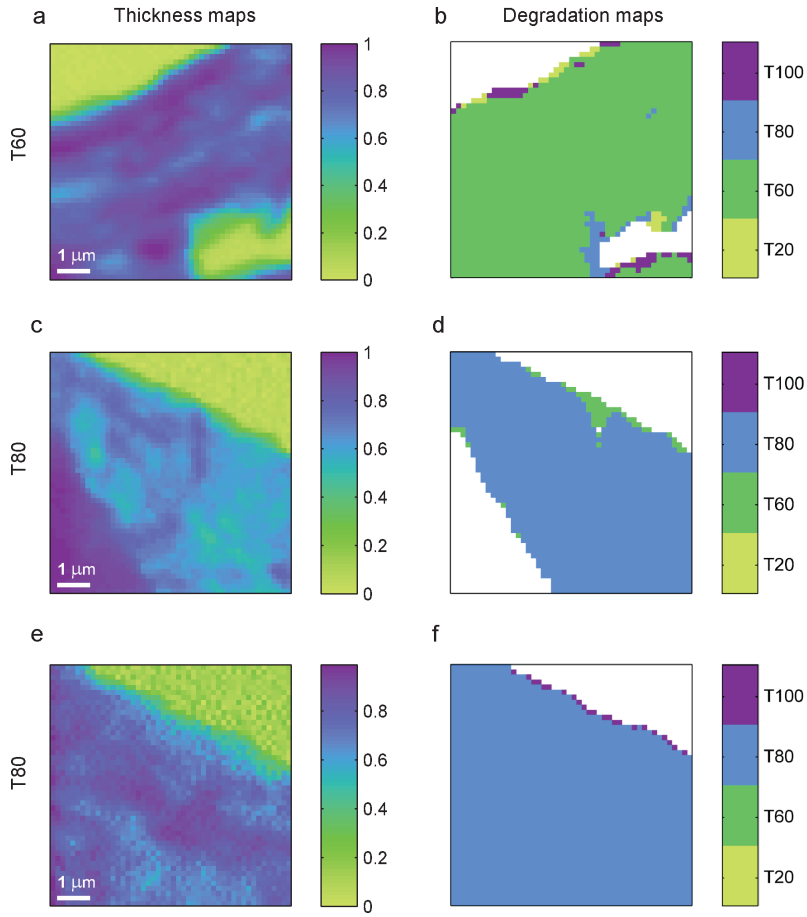

Figure 2.14: STXM maps of degraded P3HT films. Left) Thickness maps obtained at 286 eV. Right) Degradation state maps of areas with appropriate thickness, obtained from fitting reference spectra. The overall film degradation is denoted on the left and is T60: a and b. T80: c, d, e and f. [73] - Reproduced by permission of The Royal Society of Chemistry.

films. We do a 2D energy scan of degraded pure P3HT samples, and fit each point (pixel) to the reference P3HT spectra. For each pixel we estimate the lowest reduced chi-square among the reference spectra (like the outlined method for NEXAFS measurements). It produces degradation maps as shown for T100 in figure 2.13. The relative thickness map is obtained directly from an absorption map (Absorption is proportional to thickness as by Lambert-Beers law equation 2.1).

The T100 map is a special case, where parts of the film is too thick to have proper absorption spectra. This is illustrated in figure 2.13, where raw absorption and converted

optical density is shown for 3 points: one with no material, one with appropriate film thickness and one with too high film thickness. In areas with no material the optical density becomes zero, and the area is left white. In cases with too thick a film the raw intensity reaches zero in several areas (where no information is effectively obtained). This results in greatly distorted optical densities and is coloured white in the state map. The remaining T100 map is effectively at the T100 state everywhere as expected. Here "effectively" refer to the fact that some edge pixels exhibit different states. However, this is due to shared volume between edge regions and areas with no or too much material. In general the fluctuations in the edge pixels are therefore disregarded in the interpretation.

The spatial degradation maps are seen in figure 2.14. It is apparent that the maps are largely homogeneous and independent of variations in thickness. It indicates that the degradation of P3HT is inherently homogeneous even at the nano scale. Reported inhomogeneities in P3HT can therefore be solely attributed to inhomogeneity in other layers that limit the access to oxygen, water and light[64, 66]. The T80 map has a small area with T60 level degradation extending from the edge and inwards. As there is not generally observed increased degradation from edge regions, we interpret it as a cut in the film below our spatial resolution and an effect of partial volumes.

2.6 Summary and future work on X-ray absorption in OPV

We have, through soft X-ray absorption studies on thin films, determined NEXAFS spectra for P3HT and PCBM at various degradation steps and for pristine P3HT and PCBM analogues. The blend spectra of P3HT and a number of different fullerenes can be obtained through combination of spectra of the pure materials. However the mass ratio could not be obtained from these fits. It might be possible by scanning further from the absorption edge allowing for a more robust normalization.

Using linear fits from degraded material the individual degradation steps of the components in the blend was discerned. This procedure was most accurate for the PCBM which have much slower degradation, and clear degradation features compared to P3HT. We quantified decreased degradation rates in the P3HT-PCBM blend material. The blend reduced degradation rate in P3HT to a least 1/3 and the degradation rate of PCBM to 9/10 of the degradation rate in the pure material. We also showed the strength of this NEXAFS based method by performing 2D degradation mapping of P3HT films. There were a few areas that showed less degradation, but overall the degradation of P3HT was uniform on the sub-micron scale.

Future experiments

- Spatial mapping of degradation in blends:
Spatial effects in P3HT-PCBM blends are relevant since the active layer is a blend of the materials. The pure P3HT films have little initial heterogeneity and as observed in the experiments little spatial heterogeneity in the degradation. Mixed P3HT-PCBM films, on the other hand, have initial heterogeneity that might translate into heterogeneity in the degradation. Photodegradation is reduced in both P3HT and PCBM when mixed, thus the access to interfaces will likely affect the degree of degradation. Furthermore, STXM could map growing domain sizes during photo degradation caused by annealing.

- Degradation of Landfester nanoparticles:
Landfester nanoparticle films differ from BHJ due to the presence of surfactants and possible porous nature providing easier access for diffusing oxygen and water. Both of these factors could affect stability in a negative direction and with different spatial evolution of photo degradation. To evaluate the feasibility of using Landfester particles as the photoactive layer it would therefore be essential to understand differences in degradation mechanisms. In addition, large Landfester particles could be used to probe the spatial extend of reduced degradation in P3HT-PCBM blends e.g. by coating pure PCBM particles on top of a P3HT films and measure degradation rates in PCBM as a function of distance to a particle interface.

CHAPTER 3

Crystallinity and structure of photo-active nanoparticles

Chapter 1 introduced the importance of nano structure in the active layer and presented Landfester particles as a way to control morphology and enable water based inks. This chapter deals with what is inside Landfester particles[28] and how the particles are transformed when processed into films. This chapter is related to the manuscript "Structure and crystallinity in water dispersible photoactive nanoparticles for organic solar cells" submitted to Energy & Environmental Science. The specific questions this chapter seeks to answer are how the material is distributed inside the particle, how the materials order themselves i.e. crystallinity and how these two properties change when the particles are cast into a film. The chapter will present the relevance of this information for OPV application, basic scattering theory and experimentally determined structure and crystallinity for P3HT:PCBM Landfester particles in solution and as thin films.

3.1 Relevance of internal structure and crystallinity for organic solar cells

The requirements for the active layer morphology are: Domain sizes of less or equal to 10 nm to ensure charge separation and connected pathways for all domains through the 100-500 nm thick active layer to ensure charge transport. Processing the active layer material into nanoparticles gives additional possibilities to control the morphology e.g. by ensuring the domain sizes are smaller than 10 nm. By also understanding and controlling the layer formation it can be ensured that the domains are connected for good charge transport. On the sub nano scale, the molecular orientation and in particular crystallinity also plays a role in charge transport as shown by Gomez et al.[78].

What is currently known about the internal structure, layer formation and crystallinity of photoelectric Landfester nanoparticles? Mainly P3HT:PCBM particles have been investigated due to the commercial availability and status as benchmark material for OPV. **primarily by using STXM**, Dastoor et al. have found the nanoparticles to be core-shell structures with a PCBM core and P3HT shell that grows upon annealing[71, 79, 80]. Based on TEM images of single particles and AFM images they have found that the particles preserve their structure and pack hexagonally during film formation[80]. Richards et al. also found a core-shell structure by Neutron scattering[81]. They found that the internal structure could be changed by the fabrication method, e.g. sol-gel fabrication instead of Landfester methods or the addition of C60 in P3HT:PCBM Landfester particles. Furthermore, they related the internal structure to photocurrent and found that a uniform material distribution gave better photocurrent performance in particle monolayers. The best device performance with photoactive nanoparticles has been found for surfactant free particles by

Gärtner et al.[82], where the internal particle structure has not been determined. In this chapter we study the particle structure with new methods and focus on the crystallinity and layer formation of the particles, which has previously have been somewhat overlooked in the investigation of the internal structure of single particles.

3.2 Principle of SAXS

The goal of this section is to derive the theory behind X-ray scattering of nanoparticles and how it can be used to determine size. First we will look at photon scattering from a single electron, then from multiple electrons and at last from a dispersion of nanoparticles.

Scattering from a single electron

For solids in a liquid dispersion the majority of X-rays scatter elastically. Photons mainly scatter from electrons, because photons are electro-magnetic waves and electron densities take up most of the volume of any molecule. Classically, this is explained as electromagnetic waves accelerating the electrons causing them to emit radiation as dipole antennae. For unpolarized X-rays the scattered intensity, I_e , of a single electron is given by the incoming X-ray intensity, I_0, the angle between incident and scattered beam, 2θ, the classic electron radius, r_0, the distance to detection, r, the X-ray frequency, ω, and the emitting electron frequency, ω_0, [51].

$$I_e(2\theta) = r_0^2 \left(\frac{1 + cos^2(2\theta)}{2} \right) \frac{1}{r^2} \frac{\omega^4}{(\omega_0^2 - \omega^2)^2} I_0 \tag{3.1}$$

To simplify equation 3.1 we first look at the frequency term

$$\frac{\omega^4}{(\omega_0^2 - \omega^2)^2} \xrightarrow[\omega \gg \omega_0]{} 1 \tag{3.2}$$

The frequency of the emitting electron, ω_0, depends on the electron binding energy to the atom and normally results in frequencies higher than that of visible light, but lower than X-rays. For X-rays the frequency term conveniently disappears in equation 3.2 (Thomson scattering). For small angles the angle dependency disappears and the scattered intensity depends only on distance and initial intensity.

$$I_e(2\theta) \xrightarrow[\theta \to 0]{} \frac{r_0^2}{r^2} I_0 \tag{3.3}$$

The classical electron radius is $r_0 = 2.817 \cdot 10^{-15} m$, so the scattered intensity from a single electron is diminutive. We will use the scattering amplitude of one electron $f_e = \sqrt{I_e / I_0} = \frac{r_0}{r}$ as a relative measure for scattering e.g. $10 f_e$ is the amplitude corresponding to the constructive interference of 10 electrons.

So far we have only looked at the scattered intensity from a single electron. When considering multiple electrons we can not simply add the scattered intensities, but must consider interference. We will start from the two electron model and then generalize to a continuous electron distribution.

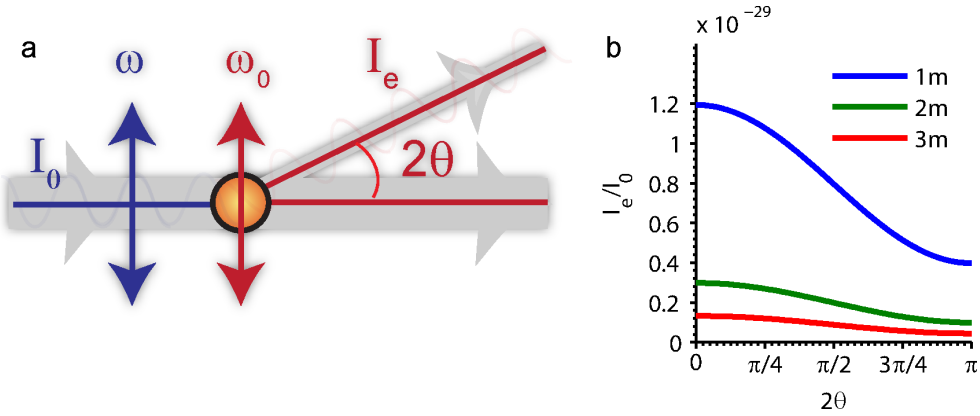

Figure 3.1: Figure 2: a) Classic interpretation of scattering; an electro-magnetic wave accelerates an electron which emits electro-magnetic radiation like a dipole antenna. b) Calculated X-ray scattering from a single electron assuming ($\omega \ll \omega_0$). Note, the angle only change the relative intensity by a factor of 2, whereas the intensity scales with the inverse distance squared. Small angles are geometrically easier to measure at longer distances, but it has to be balanced by a sufficient intensity. Wide angle X-ray scattering is therefore intrinsically easier to measure. At realistic distances for SAXS (meters) a single electron scatters a diminutive amount of incoming X-rays ($1 \cdot 10^{-29}$) compared to electron densities e.g. $3.3 \cdot 10^{23}$ electrons/cm^3 in water. Thus it requires powerful X-ray sources to detect small angle X-ray scattering.

Scattering from multiple electrons

Let us consider a plane wave with wave vector, $\bar{k}$, that hits two electrons separated by the vector, $\bar{r}$, which afterwards emit new X-rays with the wave vector , $\bar{k}'$ (see figure 3.2). The phase difference, $\Delta\Phi$, depends on the distance between the electrons, r, and the wave length, λ.

$$\Delta\Phi = \frac{1}{\lambda}\left(\bar{k}' \cdot \bar{r} - \bar{k} \cdot \bar{r}\right) \tag{3.4}$$

For simplicity we replace the wave vectors with the wave vector transfer, $\bar{Q}$ (or the momentum transfer)

$$\bar{Q} = \bar{k}' - \bar{k} \tag{3.5}$$

Intensity, I, is calculated as the Euclidian norm of the electric field, E ($I = EE^\dagger$). It means intensity is not additive and we will have to look at the amplitude of the electric field of the scattered X-rays

$$E(\bar{Q}) = \sum_{j=1}^{2} \exp\left(2\pi i \bar{Q} \cdot \bar{r_j}\right) = f_e + f_e \exp\left(2\pi i \bar{Q} \cdot \bar{r}\right) \tag{3.6}$$

This can easily be generalized to n electrons by changing the limits of the summation. However, in practice we do not know the location of each electron (and in time electrons

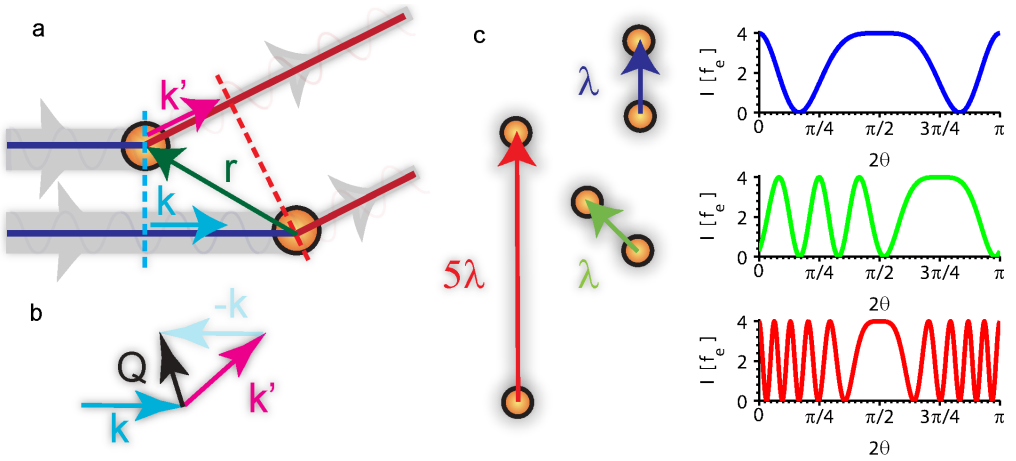

Figure 3.2: Scattering from 2 electrons. a) Scattering geometry where X-rays approach from the left with wave vector k and scatter on two electrons separated by a vector r. After scattering the wave vector is k'. The phase difference can be found in the difference in distance travelled r projected on k minus r projected on k'. This can also be found as the product between r and Q, the momentum transfer shown in (b). c) Intensity as a function of angle for different electron pairs. The scattering depends on electron distance compared to the incoming X-ray wave length, λ . Bigger distance gives a greater number of interference peaks, and depending on the relative electron position scattered X-rays have constructive or destructive interference at small angles.

will move around) but we know the electron distributions. We introduce an electron density, ρ_e, and change the summation to a volume integral.

$$E(\bar{Q}) = f_e \int \rho_e(\bar{r}) \exp\left(2\pi i \bar{Q} \cdot \bar{r}\right) dV \tag{3.7}$$

dV is a volume element e.g. for Cartesian coordinates $dV = dxdydz$. We note that $E(\bar{Q})$ is the Fourier transform of the spatial electron density. By knowing the electron distribution we can calculate the amplitude of any system, but to compare with observations we need the intensity.

$$I(\bar{Q}) = E(\bar{Q})E^{\dagger}(\bar{Q}) = f_e^2 \iint \rho_1(\bar{r_1})\rho_2(\bar{r_2}) \exp\left(2\pi i \bar{Q}(\bar{r_1} - \bar{r_2})\right) dV_1 dV_2 \tag{3.8}$$

Scattering from nanoparticles

So far we have found a general formula for scattered intensity. However, our goal is to relate the scattered intensity to the size of the nanoparticles in dispersion. In the following section we will first look at the contrast mechanism in a dispersion, averaging the phase contribution by an autocorrelation function, which through a distribution of internal distances $p(r)$ can be related to a radius of gyration R_G

For a nanoparticle dispersion both the nanoparticles and the liquid itself will scatter X-rays. We are only interested in the signal from the nanoparticles and will treat the liquid as a background signal that will be subtracted. The electron density can be written as a sum of two distributions; $\sigma_c(\bar{r})$ which is 1 inside the particles and 0 outside and $\rho_s(\bar{r})$, the perturbation in the internal electron density of the nanoparticles (relative to the average particle electron density). To get $\sigma_c(\bar{r})$ in electron density we need to multiply it with the excess electron density of the particles $\Delta\rho = \rho_x - \rho_{bg}$, where ρ_x, is the average particle electron density and, ρ_{bg} is the electron density of the surrounding liquid.

$$\rho(\bar{r}) = (\rho_x - \rho_{bg})\sigma_c(\bar{r}) + \rho_s(\bar{r}) = \Delta\rho\,\sigma_c(\bar{r}) + \rho_s(\bar{r}) \tag{3.9}$$

Notice that if the electron density of the particles and the liquid is equal, the nanoparticles will effectively be invisible and cause no scattering. Contrast can be enhanced by varying the solvent to have the greatest difference in electron density. Fors homogenous particles the internal structure terms disappear

$$\rho(\bar{r}) = \Delta\rho\,\sigma_c(\bar{r}) \tag{3.10}$$

We will now use that the scattered amplitude is the Fourier transform (FT) of the electron density, when we need to calculate the intensity.

$$I(\bar{Q}) = E(\bar{Q})E^{\dagger}(\bar{Q}) = E(\bar{Q})E(-\bar{Q}) \tag{3.11}$$

$$= \langle \mathrm{FT}[\rho(\bar{r})] \cdot \mathrm{FT}[-\rho(\bar{r})] \rangle = \langle \mathrm{FT}[\rho(\bar{r}) * \rho(-\bar{r})] \rangle \tag{3.12}$$

where $\langle\ \rangle$ denotes an average over all orientations. In the last step we used the convolution theorem which states

$$FT(g * f) = FT(f) \cdot FT(g). \tag{3.13}$$

The expression in equation (3.12) is the autocorrelation function $\gamma(\bar{r}) = \rho(\bar{r}) * \rho(-\bar{r})$

$$I(\bar{Q}) = \langle \mathrm{FT}[\gamma(\bar{r})] \rangle = \langle \int_V \gamma(\bar{r}) \exp(2\pi i \bar{Q}\bar{r}) dV \rangle \tag{3.14}$$

We need to take a spherical average because in a liquid dispersion our scattering objects will rotate freely and therefore scatter X-rays with an equal weight of all orientations. In spherical coordinates $dV = r^2 \sin(\theta) dr d\theta d\phi$, and the spherical average becomes

$$I(\bar{Q}) = \int_0^{\infty}\int_0^{\pi}\int_0^{2\pi} \gamma(\bar{r}) \exp(2\pi i \bar{Q}\bar{r}) r^2 \sin(\theta) d\theta d\phi dr = 4\pi \int_0^{\infty} r^2 \gamma(\bar{r}) \frac{\sin(2\pi Q r)}{2\pi Q r} dr \tag{3.15}$$

The auto correlation function can now take a more physical meaning, as $r^2\gamma(\bar{r}) = p(r)$ is the probability to find two points r apart in the object[37, 39]. At low particle concentration and with little interaction between the particles Brownian motion will remove all long distance correlation[37]. For that case we can disregard everything outside the particle and only integrate to a maximum diameter, D_{Max}:

$$I(Q) = 4\pi \int_0^{D_{Max}} p(r) \frac{\sin(2\pi Q r)}{2\pi Q r} dr. \tag{3.16}$$

It is also possible to find $p(r)$ from the measured intensity

$$p(r) = r^2\gamma(r)\pi = 2r^2 \int_0^\infty I(Q)\frac{\sin(2\pi Qr)}{2\pi Qr}dQ. \tag{3.17}$$

$p(r)$ depends on the size and shape of our object. It is often useful to have a shape independent number, the radius of gyration, R_G:

$$R_G^2(r) = \frac{\int_0^{D_{Max}} r^2 p(r)dr}{2\int_0^{D_{Max}} p(r)dr} \tag{3.18}$$

R_G is the average gyration ratio, and can be related to relevant distances for concrete geometries. When assuming the scatterer is a sphere the radius, R, is related to R_G by

$$R_G^2(r) = \frac{3}{5}R^2. \tag{3.19}$$

We have thus found a relation between the intensity $I(Q)$ and the particle radius, R. The most important ideas behind the derivation are shown in figure 3.3, along with calculated scattered intensity from different particle sizes.

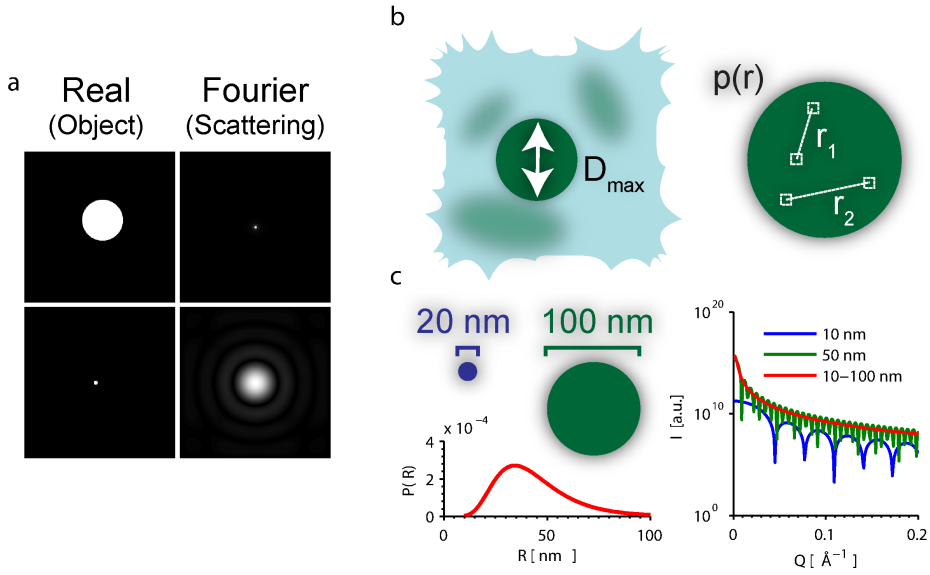

Figure 3.3: Scattering from particles. a) Going from real space to Fourier space e.g. X-rays scattering; Distances are inverted so small objects scatter to high angles and vice versa. b) Particles within a liquid have Brownian motion and destroy any long range correlation so all information beyond the maximum diameter, D_{max}, can be discarded. The scattered signal relate directly to $p(r)$, the probability that a given distance with a given electron density difference is present. c) Scattering of signal of different spherical nanoparticles. Left: illustration of mono disperse particles (radius 10 nm and 50 nm) and a log-normal size distribution (radius from 10-100 nm). To the right: Corresponding scattered intensity. The fringes disappear for poly-disperse nanoparticles and the final scattering curve is dominated by large particles due to their greater scattering.

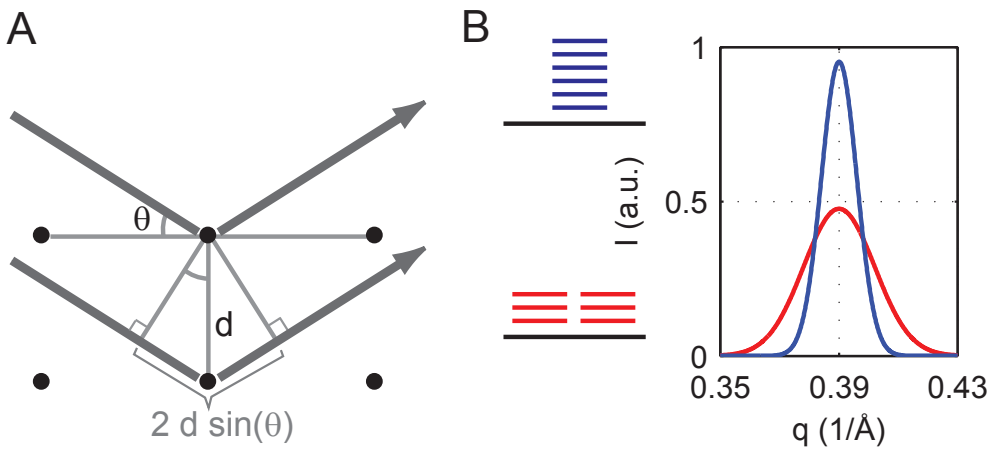

Figure 3.4: A) schematic of Braggs law with the red arrows indicating scattered X-ray. B) Schematic of Scherrer peak broadening in GIWAXS due to crystal domain size using approximate values for P3HT (100). The red and blue colors refer to the crystal domains sizes shown left of the graph. Two red crystal units are displaced to represent the same overall crystallinity as the blue crystal.

3.3 Diffraction and the Scherrer equation

Diffraction can be seen as a special case of scattering. With systematic periodicity in electron densities (crystallinity) the scattered signal will be amplified by multiple instances of similar scattering conditions (see equation 3.4) giving rise to distinct Bragg peaks. The overall geometry is illustrated in figure 3.4 and gives rise to Braggs law.

$$n\lambda = 2d\sin(\theta) \tag{3.20}$$

The crystals are not infinite so the scattered signal will not be a Dirac function but have a degree of broadening described by the Scherrer equation[56, 57]:

$$t = \frac{K\lambda}{B\cos(\theta)} \approx \frac{0.9\lambda}{B\cos(\theta)} \tag{3.21}$$

Where t is the crystal domain size, K is a geometric factor commonly approximated to 0.9, λ is the X-ray wave-length, B is the full width half maximum (FWHM) of the diffraction peak and θ is the Bragg angle. Peak broadening can also originate from the instrument, so unless the instrument broadening has been fully corrected the Scherrer equation only gives a lower cut-off on crystal sizes. A schematic example of peak broadening is shown in figure 3.4.

3.4 Experiments

A series of experiments were carried out on P3HT:PCBM Landfester particles to determine structure and crystallinity.

- Size measurements by Dynamic light scattering (DLS), SAXS and TEM
- Internal structure and crystallinity by SAXS
- Film crystallinity by GIWAXS
- Film structure by STXM

Sample preparation and measurements

Particle fabrication

The Landfester method was used to fabricate the particles[28], see also chapter 1. P3HT:PCBM 1:1 particles was made using 200 mg PCBM and 200 mg P3HT dissolved in 30 mL chloroform at 60°C for 1 hour. Pure P3HT particles used 400 mg P3HT and P3HT:PCBM 1:7 particles used 50 mg P3HT and 350 mg PCBM. 90 mL demineralized water with 20 g/L SDS was added to the solution while stirring. The dispersion was treated with 5 minutes ultrasound at 500 W with a Hielsher UIP1000hd unit with a booster horn. During ultra sound treatment the dispersion was placed in a water bath to remove excess heat, that previously had been observed to cause foaming in the dispersion. Chloroform was removed by evaporation at room temperature for 24 hours. Excess SDS was removed by dialysis (14000 nominal molecular weight) during three days with daily change of the demineralized water the dialyse tube was placed in. The concentration was increased by centrifugation in filter units (10000 nominal molecular weight).

DLS

1 mL of 1 g/L nanoparticle dispersion was measured on a Malvern Instruments Ltd, Zetasizer Nano Zs with a 633 nm He-Ne laser. The standard analysis software of the instrument was used to measure the size distribution by second order cumulant analysis. Due to the poor agreement with size distributions measured with TEM and SAXS a second DLS measurement was performed on 1 mL of 0.06 g/L nanoparticle dispersion on a 200SM goniometer from Brookhaven Instruments with a 632.8 nm He–Ne laser. The instrument was operated at a fixed scattering angle of 90°. The standard analysis software of the instrument was used for analyzing the correlation function using double exponential fitting, free form Contin analysis and second order cumulant analysis. Both experiments were carried out at room temperature with 5 min calibration time of the sample.

TEM

0.06 g/L nanoparticle dispersion was dropcast on a TEM copper grid with holey carbon film placed on a filter paper, which absorbed excess liquid. The sample was dried for 10 min at room temperature and measured with a JEOL 3000F equipped with a 300kV FEG and a 4k CCD (Gatan MSC). For imaging, a 60 μm objective aperture was used to enhance contrast, and the chosen magnification combined with a CCD binning of 2 resulted in a pixel size of 0.4 nm. From the acquired TEM images, particle sizes were measured by manually

outlining the particle perimeters, using the software ImageJ and converting the measured particle areas to particle radius using a circular approximation. For particle size distribution the bin size was chosen according to reference[83].

SAXS

SAXS measurements on the dispersed nanoparticles (6 g/L) were carried out at the MAXLab beamline I911-SAXS39. 30 mL of sample was measured in a 1 mm capillary for 60 seconds under automatic sample movement to prevent beam damage. 2% Hellmanex and demineralized water were used to rinse the sample capillary between sample changes. The particles were kept in a buffer of 0.1 M Tris, 50 mM NaCl, pH 8. For each particle type a dilution series was measured and no concentration effects were observed in the SAXS data. The experiments were carried out at room temperature.

P3HT:PCBM 1:1 particles were also measured on a laboratory setup at the technical university of Denmark. The X-ray source was a rotating copper anode operated at 40 kV/40 mA yielding Cu-Kα radiation (λ = 1.5418 Å) focused by a 2D multilayer optic and collimated by 3 pinholes. Background subtraction of the water signal was difficult as the correct transmission factor could not be obtained possibly due to use of different capillary tubes as sample holders for the particle dispersion and fluctuations in beam intensity. The background signal could be subtracted by using a scaling factor found by matching the water and particle signal at high q where only the smallest particles would contribute to the scattering and the signal therefore approximately should be the same as for water. However, the obtained signal at high q depended heavily on the q range used to scale the background signal as illustrated in figure 3.5. Despite the challenges it was possible to obtain a signal similar to the one found by the synchrotron experiment at MAXLab also shown in figure 3.5 and it illustrates the importance of careful determination of the solvent scattering.

AFM

6 mg/L nanoparticle dispersion was spin cast on freshly cleaved mica substrate at 2800 rpm. The low concentration was chosen to get isolated particles. Aggregates and connected particles started to form already with 0.06 g/L nanoparticle dispersion. Drop cast particles gave similar AFM images. AFM measurements were acquired as 5x5 micron micrographs with 1024x1024 pixels on a N8 Neos (Bruker Nano GmbH, Herzogenrath, Germany) using PPP-NCLR cantilevers (NANOSENSORS, Neuchatel, Switzerland). The AFM micrographs were post-processed with SPIP 6.2.6 software where particle height and diameter were extracted using an automated thresholding routine.

GIWAXS

A monolayer of 6 g/L particles was spin cast on float glass at 2800 rpm. Sample annealing was done on a 140°C hotplate in ambient atmosphere. Roll to roll coated samples were fabricated by slot-die coating 60 g/L P3HT:PCBM 1:1 nanoparticles on a polyethylene terephthalate substrate as described previously [27, 84]. GIWAXS measurements were performed with a Rigaku RU-200 rotating Cu anode as source, operating at 50 kV, 200 mA. The X-ray beam point source was monochromatized and collimated (λ = 1.5418 Å) by a multilayer optic[85].

STXM

The sample was prepared by roll to roll coating[27, 84] nanoparticles on top of PEDOT:PSS,

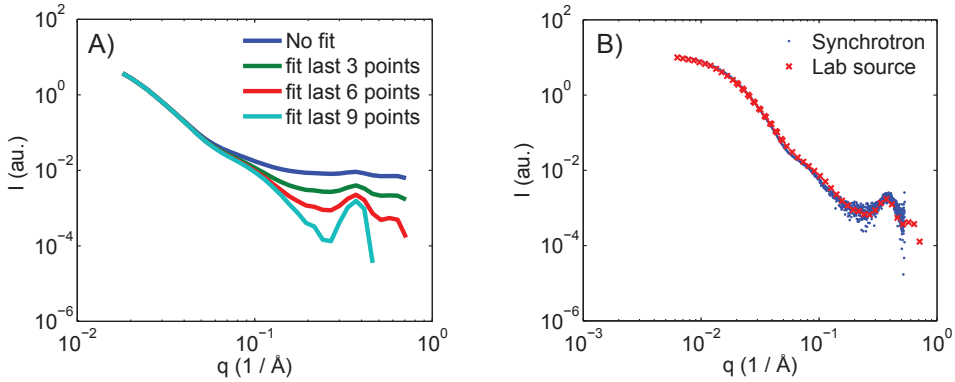

Figure 3.5: SAXS data for P3HT:PCBM 1:1 particles A) Measurements at a laboratory X-ray source at high q. The background signal from water has been subtracted with different weight factors depending on how many of the last data point at high q values were used to match water and particle signal. B) Full SAXS signal obtained by using a laboratory X-ray source (lab source) and a synchrotron.

submerging the film in a solution of potassium hydroxide and scraping the films onto a TEM copper grid. STXM measurements were recorded at the synchrotron facility BESSY II in Berlin, Germany, at the beamline UE46-PGM2. The sample was observed in the MAXYMUS STXM end station under high vacuum at the carbon edge (282-320 eV). A step size of 20 nm was used and the X-rays were detected with a photo avalanche diode. The absorption data was converted to optical density and by fitting linear combinations of reference spectra the relative material distribution maps were produced as described in chapter 2.

3.5 Particle structure

The particle size determination was carrried out on particles in suspension by DLS and SAXS and on dropcast particles using TEM. The advantage of DLS and SAXS is, that they are performed in solution and are ensemble measurements, but they both depend on choice of analysis model. TEM on the other hand have to assume that the particles conserve structure upon dropcasting, and requires sufficient sampling to provide size distributions. The results are shown in figure 3.6.

Based on literature[27, 71] and the TEM measurements a lognormal distribution is regarded as the most likely approximation to the size distribution. The lognormal probability density functions can be written as

$$f(x) = \frac{1}{x\sigma\sqrt{2\pi}} \exp\left(-\frac{(\ln(x) - \ln(\mu))^2}{2\sigma^2}\right) \tag{3.22}$$

The size distributions for the different methods are are presented in table 3.7.

The particle sizes are smaller than those reported in other studies dealing with particle structure and photovoltaic application which typically find particle radii on the order of 50

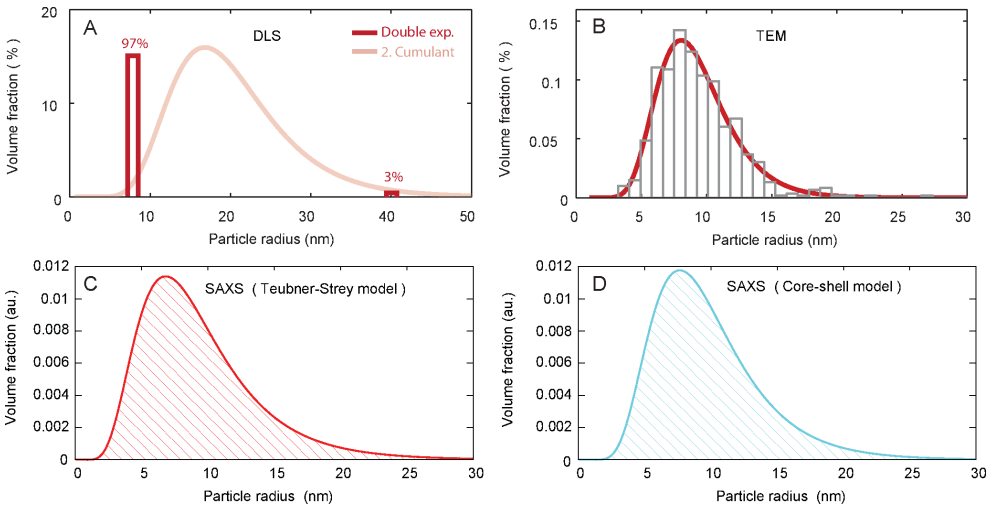

Figure 3.6: Size distributions A) DLS with double exponential analysis (bars) and errors 2. order cumulant analysis distorted by the presence of few aggregates. B) TEM size distribution with lognormal fit. C) and D) SAXS fits based on lognormal size distributions using different models for internal structure; C) Teubner-Strey model D) core-shell model.

Name		Median μ (nm)	σ^2	Mean (nm)
DLS	(2. cumulant)	19	0.35	22.6
DLS	(double exp)	8.9 (97%)	N/A	8.9
TEM		8.8	0.31	10.3
SAXS	(teubner-strey)	8.4	0.21	9.3
SAXS	(core-shell)	9.0	0.20	9.9

Table 3.7: Radial distribution for P3HT:PCBM 1:1 Landfester nanoparticles with median (μ), σ^2 and mean for lognormal distributions. Note the double exponential fit to DLS data only yields a size and not a size distribution. In general the methods agree on mean particle radius of 9-10 nm.

nm[81, 71, 79]. Kietzke et al. have with other polymers made particles with a radius of about 20 nm[29]. Satapathi et al. have also been able to achieve smaller particles for pure P3HT and PCBM by controlling the mass fraction of P3HT and surfactant concentration for PCBM with the P3HT particles reaching a radius of 7 nm[86]. The standard DLS analysis (2. order cumulant) yields larger particle sizes due to a small fraction of aggregates. Errors in DLS analysis could be present in other reports, but large particle sizes are plausible as they have also been measured by direct imaging methods such as TEM, SEM and STXM[81, 71, 79]. The smaller particle size in this study is likely a result of a difference in the fabrication process, e.g. water cooling during the sonication process, pH, material batch etc. It has

not been thoroughly investigated and could a topic for future experiments. The range of methods used and their agreement provide strong reason to trust that the particle radius in our case to be on the order of 10 nm. In regard to optimal photovoltaic performance the particle size is on the order of the exciton diffusion length, which in theory is quite optimal, as smaller particles would result in larger amounts of surfactant due to increased surface area.

Internal structure in photoactive nanoparticles by SAXS

Scattering techniques make it easier to study small structures as opposed to real space methods. For full small angle scattering analysis it is possible to directly extract intermediate information like the distribution of internal distances weighted by electron density, $p(r)$. However, to get proper real space information, it is necessary to choose a model for internal structure and particle size distribution. Our TEM measurements and literature suggest a lognormal size distribution of particle radius[27, 71]. Regarding the internal particle structure other experiments suggest a core-shell structure[81, 71, 79]. For our particles a core-shell model is not sufficient to fit the data, and we have employed a more general Teubner-Strey model for the internal structure as shown in figure 3.8. Regarding the core-shell model, the ratio of P3HT and PCBM was kept in accordance to the 1:1 mass ratio, and a fit parameter allowed for partial or complete mixing. In the fitting process the mixing parameter was driving to complete phase seperation (no mixing) with P3HT core and PCBM shell. However, as observed the model did not fit and can not be used to infer structure.

The Teubner-Strey model is not described by specific electron densities but is a more abstract geometrical model with a domain size parameter, d, and characteristic correlation length, ξ. For our model fit the parameters are:

$$d = 8.3 \text{ nm} \qquad \xi = 3.1 \text{ nm}$$

The detailed SAXS fitting was carried out by Martin Cramer and additional information can be found in the paper related to the chapter. The domain size is on the same length scale as the radius. From the SAXS model fit it is not clear what component that gives rise to the structure e.g. it could be PCBM rich domains in a P3HT rich matrix or vice versa.

If the interior only consist of spheres, the radius, r, would be half the domain size, and ξ would be the average distance between spheres. The gap between spheres, g, can be related to ξ, i.e. the average vertical distance in the system illustrated in figure 3.8c is:

$$\xi = \frac{2r(2r+g) - \pi r^2}{2r}. \tag{3.23}$$

Isolating g and replacing r with $d/2$ it becomes

$$g = \xi - \frac{4-\pi}{4}d. \tag{3.24}$$

Using the values obtained from the SAXS fit g is 1.3 nm. The domains could also mainly be located near the center with fingering (figure 3.8), so it might not be as far from the core-shell structure as the data suggest.

The Teubner-Strey model does highlight that the internal structure of the nanoparticles are more complicated than so far suggested and that only comparing 3-4 geometric

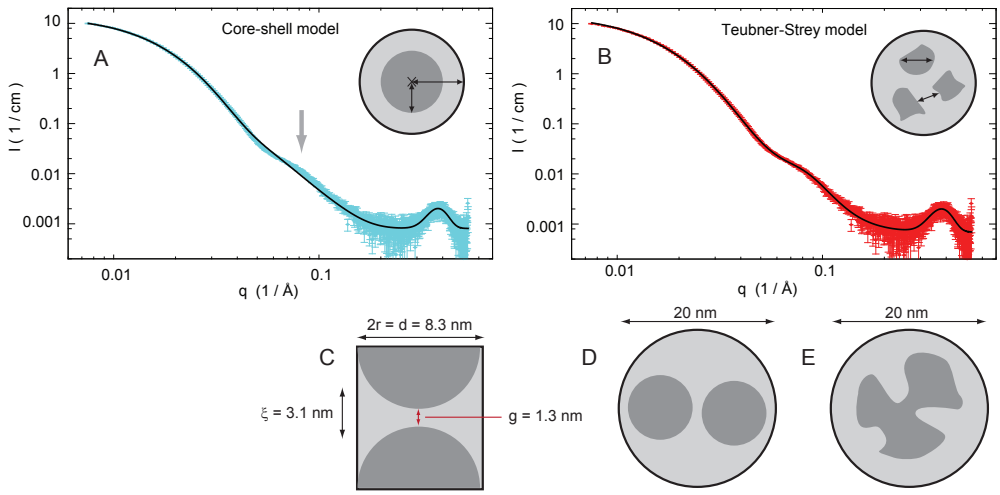

Figure 3.8: SAXS data for P3HT:PCBM 1:1 particles fitted to a A) Core-shell model and B) a Teubner-Strey model assuming lognormal distribution and a Gaussian peak from crystalline diffraction of P3HT around 0.38 $Å^{-1}$. The gray arrow in A) indicates the second shoulder in the graph not fully described by the core-shell model. C) Visualization of Teubner-Strey using spheres gives a gap distance, g, of 1.3 nm. D) Shown to scale in a 20 nm particle. E) Teubner-Strey as a central domain intermixing with the shell.

models[81, 71] provides an oversimplified picture of the structure. Considering the previous studies which all found PCBM rich cores and P3HT rich shells, the most likely structure seems to be a fingering model with a PCBM rich core.

Crystallinity of particles in dispersion

Crystallinity is important for OPV application because higher crystallinity means better charge transport[78]. This section studies the P3HT (100) reflection which was the only crystal planes that diffract at sufficiently low q to be observed in the SAXS data. Data for three kinds of Landfester particles are shown in 3.9. P3HT is a semi crystalline polymer. Mixed with PCBM the crystal domains are still formed when the mass ratio of P3HT is above 20%-30%[87, 88]. When the materials are confined in nanoparticle structures it could change their crystal behavior. On the other hand one could also imagine that the crystallinity played a role in formation of nanoparticles and for instance affected the particle size distribution. In dispersion the particles rotate freely and do not give Bragg peaks but Bragg rings. Bragg rings are also expected for cast layers, because the crystal domains are within nanoparticles which would orient themselves randomly on a substrate.

P3HT (100) Bragg peaks were observed for pure P3HT particles and P3HT:PCBM 1:1 particles but not for P3HT:PCBM 1:7 particles in dispersion as shown in figure 3.9. This is consistent with the bulk heterojunction measurements[87, 88] as the P3HT mass fraction is 12.5% and below the normal concentration from observed crystalline P3HT domains. It

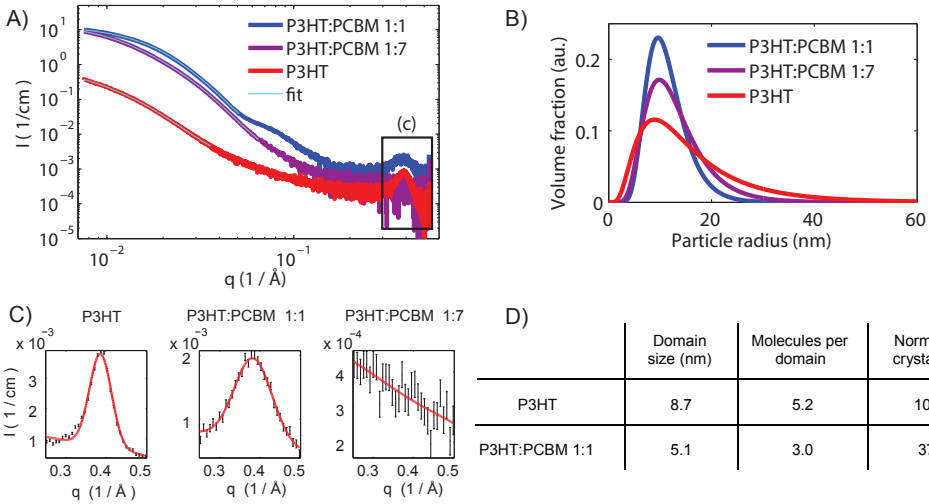

	Domain size (nm)	Molecules per domain	Normalized crystallinity
P3HT	8.7	5.2	100 %
P3HT:PCBM 1:1	5.1	3.0	37 %

Figure 3.9: A) SAXS data for Landfester particles fitted in low q with a homogenous sphere model (size in B) and with crystal P3HT (100) signal at higher q shown in C). B) Size distributions from SAXS fits. C) Gaussian fits around P3HT 100 reflection normalized for concentration. D) Crystal domain sizes and relative crystallinity extracted from fits in C).

could be interesting to see if internal crystallinity would be affected by the nanoparticle confinement, in experiments with closer sampling of P3HT and PCBM mass ratios in Landfester particles. Measuring the relative crystallinity by comparing the integrated area under the Bragg peak, we find that neat P3HT particles are 2.7 more crystalline than P3HT:PCBM 1:1 Particles. By the Scherrer equation it is also observed that the crystal domain size is 1.7 larger in pure P3HT particles than P3HT:PCBM 1:1 particles.

The particle size distribution was also found from the SAXS data by using a homogenous sphere model and fitting in the low q region shown in figure 3.9. Note, that the size distribution of the previously studied P3HT:PCBM 1:1 particles are approximately the same as found with TEM measurements and more advanced SAXS models in figure 3.6. Low q regions were used to avoid effects from internal structure (P3HT:PCBM 1:1), scattering contribution from crystal domains and problems with low quality of background measurements for the pure P3HT (which are more problematic at high q). Crystallinity only seems to be weakly linked to size distribution, i.e. the more crystalline P3HT particles are found to have a wider size distribution, whereas the less crystalline P3HT:PCBM 1:1 particles are found to have a slightly narrower size distribution than the amorphous P3HT:PCBM 1:7 particles. The median size of all particles are on the same order of magnitude so the only observed effect of crystallinity is a slightly wider size distribution at high degrees of crystallininity.

3.6 Particles cast into a layer

One thing is crystallinity in dispersion, but what really matters from a device point of view is crystallinity when the particles are cast into a layer. The crystal domains in the

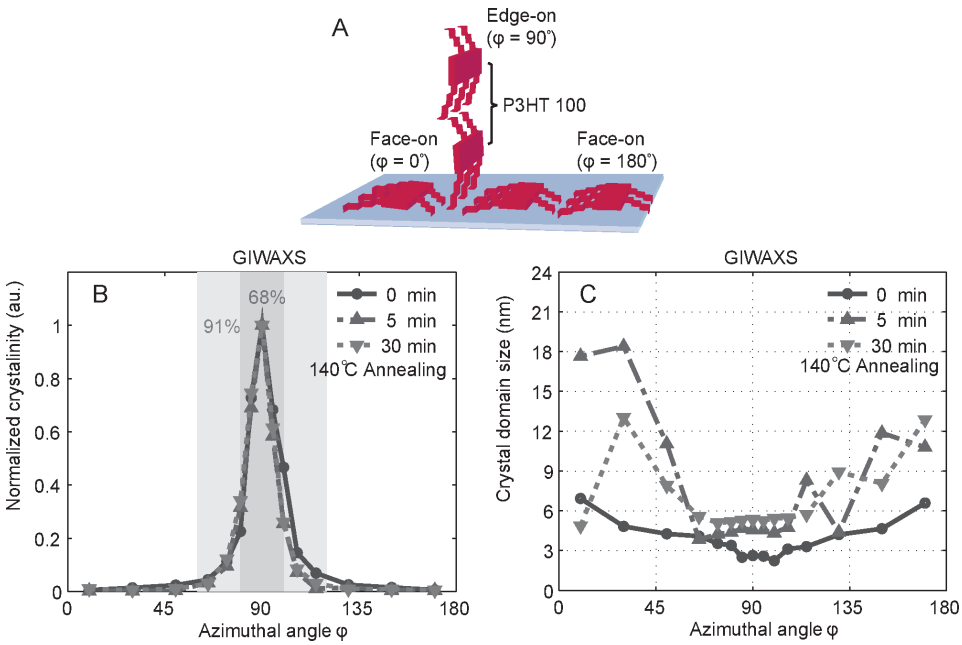

Figure 3.10: A) Schematic of P3HT orientation relative to substrate and the denoted azimuthal angle. B-C) GIWAXS measurements of P3HT (100) crystallinity in a monolayer of Landfester P3HT:PCBM 1:1 particles spincast on glass and subsequently annealed at 140^{o}C. B) Relative crystallinity as a function of azimuthal angle. C) Crystal domain size as a function of azimuthal angle.

nanoparticles are expected to orient themselves randomly, but in general P3HT orientation on a substrate can be described as face-on, denoting side-chains parallel to the substrate, or edge-on, denoting side-chains perpendicular to the substrate, illustrated in figure 3.10. The relative crystallinity and domain sizes are also plotted as a function of azimuthal angle in figure 3.10. It is observed that the relative crystal orientation even before annealing is very textured, i.e. have preferred orientation(s) and that it does not change with annealing. It is quite surprising as the spherical particles would not be expected to have a preferred orientation.

Studying single particles using atomic force microscopy (AFM) reveals that the particles deform upon contact with a mica substrate (figure 3.11). The particle diameter is reduced from about 18 nm (i.e. median of the lognormal size distribution) to an average particle height of 5.2 $\pm$ 1.2 nm. Similar deformation is observed for drop casted particles on mica, but not for particles dropcasted on holey carbon TEM grids. The particle deformation is thus likely driven by surface energies. The particle deformation has not been observed for larger particles with radius of about 50 nm[81, 71, 79]. Deformation is likely caused by surface energy levels which affect the contact angle, i.e. low contact angle means flat particles. A macroscopic study by Stapleton et al. did observe that the contact angle of polymers changed with the surface energy[89].

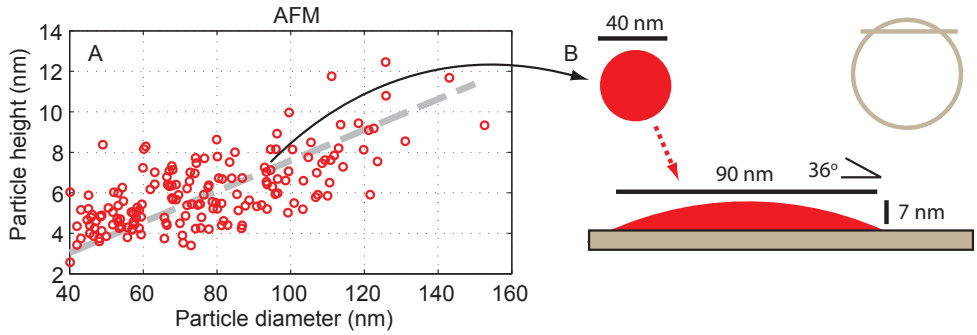

Figure 3.11: A) Scatterplot of particle diameter and particle height measured with AFM on single P3HT:PCBM 1:1 particles dropcast on mica. The fit show the general trend that the particle diameter is 13 times the particle height. B) Schematic view of a particle of a single data point, assuming an idealized particle shape of a capped sphere illustrated in gray. The original particle size is determined using conservation of volume.

Assuming the deformed particle is a capped sphere, the volume of the particle, V, can be calculated based on the contact angle, θ, and the sphere radius, r:

$$V = \pi(r^2\theta - \sin(\theta)\cos(\theta)r^2). \tag{3.25}$$

The contact angle and radius is related to the particle height, h, and particle width, w:

$$h = (1 - \cos(\theta))r \tag{3.26}$$

$$w = 2\sin(\theta)r \tag{3.27}$$

It is thus possible to calculate the contact angle and original particle volume (assuming it was a sphere), from h and w. It has been done for a representative particle shown in figure 3.11. A contact angle of 36^o for an original particle diameter of 40 nm was found. The quite large particle size could indicate an observational bias towards large particles, i.e. large particle are easier to observe. The conversions are based on a number of assumptions so the contact angles might not be accurate, but it serves as an illustration on what the particle deformation could look like.

During the particle deformation the crystal domains reorient themselves to an edge-on structure which explains the observed high degree of crystalline texturing. During the deformation process the edge-on crystal domain size is reduced to about 3 nm that increase to 6 nm meter upon annealing. Because 6 nm is also around the particle height of single particles, i.e. 5.2 ± 1.2, it is likely that the edge-on crystal domain size is limited by the layer thickness, which is also supported by larger face-on crystal domain sizes of more than 10 nm.

The crystal alignment was not only observed for a monolayer of spin coated particles but also for roll-to-roll coated particles as shown in figure 3.12. Roll-to-roll coating also involves heating so some degree of annealing effects are likely present. None the less, the strong alignment indicates that the particle shapes are lost and crystal domains reoriented

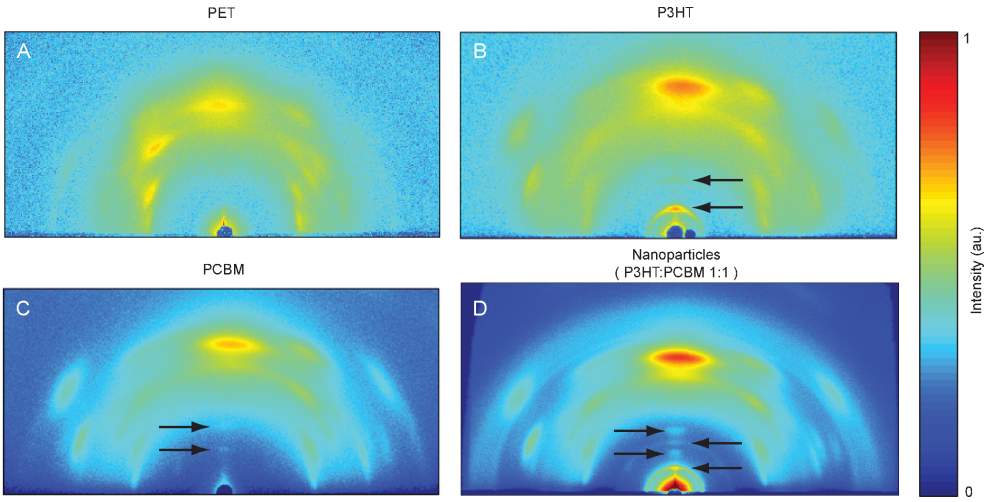

Figure 3.12: GIWAXS measurements of A) PET foil and PET with roll-to-roll coated B) P3HT from solution, C) PCBM from solution and D) P3HT:PCBM 1:1 Landfester particles from water. Left facing arrows denote P3HT (100) crystal domains, and right facing arrows denote crystalline PCBM. The measured q range is 0.15 - 2.5 $Å^{-1}$.

to the substrate in roll-to-roll processing. The particle undergo a drastic deformation in the casting process, so the internal particle structure of suspended particles is only relevant to the extend it affects the final layer structure. As a reduction in the crystal domain size is observed, the drastic morphological change of the particles causes some mixing of the material, but at the same time leave some P3HT (100) crystal domains behind.

Spatial mapping of roll-to-roll coated nanoparticles

STXM was used to chemically map roll-to-roll coated Landfester particle films as described in chapter 2. The result is shown in figure 3.13. The overall film structure is quite rough with PCBM and P3HT domains larger than 100 nm. The PCBM regions are generally thicker and exist within a matrix of P3HT. The phase separation could be caused by domains formed within the particles, which then during the morphological changes in the casting process migrated towards each other forming larger domains. These domains are then further increased in size due to annealing during the drying process in the roll-to-roll coating process. The large domains of more than 100 nm are not optimal due to the limited exciton diffusion length of 10 nm. The phase separation taking place in the particle formation might act similar to a pre-annealing step and decrease the OPV performance as observed for long annealing time of active layers cast from solvent[90].

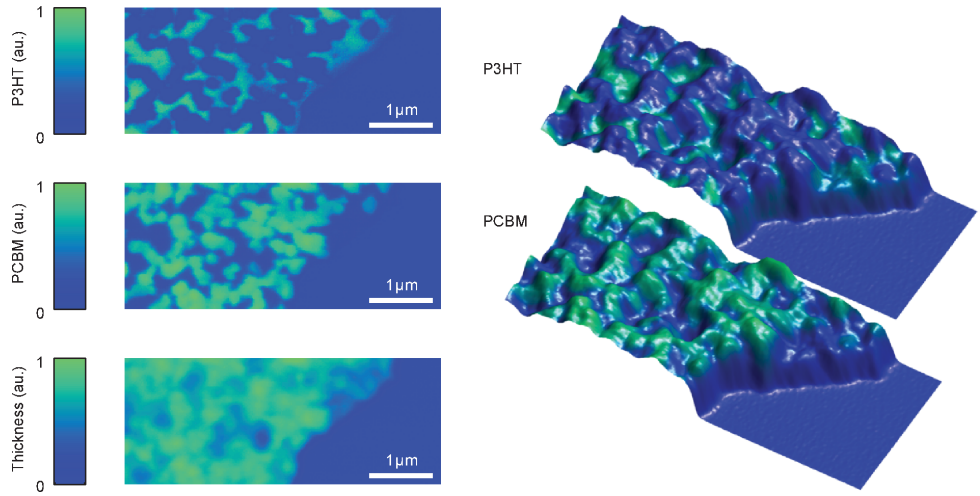

Figure 3.13: STXM maps of top) P3HT, middle) PCBM and bottom) the thickness i.e. optical density at 320 eV. To the right is shown P3HT and PCBM overlaid thickness map. Thick PCBM domains larger than 100 nm are distributed in a thinner matrix of P3HT.

3.7 Summary and future work on structure and crystallinity

The spatial distribution of P3HT and PCBM is especially relevant for optimal OPV performance of the solar cell as stated in chapter 1. The particle radius is found to be around 9 nm, which should be good for charge separation dominated by exciton diffusion length of 10 nm. The internal structure is found to be best described by a Teubner-Stey model with PCBM domains in a P3HT matrix or vice versa. Drop cast, spin coated and roll-to-roll coated Landfester particles undergo drastic morphological deformation, which causes the particles to flatten and crystalline areas to reorient themselves in relation to the substrate. Single particles deform to about 100 nm diameter and a height of 5.2 $\pm$ 1.2 nm. For roll-to-roll coated P3HT:PCBM 1:1 particles a large degree of phase separation is observed with layers with PCBM domains larger than 100 nm in a thinner matrix of P3HT. Structural summary schematics are shown in figure 3.14. The large degree of phase separation is likely detrimental to the OPV performance and could be caused by phase separation in the particles before coating opposed to material fully mixed in organic solvents when cast.

Future experiments

- The effect of crystallinity on particle size and structure:
SAXS data indicated that size distribution of pure P3HT particles could be wider due to large crystal domains. The matching sizes of internal domains and crystal sizes indicates that crystallinity could also affect the internal structure. Particles prepared with various concentration of nucleating agents could be investigated as a means to control particle size and potentially increase internal material mixing within the particles.

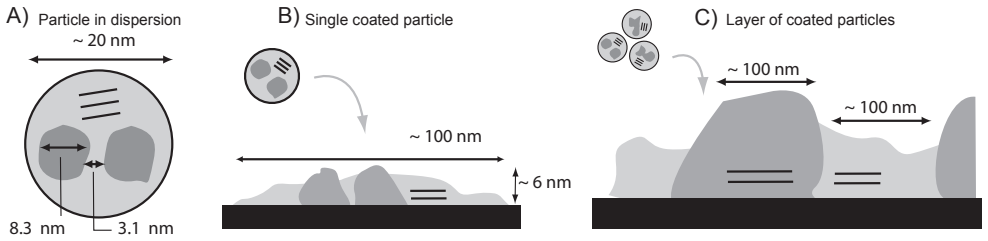

Figure 3.14: Schematic overview of P3HT:PCBM 1:1 Landfester structure. A) Particle in dispersion with crystalline P3HT regions (stripes) and internal Teubner-Strey structure with domains of PCBM in a P3HT matrix or vice versa. B) When coated in a single layer the particles deform to an approximate height of 6 nm and diameter of about 100 nm. Crystalline P3HT areas orient themselves edge-on to the substrate. C) In roll-to-roll coated layers a large degree of phase separation is observed with thicker PCBM domains in a matrix of P3HT. Crystalline areas are aligned to the substrate.

- Particle deformation:
Particle deformation was observed to depend on surface energy, i.e. particles did not deform on a TEM grid with holey carbon. Deformation could be investigated as a function of substrate surface energy, particle size, surfactant concentration and surfactant type. A better understanding of the particle deformation process would allow one to control the actual active layer morphology and thereby enhance the OPV performance.

- Spatial distribution of surfactant:
The observed drastic particle deformation likely also affect the surfactant. Because the surfactant is not photo-active nor conductive it could be the main culprit in reduced OPV performance of Landfester particles, e.g. by forming horizontal domains thereby greatly increasing the charge path. A surfactant with a unique element not present in the active materials could easily be mapped by elemental analysis.

CHAPTER 4

Spatial effects in organic tandem solar cells

This chapter investigates the material distribution inside organic tandem solar cells and is related to the publication "Water-processed organic tandem solar cells improved by quantitative 3D nanoimaging" submitted to RCS Nanoscale. The central questions this chapter seeks to answer are: How are the materials distributed within a layer? How dense are the materials? What characterizes these layers? Particularly, how does a nanoparticle layer differ from a solution-cast bulk heterojunction? These questions are essential to understand complete device structure and in turn increase performance. Ptychographic X-ray Computed Tomography (PXCT) can answer these questions successfully as demonstrated by being the first technique to provide 3D nanometer information of a complete OPV device[91, 92]. PXCT characterization is presented followed by a theoretical foundation for ptychography, theory for segmentation and partial volume effects in tomography and finally the results of an organic tandem cell investigated with PXCT.

4.1 Relevance of ptychographic X-ray computed tomography for investigating organic photovoltaics

Organic photovoltaics consist of multiple thin layers with sub micron thickness. For tandem cells the number of cast layers will increase further i.e. up to 12 layers[93] which is the number of layers for the devices investigated in this chapter. Layer roughness has been found to increase with faster solvent evaporation rates[94] which is necessary for fast, large scale production using roll-to-roll processes. Layer thickness is critical for OPV performance e.g. pinholes can result in electric shorts circuits[64] and a non-optimized thickness reduces performance[95]. Another challenge with coating multiple layers is redissolving of underlying layers[96], which makes it important to employ solvent orthogonality i.e. solvents that cannot dissolve the underlying layer. Photoactive Landfester particles cast from water (as opposed to an organic solvent) have previously been employed to achieve tandem structures[84]. Despite the importance of layer formation in OPV production and performance, the complete layer structure of a full device have been difficult to study, because it requires a high resolution in tens of nm, high penetration depth in microns of material and sufficient contrast to discern between the layers. It is easy to gain surface information from methods such as AFM, but they only probe the surface and not the full device structure. Methods such as TEM and STXM provides sufficient spatial resolution, but have limited penetration depth, typically a couple of 100 nm[91], making them hard to truly extend to 3D. Other possible techniques include TOF-SIMs imaging and FIB-SEM. However, they are both destructive techniques where the spatial resolution is somewhat compromised as different materials are destroyed at different rates. The imaging of the full OPV device structure

was a missing characterization option in the OPV community[91], and PXCT with multi-keV photons fills this void by providing high resolution, high penetration depth, phase and absorption contrast with quantitative electron density distribution as an additional feature. As an example PXCT have achieved 16 nm isotropic spatial resolution in a 6 micron thick sample[49].

4.2 Principle of ptychography

We will first define the setup and the mathematical description seen in figure 4.1 to get a better understanding of ptychography. It is a basic scattering experiment with coherent X-rays. The beam propagates towards the object and just before interacting with the electric field it can be described as the probe function, $P(r)$. As it travels through the object, $O(r)$, it interacts as described in equation 1.7 and the electric field is changed to the exit field, $E(r)$ as it leaves the object.

$$P(\bar{r})O(\bar{r}) = E(\bar{r}) \tag{4.1}$$

As the exit field propagates to the detector, D, it becomes the Fourier transform of the exit

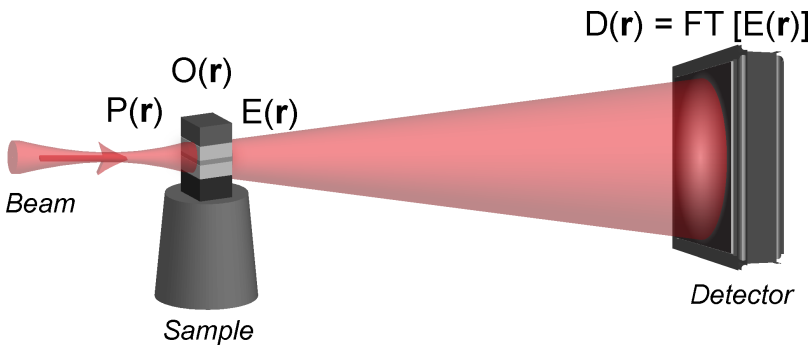

Figure 4.1: Ptychography setup. A coherent X-ray beam is directed towards the sample and just before the beam hits the sample, the electric field can be described by the probe function $P(\bar{r})$. The beam travels through the object and interacts with the object function $O(\bar{r})$ transforming the probe $P(\bar{r})$ to the exit field $E(\bar{r})$. The exit field propagate towards the detector taking the form of the Fourier transform of the exit field $FT[E(\bar{r})]$, which is denoted $D(\bar{r})$.

field $FT(E)$. To go from object (and probe) to detector field and back is described by

$$D(\bar{r}) = FT[E(\bar{r})] = FT[P(\bar{r})O(\bar{r})] \tag{4.2}$$

$$O(\bar{r}) = P(\bar{r})^{-1} IFT[D(\bar{r})], \tag{4.3}$$

where IFT is the inverse Fourier transform. In order to limit the object function to an unique solution we apply constraints. The first is simply the measured intensity at the detector as the square of the amplitude.

$$I(\bar{r}) = |D(\bar{r})|^2 = |FT[P(\bar{r})O(\bar{r})]|^2 \tag{4.4}$$

The second constraint is overlapping measurements. Ptychography uses multiple overlapping measurements to cover the sample area. It allows for arbitrary large field of views and introduces an object constraint because the same piece of object is in view more times with approximately the same probe, giving us an over-determined object. The overlapping scan and two constraints are illustrated in figure 4.2.

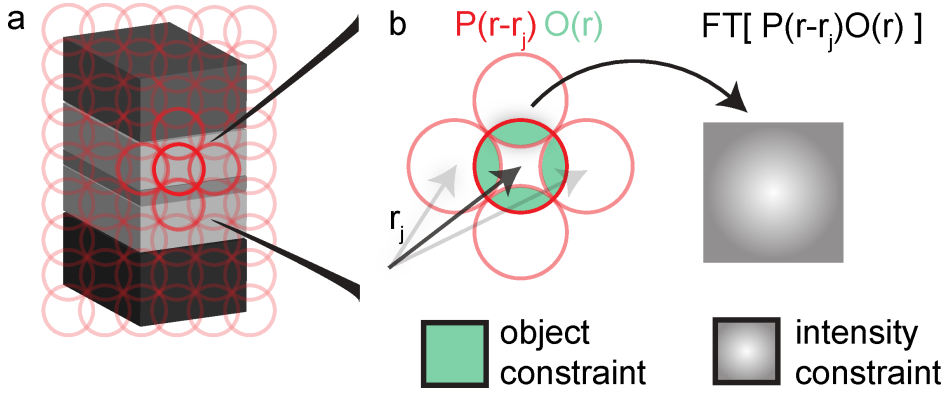

Figure 4.2: Ptychography scanning and constraints. a) The object is scanned with a series of overlapping exposures. To get good reconstruction a bigger overlap is required (0.3 diameter overlap shown in figure, whereas 0.6 diameter overlap is recommended[97]). b) Overlapping exposures can be described by a moving probe function $P(r)$that for each measurement remains the same but moves to the position r_j. The overlap thereby supplies an object constraint. The probe interacts with the object function $O(r)$ and propagates to the far field calculated as the Fourier transform $FT[P(r-r_j)O(r)]$. Here we measure the intensity, I, which gives us the intensity constraint $I = |FT[P(r-r_j)O(r)]|^2$.

In summary the two constraints are:

1. Detector intensities can be found from a known probe and object function.
2. An object (and probe) solution is constrained by the overlap in object function and the measured intensity.

So far, we have not demonstrated that the constraints are sufficient to provide a unique solution, and it might not be the case especially when also including measurement errors. However, it has been shown experimentally that the constraints are sufficient to converge towards a reasonable solution[50, 97, 98, 99]. We will outline two algorithms to get an idea of how it is possible to do the inverse problem and go from overlapping scattering measurements to an object function. The first is an intuitive algorithm proposed by Rodenburg and Faulkner[98], which cycles through overlapping exposures one at a time and slowly refine the object function. Whereas it is easy to understand it requires a known probe function. The second algorithm is a refinement by Thibault et al.[99] where the problem is treated as an optimization problem. All the exposures are processed as one massive data vector used to update the object, probe and exit field using a difference map scheme. It does not require

a priori knowledge of the probe and is therefore more useful from a practical point of view. However, it also introduces new sources of possible errors that will be discussed at the end of the chapter.

Ptychography Iterative Engine (PIE) by Rodenburg and Faulkner

The following is based on Rodenburg et al.[98].

We assume the probe function, P, is known. We make a guess of the initial object function $O(r)$ (in practice it is a matrix of random complex number representing the refractive indices). We denote the object function $O_{(g,n)}$ where g denotes a guessed version of the object function and n the number of iterations. The initial random guess is therefore $O_{(g,0)}$, but we will only deal with n and $n+1$ in the iterative procedure.

1. Calculate the exit function from the current version of the object function and the known probe function
$$E_{g,n}(\bar{r}, \bar{r_j}) = P(\bar{r} - \bar{r_j}) O_{g,n}(\bar{r}) \tag{4.5}$$

2. The guessed detector field is the Fourier transform, where k denotes the position in diffraction space:
$$D_{g,n}(\bar{k}, \bar{r_j}) = FT[E_{g,n}(\bar{r}, \bar{r_j})] \tag{4.6}$$

3. Rewrite the detector field as an amplitude and a phase, $\theta_{g,n}(\bar{k}, \bar{r_j})$:
$$D_{g,n}(\bar{k}, \bar{r_j}) = |D_{g,n}(\bar{k}, \bar{r_j})| \exp(i\theta_{g,n}(\bar{k}, \bar{r_j})) \tag{4.7}$$

4. Correct ($_c$) the amplitudes with the measured intensities $|D_c(\bar{k}, \bar{r_j})| = \sqrt{I(\bar{k}, \bar{r_j})}$:
$$D_{c,n}(\bar{k}, \bar{r_j}) = |D_c(\bar{k}, \bar{r_j})| \exp(i\theta_{g,n}(\bar{k}, \bar{r_j})) \tag{4.8}$$

5. Calculate back to the exit wave with an inverse Fourier transform:
$$E_{c,n}(\bar{r}, \bar{r_j}) = IFT[D_{c,n}(\bar{k}, \bar{r_j})] \tag{4.9}$$

6. Update the object function using the object, exit function and the two parameters; α, that prevents division by zero and β, a scalar we choose as a weight of the feedback from the newest estimate of the object function.
$$\begin{aligned} &O_{g,n+1}(\bar{r}) = \\ &O_{g,n}(\bar{r}) + \frac{|P(\bar{r}-\bar{r_j})|}{|P_{\max}(\bar{r}-\bar{r_j})|} \frac{\mathrm{M_p} P(\bar{r}-\bar{r_j})}{|P(\bar{r}-\bar{r_j})|^2+\alpha} \cdot \beta \left(E_{c,n}(\bar{r}, \bar{r_j}) - E_{g,n}(\bar{r}, \bar{r_j})\right) \end{aligned} \tag{4.10}$$
$\mathrm{M_p}$ is a mask of the known probe that is 1 everywhere the estimated probe is different from the known probe and 0 where they are the same.

7. Move to a new position r_{j+1} that ensures overlap in P with a previous position, repeat step 1-7 until convergence. The overlap in the probe illumination provides a weak support overlap constraint, as object reconstructed in one illumination is used as feedback in reconstructions of overlapping illuminations.

The convergence is measured by the sum squared error (SSE) defined by the difference in detector functions

$$SSE = \frac{\left(|D(\bar{k}, \bar{r_j})|^2 - |D_{g,n}(\bar{k}, \bar{r_j})|^2\right)^2}{N} \tag{4.11}$$

A crucial part of PIE algorithm is located in step number 6. which uses a Fienup's input output (IO) algorithm[43] to converge. We will dedicate a section to explain it.

Fienup's input output algorithm

The IO algorithms are traditionally formulated from the perspective of the exit field, E. The problem is similar to the problem in the PIE algorithm, but instead of the object, we try to find the most likely exit field constrained by the detector intensities and known object regions (a support constrain - Often air surrounding an unknown sample). The first step is to formulate the problem as an iterative algorithm. We can iterate us forward to a correct solution by starting with a guess of the exit function. The iterative step is to take a guessed exit function, E_g, pass it though a generator function (which corrects it using the intensity constraint in Fourier space) to receive a corrected exit wave E_c (see figure 4.3).

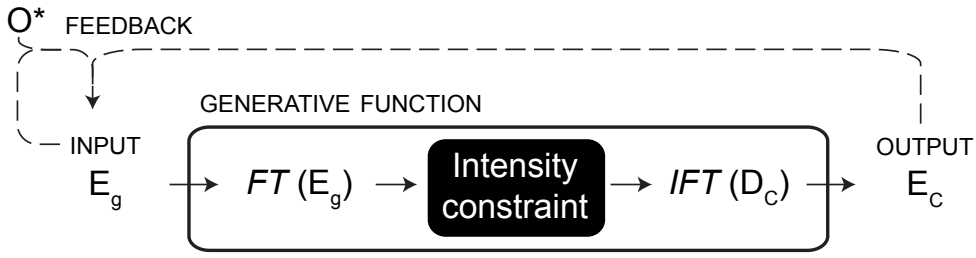

Figure 4.3: Illustration of Fienup's Input Output algorithms (IO). A guess of the exit function is passed to a generative function that outputs a corrected exit field. The generative function consists of Fourier transforming the exit field into the detector field, correcting the amplitudes based on the measured intensity and transforming back to the exit field. The advantage of viewing the process as a generative function is that the input, E_g, does not need to be a solution, but instead is the seed used to generate a new solution, E_c. This provides freedom when designing the feedback into E_g and allows us to produce faster converging algorithms than a normal error reducing approach. Traditionally the IO is formulated with an object constraint, O^*, that is incorporated into the feedback.

The elegance of the IO algorithm is only to treat E_c as a solution whereas E_g is viewed as the seed to generate solutions. This means the algorithm can take a shorter optimization route as E_g does not need to be solution in all intermediate steps, but will end up being a solution.

We need to design our feedback function so it will converge. It has been observed that a change in the input will move the output in the same direction in some linear fashion (in addition to some nonlinear terms)[100]. When there is a conflict between the output,

E_c, and the object constraint we need to change the input so the object constraint can be fulfilled expressed as:

$$E_{g,n+1} = E_{g,n} + \mathrm{M_o}\Delta E_n. \tag{4.12}$$

Where $\mathrm{M_o}$ is an object constrained violation mask (1 in points where the object constraint are violated and 0 elsewhere). ΔE_n is the change in the input that will produce an output closer to the object constraint. Because the change is approximately linear, we need a change of a factor β in the direction of the difference between desired and achieved values:

$$\Delta E_n = \beta(E_o - E_{c,n}). \tag{4.13}$$

Where E_o is the exit field of the object constraint and $E_{c,n}$ is the last estimate from the generative function. The final iteration, known as the input-output (IO) algorithm, becomes:

$$E_{g,n+1} = E_{g,n} + \mathrm{M_o}\beta\left(E_o - E_{c,n}\right). \tag{4.14}$$

We make a quick convergence check. If E_c is the correct solution and passed through the generative function, it returns itself. Furthermore, M_o will be zero for all points for the correct solution. At the correct solution, we see that we have a stable point.

$$E_g = E_{Solution} \Rightarrow E_{g+1,n} = E_{g,n} = E_{solution}$$

We can also see that if we used $E_{c,n}$ as the base of the update function instead of $E_{g,n}$ we would have similar behavior. This gives rise to the output-output (OO) algorithm

$$E_{g,n+1} = E_{c,n} + \mathrm{M_o}\beta\left(E_o - E_{c,n}\right) \tag{4.15}$$

Combining the two previous algorithms gives us a more robust algorithm, the hybrid input output (HIO) algorithm.

$$E_{g,n+1} = \begin{cases} E_{c,n} & \text{for } \mathrm{M_o} = 0 \\ E_{g,n} + \beta(E_o - E_{c,n}) & \text{for } \mathrm{M_o} = 1 \end{cases} \tag{4.16}$$

The HIO algorithm is more robust to stagnation as it unlike the IO algorithm updates pixels that satisfy the object condition to a better estimate. It does not only rely on the output to generate the input seed. Thereby it avoids problems with stagnation when an input does not change $E_{c,n}$. At the same time it is driven by $E_{c,n}$ for when $E_{c,n}$ does change.

The IO algorithm in the PIE algorithm

In the PIE algorithm, there is no object constraint. Instead, there is a probe constraint, so the IO algorithm is rewritten from the point of the object.

$$O_{n+1}(\bar{r}) = O_n(\bar{r}) + M_p\Delta O_n = O_n(\bar{r}) + M_p\beta(O_c - O_g) \tag{4.17}$$

We can rewrite the object to the exit function

$$O_{g,n}(\bar{r}) = \frac{E_{g,n}(\bar{r}, \bar{r_j})}{P(\bar{r} - \bar{r_j})} \tag{4.18}$$

So it becomes

$$\begin{aligned} O_{n+1}(\bar{r}) &= O_n(\bar{r}) + M_p\beta\frac{E_{c,n}(\bar{r},\bar{r_j})-E_{g,n}(\bar{r},\bar{r_j})}{P(\bar{r}-\bar{r_j})} \\ &= O_n(\bar{r}) + \frac{M_p}{P(\bar{r}-\bar{r_j})}\beta\left(E_{c,n}(\bar{r},\bar{r_j}) - E_{g,n}(\bar{r},\bar{r_j})\right) \end{aligned} \tag{4.19}$$

The expression is undefined for probe pixels that equal 0, but this can be remedied with a Wiener filter,($\frac{1}{x} \approx \frac{x}{|x|^2+\alpha}$) , with a small scalar α

$$O_{n+1}(\bar{r}) = O_n(\bar{r}) + \frac{M_p P(\bar{r}-\bar{r_j})}{|P(\bar{r}-\bar{r_j})|^2+\alpha}\beta\left(E_{c,n}(\bar{r},\bar{r_j}) - E_{g,n}(\bar{r},\bar{r_j})\right) \tag{4.20}$$

However, not all intensity measurements are created equal e.g. object areas exposed to high probe intensities can be determined more accurately than areas with little or no exposure from the probe. The feedback function could be improved by weighting the pixel according to intensity and thereby give better ptychography results. It is handled by multiplying a normalization factor of the probe values scaled so the highest probe value $P_{\max}$ is normalized to 1. It can be seen as an expansion of the β factor, and because the new normalization factor falls within 0 to 1, a higher β value will be needed for optimal convergence compared to the traditionally IO algorithm.

$$\begin{aligned} &O_{g,n+1}(\bar{r}) = \\ &O_{g,n}(\bar{r}) + \frac{|P(\bar{r}-\bar{r_j})|}{|P_{\max}(\bar{r}-\bar{r_j})|}\frac{\mathrm{M_p}P(\bar{r}-\bar{r_j})}{|P(\bar{r}-\bar{r_j})|^2+\alpha}\cdot\beta\left(E_{c,n}(\bar{r},\bar{r_j}) - E_{g,n}(\bar{r},\bar{r_j})\right) \end{aligned} \tag{4.21}$$

And the form is now the one known from step 6 of the PIE algorithm.

Ptychography difference map (PDM)

This section is based on work by Thibault et al.[99], which assumes the probe is the same for all exposures for one ptychography projection.

The PDM uses a difference map technique, which is a generalization of the previously mentioned HIO algorithm (a phase retrieval algorithm) and the Douglas-Rachford algorithm (a general convex optimization of sums)[101]. The idea is to express all data as a point in a Euclidian space and the two constraints as projections of that point. The best solution is found when the two constraints are fulfilled or in practice when the distance to them is minimized.

First we need to define the data points, and the two projections. We choose to work with our exit fields and express a set of all exit fields:

$$EE = (E_1(\bar{r}), E_2(\bar{r}), \ldots, E_N(\bar{r}))\,. \tag{4.22}$$

The intensity constraint projection can be described as:

$$\Pi_F(EE) : E_j \rightarrow E_j^F = amp(E_j). \tag{4.23}$$

where $amp(E_j)$ denotes step 2-5 in the PIE algorithm, with replacing the amplitude of the Fourier transform of E_j with $\sqrt{I_j}$ and transforming back to the new corrected exit field E_j^F. While not a traditional projection it has been demonstrated to work for phase retrieval and is computationally feasible. The F's in sub- and superscript simply denote the intensity constraint (it is in Fourier space).

For the second constraint, we express the overlap implicitly by relating the exit wave to the object function like in step 1 in the PIE algorithm. Because we do not guarantee that we know the probe, we need to solve it as an optimization problem where we find the probe P and object O that minimize equation 4.24.

$$\|EE - EE^O\|^2 = \sum_j \sum_{\bar{r}} |E_j(\bar{r}) - P(r - r_j)O(\bar{r})|^2. \tag{4.24}$$

We denote the probe and object that minimize equation 4.24 P_{min} and O_{min}. They can be found by any suitable optimization method; Thibault et al.[99] propose line minimization, or alternatively solving P_{min} and O_{min} one at a time by setting the other derivative to zero

$$O^{min}(\bar{r}) = \frac{\sum_j P'_{min}(\bar{r} - \bar{r_j})E_j(\bar{r})}{\sum_j |P_{min}(\bar{r} - \bar{r_j})|^2} \tag{4.25}$$

$$P^{min}(\bar{r}) = \frac{\sum_j O'_{min}(\bar{r} - \bar{r_j})E_j(\bar{r})}{\sum_j |O_{min}(\bar{r} - \bar{r_j})|^2} \tag{4.26}$$

P_{min} and O_{min} are dependent, but alternating between minimizing the expression using the current estimates for O_{min} and P_{min} for a few iterations is found to be an efficient method to find the probe and object[99].

We can now express the overlap constraint projection

$$\Pi_O(EE) : E_j \to E_j^O = P_{min}(\bar{r} - \bar{r_j})O_{min}(\bar{r}) \tag{4.27}$$

O in sub- and superscript simply denotes that we are dealing with the overlap constraint. The iterative procedure can be written as a Fienup's HIO algorithm using the projections.

$$EE_{n+1} = EE_n + \Pi_F(2\Pi_O(EE) - EE) - \Pi_O(EE) \tag{4.28}$$

This results in a single update step. Compared to the PIE algorithm the overlap projection corresponds to step 1 and 7, whereas the intensity projection corresponds to step 2-5. It is a bit different from step 6 in PIE because we are updating the exit wave, but we can easily get the object and probe – in fact we already calculate them in the overlap projection.

Like the PIE algorithm, convergence can be monitored by distance between measured and calculated detector intensities, R, or simply by the difference between iteration, ϵ:

$$R = \frac{\sum_{g,j} |\sqrt{I_j)(\bar{q})} - |FT\,(P(r - r_j)O(r))||}{E_{g,j}\sqrt{I_j(\bar{q})}} \tag{4.29}$$

$$\epsilon_{n+1} = \|EE_{n+1} - EE_n\| \tag{4.30}$$

There is no proof for convergence for non-convex datasets, but in practice convergence has been demonstrated for a number of data sets[48, 99].

Besides a more compact formulation, the simultaneous processing of all probe illumination allow us to use the overlap constraint more directly (opposed to support constraint in PIE) and determine both object and probe. However, there is one problem with our decoupling of object and probe. Given that P and O are solutions and the function 4.31,

$$f(\bar{r}) = f(\bar{r} - \bar{r_j}) \quad \forall\, \bar{r_j}, \tag{4.31}$$

Then an alternative set P' and O' will also be a solution:

$$\sum_{j,\bar{r}} P(\bar{r}-\bar{r_j})O(\bar{r}) = \sum_{j,\bar{r}} P(\bar{r}-\bar{r_j})[f(\bar{r})]^{-1}f(\bar{r})O(\bar{r}) = \sum_{j,\bar{r}} P'(\bar{r}-\bar{r_j})O'(\bar{r}) \tag{4.32}$$

So for each function $f(\bar{r})$ there will be an additional set of solutions P' and O' which the PDM algorithm can converge towards. A constant will always fulfill the requirement, $f(\bar{r}) = C$. The existence of additional f depends on the distribution of r_j. If the scans are regularly distributed like the lattice obtained by a raster scan, any function with similar frequency will fulfill the requirement for f. To counter this Dierolf et. al argues in favor of more irregular scanning schemes (e.g. concentric circles) to avoid raster scan artifacts[102]. Raster artifacts can also be suppressed by using a flat field support constraint i.e. by keeping a known featureless object area constant.

4.3 Electron density and resolution

Having obtained ptychographic projections, all the phase projections are assembled into a 3D map by computed tomographic reconstruction, see Chapter 5. As described in equation 1.6 the refractive index have a real part, β, and a complex part, δ, representing the phase. PXCT allows for the reconstruction of a 3D distribution of $\delta(\bar{r})$, which can be related to electron density, $\rho_e(\bar{r})$, using the classical atom radius, r_0, and the X-ray wavelength, λ:

$$\rho_e(\bar{r}) = \frac{2\pi\delta(\bar{r})}{r_0\lambda^2} \tag{4.33}$$

Obtaining a physical parameter such as electron density distribution is a clear advantage of PXCT compared to other techniques with arbitrary contrast. It allows the investigator to probe variation in material density at the nano scale. These can be compared to other nano studies or the bulk electron densities of a material found based on its mass density, ρ_m, and relative distribution of elements:

$$\rho_e = \rho_m \frac{N_a \sum_j a_j Z_j}{M} \tag{4.34}$$

where N_a is Avogadro's number, M is the molar mass and a_j the number of the j'th element with atom number Z_j.

Spatial resolution

It is critical to be able to estimate the spatial resolution when working with high resolution microscopy. One way to estimate image resolution in 3D is using Fourier Shell Correlation (FSC)[103]. It studies the correlation between two independent 3D maps of the same object to quantify at which spatial length scale stochastic noise becomes significant.

$$FSC(r) = \frac{\sum_{r_i \in r} F_1(r_i) \cdot F_2(r_i)^*}{\sqrt{\sum_{r_i \in r} |F_1(r_i)|^2 \cdot \sum_{r_i \in r} |F_2(r_i)|^2}} \tag{4.35}$$

where F_j is the Fourier transform of the j'th image, and * denotes the complex conjugate and r is a radius corresponding to a shell in the 3D Fourier transforms.

The resolution can be found by comparing the FSC curve to a threshold curve. Different threshold curves have been proposed, but this work uses the 0.5 bit information threshold curve. The threshold curves can be theoretically derived by relating the FSC curves to signal to noise ratio (SNR) as done by van Heel and Schartz[103]:

$$FSC(r, SNR) = \frac{SNR(r) + 2/\sqrt{n(r)} \cdot \sqrt{SNR(r)} + 1/\sqrt{n(r)}}{SNR(r) + 2/\sqrt{n(r)} \cdot \sqrt{SNR(r)} + 1}. \tag{4.36}$$

Where $n(r)$ is the number of voxel at the radius r. Choosing a desired SNR allows one to compute the threshold curve, and find the spatial resolution at the intersection with the FSC curve. Using a SNR of one yields a 1 bit information threshold curve.

In practice, the two independent 3D maps are found by dividing the total number of projections in two and using each half to produce a 3D map. In the final reconstruction (using all projections) the SNR is expected to be twice that of the tomograms used in FSC. The SNR requirement is, in practice, often halved to estimate the resolution in the final reconstruction. Note this does not give rise to the half bit information criterion. This criterion is used based on its empirical agreement with other methods for determination of spatial resolution in X-ray crystallography[104]. The criterion has also proven consistent with other spatial resolution measurements in PXCT[49]. It corresponds to a SNR of 0.4.[103].

Another resolution concern is a basic limit from information theory known as the Shannon/Nyquist sampling theorem. It states that one have to sample at twice the resolution level to reconstruct a signal unambiguously. For computed tomography, angular resolution depends on a sufficient number of projections compared to the object size:

$$R > \frac{\pi}{2} \frac{L_O}{N_{proj}} \tag{4.37}$$

Where R is the spatial resolution, L_O is the object size and N_{proj} is the number of evenly spaced projections. Note that the Shannon/Nyquist sampling theorem only sets a lower limit for spatial resolution, so in practice the obtained resolution will be somewhat above the limit.

4.4 Segmentation theory

This section introduces two concepts: Markov random field segmentation and partial volumes. Markov random field segmentation is a useful alternative to threshold segmentation when expected values for different segments overlap and nearest neighbor information can be used to differentiate segments. Understanding partial volumes is important to model them properly and these model functions are essential for formulating and performing Markov random fields segmentation.

Markov random fields

Markov random field segmentation states that the probability of a label at a given position, i, can be described by the given label of that position f_i and the labels of its nearest neighbors, f_{N_i}, where N_i is the positions of i's nearest neighbors. Using Gibbs sampling[105] the

expression becomes

$$P(f_i|f_{N_i}) = \frac{1}{Z}\exp\left(\alpha_i f_i + \sum_{j\in N_i}\beta_{i,j} f_i f_j\right), \tag{4.38}$$

where Z is a normalization factor, α_i is the a priori probability for the label f_i and $\beta_{i,j}$ is the interaction cost of i'th and j'th label.

The Markov fields can be conditioned to observed data x_i, but we need to know the expected data distribution of each label. Pure materials are expected to produce Gaussian data distributions, whereas the distribution of partial volumes will be investigated in a later section. Assuming a Gaussian relation between label and data gives the following probability:

$$P(x_i|f_i) = \frac{1}{2\pi\sigma_{f_i}^2}\exp\left(\frac{-(x_i-\mu_{f_i})^2}{2\sigma_{f_i}^2}\right), \tag{4.39}$$

where the expected mean of f_i is μ_{f_i} and the expected variance is $\sigma_{f_i}^2$. However, a segmentation process is a reverse problem where the observed values x are known and f needs to be found. This probability can be formulated using Bayes' theorem:

$$P(A_i|B) = \frac{P(B|A_i)P(A_i)}{P(B)} = \frac{P(B|A_i)P(A_i)}{\sum_j P(B|A_j)P(A_j)}. \tag{4.40}$$

For the label probability of the Markov random field, it becomes:

$$P((f_i|f_{N_i})|x_i) = \frac{P(x_i|(f_i|f_{N_i}))P(f_i|f_{N_i})}{P(x_i)}. \tag{4.41}$$

The expected function value of a label should not depend on the neighbors, thus

$$P(x_i|(f_i|f_{N_i})) = P(x_i|f_i). \tag{4.42}$$

Equation 4.41 now yields

$$P(f_i|f_{N_i}, x_i) = \frac{P(x_i|f_i)P(f_i|f_{N_i})}{P(x_i)} = \frac{P(x_i|f_i)P(f_i|f_{N_i})}{\sum_{j\in J} P(x_i|f_j)P(f_j|f_{N_j})}, \tag{4.43}$$

where J is a set of all possible labels.

In practice, the result of Markov fields can be calculated by iterating over all i until a steady state is found. However, this must be done without introducing systematic tracing errors. For a grid of squares where only fields in direct horizontal or vertical contact are considered neighbors, this can be done by using a checker board pattern and alternating between evaluating the "white" and "black" areas of the board. A result of Markov segmentation in a simulated data set with different noise levels using various β values can be seen in figure 4.4. Too low β values do not suppress the noise, whereas too high beta values wrongly connect areas and suppress small features. Graph-cut methods can be used avoid numerous simulations and guarantee an optimum is found, for practical implementation of a graph-cut algorithm see reference [106].

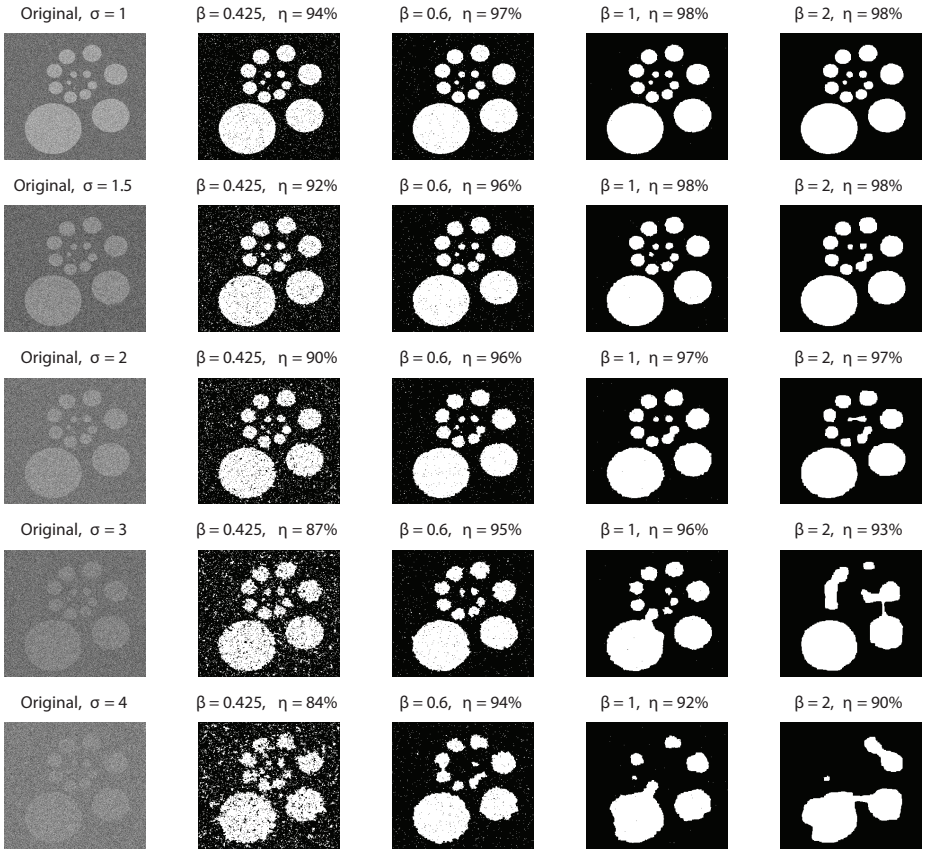

Figure 4.4: Left column shows the source images and the rest show Random markov field segmentation conditioned by the source image. The σ values denote standard deviation in the Gaussian noise added to the ground truth. β is the smoothing parameter, (for label space J={-1, 1}. η is the classification efficiency denoting how many pixels were correctly classified compared to the ground truth. All segmentation is based on 500 iterations - which from observations were found to be enough to reach an equilibrium. As the border was not updated it was initialized as black.

Partial Volumes

The relationship between a label and data was assumed to be Gaussian in the previous section on Markov random fields. This is a reasonable assumption for an area with a pure material, but is not necessarily true for regions with material interfaces i.e. two or more materials in the same region. This section is dedicated to finding a function describing intensity distributions obtained from partial volumes.

Partial volume effects are simulated by first placing a cylinder of one material inside another material, secondly reducing the spatial resolution and calculating new voxel

intensities based on volume fraction and thirdly recording the intensity of all partial volume voxels. This represents the resolution limit of the actual measurement, shown in figure 4.5 e.g. materials first shown with 1 nm resolution and afterwards measured with 30 nm spatial resolution. The orientation of the cylinder was kept constant and the simulation is equivalent to the 2D case of placing a circle of one material inside another material. Simulation was performed by placing material with expected value of 1 in a material with expected value of 0. The cylinder radius used was 0.6 of the measurement resolution and the resulting intensity distribution is shown in figure 4.5.

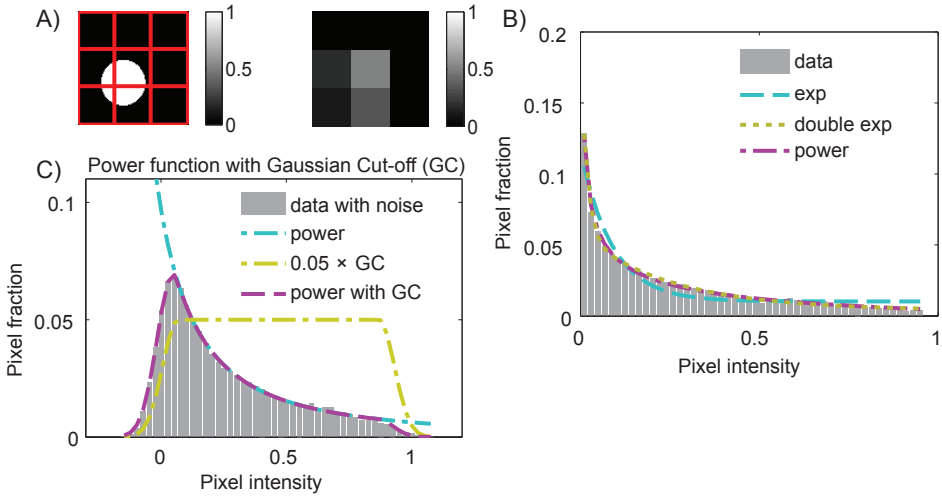

Figure 4.5: A) Illustration of the simulation process, where a white cylinder with value 1 is placed in a matrix of material with value 0. The coarser resolution is calculated based on volume ratio. B) Obtained intensity histogram from 10000 randomly placed cylinders fitted with a exponential function, a double exponential function and a power law. C) Intensity histogram obtained by adding Gaussian noise to the coarse voxel intensity with a standard deviation of 0.05. It is fitted by a power law combined with a step function with Gaussian cut-offs.

The histogram of the recorded intensities from partial volumes was fitted using three different functions as shown in figure 4.5 and table 4.6. Poisson statistics was assumed and goodness of fit was found using reduced least chi square, χ^2_{red}. It showed that the best fit was obtained using a power law (see table 4.6).

Experiments will have measurement errors, which we will account for by adding Gaussian noise with a standard deviation of 0.05. The obtained intensity histogram was fitted using the previously determined power law, combined with a step function with Gaussian cut-offs:

$$f(x) = p_1 \cdot (x - p_3)^{p_2} \cdot \begin{cases} \frac{\text{Gauss}(x,p_5,p_4)}{\text{Gauss}(p_5,p_5,p_4)} & \text{if } x \leq p_5 \\ 1 & \text{if } p_5 < x < p_6 \\ \frac{\text{Gauss}(x,p_6,p_4)}{\text{Gauss}(p_6,p_6,p_4)} & \text{if } x \geq p_6 \end{cases}$$

Name	Formula	χ^2_{red}
Exp	$f(x) = p_1 \cdot \exp(p_2 \cdot x) + p_3$	23.6
Double exp	$f(x) = p_1 \cdot \exp(p_2 \cdot x) + p_3 \cdot \exp(p_4 \cdot x) + p_5$	1.95
Power	$f(x) = p_1 \cdot x^{p_2} + p_3$	1.54

Table 4.6: Functions fitted to intensity histograms from partial volumes and the resulting χ^2_{red} calculated assuming Poisson statistics.

where

$$\text{Gauss}(x, \mu, \sigma) = \exp\left(\frac{-(x-\mu)^2}{2\sigma^2}\right)$$

The resulting fit is shown along with the Gaussian function and the step function in figure 4.5. The goodness of the resulting fit was found to be $\chi^2_{red} = 1.06$. Thus, the function was deemed able to accurately describe the partial volume effects. The functions are only validated for the described system, so it is possible it is only a special case of a more general description of partial volumes. Further work could be dedicated to more detailed simulations, but for now we will use the obtained function to describe partial volumes in general.

4.5 Experimental results

Name	Electron density Å^{-3}
Silver	(Not in sample)
PEDOT:PSS	0.42
PDTSBT-F:PCBM (BHJ)	0.39
Zinc oxide	1.58
PEDOT:PSS	0.42
P3MHOCT:PCBM (NP)	0.40
Zinc oxide	1.58
PEDOT:PSS	0.42
Silver	2.75
PET	0.45

Table 4.7: Electron densities of materials in the cell by layer sequence.

This section will go through PXCT imaging of an tandem cell and how it can help understand and optimize the structure, in particular, an active layer cast from water dispersible Landfester nanoparticles.

Tandem device structure

The tandem cell is produced by slot die coating on a mini roll coater[107]. The mini roll coater is a good model for large scale fabrication of roll-to-roll coating, and still suitable for

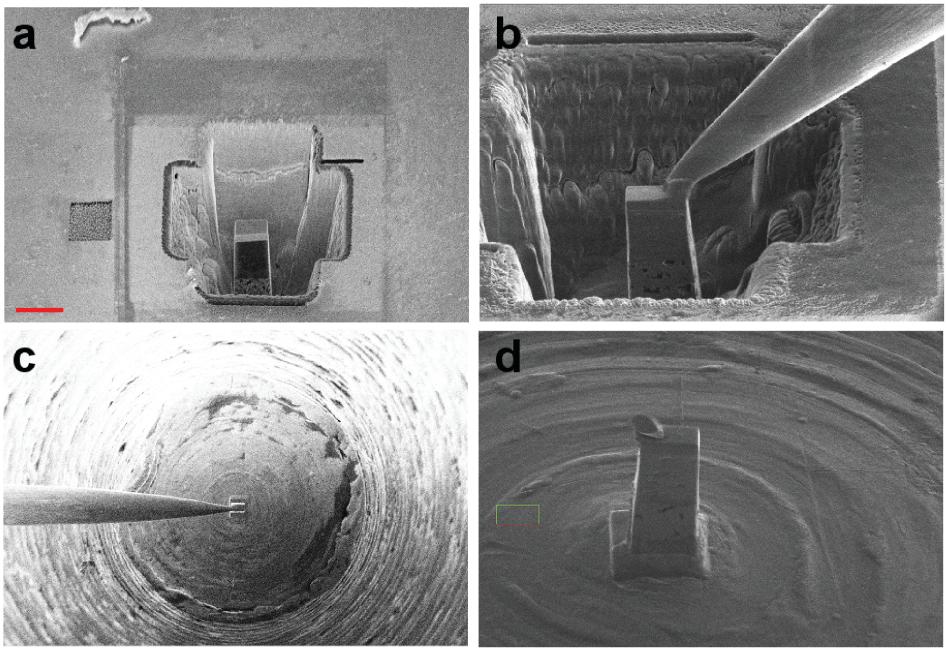

Figure 4.8: Sample preparation of OPV prism. A) After depositing a thin protective platinum layer surrounding material is milled away with an ion beam. B) A wolfram omniprobe is attached to the sample by platinum deposition and the support is cut. C) The sample is removed with the omniprobe and attached to the sample holder (a gold-coated brass pin 100 μm across). d) The omniprobe is cut loose. Scalebar in a) is 10 μm.

small scale experiments with little material use on small sample areas making it possible to quickly iterate through experiments.

The structure of the device is shown in table 4.7. The structure was chosen to include a photoactive layer of Landfester particles cast from water and a photoactive layer cast from organic solvent. This provides the opportunity to compare the layer structures as well as imaging the other layer interfaces present in a tandem device. The overall structure was based on proven tandem architecture enabled by PXCT[92].

Sample preparation for PXCT was carried out using focused ion beam (FIB) milling as illustrated in figure 4.8 for a different sample with similar preparation. To protect the sample, gold was sputtered on top of the sample and an additional organic platinum layer was deposited. A 6.2 μm $\times$ 5.5 μm prism of tandem cell was milled out using FIB. A wolfram tip was welded to the sample by platinum deposition, and used to move the sample onto the sample holder. A final platinum deposition fastened the sample to the sample holder.

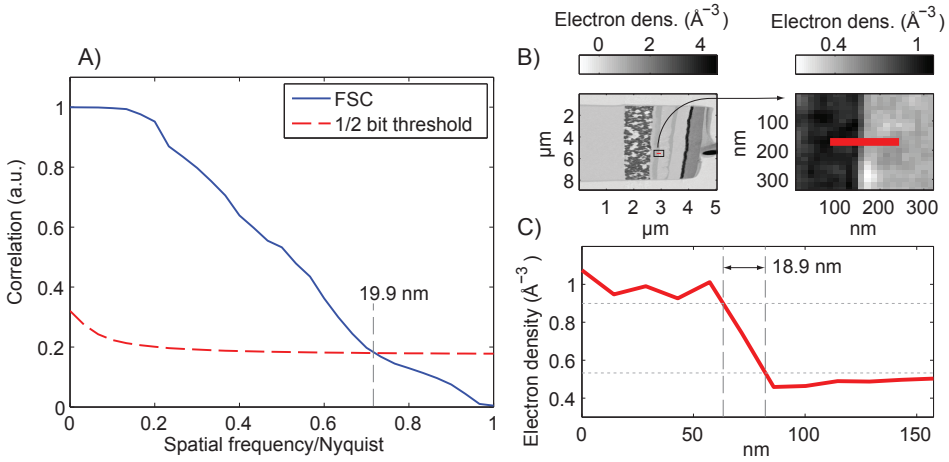

Figure 4.9: A) FSC showing a spatial resolution of 19.9 nm B) visual image of line scan area presented in C) showing 18.9 nm spatial resolution with a 10%-90% rule.

PXCT experiment

The PXCT experiment was carried out at the CSAXS, PSI Switzerland using a previously described setup[49]. A coherent 6.2 keV X-ray beam was focused by a Fresnel zone plate leaving a flux of $3.6{\cdot}10^8$ photons/s. The sample was placed at a distance of about 1 mm downstream of the focus providing a beam diameter of about 3.3 μm at the sample position. The sample was protected by a gentle flow of nitrogen. Ptychographic scans covered an area of 10×5 μm^2 (horizontal $\times$ vertical) and was performed in a pattern of concentric circles with a radial step size of 0.8 μm. Diffraction patterns were recorded with a Pilatus 2M detector[108] placed 7.389 m downstream from the sample using an exposure time of 0.1 s.

470 ptychographic projections were recorded covering a range of 180°. Problems with missing data due to gaps between detector modules were circumvented by acquiring projections at alternating detector positions[49] and reconstructing the scans using identical illumination probes as described previously[109]. The ptychographic reconstruction used 200 iterations of a difference map based algorithm[99] followed by 100 iterations of maximum likelihood refinement[110]. Ptychographic reconstructions were performed using a region of 600×600 pixels centered around the diffraction intensity yielding reconstructed images with a pixel size of 14.3 nm.

The reconstructed phase images from all projections were used for tomographic reconstruction after post-processing and alignment according to the procedure described in reference [111] and a tomographic alignment algorithm that further refined the horizontal position of the projections as described in reference[112]. The spatial resolution was estimated to be about 20 nm by Fourier shell correlation and line scans as shown in figure 4.9.

X-ray dose estimation

X-ray dose, d, is estimated by number of photons, N_0, photon energy E_p, absorption coefficient of the material, μ and density of the material ρ:

$$d = \frac{\mu N_p E_p}{\rho}. \tag{4.44}$$

The experimental parameters are $3.7{\cdot}10^7$ photons/m^2 in our ptychographic scans over 470 projections with an energy of 6.2 keV. This yields a dose of about $8.0{\cdot}10^7$ Gy in PEDOT:PSS, and $7.1{\cdot}10^8$ Gy in silver. Note the calculations are surface dose and generally overestimate the total dose e.g. the thickness of the silver is about three times its attenuation length. No damage was observed during the experiment, and a nitrogen flow is believed to be sufficient to prevent spatial degradation at these doses.

Photoelectric results

The photoelectric performance of the constructed OPV tandem devices with one photo active layer consisting of Landfester particles was characterized before PXCT experiments (for photoelectric characterization see chapter 1). The results are shown in table 4.10, along with results from previous experiments using the same materials as BHJ in single and tandem devices.

	V_{OC} (V)	J_{SC} (mA cm^{-2})	FF (%)	PCE (%)
Tandem BHJ_1-NP_2	0.52	0.67	35.7	0.12
Tandem[92] BHJ_1-BHJ_3	1.32	4.3	46.9	2.67
Single[92] BHJ_1	0.61	4.98	45.2	1.37
Single[113] BHJ_2	0.65	4.09	33.6	0.90
Single[92] BHJ_3	0.83	5.40	49.0	2.20

Table 4.10: Photo electric characterization of the investigated tandem device with an active layer of Landfester particles (top) and previously reported results for the same materials in tandem and single junctions. Here $_1$ denotes PDTSBT-F:PCBM, $_2$ denotes P3MHOCT:PCBM and $_3$ denotes PBDTTTzT:PCBM.

The basic concept in a tandem cell is that both photoactive layers build up potential. A clear sign of a working tandem cell is therefore a V_{OC} larger than the V_{OC} of single junction devices with the two materials. The tandem cell with the Landfester NP layer have both a V_{OC} and a J_{SC} smaller than the single junction devices with either material. The tandem structure itself has been proven to work using two BHJ and did produce V_{OC} larger than the single junctions[92]. Since the only change is the replacement of a BHJ with a Landfester active layer, the lower performance can either be caused by intrinsic worse photoelectric performance of the NP layer or structural changes caused by the NP layer. The structure is investigated using PXCT.

Tomographic results

PXCT allows one to obtain the electron density of the tandem structure. The materials used and their expected electron densities are shown in table 4.7. The organic materials PEDOT:PSS and the two active layer materials show little difference between their electron densities compared to the other materials. It is therefore challenging to separate these materials into different segments, and any such segmentation will be quite uncertain. PEDOT:PSS and active layer materials will be considered as one in the further analysis and referred to as organic material i.e. PEDOT:PSS + PDTSBT-F:PCBM as organic BHJ and PEDOT:PSS + P3HT:PCBM as organic NP.

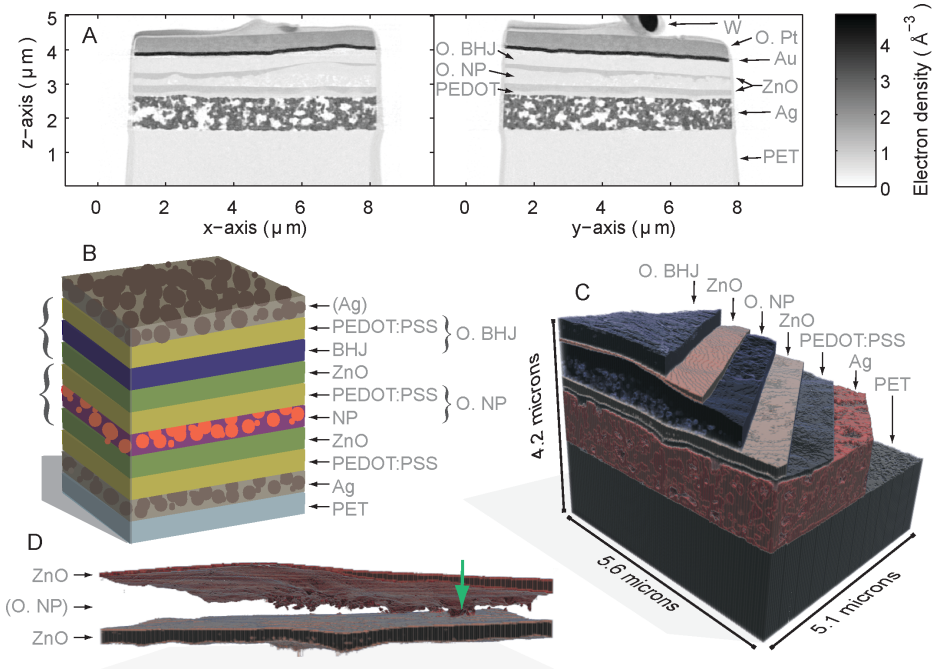

Figure 4.11: A) Central slices from the PXCT data of the OPV tandem cell with materials annotations. Note wolfram (W), organic molecules with platinum (O. Pt) and gold (Au) are part of the sample preparation. PEDOT is short for PEDOT:PSS. B) Schematics of the sample with annotations similar to C) a 3D rendering of the segmented layers in the PXCT data. The abbreviations used are organic BHJ (O. BHJ), zinc oxide (ZnO), organic NP (O. NP) and silver (Ag). D) Contacts observed between the two zinc oxide layers marked by the green arrow.

The obtained PXCT tomogram in figure 4.11 is shown along with expected layer structure. The initial observations indicate a homogeneous organic BHJ, whereas especially the bottom of the organic NP layer have heterogeneities in form of spots with lower electron densities. This could be related to the P3HT-PCBM Landfester particles. If that is the case

the Landfester particles only partially cover the surface and have high variation in thickness. A closer examination of the organic NP layer shows penetration of the zinc oxide into the organic NP layer. There is even a point where zinc oxide clearly penetrates the layer i.e. the green arrow in figure 4.2. Penetration results in a short circuit of the active layer, which also explains the low V_{OC} and J_{SC} of the tandem structure, as it is effectively a single junction with a long path length to one of the electrodes.

Segmentation

Segmentation was performed using the expected layer structure and electron densities. The tomogram was initial partitioned into subtomograms using the maximum gradients at the interfaces as rough separators. Air and residual redepositions from the FIB process was removed so only the interior of the tomogram was considered. The electron density histogram was fitted using Gaussian functions and power laws with Gaussian cuts-offs to explain pure materials and material mixtures, respectively. These functions were used to calculate probability maps i.e. probability of a pixel at a given electron density belonging to a given segment. The probability was used as input for the Markov random field segmentation, where the beta parameters was fitted to minimize the segmented distance to the probability functions. Compared to threshold segmentation, which was also explored, Markov random field reduced the distance to the probability functions and visually removed noise in the segmentation, as shown in figure 4.12.

One risk of using Markov random field segmentation is removal of features e.g. one-pixel features where the neighbors have a different label. However, one could wonder whether it is truly possible to distinguish one-pixel features from noise, and if such errors are preferred to gain more robust and sensible segmentation. Also note that the division of the tomogram into subtomograms was necessary to avoid false labeling e.g. the partial volumes between silver and air include electron densities belonging to zinc oxide even though we have no reason to suspect zinc oxide is located in the middle of the silver electrode. These problems are not unique to Markov random field but considered a general problem in segmentation, where more than one segment might yield the same electron density.

Electron densities

The expected electron densities are shown in table 4.7. With the segmentation described previously, the determined electron densities of each segment can be compared to the theoretically predicted values. Most electron densities agrees with the values calculated from theory, but 3 layers: zinc oxide, silver electrode and organic NP layer showed either deviating electron densities or signs of porous structures, as shown in figure 4.13.

Zinc oxide shows an electron density of only 0.96 $Å^{-3}$, whereas the expected value is 1.60 $Å^{-3}$. The zinc oxide layer is cast from nanoparticles so the lower electron density is likely an indication of porosity in the layer. According to the PXCT experiment 60% of the volume consist of zinc oxide in the layer.

The silver electrode has three segments: Pure silver, pure air, and material mixtures at interfaces. Both the silver and air have Gaussian distributions with mean values at the expected electron densities. The PEDOT:PSS does not penetrate deeply into the porous silver electrode compared to another PXCT study[92], but resides at the surface. In the other experiment, a thicker layer of PEDOT:PSS was used when manufacturing the

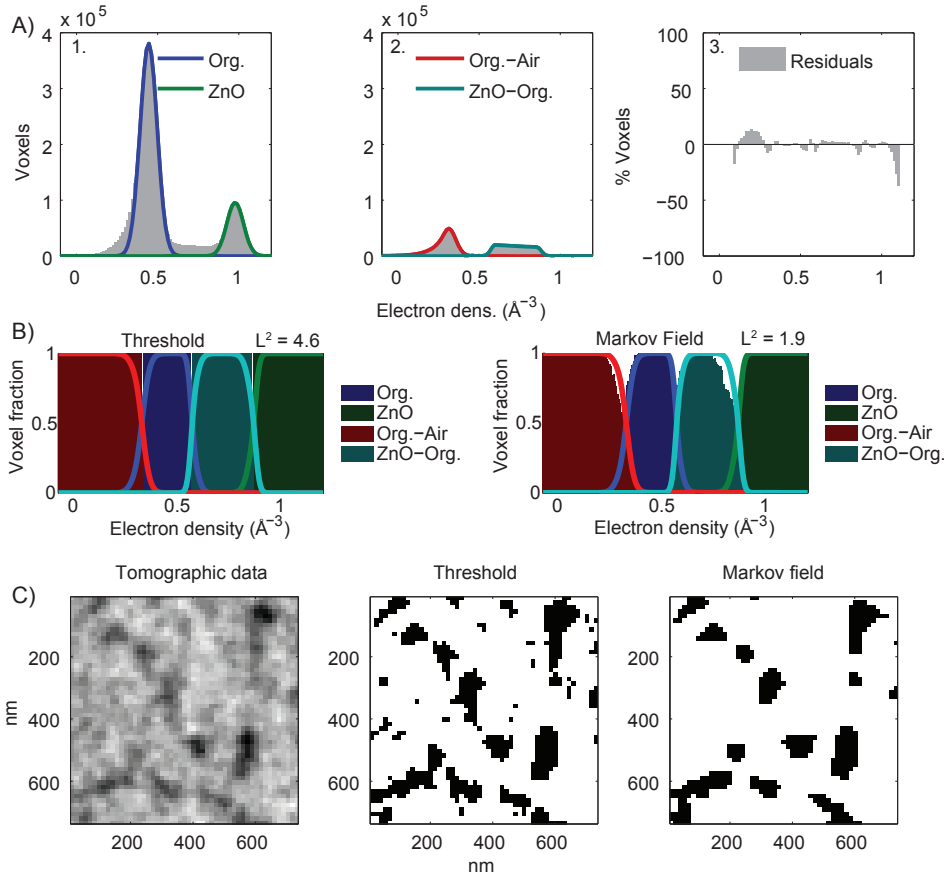

Figure 4.12: A) Histogram from a subset of the PXCT tomogram subsequently fitted with 1) Gaussians for pure materials and 2) power laws with Gaussian cut-offs for material blends leaving practical no residuals 3). B) Lines show the expected segment fraction at a given energy, and solid areas show the actual segmentation. The distance is evaluated by the L^2 showing Markov random field outperform thresholding. The visual effect is shown in figure C) on an area organic NP area with air pockets.

flextrode[114] and the larger amount of material might be the reason for the penetration into the electrode[92]. Another possibility is that previous experiments had misaligned ptychography projections which would blur the tomogram and make it more difficult to see the pure air phase.

The organic NP layer have both a pure organic phase and mixture of air and organic materials. The mixture of organic material and air is located in spots distributed throughout the lower levels of the organic NP layer. If there existed a significant amount voxels with only air there would be a significant Gaussian distribution with mean value at 10^{-3}Å$^{-}3$, which is the expected electron density of air. This is not the case and is interpreted as the air volumes

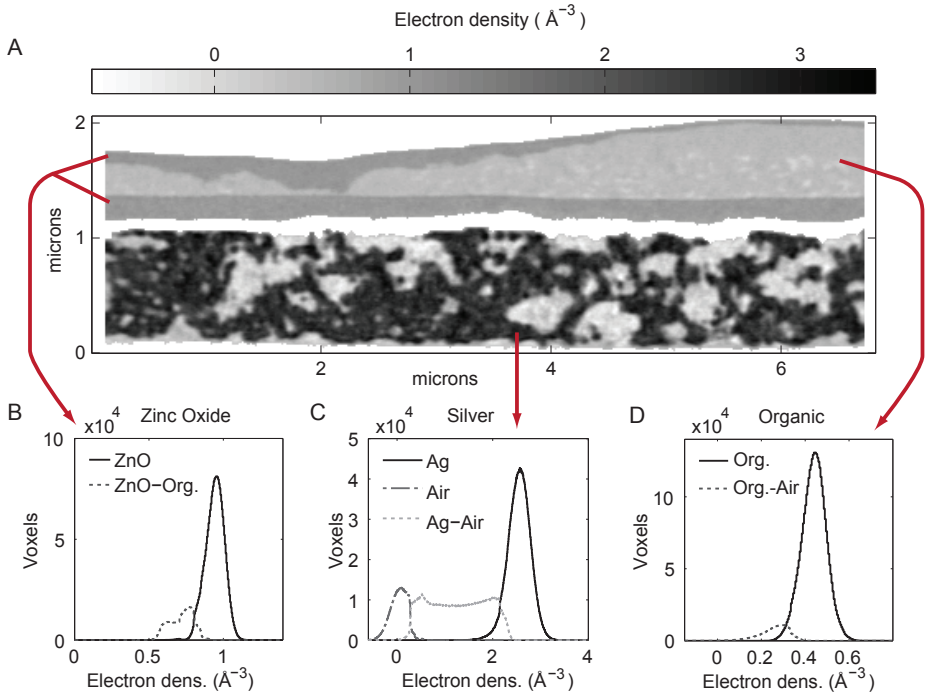

Figure 4.13: A) Slice of the PXCT tomogram near the zinc oxide contact. Electron density histograms of the segments in A) Zinc oxide B) Silver and C) the organic NP layer. Partial volume effects are observed between the layer interfaces and between air and material in the porous silver and organic NP layer.

being smaller than the spatial resolution (20 nm), so only partial volumes are detected. We can confidently attribute the partial volumes to the presence of air, because it is the only reasonable material with lower electron density than organic material. Furthermore, the spots are localized indicating that they could be result of stacked Landfester nanoparticles with air pockets between them. Even though we do not have the spatial resolution to fully resolve the porosity, we can, through the models for partial volumes, obtain information on sub resolution air regions.

Interface analysis

PXCT provide the full 3D structure of the device, and allows interface investigation that is otherwise not possible. Existing interface investigation methods rely on exposed surfaces such as AFM measurements or are destructive e.g. TOF-SIMS. PXCT allows for a unique full 3D view and interface analysis as shown in figure 4.14.

A top-bottom interface correlation measures the direct correlation of surface shape i.e. interfaces with the same locations of local maxima and minima will have a high positive correlation, whereas two interfaces where the local maxima of one is placed at the minima of the other (and vice versa) will have a high negative correlation. Interface correlation is

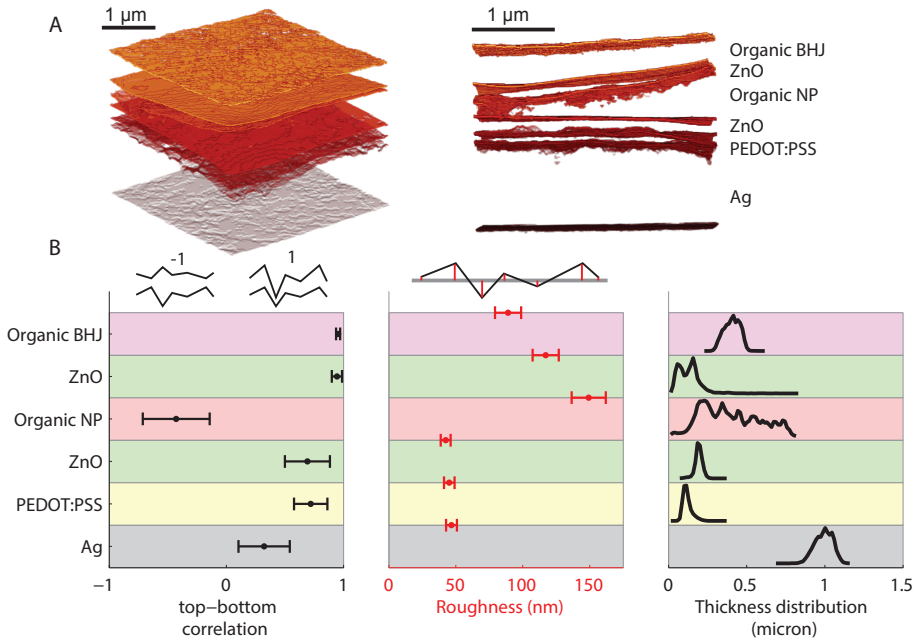

Figure 4.14: A) Extracted sub section of the layer interfaces. B) Obtained interface and layer parameters. Left) Correlation between top and bottom interface, middle) Surface roughness and right) histogram of thickness in the layer. The tail in the top zinc oxide layer is due to spikes through the organic NP layer.

not limited to minima and maxima, but helps to understand the method. The correlation between the top and bottom of a layer reveal information about a layer formation process i.e. the cast layer follows the structure below, is indifferent to it or invert it by a positive, zero or negative correlation respectively.

The results shown in figure 4.14, shows an overall trend of positive top bottom correlation. The 1 micron thick silver layer consisting of nanoparticles has a slight positive to no correlation, whereas all other layers, with the exception of organic NP layer, have a clear positive top-bottom interface correlation. The overall positive top-bottom interface correlation is beneficial as it minimizes the risk of shorts circuits and allow for non-smooth surfaces, as perturbations in layer thickness simply propagate. The organic NP layer increases the risk of short circuits due to the negative top-bottom correlation. A possible explanation for this behavior is that initial nanoparticles adhere to the surface at minima, and the subsequent nanoparticles grow by adhering to residing particles due to their polar surfaces. A way to mitigate this layer formation is to make particles without polar surfaces i.e. use no or non-polar surfactants.

Interfaces can also be characterized by roughness as shown in figure 4.14. Roughness measures the average displacement from a completely planar surface. Again the nanoparticle layer distinguishes itself by a high overall roughness, and compared to the other layers, introducing a steep increase in roughness that only gradually decreases in subsequent layers due to their positive top-bottom layer correlation. This also manifests itself in the layer

thickness distribution shown in figure 4.14, where the organic NP layer has a wide distribution compared to the other layers. The tail in the top zinc oxide layer is a product of the spikes penetrating through the active layer. The double peak in the zinc oxide is also a product af the roughness in the organic NP layer, as high regions have a thin layer of zinc oxide and low regions have a thicker zinc oxide layer on top. This can be explained by zinc oxide flowing towards the lowest regions while drying thereby creating two different thicknesses.

The overall properties of the organic nanoparticle layer is undesirable in organic photovoltaics, as they increase the risk of shorts circuits and makes it challenging to optimize active layer thickness. Furthermore, some of the undesirable traits such as the high roughness are transferred to the subsequent layers as indicated by the large observed difference between the roughness of the zinc oxide layer cast before and after the organic nanoparticle layer. The initially observed short circuit of the organic nanoparticle layer is not a unique random occurrence, but a likely product of the problematic layer formation of the Landfester nanoparticles. Layer formation could likely be improved by having non-polar nanoparticles, and porosity be reduced by annealing the particles before casting subsequent layers. However, long annealing times are also detrimental to the performance of OPV devices containing Landfester nanoparticles[115].

Improved photoelectric performance

It is worth investigating if an improved nanoparticle layer would indeed result in improved device performance before experimenting with a series of modified Landfester nanoparticles. One way to test this is to remove the observed shorts circuits in the nanoparticle layer by filling open cracks with a less conductive material that prevent the short circuits from forming. Obvious candidates are the active layer materials themselves because they also possess appropriate energy levels.

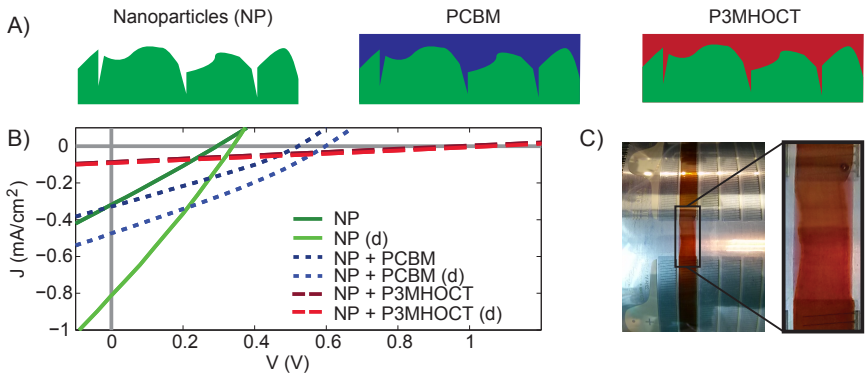

Figure 4.15: A) Schematic of different NP layer modifications from the left: only NPs, NPs with PCBM on top, and NPs with P3MHOCT on top. B) JV-curves for tandem devices with the different layers, where (d) denotes measurements with double illumination. C) Photograph of a NP layer with P3MHOCT on top. The NP layer is at least partially preserved as indicated by the NP dewetting edges visible through P3MHOCT.

The schematic construction of the active layer and photoelectric characterization of tandem devices with extra PCBM or P3MHOCT are shown in figure 4.15. More than half of the devices made only with nanoparticles were non-functional and had resistor behavior. The devices were tested both with front illumination and double illumination where simulated sunlight is applied from both sides of the device as described previously[93].

P3MHOCT gives a better performance than PCBM as the energy levels are closer aligned with the PEDOT:PSS i.e. both are hole conductors. Most notable, the device performance increase to clear tandem performance with V_{OC} above 1 V (higher than then single junction devices reported in table 4.10) when P3MHOCT is filling up the porosity and smoothing the roughness of the photo active nanoparticle layer. It is possible that the organic solvent in the P3MHOCT partly redissolves the underlying layer. However, visual observations indicate that the nanoparticle layer at least is partially conserved as shown in figure 4.15.

Thus, it is possible to achieve tandem performance with the nanoparticles, if proper layer formation is achieved. In this case, it was done using the extra intermediate layer of P3MHOCT, but future experiments could improve the coatability and layer formation by using particles with non-polar surfactants. This work highlights the need for future development and improvement of Landfester nanoparticle layer formation.

4.6 Summary and future experiments

PXCT is ideal for investigating OPV structures due to its penetration depth (microns using multi-keV photons), increased contrast by obtaining phase information, quantitative determination of electron densities and high spatial resolution e.g. 20 nm for the experiment presented here. The structure of an OPV tandem cell with one traditional BHJ active layer, and one active layer cast from Landfester nanoparticles was investigated. Initial poor photoelectric device performance was linked to electric short circuits through the active Landfester particle layer observed in the PXCT tomogram. Furthermore, porosity was observed in the silver electrode, in the Landfester particle layer and indirectly in the zinc oxide layers due to their reduced electron densities. All observed porosity is attributed to the fact that the layers are cast from nanoparticles.

An in-depth layer analysis indicated generally desirable layer formation of the materials e.g. consistent layer thickness. The Landfester particle layer is an exception with negative top-bottom interface correlation, wide thickness distribution and high surface roughness that is only gradually decreased in subsequent layers. A possible layer formation mechanism is initial Landfester particles locating themselves in local minima, and subsequent particles adhering to the first due to the polar particle surfaces. If such behavior is indeed the explanation for the layer formation it could be circumvented by using Landfester particles with non-ionic surfactant or using surfactant free particles.

The possible photoelectric result of increasing the layer formation properties, and thereby preventing electric short circuits through the active layer, was tested by coating photo active material on top of the nanoparticle layer. Clear tandem performance was reached using P3MHOCT which gave above 1 volt of V_{OC} compared to a maximum V_{OC} around 0.6 volt for single junction devices using the same photoactive materials. The experiment shows that improved layer formation of the Landfester nanoparticles will improve the device performance.

Future experiments

- Element sensitive tomography:
Even though the PXCT method increase contrast by accessing the phase information, many OPV materials are intrinsically difficult to segment due to their similar electron density. Elemental sensitive techniques such as X-ray fluorescence tomography[116], could achieve contrast by probing unique elements e.g. locate PCBM regions by absence of sulfur or PDTSBT-F by probing for fluorine. The chemical contrast needs to be matched by an appropriate spatial resolution. If only 2D resolution is needed energy resolved TEM or STXM could also be considered.

- Labscale nano tomography:
One of the disadvantages of PXCT is the requirement for highly coherent sources and high flux, only achievable at large scale synchrotron facilities. An easier access to tomographic data would mean a larger sample throughput, which allows better sample statistics and enable studies comparing different processing parameters. The imaging portal at the Technical University of Denmark expects to commission such a lab system at the end of 2015, using a Excillum X-ray source and possibly approaching 50 nm spatial resolution. Ongoing systematic studies with such a system might benefit the future development of OPV similar to the increased understanding PXCT achieved for the Landfester nanoparticles layer.

- PXCT on perovskite and other complex energy materials:
PXCT holds a unique ability for non-destructive high resolution 3D imaging. Perovskites constitute an upcoming photovoltaic technology already having achieved high performance of 20%[117, 118]. However, perovskites are also facing challenges with an unstable structure[119]. PXCT could help uncover some of the structural changes and is to improving stability even though the sample preparation might prove difficult with such unstable materials. Other relevant energy materials could be battery and fuel cells materials.

CHAPTER 5

Tomographic alignment

In chapter 4, we introduced PXCT as a powerful tool to characterize organic photovoltaics. The specific PXCT experiment had about 20 nm spatial resolution, but for many applications even higher resolution would be desired e.g. to study the distribution of P3HT and PCBM in nanoparticles and active layers in general. In the last chapter we even documented the existence of sub-resolution porosity as partial volumes whereas higher resolution would be able to resolve them directly. One of the challenges with high resolution computed tomography is the mechanical sensitivity, where displacement on the nanometer scale will be present even in sophisticated experimental setups[111, 112]. To achieve nanometer resolution and reliable data, there is a need to correct for displacements - preferable in an automatic and reproducible way. This chapter will outline some general approaches to tomographic reconstruction and how they can be used to automate alignment and ensure the best possible resolution in future experiments.

5.1 Introduction

Tomographic 3D reconstruction is a general tool to go from 2D imaging originating from some sort of object to an accurate 3D model of the object. It is most commonly known in from macroscopic application in medicine but tomography is equally important on the micron and nanometer scale. Tomography on this scale is needed to study porosity, flow, cracks leading to mechanical failure, biological cells, etc.[120, 121, 122, 123]. Tomography itself is an inverse problem i.e. given a 3D model it is easy to find the expected 2D projections unambiguously, but given the 2D projections it is not trivial to put together a 3D model.

There are two main paths to deal with the inverse problem of tomographic reconstruction: Analytical reconstruction and algebraic reconstruction. The analytical reconstruction is the fastest and most widely used in the X-ray tomography community. The standard method and is known as Filter Back Projection (FBP)[124, 125]. The theoretical framework behind it, assumes a continuous description of object and projections and deals with the mathematical transformation between object and projections. In computer implementations approximations have been made to accommodate for the discrete nature of detectors and computation in general.

Algebraic reconstructions methods work with a discretized version of both object and projections, with a large transformation matrix that convert a 3D object to the 2D projection and the correct 3D object is found by minimizing the distance to the observed 2D projections. The matrix can generally not be inverted since it is for most cases not quadratic, and even pseudo-inversion is problematic as the matrix often does not have full rank. Even with full rank the matrix is ill-conditioned, so pseudo-inversion will not lead to a good solution. The conversion matrix is also quite large because the matrix scale with the number of projections and the object diameter cubed, which mean we are limited to fast algorithms that use various approximations to solve the optimization problem efficiently

e.g. Simultaneous Algebraic Reconstruction Technique (SART)[126]. An advantage of the algebraic reconstruction algorithms are the possibility to include regularization terms that contain prior knowledge like total variation (TV) which due to regularization have been able to successfully reconstruct 3D objects using only a few 2D projections[127].

From a reconstruction point of view the problem ends when an estimate of the 3D object is obtained. However, given that is it the correct 3D object, it should be easy to produce the 2D projections and match them to the observed data. If there is a mismatch between the calculated 2D projections and the observed data, it must be because of errors in the observed data or the geometry e.g. the projection angles were wrong. The key idea is to estimate displacement of the angle, translation or tilt by finding a displacement that reduce the distance to the observed 2D data i.e. projection distance minimization. Using the new displaced 2D projection a better 3D object can be reconstructed. The process can continue and is generally known as projection matching. The idea behind the algorithm is not new but for this work our implementation of the Estimated Movement by Iterative Logic machine, EMIL machine.

Projection distance minimization has been explored by Parkinson et al. who used a similar concept to align biological micro CT samples[128]. A different set of parameters was used by Tran et al. to align TEM projections, where a magnification factor is present[129]. Bleichrod et al. have worked on aligning binary tomographic data and combining the tomographic reconstruction and projection alignment into a single optimization problem[130, 131]. There have also been taken different approaches where physical principles such as mass profiles have been used to align projections[111, 112]. However, in most of these cases the alignment have been used to remove artifacts and not directly to argue for improved resolution nor the very necessity to utilize alignment algorithms to enable high resolution computed tomography, which is the main focus of this chapter.

Because, tomography can be used in 2D with 1D projections, and these examples are easier to illustrate and explain, this chapter will only have examples with 2D objects and 1D projections. 3D reconstruction can be performed by doing 2D reconstruction of one layer of the 3D stack at a time (for parallel beam geometry), or by extending the reconstruction geometry to 3D. For such extensions see the references[132, 133].

Tomographic reconstruction

Understanding the inverse problem of tomographic reconstruction requires understanding the forward problem of a tomographic projection. It is normally formulated using Lambert Beers law for X-ray absorption tomography, combined with various geometries such as parallel beam, fan beam or cone beam. We will only deal with the simplest case, the parallel beam geometry, seen in figure 5.1.

The absorption coefficient of a single ray, μ_{Ray}, can be found by dividing the object into multiple pieces of length, x, each with its own absorption coefficient, μ_i, as illustrated in figure 5.1b.

$$I = I_0 \Pi_{i=1}^{n} \exp(-\mu_i x) = I_0 \exp(-x \sum_{i=1}^{n} \mu_i) \tag{5.1}$$

$$\mu_{Ray} = -\frac{1}{x} \ln\left(\frac{I}{I_0}\right) = \sum_{i=1}^{n} \mu_i \tag{5.2}$$

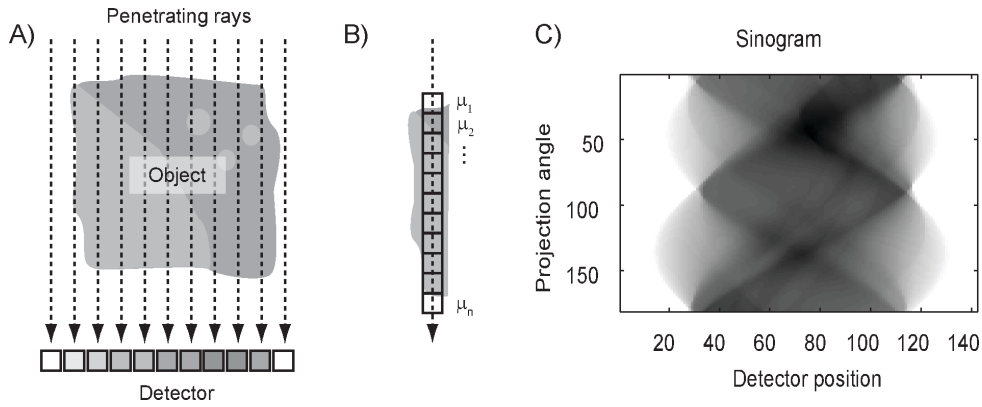

Figure 5.1: A) Schematics of parallel beam geometry with a set of penetrating rays interacting with an object and afterwards getting detected. B) For X-ray absorption the interaction with the object can be written as a series of absorption events that add linearly. Tomography consist of exposures from multiple angles and the complete data set from the detector can be presented as a sinogram where the projection of each angle is shown after each other.

The absorption coefficient is thus a linear combination of the individual absorption coefficients simply found as the sum. A complete tomography dataset have measurements for each detector pixel and object angle shown as a sinogram in figure 5.1c. Knowing a continuous description of the object, $f(x, y)$, the sinogram, g can be found by line integrals:

$$g(s, \theta) = R(f) = \int_{-\infty}^{\infty} f(s\cos\theta - u\sin\theta, s\sin\theta + u\cos\theta)du \tag{5.3}$$

where s is pixel location relative to the center and θ is the angle. It is known as the Radon transform, R, and consists of a line integral shifted by s and rotated by θ.

Knowing a discrete description of the object, x, projections can be also be found by linear algebra:

$$Ax = b \tag{5.4}$$

where A is a transformation matrix and b is all projections i.e. the sinogram. Note that the basic linearity required for these formulation does not only hold for the absorption cross sections but also phase contrast, which is merely the complex component of the absorption coefficient. It even holds for scattering cross section allowing one to perform SAXS tomography[134]. However, There are also some physical effects not accounted for in normal absorption tomography e.g. beam hardening where multi chromatic X-rays have different absorption coefficients and thereby introduce nonlinear effects. Such effects will show up as artifacts in the tomographic reconstruction. Here, we will not go into details of such artifacts, but simply note that assumption of linearity is a reasonable but not perfect approximation for tomography.

5.2 Analytic reconstruction

In the analytic response we seek to find an inverse Radon transform, R^{-1}

$$f(x,y) = R^{-1}(g(s,\theta)) = R^{-1}R(f(x,y)) = f(x,y) \tag{5.5}$$

This requires the use of an the Fourier slice theorem, which states that the Fourier transform, FT, of a parallel beam projection equals a slice of the 2D Fourier transform, FT_2, of the object[133] illustrated in figure 5.2.

$$\mathrm{FT}g(t,\theta) = \mathrm{FT}_2(f)(x,y) = F(t\cos\theta, t\sin\theta) \tag{5.6}$$

Here t is the spatial frequency of s i.e. $t = s^{-1}$. The object $f(x,y)$ can be found using the inverse Fourier transform.

$$f(x,y) = \frac{1}{2}\int_0^{2\pi}\int_{-\infty}^{\infty} \mathrm{FT}g(t,\theta)\exp(i2\pi t(y\cos\theta - x\sin\theta)|t|dtd\theta \tag{5.7}$$

$$= \frac{1}{2}\int_0^{2\pi}\int_{-\infty}^{\infty} g(t,\theta)\int_{-\infty}^{\infty}\exp(i2\pi t(y\cos\theta - x\sin\theta - s)|t|dtdsd\theta \tag{5.8}$$

$$= \int_0^{2\pi}(g * r)(\theta, y\cos\theta - x\sin\theta)d\theta \tag{5.9}$$

Where r is known as a ramp filter.

$$r(s) = \frac{1}{2}\int_{-\infty}^{\infty}|t|\exp(i2\pi ts)dt. \tag{5.10}$$

If one for a moment ignores the ramp filter in equation 5.9, the physical interpretation of the equation is to take the projections, g, and for all angles, θ, back-project them along their projection axis to find the object f(x,y). Since the ramp filter is missing an object with simple back-projection will be blurred as illustrated in 5.2 as the ramp filter act as a high pass filter. Since it is a high pass filter the ramp filter also enhance the 1 pixel fluctuations i.e. noise. This effect can be removed by setting the highest frequencies to zero producing a Ram-Lak filter shown in figure 5.2.

The ramp filter itself is easiest applied in the Fourier domain because only $|t|$ will be left and the convolution become a product due to the convolution theorem, see equation 3.13. Practically the procedure is to Fourier transform the projection, g, apply inverse Fourier transform, IFT, and back-project it to reconstruct the object i.e. FBP.

$$g * r = \mathrm{IFT}(\mathrm{FT}(g * r)) = \mathrm{IFT}(\mathrm{FT}(g)\mathrm{FT}(r)) = \mathrm{IFT}(\mathrm{FT}(g)|t|) \tag{5.11}$$

The derivation has only been for a continuous description, but in practice everything is discrete. There are thus some considerations when using Fourier transforms and the possibility to use alternative filters. For further details on FBP see references[135, 136, 133].

5.3 Algebraic reconstruction

In algebraic reconstruction we seek to solve a large set of linear equations (equation 5.4), or more accurately find the object x, that minimizes the distance to the measured projections.

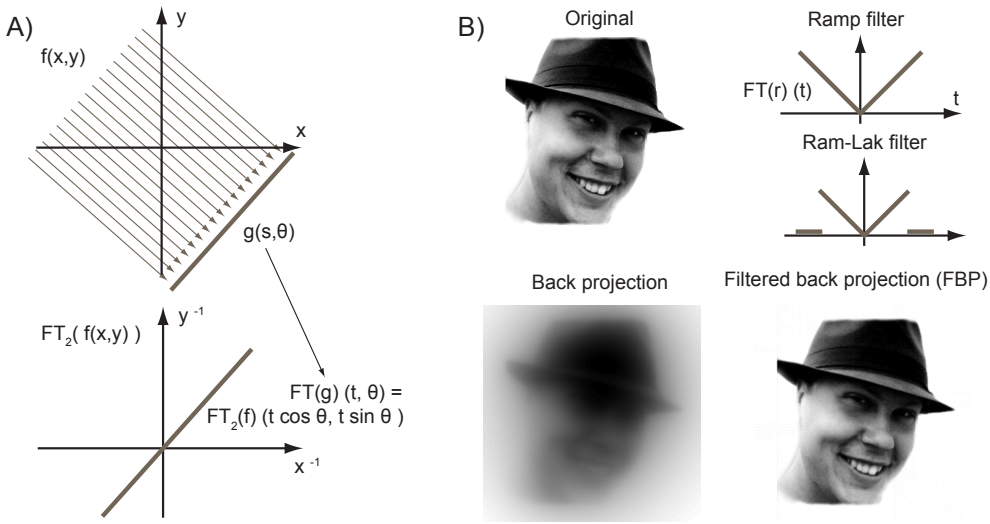

Figure 5.2: A) Illustration of Fourier slice theorem where the the Fourier transform, FT, of a projection, g, corresponds to a line $(t\cos\theta, t\sin\theta)$ in the two dimensional Fourier transform, FT_2, of the object, f. B) Filtering effects shown by a simple reconstruction by back-projection and a reconstruction where a Ram-Lak filter have been applied (both reconstructed from 180 projections).

The distance can be calculated by any norm desired, but the L2 norm is attractive due to the ease of solving the minimization problem.

$$\arg\min_x \|Ax - b\|_2 \tag{5.12}$$

The convenience of the L2 norm is that this minimization is equivalent to solving the normal equation[137]

$$A^T Ax = A^T b \tag{5.13}$$

$A^T A$ is positive semi-definite and the equation can be solved by pseudo inversion, QR factorization or principal component decomposition[138]. However, in practice it is expensive in random access memory (RAM) as A and x are quite big matrices i.e. A scale with detector pixels, number of projections and object size, whereas the object, x, scales with the side lengths cubed. A rough estimate with a relevant order of magnitude would be 1000 projections of 1000×1000 detector pixels producing a 1000×1000×1000 tomogram equals an A matrix with 10^{18} elements.

A different approach is to find an approximate solution by using iterative algorithms with fast computable steps. One such algorithm is the algebraic reconstruction technique, ART, algorithm which use the information from one ray at a time by looking at the i'th row of the A matrix, a_i, and the i'th element in the b vector, b_i.

$$x^{k+1} = x^k + \lambda_k \frac{b_i - \langle a_i, x^k \rangle}{\|a_i\|^2} a_i \tag{5.14}$$

Where γ_k is a relaxation parameter, k is the iteration number, and i is the ray / detector number. Since, the algorithm keeps looping through the rays i is equal to k modulus the number of rays. The equation of each ray can be seen as a hyperplane, and the ART algorithm approaches the intersection of all the hyperplanes by projecting the object onto each plane in succession as illustrated in figure 5.3. There are numerous other algorithms and further details on stopping criteria etc. see figure 5.3.

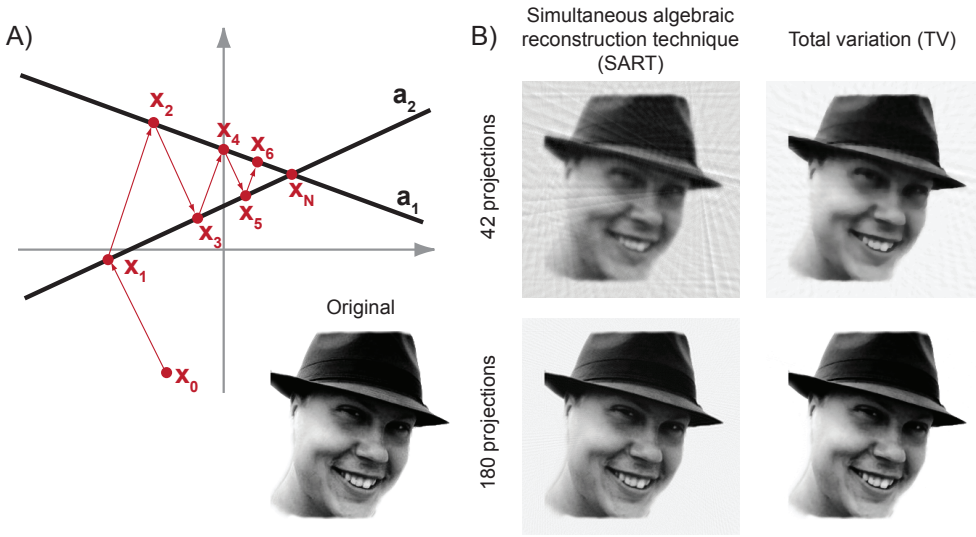

Figure 5.3: A) Illustration of the ART algorithm with two hyperplanes a_1 and a_2. A random guess of the object, x_0, is projected onto the hyperplanes in succession approaching the intersection, x_N. B) Algebraic reconstruction using the AIRTOOLS toolbox[139] with different number of projections. Total variation allow better reconstruction with fewer projections due to a regularization that suppress the noise.

One advantage of algebraic reconstruction is they can easily adopt different geometries, because the solution algorithm does not need to be reformulated but there just need to be calculated different intersections between the rays and the object. Another advantage is that the solutions can be subject to an additional regularization term, $R(x)$, expressed as:

$$\arg\min_x \|Ax - b\|_2 + R(x) \tag{5.15}$$

This regularization term, can be used to include prior knowledge by penalizing solutions that does not meet the regularization requirement. One such regularization is total variation[127], which favors objects with homogeneous areas and as few discrete jumps as possible. This is especially powerful when reconstructing objects with few projections where noise is suppressed as illustrated in figure 5.3.

5.4 Tomographic alignment

The PXCT data presented in chapter 4 was reconstructed using analytical reconstruction. However, before it could be done a series of alignment algorithms needed to be applied to account for sample movement during the experiment[111, 112]. These alignments algorithms are critical for spatial resolution in the sample and presently do not take angular and tilt displacement into account. Algebraic reconstruction algorithms will be used when implementing the EMIL machine because they have flexible system geometry enabling angular and tilt corrections. The combined set of x-, y-position, angle and tilt will be referred to as parameters, p.

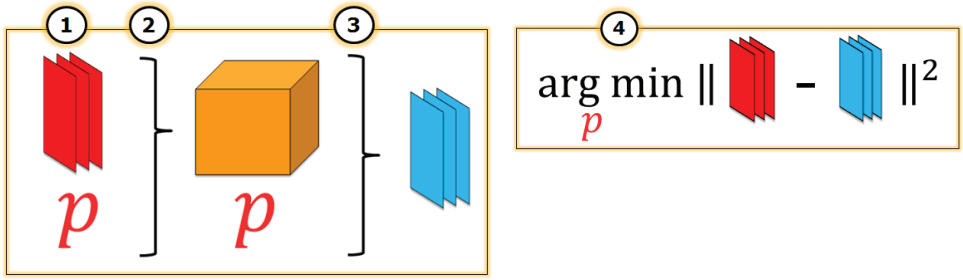

Figure 5.4: Illustration of the EMIL machine. 1) Projections and parameters, p, are recorded. 2) They are reconstructed to an object. 3) Projections are computed from the object using p. 4) p are updated by minimizing a norm e.g. L_2 norm of the recorded and calculated projections. Step 2-4 are repeated until sufficient convergence is achieved.

The key ideas of the EMIL machine are shown in figure 5.4 and is:

1. Obtain projection and projection parameters from the experiment.
2. Reconstruct object using current parameters.
3. Produce projections from the reconstruction.
4. Calculate projection distance i.e. difference between measured projections and projections from the reconstruction.
5. Update parameters and go to 2. unless stopping criteria is met.

The reconstruction can be done with any algebraic reconstruction algorithm with the possibility to employ regularization. Most test experiments presented here will employ SART. Projections are produced by forward projection as described in equation 5.4. The projections can be compared by various norms, here a L_2-norm is used with equal weight to every projection pixel. The parameter update is a basic optimization algorithm which minimize the projection distance as a function of parameters, p. The optimization problem can be stated as:

$$\arg\min_{p} \|A(p)x(p) - b\|_2 \tag{5.16}$$

Where $x(p)$ is the regular algebraic reconstruction

$$x(p) = \arg\min_x \|A(p)x - b\|_2. \tag{5.17}$$

This is a nested optimization problem, which is computationally expensive. It can be mitigated by using the previous solution to $x(p)$ in equation 5.17 as start guess when updating $x(p)$ for a new p. Another option is to allow solving equation 5.16 without updating $x(p)$ i.e. do multiple forward projections and corrections of p, before doing an object reconstruction. In that case the modified EMIL machine becomes:

1. Obtain projection and projection parameters from the experiment.
2. Reconstruct object using current parameters.
3. Produce projections from the reconstruction.
4. Calculate projection distance i.e. difference between measured projections and projections from the reconstruction.
5. Update parameters and go to 3. unless stopping criteria are met.
6. Update parameters and go to 2. unless stopping criteria are met.

Preliminary results

The EMIL machine was first implemented in MATLAB using the AIRTOOLS package[139] for algebraic reconstruction, rotation angles as the only parameters and the build-in non-linear least-squares solver `lsqnonlin` in MATLAB for minimization. Rotation angles were used as the only parameter as it was already supported by the AIRTOOLS package, whereas tilt and translation were not supported. The EMIL machine was tested using an object consisting of a down scaled 2D slice of the segmentation PXCT data presented in chapter 4. This was chosen as a relevant test sample while allowing sufficiently quick run time for fast debugging.

Data was simulated by first selecting a given set of regular spaced angles, false angles, as one would design a experiment to have. The true angles were then generated by adding Gaussian distributed angle deviations to the false angles simulating unknown experimental error in the angular positioning. The true angles were used along with the object to forward-project "data" for the simulation. The data and false angles where given as input to the EMIL machine and a set of corrected angles were produced. The results and comparison to the ground truth (true angles) are shown in figure 5.5.

It is hard to discern any visual difference between the different reconstructions despite using angular deviations with a standard deviation of two degrees. However, the angular deviations are in general much smaller for the corrected angles compared to the false angles. There are some outliers near 0 and 90 degrees for the corrected angles, which might be due to the discretization i.e. forward-projections parallel to the pixel sides will change little as a

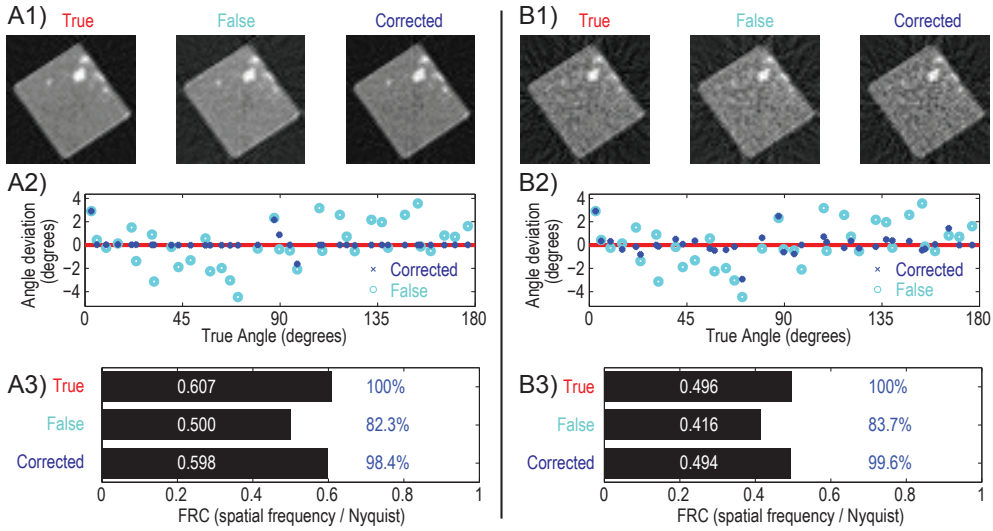

Figure 5.5: EMIL machine on a simulated 50×50 pixel problem with 36 projection. A) Without noise and B) with Poisson noise added to the projections. 1) Reconstructions based on the true, false and corrected angles. 2) Angle deviation of each projection before and after EMIL machine correction. 3) Spatial resolution determined by FSC for each set of reconstructions.

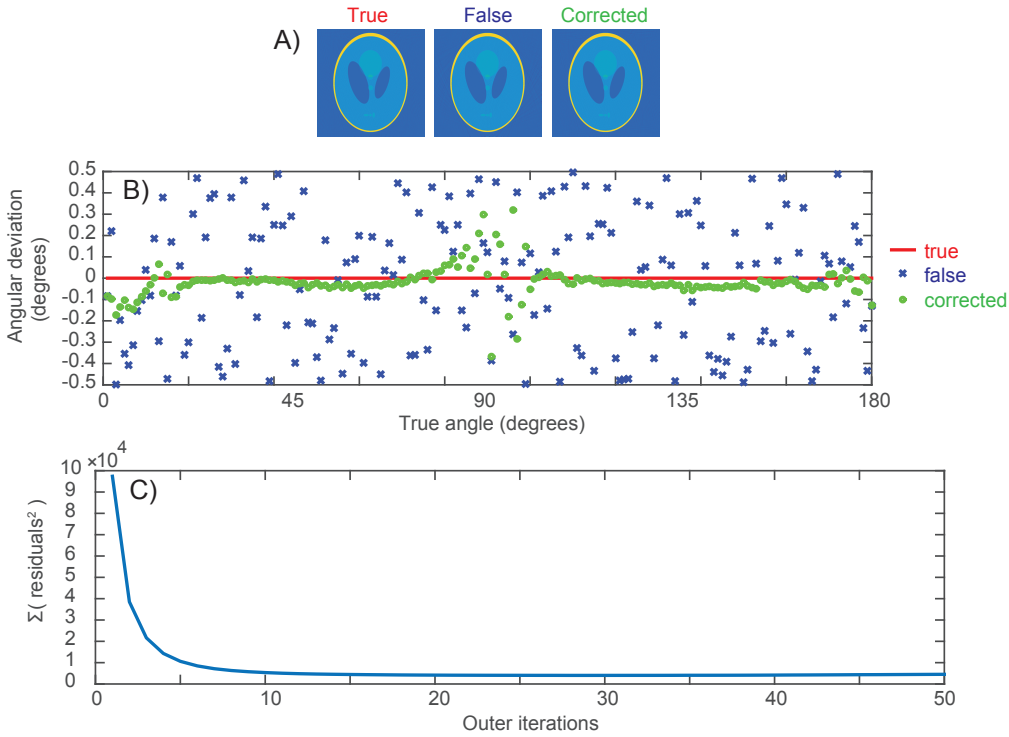

Figure 5.6: Modified EMIL machine on a simulated 1001×1001 pixel problem with 180 projections. A) Reconstructions based on the true, false and corrected angles. B) Angle deviation of each projection before and after EMIL machine correction. C) Convergence measured as L2-norm of residuals between all projection pixels at the end of each outer iteration.

function of angle. The most important feature is the spatial resolution estimated by Fourier ring correlation (FRC) the 2D case of FSC described in chapter 4. It shows that due to the false angles about 20% of the spatial resolution is lost and most of it i.e. 90% of the lost resolution can be regained by the EMIL machine.

A test simulation was also performed with Poisson noise added to the data to simulate experimental detector noise (figure 5.5B). The noise reduces the overall reconstruction quality as observed on the lower FRC numbers. The EMIL machine improves spatial resolution even with the added noise as observed by the near perfect recovery of spatial resolution by the corrected angles.

The examples showed promising results for the EMIL machine. However, The computation speed needed to be increased to be relevant for real datasets. This was achieved by switching to ASTRA[140, 141], an algebraic reconstruction package with GPU capabilities, and using the modified EMIL machine, where multiple forward-projections could be done for each reconstruction. The code was tested on a larger Shepp-Logan phantom object with angular deviations lower than 0.5 degrees as shown in figure 5.6.

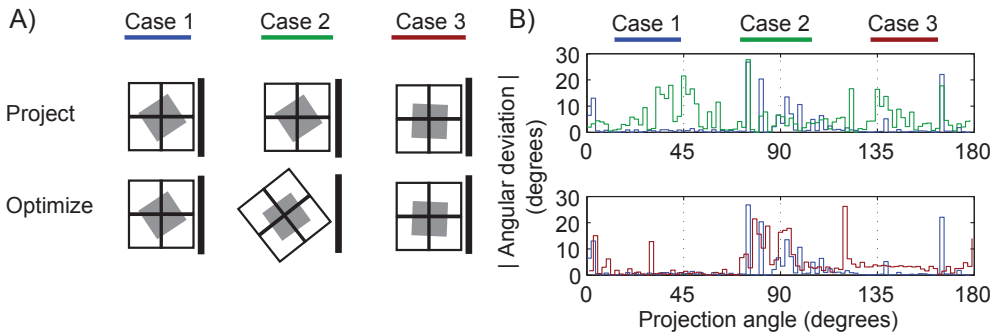

Figure 5.7: A) Illustration of 3 cases: 1. The normal case, 2. A case where all projections are shifted by 45 degree before optimization, which is equal to rotating the discretization. 3. A case where the object is rotated 45 degree before projection. B) Optimization result using the object from figure 5.5 and 90 projections. Absolute value of angular deviation are shown for each projection angle for each case. The tendency to high deviations near 0 and 90 degrees depend on the discretization as seen on the difference between case 1 and 2 (top), and is not object dependent as seen on similar behavior of case 1 and case 3 (bottom).

The reconstructions show little difference. The angular deviations are observed to be much larger for the false angles compared to the corrected angles. Larger than average deviations are found near 0 and 90 degrees for the corrected angles. This could be a problem with the discretization. If that is the case, it could be solved by simply performing a second optimization with the EMIL machine where all angles are rotated by 45 degrees. The two datasets could then be stitched together and avoid bad convergence near 0 and 90 degrees. This is tested and shown in figure 5.7, indicating the problem is due to the discretization. The tilt parameter is somewhat similar to the rotation angle parameter, so it might be advantageous to tilt all projections by 45 degrees before optimization when extending the algorithm to 3D. The modified EMIL machine converges quickly as seen in figure 5.7C and less than 10 reconstructions are needed for the majority of the improvement.

5.5 Summary

A projection matching algorithm, the EMIL machine, has been proposed to resolve misalignment in tomographic datasets. In simulations, it has demonstrated the ability to decrease angular deviations of projections and thereby increase the spatial resolution i.e. recover more than 98% of maximum spatial resolution. There have been observed some problems with angle deviation minimization near 0 and 90 degrees which is due to the discretization i.e. alignment of pixel and projection orientation. It can be solved by performing two optimizations with rotated angles and combining the two solutions.

The EMIL machine has been combined with the ASTRA toolbox[140, 141] to allow for fast forward-projections and reconstructions supporting GPU computation. The EMIL machine has also been modified to reuse the same reconstruction multiple times, thereby

reducing the need for computationally expensive reconstructions. In the simulation less than 10 reconstructions were needed to achieve the majority of the convergence.

Experiments

- Extend EMIL machine to 3D and all parameters:
The EMIL machine needs to be extended to 3D to include translation and tilt parameters. These are essential to fully align experimental PXCT dataset and quantify the performance such as the spatial resolution improvement in real data sets. The EMIL machine could also be compared to other projection distance minimization algorithms[128, 130] or the translation alignments already in use [111, 112].

- Enable lab-scale nanometer CT
The imaging portal at the Technical University of Denmark expects to commission a lab CT system at the end of 2015, using an Excillum X-ray source and possibly approaching 50 nm spatial resolution. In order to achieve the maximum spatial resolution, a projection alignment algorithm will likely be needed because sample movement is inevitable at long exposure times and with various vibration sources present. The EMIL machine could be tested on this system and proposed as a general tool to enable high resolution tomography.

- Refine PXCT data from raw scattering data
The EMIL machine originates from the basic desire to improve PXCT data. Currently, PXCT data are created by reconstructing coherent scattering data into 2D projections using ptychography and afterwards reconstructing 2D projections into a 3D object using tomography. It is a robust way to generate 3D objects, but distances the result from the raw data. The 3D object can be directly linked to the scattering data by formulating a forward coherent scattering projection. Such as projection will roughly consist of taking the probe obtained from ptychography, propagating it through the 3D object and Fourier transforming and squaring it to get to the scattering data. The 3D object could then be refined (like the parameters in EMIL machine) by minimizing the distance between forward-projected scattering data and the measured data. This refinement could never replace the ptychographic reconstruction, as it is needed to obtain the probe. However, it would ensure that the 3D object was not only consistent with the ptychographic reconstructions but also with the raw data itself.

CHAPTER 6

Conclusion

The aim of the project was to characterize the nano structures present in organic photovoltaics, in particular photoactive layers cast from water dispersible Landfester particles. The ultimate goal is to increase the performance of Landfester particles layers so they become a viable alternative to photoactive layers cast from organic solvent. This dissertation contributes to that effort by providing structural characterization of active layer materials and insights into the challenges that still remain.

X-ray absorption near edge spectroscopy was used to investigate the photodegradation rate of the photoactive materials P3HT and PCBM. When mixed, the degradation rates of the materials were reduced: P3HT to at least 1/3 of the degradation rate of pure P3HT, and PCBM to 9/10 of the degradation rate of pure PCBM. Photodegradation was investigated spatially by employing energy resolved scanning transmission X-ray microscopy which found that pure P3HT layers showed no spatial heterogeneity after photodegradation at the sub-micron scale. Other experiments have found degradation heterogeneity as a result of interface layers limiting diffusion of oxygen to the active layer[66]. Thus, it seems that spatial mapping of photo degradation is most relevant when employed on a full device structure and not for an isolated model system.

P3HT:PCBM 1:1 Landfester particle with a mean particles radius of less than 10 nm were produced. This is theoretically ideal, as the exciton diffusion length is on the order of 10 nm. The particle size should therefore ensure that all excitons can separate. The internal structure was characterized using small angle X-ray scattering and found to be best described by a Teubner-Strey model, as opposed to earlier simpler core-shell models. It means that the internal structure on average consists of 8.3 nm sized domains separated by a distance of 3.1 nm. Crystalline P3HT regions exist within the particles with an average crystal domain size of 5.1 nm. Cast particles do not retain their structure but are flattened on the substrate with a maximum particle height of 5.2 ± 1.2 nm. A rough estimate yields a contact angle of 36 degrees, assuming the particles are shaped as spherical caps. The particle deformation is also observed in the crystalline P3HT domains. If the spherical structure was conserved the crystal domains would be randomly oriented. Instead, we observe that 90% of the domains are aligned edge-on with the substrate before any annealing has taken place. The average P3HT crystal domain size is reduced to 3 nm in the cast layer, but return to 6 nm upon annealing at 140^{o}C. Crystalline P3HT and PCBM domains also show clear texturing when the nanoparticles are roll to roll coated on a flexible substrate. Energy resolved scanning transmission X-ray absorption microscopy shows that the P3HT and PCBM domain phase separate into 100 nm sized domains in the roll-to-roll coated films. The particle deformation and heating needed to dry the film in the roll-to-roll coating process likely contribute to the growth in domain size. The observed transition from small domains of 8.3 nm in the dispersed nanoparticles to the large domain size of 100 nm in the roll-to-roll coated layer highlight the need for understanding and optimizing the film formation properties of Landfester nanoparticles.

A full structure of a roll coated organic photovoltaic tandem cell was imaged at 20 nm spatial resolution using ptychographic X-ray computed tomography. The structure contained two photoactive layers: One cast from organic solvent and the other from water (dispersed Landfester nanoparticles). The layer cast from an organic solvent was observed to be uniform, whereas the layer cast from Landfester nanoparticles was porous containing sub 20 nm air pockets. The silver nanoparticle electrode formed a porous layer with clear air domains present, as opposed to earlier, where PEDOT:PSS was observed penetrating into the silver electrode[92]. No visible air domains were present in zinc oxide nanoparticle layers. However the electron density was reduced to 60% of the expected value, indicating that zinc oxide layers must be porous on length scales below the resolution limit. The photoelectric performance of the device was below what could be expected from a tandem cell i.e. the device open circuit voltage was not above the open circuit voltage of single junctions with either photoactive materials. This was in agreement with the tomography data, which found the active nanoparticle layer short circuited by penetrating zinc oxide. The penetration was made possible by a Landfester nanoparticle layer with a wide layer thickness distribution and high surface roughness compared to the other layers in the tandem structure. The Landfester nanoparticle layer was found as the only layer to have a negative top-bottom interface correlation. It indicates that the layer was formed by first having particles situated in local height minima on the substrate and subsequent particles growing the layer from these first particles. The photoelectric performance of the device was improved by taking the polymer present in the Landfester particles and coating it from a solution on top of the Landfester particles. It is believed that this process filled the porous layers and thus prevented any short circuit from forming. The result was a device with a high open circuit voltage, a voltage that could only be achieved by a functional tandem junction. It demonstrates that Landfester particles with improved layer formation can achieve enhanced photoelectric performance. Thus, it is therefore critical to improve the film formation of the Landfester particles, so they form homogeneous layers with sufficient thickness. One possible solution would be particles produced with a non-polar surfactant.

Ptychographic X-ray computed tomography provides high resolution 3D data ideal for studying nano structures in organic photovoltaics. However, an even higher resolution is desirable to resolve the porosity mentioned in the previous section and the spatial distribution of materials in the photoactive layers. A basic requirement to increase the spatial resolution is proper alignment of the 2D projections that are used to reconstruct the 3D data. An alignment algorithm was proposed to estimate movement by iterative logic using projection distance minimization. An initial implementation of the algorithm is tested on simulated data with angle displacements. The algorithm is able to reduce the angular displacements that otherwise reduces the spatial resolution measured by Fourier ring correlation. In the simulations, the angular displacement lower the resolution to about 83% of the resolution with no displacements. The algorithm was able to regain more than 96% of the maximum possible resolution. It also provided a decrease in angular displacement and improved resolution, when Poisson noise was added to the projections. A modification of the algorithm made it possible to achieve the majority of the convergence with less than ten tomographic reconstruction steps. Adoption of a reconstruction toolbox that supports parallelization with graphics cards allowed to optimize larger tomographic problems. The algorithm is suited for further development where translation and tilt can be included in the optimization process. It could also play a role in enabling nanometer resolution in laboratory scale tomography.

The main conclusion of the project was that in order to enable water dispersible Landfester particles, their layer formation properties need to be improved. The improvement of the Landfester particle layer should consist of keeping the domain size of the photoactive materials below hundreds of nanometer, reducing the porosity of the layer, ensuring full substrate coverage, providing a narrow thickness distribution, reducing the surface roughness and ensuring a positive top-bottom correlation of the layer. It is conjectured that such improvements could be achieved by altering the particle surface energy by utilizing a non-polar surfactant. An alternate approach would be to utilize a photoactive polymer as surfactant thereby removing the inactive component of the Landfester particles. The outlined techniques and data-analysis employed in the project are well suited to provide feedback during the development of techniques to improve layer formation of the Landfester particles. 2D projections could be aligned by estimating movement through iterative logic to further improve spatial resolution in the tomographic technique. Such an alignment algorithm would also have general application in computed tomography.

Bibliography

[1] British Petroleum Company. *BP Statistical Review of World Energy June 2014 About this review*. British Petroleum, London, 2014.

[2] D. Reay. Spring-time for sinks. *Nature*, 446(April), 2007.

[3] IPCC. *Climate Change 2007: Synthesis Report. Contribution of Working Groups I, II and III to the Fourth Assessment Report of the Intergovernmental Panel on Climate Change [Core Writing Team, Pachauri, R.K and Reisinger, A. (eds.)]*. IPCC, Geneva, Switzerland, 2007.

[4] R. Perez and M. Perez. A fundamental look at energy reserves for the planet. *The IEA SHC Solar Update*, 50:2, 2009.

[5] International Energy Agency. *Energy balance of non-oecd countries*. International Energy Agency, Paris, 2012.

[6] O. A. Hurricane, D. A. Callahan, D. T. Casey, P. M. Celliers, C. Cerjan, E. L. Dewald, T. R. Dittrich, T. Döppner, D. E. Hinkel, L. F. Berzak Hopkins, J. L. Kline, S. Le Pape, T. Ma, A. G. MacPhee, J. L. Milovich, A. Pak, H.-S. Park, P. K. Patel, B. A. Remington, J. D. Salmonson, P. T. Springer, and R. Tommasini. Fuel gain exceeding unity in an inertially confined fusion implosion. *Nature*, 506(7488):343–8, February 2014.

[7] S. Lee and S. H. Saw. Nuclear fusion energy—mankind's giant step forward. *Journal of fusion energy*, pages 2–8, 2011.

[8] J. E. Carlé and F. C. Krebs. Technological status of organic photovoltaics (OPV). *Solar Energy Materials and Solar Cells*, 119:309–310, December 2013.

[9] M. A. Green, K. Emery, Y. Hishikawa, W. Warta, and D. D. Ewan. Solar cell efficiency tables (Version 45). *Progress in Photovoltaics: Research and Applications*, 23:1–9, 2015.

[10] M. Corazza, F. C. Krebs, and S. A. Gevorgyan. Predicting, categorizing and intercomparing the lifetime of OPVs for different ageing tests. *Solar Energy Materials and Solar Cells*, 130:99–106, 2014.

[11] D. M. Powell, M. T. Winkler, H. J. Choi, C. B. Simmons, D. B. Needleman, and T. Buonassisi. Crystalline silicon photovoltaics: a cost analysis framework for determining technology pathways to reach baseload electricity costs. *Energy & Environmental Science*, 5:5874, 2012.

[12] D. A. R. Barkhouse, O. Gunawan, T. Gokmen, T. K. Todorov, and D. B. Mitzi. Device characteristics of a 10.1% hydrazine-processed Cu2ZnSn(Se,S)4 solar cell. *Progress in Photovoltaics: Research and Applications*, 20:6–11, 2012.

[13] N. Espinosa, M. Hösel, D. Angmo, and F. C. Krebs. Solar cells with one-day energy payback for the factories of the future. *Energy & Environmental Science*, 5(1):5117, 2012.

[14] F. C. Krebs, N. Espinosa, M. Hösel, R. R. Sø ndergaard, and M. Jø rgensen. 25th Anniversary Article: Rise to Power - OPV-Based Solar Parks. *Advanced Materials*, 26(1):29–39, January 2014.

[15] E. Levinson. *2014 Global Agricultural Productivity Report*. Global Harvest Initiative, 2014.

[16] T. Harinarayana and K. S. V. Vasavi. Solar Energy Generation Using Agriculture Cultivated Lands. *Smart Grid and Renewable Energy*, 5(February):31–42, 2014.

[17] J. G. Levine. *Pumped hydroelectric energy storage and spatial diversity of wind resources as methods of improving utilization of renewable energy sources*. PhD thesis, University of Colorado, 2007.

[18] B. V. Mathiesen, H. Lund, and K. Karlsson. 100% Renewable energy systems, climate mitigation and economic growth. *Applied Energy*, 88(2):488–501, 2011.

[19] M. Z. Jacobson. Short-term effects of controlling fossil-fuel soot, biofuel soot and gases, and methane on climate, Arctic ice, and air pollution health. *Journal of Geophysical Research: Atmospheres*, 115(14), 2010.

[20] M. Z. Jacobson and M. A. Delucchi. Providing all global energy with wind, water, and solar power, Part I: Technologies, energy resources, quantities and areas of infrastructure, and materials. *Energy Policy*, 39(3):1154–1169, 2011.

[21] M. A. Green. Self-consistent optical parameters of intrinsic silicon at 300 K including temperature coefficients. *Solar Energy Materials and Solar Cells*, 92(11):1305–1310, 2008.

[22] P. E. Shaw, A. Ruseckas, and I. D. W. Samuel. Exciton Diffusion Measurements in Poly(3-hexylthiophene). *Advanced Materials*, 20(18):3516–3520, July 2008.

[23] R. Corkish, D. S.-P. Chan, and M. A. Green. Excitons in silicon diodes and solar cells: A three-particle theory. *Journal of Applied Physics*, 79(1996):195, 1996.

[24] Y. Min Nam, J. Huh, and W. Ho Jo. Optimization of thickness and morphology of active layer for high performance of bulk-heterojunction organic solar cells. *Solar Energy Materials and Solar Cells*, 94(6):1118–1124, 2010.

[25] K. Svendsen and K. S. Rognes. Exposure to organic solvents in the offset printing industry in Norway. *The Annals of occupational hygiene*, 44(2):119–124, 2000.

[26] F. C. Krebs, S. A. Gevorgyan, and J. Alstrup. A roll-to-roll process to flexible polymer solar cells: model studies, manufacture and operational stability studies. *Journal of Materials Chemistry*, 19:5442, 2009.

[27] T. R. Andersen, T. T. Larsen-Olsen, B. Andreasen, A. P. L. Böttiger, J. E. Carlé, M. Helgesen, E. Bundgaard, K. Norrman, J. W. Andreasen, M. Jø rgensen, and F. C. Krebs. Aqueous processing of low-band-gap polymer solar cells using roll-to-roll methods. *ACS nano*, 5(5):4188–96, May 2011.

[28] K. Landfester. The Generation of Nanoparticles in Miniemulsions. *Advanced Materials*, 13(10):765–768, May 2001.

[29] T. Kietzke, D. Neher, M. Kumke, R. Montenegro, K. Landfester, and U. Scherf. A Nanoparticle Approach To Control the Phase Separation in Polyfluorene Photovoltaic Devices. *Macromolecules*, 37(13):4882–4890, June 2004.

[30] A. Assmus. Early History of X Rays. *http://www.slac.stanford.edu/pubs/beamline/25/2/25-2-assmus.pdf*, 1995.

[31] L. H. Teldo-Pereyra. X-Rays Surgical Revolution. *Investigative Surgery*, 22(5):327–332, 2009.

[32] W. Friedrich, P. Knipping, and M. von Laue. *Interferenz-Erscheinungen bei Röntgenstrahlen, von W. Friedrich, P. Knipping und M. Lane.* München: Verlag der Königlich-Bayerischen Akademie der Wissenschaften., 1912.

[33] W. L. Bragg. The Structure of Some Crystals as Indicated by their Diffraction of X-rays. *Proc. R. Soc. Lond.*, A89(610):248–277, 1913.

[34] E. Abola, P. Kuhn, T. Earnest, and R. C. Stevens. Automation of X-ray crystallography. *Nature structural biology*, 7 Suppl(november):973–7, November 2000.

[35] P. Krishnamurti. *Studies in X-ray Diffraction.* Calcutta University Press, 1930.

[36] A. Guinier, G. Fournet, and K. L. Yudowitch. *Small-angle scattering of X-rays.* New York: Wiley, 1955.

[37] O. Glatter and O. Kratky. *Small angle X-ray scattering*, volume 102. Academic press London, 1982.

[38] C. D. Putnam, M. Hammel, G. L. Hura, and J. A. Tainer. X-ray solution scattering (SAXS) combined with crystallography and computation: defining accurate macromolecular structures, conformations and assemblies in solution. *Quarterly reviews of biophysics*, 40(3):191–285, August 2007.

[39] A. F. Craievich. Synchrotron SAXS Studies of Nanostructured Materials and Colloidal Solutions . A Review 2 . The LNLS Synchrotron Source. 5(1):1–11, 2002.

[40] J. C. Elliott and S. D. Dover. X-ray microtomography. *Journal of Microscopy*, 126:211–213, 1982.

[41] D. Sayre. The squaring method: a new method for phase determination. *Acta Crystallographica*, 5(1):60–65, January 1952.

[42] R. W. Gerchberg and W. O. Saxton. A Practical Algorithm for the Determination of Phase from Image and Diffraction Plane Pictures. 35(2), 1972.

[43] J. R. Fienup. Phase retrieval algorithms: a comparison. *Applied optics*, 21(15):2758–69, August 1982.

[44] J. R. Fienup. Phase retrieval algorithms: a personal tour [Invited]. *Applied optics*, 52(1):45–56, January 2013.

[45] W. Hoppe. Trace Structure Analysis, Ptychography , Phase Tomography. *Ultramicroscopy*, 10:187–198, 1982.

[46] J. M. Rodenburg. Ptychography: early history and 3D scattering effects. 8678:867809–867809–10, December 2012.

[47] J. Miao, P. Charalambous, J. Kirz, and D. Sayre. Extending the methodology of X-ray crystallography to allow imaging of micrometre-sized non-crystalline specimens. 400(July):342–344, 1999.

[48] M. Dierolf, A. Menzel, P. Thibault, P. Schneider, C. M. Kewish, R. Wepf, O. Bunk, and F. Pfeiffer. Ptychographic X-ray computed tomography at the nanoscale. *Nature*, 467(7314):436–9, September 2010.

[49] M. Holler, A. Diaz, M. Guizar-Sicairos, P. Karvinen, E. Färm, E. Härkönen, M. Ritala, A. Menzel, J. Raabe, and O. Bunk. X-ray ptychographic computed tomography at 16 nm isotropic 3D resolution. *Scientific reports*, 4:3857, January 2014.

[50] K. A. Nugent. *Coherent methods in the X-ray sciences*, volume 59. January 2010.

[51] J. Als-Nielsen and D. McMorrow. *Elements of Modern X-ray Physics*. John Wiley & Sons Ltd., 2001.

[52] A. Momose, T. Takeda, and Y. Itai. Phase-contrast x-ray computed tomography for observing biological specimens and organic materials. *Review of Scientific Instruments*, 66(2):1434, 1995.

[53] M. Bech. *Ph . D Thesis; X-ray imaging with a grating interferometer*. PhD thesis, University of Copenhagen, 2009.

[54] F. Pfeiffer, T. Weitkamp, O. Bunk, and C. David. Phase retrieval and differential phase-contrast imaging with low-brilliance X-ray sources. *Nature Physics*, 2(4):258–261, March 2006.

[55] J. Stöhr. *NEXAFS spectroscopy*. Springer-Verlag, 1996.

[56] P. Scherrer. Bestimmung der Grösse und der inneren Struktur von Kolloidteilchen mittels Röntgenstrahlen [Determination of the size and internal structure of colloidal particles using X-rays]. *Göttinger Nachrichten Math. Phys.*, 2:98–100, 1918.

[57] U. Holzwarth and N. Gibson. The Scherrer equation versus the'Debye-Scherrer equation'. *Nature Nanotechnology*, 6(September):21027, 2011.

[58] K. Norrman, M. V. Madsen, S. A. Gevorgyan, and F. C. Krebs. Degradation patterns in water and oxygen of an inverted polymer solar cell. *Journal of the American Chemical Society*, 132(47):16883–92, December 2010.

[59] N. Grossiord, J. M. Kroon, R. Andriessen, and P. W. M. Blom. Degradation mechanisms in organic photovoltaic devices. *Organic Electronics*, 13(3):432–456, March 2012.

[60] M. Jø rgensen, K. Norrman, and F. C. Krebs. Stability/degradation of polymer solar cells. *Solar Energy Materials and Solar Cells*, 92(7):686–714, July 2008.

[61] M. Manceau, A. Rivaton, J.-L. Gardette, S. Guillerez, and N. Lemaître. The mechanism of photo- and thermooxidation of poly(3-hexylthiophene) (P3HT) reconsidered. *Polymer Degradation and Stability*, 94(6):898–907, June 2009.

[62] M. Manceau, J. Gaume, A. Rivaton, and J.-L. Gardette. Further insights into the photodegradation of poly (3-hexylthiophene) by means of X-ray photoelectron spectroscopy. *Thin Solid Films*, 518(23):7113–7118, 2010.

[63] M. O. Reese, A. M. Nardes, B. L. Rupert, R. E. Larsen, D. C. Olson, M. T. Lloyd, S. E. Shaheen, D. S. Ginley, G. Rumbles, and N. Kopidakis. Photoinduced Degradation of Polymer and Polymer-Fullerene Active Layers: Experiment and Theory. *Advanced Functional Materials*, 20(20):3476–3483, October 2010.

[64] K. Feron, T. J. Nagle, L-J. Rozanski, B. B. Gong, and C. J. Fell. Spatially resolved photocurrent measurements of organic solar cells: Tracking water ingress at edges and pinholes. *Solar Energy Materials and Solar Cells*, 109:169–177, February 2013.

[65] V. S. Smentkowski, G. Zorn, A. Misner, G. Parthasarathy, A. Couture, E. Tallarek, and B. Hagenhoff. ToF-SIMS depth profiling of organic solar cell layers using an Ar cluster ion source. *Journal of Vacuum Science & Technology A: Vacuum, Surfaces, and Films*, 31(3):030601, 2013.

[66] K. Norrman, N. B. Larsen, and F. C. Krebs. Lifetimes of organic photovoltaics: Combining chemical and physical characterisation techniques to study degradation mechanisms. *Solar Energy Materials and Solar Cells*, 90(17):2793–2814, November 2006.

[67] B. A. Collins and H. Ade. Quantitative compositional analysis of organic thin films using transmission NEXAFS spectroscopy in an X-ray microscope. *Journal of Electron Spectroscopy and Related Phenomena*, 185(5-7):119–128, August 2012.

[68] B. Watts, S. Swaraj, D. Nordlund, J. Lüning, and H. Ade. Calibrated NEXAFS spectra of common conjugated polymers. *The Journal of chemical physics*, 134(2):024702, January 2011.

[69] D. S. Germack, C. K. Chan, B. H. Hamadani, L. J. Richter, D. A. Fischer, D. J. Gundlach, and D. M. DeLongchamp. Substrate-dependent interface composition and charge transport in films for organic photovoltaics. *Applied Physics Letters*, 94(23):233303, June 2009.

[70] B. Watts, T. Schuettfort, and C. R. McNeill. Mapping of Domain Orientation and Molecular Order in Polycrystalline Semiconducting Polymer Films with Soft X-Ray Microscopy. *Advanced Functional Materials*, 21(6):1122–1131, March 2011.

[71] K. B. Burke, A. J. Stapleton, B. Vaughan, X. Zhou, A. L. D. Kilcoyne, W. J. Belcher, and P. C. Dastoor. Scanning transmission x-ray microscopy of polymer nanoparticles: probing morphology on sub-10 nm length scales. *Nanotechnology*, 22(26):265710, July 2011.

[72] T. Tromholt, M. V. Madsen, J. E. Carlé, M. Helgesen, and F. C. Krebs. Photochemical stability of conjugated polymers, electron acceptors and blends for polymer solar cells resolved in terms of film thickness and absorbance. *Journal of Materials Chemistry*, 22(15):7592, 2012.

[73] E. B. L. Pedersen, T. Tromholt, M. V. Madsen, A. P. L. Bottiger, M. Weigand, F. C. Krebs, and J. W. Andreasen. Spatial degradation mapping and componentwise degradation tracking in polymer-fullerene blends. *Journal of Materials Chemistry C*, 2:5176, 2014.

[74] I. E. Brumboiu, A. S. Anselmo, B. Brena, A. Dzwilewski, K. Svensson, and E. Moons. Near-edge X-ray absorption fine structure study of the C 60 -derivative PCBM. *Chemical Physics Letters*, 568-569:130–134, 2013.

[75] C. R. McNeill, B. Watts, L. Thomsen, W. J. Belcher, A. L. D. Kilcoyne, N. C. Greenham, and P. C. Dastoor. X-ray spectromicroscopy of polymer/fullerene composites: quantitative chemical mapping. *Small*, 2(12):1432–5, December 2006.

[76] D. W. Hogg, J. Bovy, and D. Lang. Data analysis recipes: Fitting a model to data. *arXiv preprint arXiv:1008.4686*, 2010.

[77] R. Andrae, T. Schulze-Hartung, and P. Melchior. Dos and don'ts of reduced chi-squared. *arXiv preprint arXiv:1012.3754*, pages 1–12, 2010.

[78] E. D. Gomez, K. P. Barteau, H. Wang, M. F. Toney, and Y.-L. Loo. Correlating the scattered intensities of P3HT and PCBM to the current densities of polymer solar cells. *C1. E. D. Gomez, K. P. Barteau, H. Wang, M. F. Toney, and Y.-L. Loo, Chem. Commun., 2011, 47, 436–438.hemical Communications*, 47:436–438, 2011.

[79] N. P. Holmes, K. B. Burke, P. Sista, M. Barr, H. D. Magurudeniya, M. C. Stefan, A. L. A. Kilcoyne, X. Zhou, P. C. Dastoor, and Warwick J. Belcher. Nano-domain behaviour in P3HT:PCBM nanoparticles, relating material properties to morphological changes. *Solar Energy Materials and Solar Cells*, 117:437–445, 2013.

[80] S. Ulum, N. Holmes, D. Darwis, K. Burke, A. L. D. Kilcoyne, X. Zhou, W. Belcher, and P. Dastoor. Determining the structural motif of P3HT : PCBM nanoparticulate organic photovoltaic devices. *Solar Energy Materials and Solar Cells*, 110:43–48, 2013.

[81] J. J. Richards, C. L. Whittle, G. Shao, and L. D. Pozzo. Correlating Structure and Photocurrent for Composite Semiconducting Nanoparticles with Contrast Variation Small-Angle Neutron Scattering and Photoconductive Atomic Force Microscopy. *ACS nano*, 8(5):4313–4324, 2014.

[82] S. Gärtner, M. Christmann, S. Sankaran, H. Röhm, E.-M. Prinz, F. Penth, A. Pütz, A. E. Türeli, B. Penth, B. Baumstümmler, and A. Colsmann. Eco-Friendly Fabrication of 4% Efficient Organic Solar Cells from Surfactant-Free P3HT:ICBA Nanoparticle Dispersions. *Advanced Materials*, 26:6653–6657, September 2014.

[83] D. Freedman and P. Diaconis. On the histogram as a density estimator:L 2 theory. *Zeitschrift für Wahrscheinlichkeitstheorie und Verwandte Gebiete*, 57:453–476, 1981.

[84] T. T. Larsen-Olsen, T. R. Andersen, B. Andreasen, A. P. L. Böttiger, E. Bundgaard, K. Norrman, J. W. Andreasen, M. Jø rgensen, and F. C. Krebs. Roll-to-roll processed polymer tandem solar cells partially processed from water. *Solar Energy Materials and Solar Cells*, 97:43–49, February 2012.

[85] D. Apitz, R. P. Bertram, N. Benter, W. Hieringer, J. W. Andreasen, M. M. Nielsen, P. M. Johansen, and K. Buse. Investigation of chromophore-chromophore interaction by electro-optic measurements, linear dichroism, x-ray scattering, and density-functional calculations. *Physical Review E - Statistical, Nonlinear, and Soft Matter Physics*, 72:1–10, 2005.

[86] S. Satapathi, H. S. Gill, L. Li, L. Samuelson, J. Kumar, and R. Mosurkal. Synthesis of nanoparticles of P3HT and PCBM for optimizing morphology in polymeric solar cells. *Applied Surface Science*, 323:13–18, December 2014.

[87] J. Y. Kim and C. D. Frisbie. Correlation of Phase Behavior and Charge Transport in Conjugated Polymer / Fullerene Blends. *J. Phys. Chem. C*, 112:17726–17736, 2008.

[88] A. P. L. Böttiger, M. Jø rgensen, A. Menzel, F. C. Krebs, and J. W. Andreasen. High-throughput roll-to-roll X-ray characterization of polymer solar cell active layers. *Journal of Materials Chemistry*, 22(42):22501, 2012.

[89] A. Stapleton, B. Vaughan, B. Xue, E. Sesa, K. Burke, X. Zhou, G. Bryant, O. Werzer, A. Nelson, A. L. D. Kilcoyne, L. Thomsen, E. Wanless, W. Belcher, and P. Dastoor. A multilayered approach to polyfluorene water-based organic photovoltaics. *Solar Energy Materials and Solar Cells*, 102:114–124, 2012.

[90] Y.-C. Huang, Y.-C. Liao, S.-S. Li, M.-C. Wu, C.-W. Chen, and W.-F. Su. Solar Energy Materials & Solar Cells Study of the effect of annealing process on the performance of P3HT / PCBM photovoltaic devices using scanning-probe microscopy. *Solar Energy Materials and Solar Cells*, 93:888–892, 2009.

[91] W. Chen, M. P. Nikiforov, and S. B. Darling. Morphology characterization in organic and hybrid solar cells. *Energy & Environmental Science*, 5(8):8045, 2012.

[92] H. F. Dam, T. R. Andersen, E. B. L. Pedersen, K.T. S. Thydén, M. Helgesen, J. E. Carlé, P. S. Jø rgensen, J. Reinhardt, R. R. Sø ndergaard, M. Jø rgensen, E. Bundgaard, F. C. Krebs, and J. W. Andreasen. Enabling Flexible Polymer Tandem Solar Cells by 3D Ptychographic Imaging. *Advanced Energy Materials*, August 2014.

[93] T. R. Andersen, H. F. Dam, B. Andreasen, M. Hösel, M. V. Madsen, S. A. Gevorgyan, R. R. Sø ndergaard, M. Jø rgensen, and F. C. Krebs. A rational method for developing and testing stable flexible indium- and vacuum-free multilayer tandem polymer solar cells comprising up to twelve roll processed layers. *Solar Energy Materials and Solar Cells*, 120:735–743, January 2014.

[94] K. E. Strawhecker, S. K. Kumar, J. F. Douglas, and A. Karim. The Critical Role of Solvent Evaporation on the Roughness of Spin-Cast Polymer Films. *Macromolecules*, 34(14):4669–4672, 2001.

[95] S.-H. Lee, J.-H. Kim, T.-H. Shim, and J.-G. Park. Effect of interface thickness on power conversion efficiency of polymer photovoltaic cells. *Electronic Materials Letters*, 5(1):47–50, 2009.

[96] C. Newby, J.-K. Lee, and C. K. Ober. The solvent problem: Redissolution of macromolecules in solution-processed organic electronics. *Macromolecular Research*, 21(3):248–256, April 2013.

[97] O. Bunk, M. Dierolf, S. Kynde, I. Johnson, O. Marti, and F. Pfeiffer. Influence of the overlap parameter on the convergence of the ptychographical iterative engine. *Ultramicroscopy*, 108(5):481–7, April 2008.

[98] J. M. Rodenburg and H. M. L. Faulkner. A phase retrieval algorithm for shifting illumination. *Applied Physics Letters*, 85(20):4795, 2004.

[99] P. Thibault, M. Dierolf, O. Bunk, A. Menzel, and F. Pfeiffer. Probe retrieval in ptychographic coherent diffractive imaging. *Ultramicroscopy*, 109(4):338–43, March 2009.

[100] J. R. Fienup. Reconstruction Reconstruction and and synthesis synthesis applications applications of an iterative algorithm. *Transformations in Optical Signal Processing*, 373, 1981.

[101] J. Douglas and H. H. Rachford. On the Numerical Solution of Heat Conduction Problems in Two and Three Space Variables. *Transactions of the American Mathematical Society*, 82(2):421–439, 2013.

[102] M. Dierolf, P. Thibault, A. Menzel, C. M. Kewish, K. Jefimovs, I. Schlichting, K. V. König, O. Bunk, and F. Pfeiffer. Ptychographic coherent diffractive imaging of weakly scattering specimens. *New Journal of Physics*, 12(3):035017, March 2010.

[103] M. Van Heel and M. Schatz. Fourier shell correlation threshold criteria. *Journal of Structural Biology*, 151:250–262, 2005.

[104] P. B. Rosenthal and R. Henderson. Optimal determination of particle orientation, absolute hand, and contrast loss in single-particle electron cryomicroscopy. *Journal of Molecular Biology*, 333(4):721–745, 2003.

[105] S. Geman and D. Geman. Stochastic Relaxation, Gibbs Distributions, and the Bayesian Restoration of Images. *IEEE Transactions on Pattern Analysis and Machine Intelligence*, PAMI-6(6):721–741, 1984.

[106] Yuri Boykov and Vladimir Kolmogorov. An experimental comparison of min-cut/max-flow algorithms for energy minimization in vision. *IEEE transactions on pattern analysis and machine intelligence*, 26(9):1124–37, September 2004.

[107] H. F. Dam and F. C. Krebs. Simple roll coater with variable coating and temperature control for printed polymer solar cells. *Solar Energy Materials and Solar Cells*, 97:191–196, February 2012.

[108] P. Kraft, A. Bergamaschi, C. Bronnimann, R. Dinapoli, E. F. Eikenberry, H. Graafsma, B. Henrich, I. Johnson, M. Kobas, A. Mozzanica, C. M. Schleputz, and B. Schmitt. Characterization and calibration of PILATUS detectors. *IEEE Transactions on Nuclear Science*, 56(3):758–764, 2009.

[109] M. Guizar-Sicairos, I. Johnson, A. Diaz, M. Holler, P. Karvinen, H.-C. Stadler, R. Dinapoli, O. Bunk, and A. Menzel. High-throughput ptychography using Eiger-scanning X-ray nano-imaging of extended regions. *Optics Express*, 22(10):14859, 2014.

[110] P. Thibault and M. Guizar-Sicairos. Maximum-likelihood refinement for coherent diffractive imaging. *New Journal of Physics*, 14, 2012.

[111] M. Guizar-Sicairos, A. Diaz, M. Holler, M. S. Lucas, A. Menzel, R. A. Wepf, and O. Bunk. Phase tomography from x-ray coherent diffractive imaging projections. *Optics express*, 19(22):21345–57, October 2011.

[112] M. Guizar-Sicairos, J. J. Boon, K. Mader, A. Diaz, A. Menzel, and O. Bunk. Quantitative interior x-ray nanotomography by a hybrid imaging technique. *Optica*, 2(3):259–266, 2015.

[113] T. Tromholt, S. A. Gevorgyan, M. Jø rgensen, F. C. Krebs, and K. O. Sylvester-Hvid. Thermocleavable materials for polymer solar cells with high open circuit Voltage-A Comparative Study. *ACS Applied Materials and Interfaces*, 1(12):2768–2777, 2009.

[114] M. Hösel, R. R. Sø ndergaard, M. Jø rgensen, and F. C. Krebs. Fast Inline Roll-to-Roll Printing for Indium-Tin-Oxide-Free Polymer Solar Cells Using Automatic Registration. *Energy Technology*, 1(1):102–107, January 2013.

[115] B. Vaughan, E. L. Williams, N. P. Holmes, P. Sonar, A. Dodabalapur, P. C. Dastoor, and W. J. Belcher. Water-based nanoparticulate solar cells using a diketopyrrolopyrrole donor polymer. *Physical chemistry chemical physics : PCCP*, 16(6):2647–53, 2014.

[116] M. D. De Jonge and S. Vogt. Hard X-ray fluorescence tomography-an emerging tool for structural visualization. *Current Opinion in Structural Biology*, 20(5):606–614, 2010.

[117] L. Kazmerski. Best Research Cell Efficiencies Chart; National Renewable Energy Laboratory (NREL), 2014.

[118] M. A. Green, A. Ho-Baillie, and H. J. Snaith. The emergence of perovskite solar cells. *Nature Photonics*, 8(7):506–514, 2014.

[119] Y.-B. Cheng, Y. Han, S. Meyer, Y. Dkhissi, K. Weber, J. Pringle, U. Bach, and L. Spiccia. Degradation observations of encapsulated planar CH3NH3PbI3 perovskite solar cells at high temperatures and humidity. *J. Mater. Chem. A*, pages 8139–8147, 2015.

[120] J. Y. Buffiere, E. Maire, J. Adrien, J. P. Masse, and E. Boller. In situ experiments with X ray tomography: An attractive tool for experimental mechanics. *Proceedings of the Society for Experimental Mechanics, Inc.*, 67:289–305, 2010.

[121] P. R. Shearing, J. Gelb, and N. P. Brandon. X-ray nano computerised tomography of SOFC electrodes using a focused ion beam sample-preparation technique. *Journal of the European Ceramic Society*, 30(8):1809–1814, 2010.

[122] P. Schneider, M. Stauber, R. Voide, M. Stampanoni, L. R. Donahue, and R. Müller. Ultrastructural properties in cortical bone vary greatly in two inbred strains of mice as assessed by synchrotron light based micro- and nano-CT. *Journal of bone and mineral research : the official journal of the American Society for Bone and Mineral Research*, 22(10):1557–1570, 2007.

[123] P. Maruvada, N. I. Dmitrieva, J. East-Palmer, and P. M. Yen. Cell cycle-dependent expression of thyroid hormone receptor-beta is a mechanism for variable hormone sensitivity. *Molecular biology of the cell*, 15(4):1895–1903, 2004.

[124] J. Radon. Über die Bestimmung von Funktionen durch ihre Integralwerte längs gewisser Mannigfaltigkeiten. *Berichte über die Verhandlungen der Königlich-Sächsischen Akademie der Wissenschaften zu Leipzig, Mathematisch-Physische Klasse*, 69:262–277, 1917.

[125] J. Radon. On the Determination of Functions from Their Integral Values along Certain Manifolds. *IEEE transactions on medical imaging*, 5(4):170–176, 1986.

[126] A. H. Andersen and A. C. Kak. SART_84.pdf. *Ultrason Imaging*, 6(1):81–94, 1984.

[127] E. Y. Sidky and X. Pan. Image reconstruction in circular cone-beam computed tomography by constrained, total-variation minimization. *Physics in medicine and biology*, 53(17):4777–4807, 2008.

[128] D. Y. Parkinson, C. Knoechel, C. Yang, C. A. Larabell, and M. A. Le Gros. Automatic alignment and reconstruction of images for soft X-ray tomography. *Journal of structural biology*, 177(2):259–66, February 2012.

[129] V.-D. Tran, M. Moreaud, É. Thiébaut, L. Dénis, and J.-M. Becker. Robust registration of electron tomography projections without fiducial markers. 8657:86570R, February 2013.

[130] F. Bleichrodt and K. J. Batenburg. Automatic Optimization of Alignment Parameters for Tomography Datasets. In Joni-Kristian Kämäräinen and Marku Koskela, editors, *Image analysis*, pages 489–500. Springer-Verlag, 2013.

[131] F. Bleichrodt, J. D. Beenhouwer, J. Sijbers, and K. J. Batenburg. Aligning Projection Images from Binary Volumes. *Fundamenta Informaticae*, 135:21–42, 2014.

[132] A. C. Kak. *Algebraic Reconstruction Algorithms*. 2001.

[133] T. M. Buzug. *Computed Tomography*. 2011.

[134] J. M. Feldkamp, M. Kuhlmann, S. V. Roth, A. Timmann, R. Gehrke, I. Shakhverdova, P. Paufler, S. K. Filatov, R. S. Bubnova, and C. G. Schroer. Recent developments in tomographic small-angle X-ray scattering. *Physica Status Solidi A-Applications and Materials Science*, 206(8):1723–1726, 2009.

[135] A. C. Kak and M. Stanley. Algorithms for Reconstruction with Nondiffracting Sources. *Principles of Computerized Tomographic Imaging*, (1):49–112, 1999.

[136] H. Turbell. *Cone-Beam Reconstruction Using Filtered Backprojectionn*. Number 672. 2001.

[137] F. Tabak. *Robust Algorithms for Discrete Tomography*. PhD thesis, Delft University of Technology, 2012.

[138] J. Nocedal and S. J. Wright. *Least-Squares Problems*. 2006.

[139] P. C. Hansen and M. Saxild-Hansen. AIR tools - A MATLAB package of algebraic iterative reconstruction methods. *Journal of Computational and Applied Mathematics*, 236(8):2167–2178, 2012.

[140] W. J. Palenstijn, K. J. Batenburg, and J. Sijbers. Performance improvements for iterative electron tomography reconstruction using graphics processing units (GPUs). *Journal of Structural Biology*, 176(2):250–253, 2011.

[141] W J. Palenstijn, K. J. Batenburg, and J. Sijbers. The ASTRA Tomography Toolbox. *13th International Conference on Computational and Mathematical Methods in Science and Engineering*, pages 1–7, 2013.

Article Appendix

Publication I (Published)

Emil B. L. Pedersen, Thomas Tromholt, Morten V. Madsen, Arvid P. L. Böttiger, Markus Weigand, Frederik C. Krebs and Jens W. Andreasen

Spatial degradation mapping and component-wise degradation tracking in polymer–fullerene blends

([73] - Reproduced by permission of The Royal Society of Chemistry)

Publication II (Published)

Henrik F. Dam, Thomas R. Andersen, Emil B. L. Pedersen, Karl T. S. Thydén, Martin Helgesen, Jon E. Carlé, Peter S. Jørgensen, Juliane Reinhardt, Roar R. Søndergaard, Mikkel Jørgensen, Eva Bundgaard, Frederik C. Krebs and Jens W. Andreasen

Enabling Flexible Polymer Tandem Solar Cells by 3D Ptychographic Imaging

([92] - Reproduced by permission of John Wiley and Sons)

Publication III (Manuscript)

Emil. B. L. Pedersen, Martin C. Pedersen, Søren B. Simonsen, Rasmus G. Brandt, Arvid P. L. Böttiger, Thomas R. Andersen, Wu Jiang, Xie Zhiyuan, Frederik C. Krebs, Lise. Arleth and Jens W. Andreasen

Structure and crystallinity in water dispersible photoactive nanoparticles for organic solar cells

Publication IV (Manuscript)

Emil B. L. Pedersen, Dechan Angmo, Henrik F. Dam, Karl T. S. Thydén, Thomas R. Andersen, Eerik T. B. Skjønsfjell, Frederik C. Krebs, Mirko Holler, Ana Diaz, Manuel Guizar-Sicairos, Dag W. Breiby and Jens W. Andreasen

Water-processed organic tandem solar cells improved by quantitative 3D nanoimaging

Journal of Materials Chemistry C

PAPER

View Article Online
View Journal | View Issue

Spatial degradation mapping and component-wise degradation tracking in polymer–fullerene blends†

Cite this: J. Mater. Chem. C, 2014, 2, 5176

E. B. L. Pedersen,[a] T. Tromholt,[a] Morten V. Madsen,[a] A. P. L. Böttiger,[a] M. Weigand,[b] F. C. Krebs[a] and J. W. Andreasen*[a]

Received 6th January 2014
Accepted 13th April 2014

DOI: 10.1039/c4tc00028e

www.rsc.org/MaterialsC

Using X-ray absorption the effects of photodegradation in active layer materials for polymer solar cells are investigated. Through the observation of changes in the X-ray absorption energy spectra the degradation of the individual components is tracked in blends of poly-3-hexyl-thiophene (P3HT) and C_{60} butyric acid methyl ester (PCBM). The degradation rates in the blend are decreased by a factor of 3 for P3HT and by a factor between 1.1 and 2.3 for PCBM compared to the pure materials. For P3HT, degradation is resolved spatially using scanning transmission X-ray microscopy and the photodegradation process is found to be intrinsically homogeneous at the nanometer scale.

Introduction

With the improving performance reported for polymer solar cells (PSCs),[1,2] the importance of increasing the operational lifetime at the device level becomes central for the realization of OPVs as a scaled commercially available energy technology.[3,4] When exposed to sunlight and components in the ambient atmosphere such as water and oxygen, a number of effects occur in parallel by which the overall device performance decreases. Extensive work has been directed towards understanding these degradation mechanisms and developing new materials and geometries that can increase the device lifetime.[3,5,6] Hereby, the device lifetime has been observed to increase from days to months and years. Lifetimes in the range of 1–2 years have been reached and a range of 3–5 years is realistic in the near future.[7,8]

Conventionally, the device stability is assessed by exposing the functioning device to simulated sunlight while measuring the electrical performance through *I–V* characterization.[8,9] Although this approach provides a measure of the operational stability, it is a macroscopic method that gives no insight or explanations for the failure in terms of degradation mechanisms or failure mode. Whereas a trial-and-error approach can be followed by processing solar cells with different polymers or architectures to obtain more stable devices, a more rigorous approach is to study the intrinsic stability of the individual components under certain sets of conditions and thereby chart the preponderant degradation mechanisms and failure modes. Hereby, unstable components, interfaces or contacts of the device can be identified and work can be focused on remedying these, finding alternatives or simply replacing these components with better alternatives.

One device degradation mechanism that has often been found to be dominant is the degradation of the photoactive layer, where especially bleaching of the polymer has been demonstrated to be a key mechanism limiting the solar cell stability mainly in the presence of oxygen. As the photoactive polymer is exposed to light and oxygen, the polymer is prone to react chemically which implies a loss of conjugation thus affecting light absorption, charge transport and charge collection efficiency. By monitoring the gradual photobleaching of a large range of polymers when exposed to simulated sunlight, chemically stable functional groups have been identified.[10,11] This information may be combined with chemical analysis of the degradation products as obtained from infra-red spectroscopy by which the degradation mechanisms responsible for the polymer bleaching can be elucidated.[12–14]

The above described techniques address the photoactive layer on a macroscopic level. Other experiments have indirectly mapped degradation on the microscopic level for chemical structures. A recent experiment mapped the photocurrent and quantum efficiency for chemical structures that form 10–100 micron domains with lower EQE during degradation.[15] Although such methodologies allow for mapping degradation, they involve complete devices and results are often subject to influence by electrodes and barrier layers rather than the degradation of the active layer itself.

Other methods useful for degradation mapping of PSC materials are fluorescence microscopy and Time of Flight Secondary Ion Mass Spectroscopy (TOF-SIMS).[16] These methods have been used to map degradation in C_{60}/C_{12}-PSV

[a]Department of Energy Conversion and Storage, Technical University of Denmark, Frederiksborgvej 399, 4000 Roskilde, Denmark. E-mail: jewa@dtu.dk

[b]Max Planck Institute for Intelligent Systems, Heisenbergstr. 3, 70569 Stuttgart, Germany

† Electronic supplementary information (ESI) available: Derivation of linear combinations of optical density from the Lambert–Beer law, full chi square table fits to blend P3HT–PC_{60}BM, NEXAFS data for fullerenes presented in Table 1, and the degradation map of P3HT T100. See DOI: 10.1039/c4tc00028e

(poly(didodecylstilbenevinylene)) devices, where diffusion of oxygen into the active layer was tracked through pinholes in the aluminum cathode.[17] TOF-SIMS allows tracking of elements entering the PSC materials, but has no sensitivity to other chemical changes. Fluorescence microscopy requires a change in the emitted fluorescence during degradation, and can normally only separate between degraded and undegraded regions, but cannot assess the level of degradation in a quantitative manner.

Compared to the above mentioned methods, Scanning Transmission X-ray Microscopy (STXM) can provide direct mapping of degradation. STXM has recently been applied in the field of PSCs, as this technique combines energy and nano-meter spatial resolution (Near-Edge X-ray Absorption Fine Structure – NEXAFS) allowing for microscopy and chemical analysis in parallel. With this technique, imaging of the features can be combined with modeling to give a resolution down to 10 nm.[18] Furthermore, properties such as the molecular orientation[19,20] and the evolution of domains[21] over time have been directly imaged. Finally, the spectral information allows for quantifying the ratio of different components in the film by which *composition maps* can be obtained. Following these approaches composition maps have been demonstrated for the poly(phenylenevinylene) MDMO–PPV blended with phenyl-C_{60} butyric acid methyl ester ($PC_{60}BM$)[22] and poly(3-hexyl-thiophene) (P3HT) blended with $PC_{60}BM$,[21,23] where the NEXAFS spectrum of the blend is fitted as a linear combination of the NEXAFS spectra of the individual components. Only limited work has been performed on the topic of degradation with STXM. The effect of degradation on the NEXAFS absorption of conjugated polymers by *in situ* X-ray[24,25] has been reported, where pronounced effects were observed for the polymer (P3HT).

We have shown (see ESI†) that the approach for obtaining linear combinations of the NEXAFS spectra of the individual components as demonstrated for P3HT and $PC_{60}BM$ can be applied for 5 other fullerene derivatives C_{60}, C_{70}, $PC_{70}BM$, bis$PC_{60}BM$ and ICBA (for systematic names see Experimental). Additionally, by combining the NEXAFS spectra of P3HT and $PC_{60}BM$ at different degradation levels, it is possible to identify the individual degradation states of P3HT and $PC_{60}BM$ in blends. We extend this method to spatial mapping of degradation in P3HT through STXM measurements.

Results

The method we use to treat the data can be outlined as follows: spectra of degraded blend films are compared to measured reference spectra, and the similarity is quantified. This allows us to find the state of unknown samples based on the known state of the reference samples. For absorption data the method can be extended to linear combinations according to the Lambert–Beer law (see also ESI†). Thus, the state of material mixtures can be determined based on the known states of the pure components – which in most cases is easier to understand and control.

The essence of the method is to fit a spectrum with a reference spectrum (or a linear combination of multiple reference spectra) and measure the goodness of fit by a reduced chi-square (for more details see Experimental section). The method falls between composition mapping,[21,23,26] which only requires measurements at a few selected energies, and traditional peak fitting which needs complete spectra with high energy resolution. This method only needs enough data points to perform meaningful fitting, but measured for multiple reference samples in different states since the method only determines the closest matching reference.

To check the robustness and validity of the method, we have conducted a small side study with P3HT and various fullerenes (see ESI†). We find that for differences in the reduced chi-square greater than 0.1 we are able to determine the correct chemical composition.

For photodegraded P3HT–PCBM blends we use the outlined method to assign individual degradation levels to P3HT and PCBM in the blend. The degradation nomenclature is based on the photoabsorbance of visible light (400–600 nm wavelength) where T100 represents the pristine material and T80 that 80% absorption is retained, relative to the pristine state. Fig. 1 shows the NEXAFS spectra of degraded P3HT, $PC_{60}BM$ and P3HT–$PC_{60}BM$ blends. For all degradation processes, the peak positions shift to higher energies as a function of photodegradation. For P3HT the spectral differences are small between T60, T80 and T100 compared to T20. $PC_{60}BM$ shows a gradual blue shift of the first two peaks and a reversal of weight between the first and third peaks as a function of photodegradation. The blend spectra combine the features of P3HT and $PC_{60}BM$. The T100 blend spectrum resembles a linear combination of $PC_{60}BM$ T100 and P3HT T100. The spectrum of the most degraded blend, T40, resembles the $PC_{60}BM$ T60 spectrum. Note that the two different T60 blend spectra come from the same film but different positions.

Each blend spectrum has been assigned degradation steps of P3HT and $PC_{60}BM$ based on the best linear combination of P3HT and $PC_{60}BM$ spectra. The range in P3HT degradation indicates fits where the difference in the reduced chi square is less than 0.1 (as established in our test of robustness of the method). P3HT is denoted as T0 in one T60 blend and the T40 blend as it is not assigned any weight in the fit *i.e.* the P3HT spectrum does not contribute significantly to the blend spectrum.

Fig. 2 is based on energy resolved STXM and shows spatial thickness maps of P3HT in different degradation states and their associated degradation maps. Each P3HT STXM dataset is fitted by the 4 NEXAFS reference degradation spectra of P3HT (T100, T80, T60, and T20). Each point in an energy resolved STXM map contains a whole NEXAFS spectrum and the degradation state is found as the best fit among the reference spectra. By assigning a degradation step to each point we produce the spatial degradation maps shown in Fig. 2. Seen on the T60 and T80 maps the contrast goes down to the pixel level (1 pixel equals 159 nm) which is also the spatial resolution since the beam diameter is smaller (31 nm). The degradation maps show largely homogeneous degradation except a few pixel sized regions in T60 and T80 in addition to all the edge regions. At the edge it is likely that the signal will partially be from the sample and partially from the direct beam. The edge values therefore have low validity.

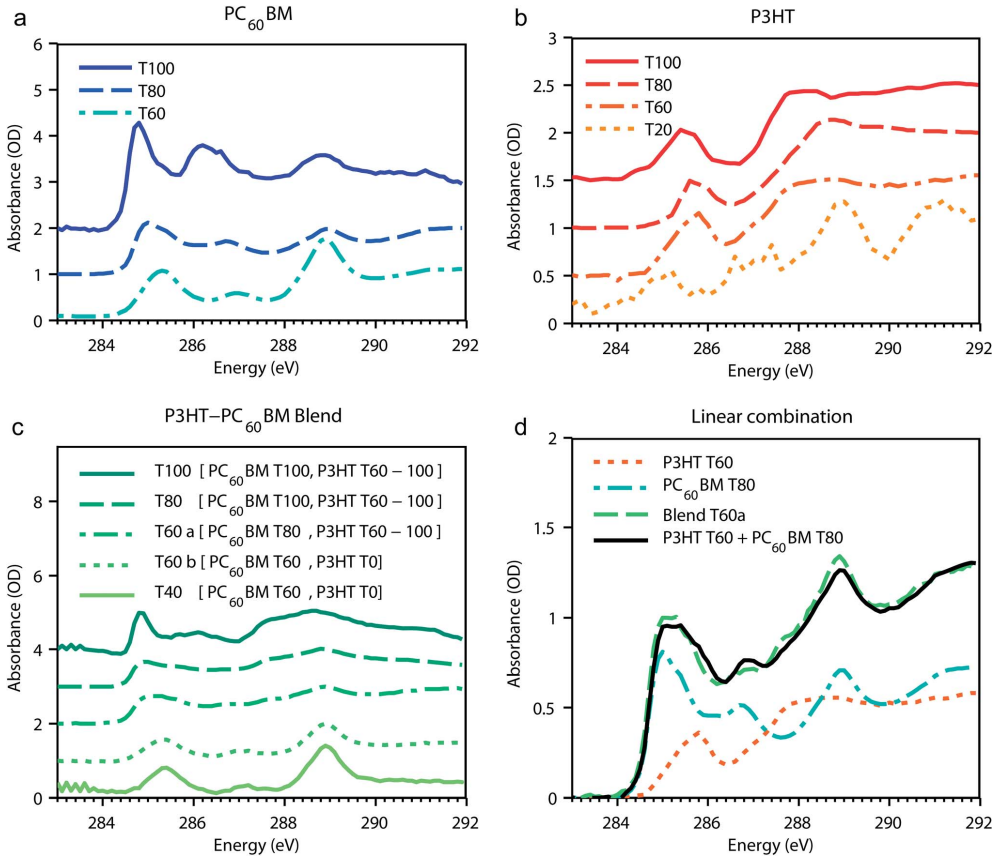

Fig. 1 NEXAFS spectra for pristine and degraded (a) $PC_{60}BM$, (b) P3HT and (c) P3HT–$PC_{60}BM$ blends (1 : 1) in the 283–292 eV range. For the blends, the degradation states of the components are shown in the legend. These degradation steps have been found to be the most likely linear combinations of degraded P3HT and $PC_{60}BM$ spectra – an example is shown for blend T60a in (d). The most likely degradation state is found by the lowest reduced chi square. The ranges in P3HT indicate regions of intervals with similar reduced chi square values.

Discussion

We report the spectra of P3HT, $PC_{60}BM$ and P3HT–$PC_{60}BM$ blends degraded under controlled conditions. For $PC_{60}BM$, the absorption peaks shift to higher energies and the relative peak height is changed in the degradation process. Recent DFT calculations have determined the contribution of individual carbon elements to the $PC_{60}BM$ NEXAFS spectrum.[27] From the calculations we see that the contribution to the spectra at the lowest energies in the first peak comes from the carbon atoms in the fullerene cage. If some of these cage atoms are oxidized, the first peak will be shifted to higher energy. Furthermore, the peak near 289 eV increases in relative intensity compared to the first peak. The calculations show that the side chain of $PC_{60}BM$ mainly contributes to the peak near 289 eV, thereby indicating that the side chain is unchanged whereas the carbon cage oxidizes. This interpretation of $PC_{60}BM$ degradation through oxidation of the carbon cage is supported by MALDI-TOF studies.[28]

The P3HT spectra show less pronounced differences than $PC_{60}BM$. The T60–T100 spectra are very similar to a drastically changed spectrum for T20. The noise in the T20 pattern arises due to low X-ray absorption at the very degraded state. The similarities in the first P3HT spectra make it difficult to extract information regarding the P3HT degradation pathway. When determining the component-wise degradation in P3HT–PCBM blends, similar spectra contribute to the ambiguity in the assessed degradation state.

The method of linear fitting reference spectra is general and can be used to track the degradation behavior in any blend of

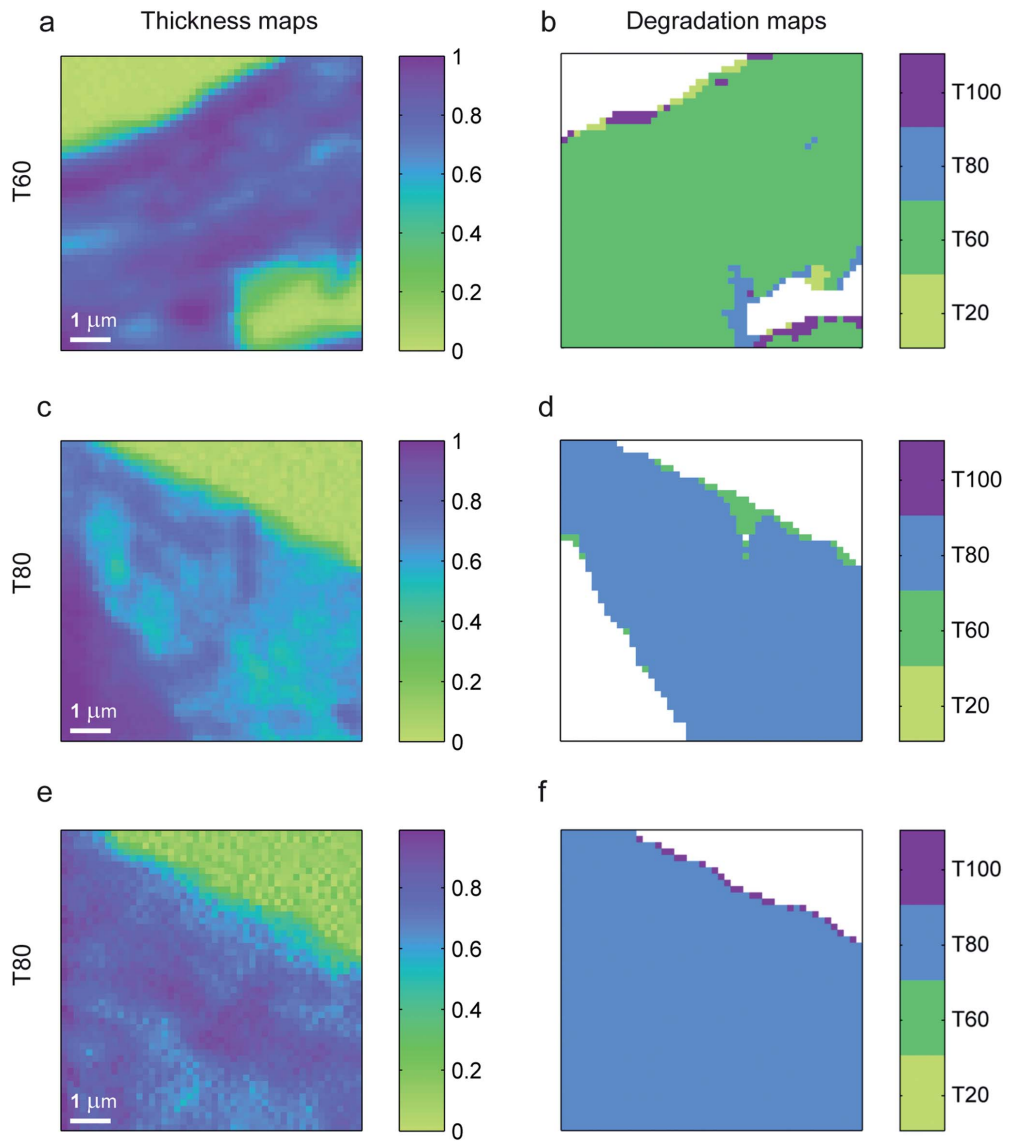

Fig. 2 (a, c and e) Relative thickness of P3HT samples from STXM maps at 286 eV. The variation in thickness is a product of the fabrication method (scraped off glass substrates). (b, d and f) Degradation step found from energy resolved STXM maps. The degradation steps were assigned point by point by fitting the different P3HT reference spectra and choosing the reference with the lowest reduced chi square. Thin areas with no sample and thick areas with no photon penetration are colored white in the degradation maps (see also ESI†). (a and b) P3HT degraded to the T60 level. (c–f) P3HT degraded to the T80 level. For pristine P3HT (T100) see ESI.†

materials. For the P3HT–$PC_{60}BM$ blend we see that $PC_{60}BM$ degrades at a slower rate than P3HT – similar to the pure materials where $PC_{60}BM$ also endures longer exposure than P3HT before reaching the same degradation level.[10]

The contact between the two materials improves the stability of both. In our experiment it can be quantified through the degradation rates. The degradation rates of pure P3HT and PCBM have previously been reported to be 2.5% per hour for P3HT and 0.36% per hour for $PC_{60}BM$.[10] With our new measurements we can estimate the degradation rates of the materials within the blend by combining the results in Fig. 1 with the known exposure times (see ESI†).

Assuming that P3HT reaches T0 when the blend reaches T60 the degradation rate of P3HT goes from 2.5% per hour to 0.82% per hour – a decrease to 1/3 of the original degradation rate. For $PC_{60}BM$ the decrease is somewhat lower with an original rate of 0.36% per hour and a rate in the blend between 0.16% per hour and 0.33% per hour (see Fig. 1 where $PC_{60}BM$ for the T60 blend samples is either T60 or T80). This corresponds to a decreased degradation rate between a factor of 1.1 and 2.3 for $PC_{60}BM$.

The decrease in the P3HT degradation rates has been conjectured to be caused by $PC_{60}BM$ quenching the excited state of P3HT.[28] For $PC_{60}BM$ the reduction in the degradation rate might arise because the flow of electrons fills up vacant spaces in the homo level thereby reducing the oxidation rate. For the P3HT–$PC_{60}BM$ blends, P3HT remains the fastest degraded component and it therefore remains most important to understand the P3HT degradation process.

By using STXM, the outlined method can map degradation spatially. We demonstrate this for pure P3HT to probe the intrinsic behavior in the degradation process. It removes any heterogeneity present in material blends and leaves us with a pure P3HT signal – removing the ambiguity in P3HT degradation we have in the P3HT–$PC_{60}BM$ blends. Through the STXM mapping of P3HT we provide the first nanoscale maps of degradation in a PSC relevant polymer. The spatial maps reveal that P3HT degrades largely homogeneously at the nanoscale. It indicates that polymer degradation is an evenly distributed process with no observed cooperative effects *e.g.* no domain growth of early degraded regions. Our method shows a few domains near the resolution limit, so domain formation below the 100 nm is a possibility. There might be surface dependencies in the degradation process like oxygen diffusion, but our experiment shows that in an ambient atmosphere the degradation is intrinsically homogeneous, even with thickness variations in the samples *e.g.* P3HT T60 in Fig. 2. Our results imply that the reported domain-wise degradation for whole devices[15,17] is not an intrinsic behavior in the active layer. The domain-wise degradation would instead predominantly be regulated by heterogeneities in the barrier and anode/cathode layers that limit the access of oxygen and water.

Experimental

Regio-regular P3HT (regio-regularity 91.7%, $M_n = 28.8$ kDa) was obtained from Rieke Metals (batch PTL 10–87), $PC_{60}BM$, bisPCBM (bis(1-[3-(methoxycarbonyl)propyl]-1-phenyl)-[6.6]C_{62}) and $PC_{70}BM$ ([6,6]-phenyl-C_{70}-butyric acid methyl-ester) from Solenne, C_{60} ((C_{60}-Ih)[5,6]fullerene) and C_{70} (C_{70}-Ih)[5,6] fullerene) from Aldrich, and ICBA (1′,1″,4′,4″-tetrahydrodi[1,4] methanonaphthaleno[5,6]fullerene-C_{60}) from Plextronics.

Controlled photodegradation

All blends were processed from chlorobenzene in ratios of 1 : 1. Approximately 50 nm films were obtained by spin coating onto silicon nitride membranes obtained from Silson (membrane area 1 × 1 mm and thickness 100 nm). Pure P3HT samples were prepared by spin coating on glass, followed by controlled photodegradation. Degradation under simulated sunlight was performed with an unfiltered Osram 1200 W HMI lamp with a light intensity of 0.1 W cm^{-2} at 30 °C in an ambient atmosphere with a light spectrum close to AM1.5G. The degradation state of the films was obtained from the gradual decrease of UV-vis absorption as described by Tromholt *et al.*[10] T100 indicates the pristine material and T80 that 80% of the pristine photoabsorbance is left in the wavelength interval of 400–600 nm.

Sample preparation for NEXAFS experiments

Samples spin cast on silicon nitride membranes could be used directly for NEXAFS experiments (the reason why this preparation was preferred). The pure P3HT samples spin cast on glass were scraped off with a scalpel and placed on transmission electron microscopy copper grids. A floating off scheme was first tried, but it was observed that the photodegraded films wrinkled and disintegrated into pieces when released from the substrate. Floating of the films was thus not deemed suitable for studying the film morphology, whereas it was conjectured that scraping off was more likely to preserve the film morphology.

STXM and NEXAFS experiments

STXM and NEXAFS measurements were recorded at the synchrotron facility BESSY II in Berlin, Germany, at the beamline UE46-PGM2. All samples were observed in the MAXYMUS STXM end station under high vacuum at the carbon edge (282–292 eV, 1 eV resolution). The short energy range was chosen to minimize the exposure, so little or no uncontrolled degradation would occur due to the X-ray dose. In addition the beam was defocused to a diameter of 31 nm. In most experiments, the X-rays were detected using a photomultiplier tube, but the pure P3HT sample data were acquired with a photo avalanche diode. The spectra in the two experiments have been energy calibrated by the pristine P3HT absorption peaks. When measuring samples on silicon nitride membranes, the direct beam was measured in separate measurements without the sample, since the whole membranes were covered with the material. This is not ideal from a spectroscopic point of view, but we deemed it more important to conserve the morphology of the samples by avoiding transfer of the films after the photodegradation process.

Data treatment of NEXAFS and STXM data

All data were converted to optical density using the measured sample and pure beam intensity, and then normalized to

0 pre-edge and 1 post-edge similar to the procedure by Dhez *et al.*[29] The measured visual absorbance was related to NEXAFS spectra of the samples and these spectra were used as the reference spectra for the various states of the materials (shown in Fig. 1). For each P3HT–PCBM blend spectrum we fitted all linear combinations of pure P3HT and PCBM reference spectra and estimated the best fits by the reduced chi square (shown in the ESI†). Component-wise degradation was estimated based on the best fits. A similar procedure was used to generate 2D degradation maps of P3HT. Energy resolved STXM data were converted to NEXAFS spectra for each point *e.g.* a 4 × 4 point STXM scan would result in 16 individual NEXAFS spectra. Each NEXAFS spectrum was fitted by the 4 P3HT reference spectra and assigned a degradation state based on the best fit. Thin regions with no P3HT and thick regions with too high absorbance were removed since they could not provide valid P3HT NEXAFS spectra as described in the ESI.†

Conclusions

We explored photodegradation in an ambient atmosphere for PSC materials using soft X-ray absorption microscopy. For P3HT–fullerene blends we demonstrated that individual components/degradation states can be found from linear combinations of spectra from pure materials/degradation states. This is done by finding the linear combination with the lowest reduced chi-square. We present the first reported NEXAFS spectra of degraded P3HT and $PC_{60}BM$, which support that $PC_{60}BM$ degrades through oxidation of the carbon cage. We find that P3HT degrades faster than $PC_{60}BM$ in the blend material, but the degradation rate of both materials is reduced when mixed. For P3HT, the degradation rate drops by a factor of 3 and for $PC_{60}BM$ the drop is between a factor of 1.1 and 2.3. Finally, we demonstrated that STXM can be used to produce nanoscale degradation maps of P3HT. We find that P3HT degradation is intrinsically a homogeneous process and that the previously observed degraded domains in whole devices are due to the effects of inhomogeneity in the barrier or electrode layers.

Acknowledgements

We gratefully acknowledge financial support from The Danish Council for Strategic Research through the WAPART project from The Danish National Research Foundation, and from The Danish Council for Independent Research | Natural Sciences, through the DANSCATT grant. We also express our gratitude to Michael Bechtel, for kind assistance during the experiments with the STXM at MAXYMUS, BESSY II, by the MPI for Intelligent Systems, Department Schütz.

Notes and references

1 C. Small, S. Chen, J. Subbiah, C. Amb, S. Tsang, T. Lai, J. Reynolds and F. So, *Nat. Photonics*, 2011, 1–6.
2 J. You, L. Dou, K. Yoshimura, T. Kato, K. Ohya, T. Moriarty, K. Emery, C.-C. Chen, J. Gao, G. Li and Y. Yang, *Nat. Commun.*, 2013, **4**, 1446.
3 M. Jørgensen, K. Norrman, S. A. Gevorgyan, T. Tromholt, B. Andreasen and F. C. Krebs, *Adv. Mater.*, 2012, **24**, 580–612.
4 M. O. Reese, S. A. Gevorgyan, M. Jørgensen, E. Bundgaard, S. R. Kurtz, D. S. Ginley, D. C. Olson, M. T. Lloyd, P. Morvillo, E. A. Katz, A. Elschner, O. Haillant, T. R. Currier, V. Shrotriya, M. Hermenau, M. Riede, K. R. Kirov, G. Trimmel, T. Rath, O. Inganäs, F. Zhang, M. Andersson, K. Tvingstedt, M. Lira-Cantu, D. Laird, C. McGuiness, S. (Jimmy) Gowrisanker, M. Pannone, M. Xiao, J. Hauch, R. Steim, D. M. DeLongchamp, R. Rösch, H. Hoppe, N. Espinosa, A. Urbina, G. Yaman-Uzunoglu, J.-B. Bonekamp, A. J. J. M. van Breemen, C. Girotto, E. Voroshazi and F. C. Krebs, *Sol. Energy Mater. Sol. Cells*, 2011, **95**, 1253–1267.
5 M. Lira-Cantu, D. M. Tanenbaum, K. Norrman, E. Voroshazi, M. Hermenau, M. T. Lloyd, G. Teran-Escobar, Y. Galagan, B. Zimmermann, M. Hosel, H. F. Dam, M. Jorgensen, S. Gevorgyan, L. Lutsen, D. Vanderzande, H. Hoppe, R. Roesch, U. Wuerfel, R. Andriessen, A. Rivaton, G. Y. Uzunoglu, D. Germack, B. Andreasen, M. V Madsen, E. Bundgaard and F. C. Krebs, in *Reliability Of Photovoltaic Cells, Modules, Components, And Systems V*, ed. N. G. Dhere and J. H. Wohlgemuth, 2012, vol. 8472.
6 P. Favia, E. Voroshazi, P. Heremans and H. Bender, *J. Mater. Sci.*, 2012, **48**, 2908–2919.
7 C. J. Brabec, S. Gowrisanker, J. J. M. Halls, D. Laird, S. Jia and S. P. Williams, *Adv. Mater.*, 2010, **22**, 3839–3856.
8 C. H. Peters, I. T. Sachs-Quintana, J. P. Kastrop, S. Beaupré, M. Leclerc and M. D. McGehee, *Adv. Energy Mater.*, 2011, **1**, 491–494.
9 S. A. Gevorgyan, A. J. Medford, E. Bundgaard, S. B. Sapkota, H.-F. Schleiermacher, B. Zimmermann, U. Würfel, A. Chafiq, M. Lira-Cantu, T. Swonke, M. Wagner, C. J. Brabec, O. Haillant, E. Voroshazi, T. Aernouts, R. Steim, J. A. Hauch, A. Elschner, M. Pannone, M. Xiao, A. Langzettel, D. Laird, M. T. Lloyd, T. Rath, E. Maier, G. Trimmel, M. Hermenau, T. Menke, K. Leo, R. Rösch, M. Seeland, H. Hoppe, T. J. Nagle, K. B. Burke, C. J. Fell, D. Vak, T. B. Singh, S. E. Watkins, Y. Galagan, A. Manor, E. A. Katz, T. Kim, K. Kim, P. M. Sommeling, W. J. H. Verhees, S. C. Veenstra, M. Riede, M. Greyson Christoforo, T. Currier, V. Shrotriya, G. Schwartz and F. C. Krebs, *Sol. Energy Mater. Sol. Cells*, 2011, **95**, 1398–1416.
10 T. Tromholt, M. V. Madsen, J. E. Carlé, M. Helgesen and F. C. Krebs, *J. Mater. Chem.*, 2012, **22**, 7592.
11 M. Manceau, E. Bundgaard, J. Eggert Carlé, O. Hagemann, M. Helgesen, R. Søndergaard, M. Jørgensen and F. C. Krebs, *J. Mater. Chem.*, 2011, **21**, 4132–4141.
12 M. Manceau, J. Gaume, A. Rivaton and J. Gardette, *Thin Solid Films*, 2010, **518**, 7113–7118.
13 A. Rivaton, S. Chambon, M. Manceau, J.-L. Gardette, N. Lemaître and S. Guillerez, *Polym. Degrad. Stab.*, 2010, **95**, 278–284.
14 M. Manceau, A. Rivaton, J.-L. Gardette, S. Guillerez and N. Lemaître, *Polym. Degrad. Stab.*, 2009, **94**, 898–907.
15 K. Feron, T. J. Nagle, L. J. Rozanski, B. B. Gong and C. J. Fell, *Sol. Energy Mater. Sol. Cells*, 2013, **109**, 169–177.

16 B. Andreasen, D. M. Tanenbaum, M. Hermenau, E. Voroshazi, M. T. Lloyd, Y. Galagan, B. Zimmernann, S. Kudret, W. Maes, L. Lutsen, D. Vanderzande, U. Würfel, R. Andriessen, R. Rösch, H. Hoppe, G. Teran-Escobar, M. Lira-Cantu, A. Rivaton, G. Y. Uzunoğlu, D. S. Germack, M. Hösel, H. F. Dam, M. Jørgensen, S. A. Gevorgyan, M. V. Madsen, E. Bundgaard, F. C. Krebs and K. Norrman, *Phys. Chem. Chem. Phys.*, 2012, **14**, 11780–11799.
17 K. Norrman, N. B. Larsen and F. C. Krebs, *Sol. Energy Mater. Sol. Cells*, 2006, **90**, 2793–2814.
18 K. B. Burke, A. J. Stapleton, B. Vaughan, X. Zhou, A. L. D. Kilcoyne, W. J. Belcher and P. C. Dastoor, *Nanotechnology*, 2011, **22**, 265710.
19 B. Watts, T. Schuettfort and C. R. McNeill, *Adv. Funct. Mater.*, 2011, **21**, 1122–1131.
20 D. S. Germack, C. K. Chan, B. H. Hamadani, L. J. Richter, D. A. Fischer, D. J. Gundlach and D. M. DeLongchamp, *Appl. Phys. Lett.*, 2009, **94**, 233303.
21 B. Watts, W. J. Belcher, L. Thomsen, H. Ade and P. C. Dastoor, *Macromolecules*, 2009, **42**, 8392–8397.
22 C. R. McNeill, B. Watts, L. Thomsen, W. J. Belcher, A. L. D. Kilcoyne, N. C. Greenham and P. C. Dastoor, *Small*, 2006, **2**, 1432–1435.
23 K. Burke, W. Belcher and L. Thomsen, *Macromolecules*, 2009, **42**, 3098–3103.
24 H. Ahn, D. Oblas and J. Whitten, *Macromolecules*, 2004, **37**, 3381–3387.
25 L.-L. Chua, M. Dipankar, S. Sivaramakrishnan, X. Gao, D. Qi, A. T. S. Wee and P. K. H. Ho, *Langmuir*, 2006, **22**, 8587–8594.
26 B. A. Collins and H. Ade, *J. Electron Spectrosc. Relat. Phenom.*, 2012, **185**, 119–128.
27 I. E. Brumboiu, A. S. Anselmo, B. Brena, A. Dzwilewski, K. Svensson and E. Moons, *Chem. Phys. Lett.*, 2013, **568–569**, 130–134.
28 M. O. Reese, A. M. Nardes, B. L. Rupert, R. E. Larsen, D. C. Olson, M. T. Lloyd, S. E. Shaheen, D. S. Ginley, G. Rumbles and N. Kopidakis, *Adv. Funct. Mater.*, 2010, **20**, 3476–3483.
29 O. Dhez, H. Ade and S. G. Urquhart, *J. Electron Spectrosc. Relat. Phenom.*, 2003, **128**, 85–96.

ADVANCED ENERGY MATERIALS
www.advenergymat.de

Enabling Flexible Polymer Tandem Solar Cells by 3D Ptychographic Imaging

*Henrik F. Dam, Thomas R. Andersen, Emil B. L. Pedersen, Karl T. S. Thydén, Martin Helgesen, Jon E. Carlé, Peter S. Jørgensen, Juliane Reinhardt, Roar R. Søndergaard, Mikkel Jørgensen, Eva Bundgaard, Frederik C. Krebs, and Jens W. Andreasen**

The realization of a complete tandem polymer solar cell under ambient conditions using only printing and coating methods on a flexible substrate results in a fully scalable process but also requires accurate control during layer formation to succeed. The serial process where the layers are added one after the other by wet processing leaves plenty of room for error and the process development calls for an analytical technique that enables 3D reconstruction of the layer stack with the possibility to probe thickness, density, and chemistry of the individual layers in the stack. The use of ptychography on a complete 12-layer solar cell stack is presented and it is shown that this technique provides the necessary insight to enable efficient development of inks and processes for the most critical layers in the tandem stack such as the recombination layer where solvent penetration in fully solution processed 12-layer stacks is critical in eleven of the steps.

1. Introduction

The functionality of wet processed organic/inorganic multilayer stacks delicately relies on the quality of the individual layers in the stack and the robustness of previously processed layers to subsequently processed layers. The most extreme case is the fully wet processed polymer tandem solar cell that may be composed of as many as 12–14 layers.[1] A defect in just one of the interfaces may completely overthrow the device functionality and lead to failure. Finding the cause for the failure requires nanoscopic insight into the sample itself. A laboratory study of a sub-set of the layers might be useful but the ultimate technique must encompass the possibility for detailed analysis of the entire stack in both its functional and non-functional form. Ideally the technique enables a complete 3D reconstruction of the sample with detailed insight into the thickness and chemistry of the individual layers of the stack. In addition to the analytical technique, several other tools must be developed or tailored to fit the purpose of studying film formation and extraction of unscathed excerpts from the multilayer stack for analysis.

The solution processed polymer and organic solar cell is a very good example of a device where functionality is deeply rooted in the stacking of layers with the multijunction organic solar cell representing the ultimate case. The field of organic solar cells has to a large extent been based upon the vision of fast production of large areas of solar cells at very low cost. One of the means envisaged to achieve this is roll-to-roll (R2R) solution processing on flexible substrates. This has also been demonstrated although there is a large gap between the performance reached for very small area devices and devices with a practical size of square meters or more. The scalability has however been proven in a recent study where it was shown that serial connection on the km scale at total processing speeds in the m min^{-1} range for finished and laminated cells[2] was possible, allowing up to 10 kV from a 100 m long module with full scaling of the power extraction. The fact that samples of organic solar cell modules (10×14.2 cm^2) can be acquired by anyone free of charge[3,4] also illustrates a cost level approaching what was originally envisaged. The low cost has been achieved through use of the previously reported Flextrode substrate[2,5] dispensing with the otherwise commonly employed indium tin oxide (ITO) electrode, accompanied by careful optimization of the process conditions using tools such as life cycle analysis[6] to bring down the amount of material and energy used in the process.

However, the performance of the organic solar cell is still not at the desired level. Although efficiencies of up to 12% have been achieved for small scale laboratory devices,[7–11] these results have been obtained using rigid glass substrates, expensive and scarce ITO for the transparent electrode and by use

Dr. H. F. Dam, Dr. T. R. Andersen, E. B. L. Pedersen, Dr. K. T. S. Thydén, Dr. M. Helgesen, Dr. J. E. Carlé, Dr. P. S. Jørgensen, Dr. R. R. Søndergaard, Dr. M. Jørgensen, Dr. E. Bundgaard, Prof. F. C. Krebs, Dr. J. W. Andreasen
Department of Energy Conversion and Storage
Technical University of Denmark
Frederiksborgvej 399 DK-4000, Roskilde, Denmark
E-mail: jewa@dtu.dk
J. Reinhardt
Deutsches Elektronen-Synchrotron DESY
D-22607, Hamburg, Germany

DOI: 10.1002/aenm.201400736

of processing methods which are not directly transferable to large scale production. For R2R processed solar cells on flexible substrates the performance is in the 2–4% range[12] for large area devices, which is a consequence of the difficulties involved in the precise processing of a multilayer stack on a flexible, moving substrate.

One way to increase the efficiency of solar cells is to use complementary light absorbing materials, each absorbing a specific part of the solar spectrum, working in tandem as a multi-junction.[13–15] This allows for absorption of a broader part of the solar spectrum and in theory a larger conversion efficiency, but also requires current matching of the different junctions and demands efficient recombination layers between the subcells. The recombination layers must act both as charge selective layers in the individual junctions as well as good media for combining opposing charges from the adjacent junctions in order to minimize current loss. Polymer tandem solar cells have been reported on several occasions but only very few have been using R2R or R2R compatible processing.[16–19] Polymer tandem solar cells often consist of 10–14 distinct layers, all of which have to be continuous and homogeneous in thickness. Especially on flexible substrates this constitutes an enormous challenge as each layer should not only be processed with high accuracy and uniformity, but are also required to be able to sustain subsequent flexing. Andersen et al. recently demonstrated such roll-coated architecture achieving 1.3% efficiency using double sided illumination of a flexible tandem cell of poly(3-hexylthiophene):phenyl-C_{61}-butyric acid methyl ester (P3HT:PCBM|P3HT:PCBM)[18] and although this is an impressive result on a flexible substrate the double junction did not exceed the single junction with respect to efficiency which is the primary goal of tandem cells and it was clear that more powerful techniques were needed for the process and stack development.

In this report we present the use of in situ X-ray structural characterization during coating, excerption of the entire multilayer stack using focused ion beam milling (FIB) and high resolution X-ray phase contrast imaging (known as ptychography) of 12-layer polymer tandem solar cells on flexible ITO-free substrates using complementary low and high band gap polymers. The methodology allowed us to efficiently develop the coating and drying process for each layer thus enabling successful wet processing under ambient conditions of all layers yielding large area flexible tandem solar cells.

2. Results and Discussion

2.1. Roll Processing and Roll-2-Roll Analysis

First attempts at roll processing of the complete tandem solar cell stack on flexible substrates proved unsuccessful, with solar cells functioning as single junctions as result. Visual inspection during coating gave indications that the integrity of the recombination layer might be compromised during coating by solvent penetration from the overlying layers. To overcome this problem, we needed to develop the process for the multilayer stack and an analytical technique enabling careful study of the film formation while in progress. Until now, most studies on films for organic electronics are studies ex situ such that the relevant film or interface is created in an experimental setup where the study is possible. This reductionistic approach proved to be insufficient in our case and we had to develop a small R2R coating machine such that the mechanism of multilayer film formation could be studied in situ using X-rays during deposition of one layer on top of the next. This was realized by further development of a previously developed R2R X-ray scattering apparatus[20] such that it was possible to actually coat the film and study it using X-ray scattering while drying as shown in **Figure 1**. The small R2R coater was integrated with a grazing incidence small angle X-ray scattering (GISAXS) system and used to analyze the crystallinity of a P3HT:PCBM bottom cell during coating of the different layers of the stack. The use of an R2R setup lies with the need to identify the crystallinity of the bottom cell, while being subjected to solvent. The assumption was that the crystallinity of the bottom cell would be affected by solvation during coating, if solvent penetrated the recombination layer. Therefore, GISAXS patterns of each layer were obtained in situ during coating conducted at a controlled distance from the X-ray probe point, allowing measurement at a position with a constant wet-layer thickness.

We found that we could detect the crystalline signal (*100* reflection) from the lamellar stacking of P3HT in the P3HT:PCBM sub-cell during coating, at a position just after the drying front of the film (bottom left in Figure 1). The signal could still be distinguished during coating of the recombination layer consisting of PEDOT:PSS F40 (second from left) and ZnO (middle), with the latter also giving a very strong small angle scattering contribution because of the nano-crystalline structure. However, with the coating of the second sub-cell from chlorobenzene (second from right in Figure 1), the intermediate layer was clearly solvent saturated as evidenced by the reduction in small angle scattering intensity from the porous ZnO layer, now completely penetrated by solvent, and the concomitant disappearing of the *100* reflection from P3HT because of solvation. The P3HT recrystallizes with evaporation of the chlorobenzene, but redistribution of material throughout the recombination layer, surely leads to device failure. By coating the stack with a layer of butanol, which is not a solvent for the underlying layers, we tested that the elimination of P3HT diffraction is not due to the presence of a wet layer alone (bottom right in Figure 1).

Having established the catastrophic failure mechanism by solvent penetration during coating, we proceeded to investigate potential improvements of the solvent resistance of the intermediate recombination layer. One of the most challenging parts of manufacturing multi-layer coated devices using only wet processing lies with the ability to keep the individual layers separate. Moreover, keeping the layers thin enough to allow a high transparency and a good conductivity and still using optimal solvent combinations for the active layer blends for both top and bottom sub cells in a tandem stack, increases the difficulty further. Experiments with an additional Clevious P VP AL 4083 poly(3,4-ethylenedioxythiophene):polystyrene sulfonate (PEDOT:PSS) layer succeeded, yielding functional tandem solar cell stacks on a flexible substrate. This combination using two PEDOT:PSS types and a zinc oxide layer as a recombination layer presumably has a better solvent

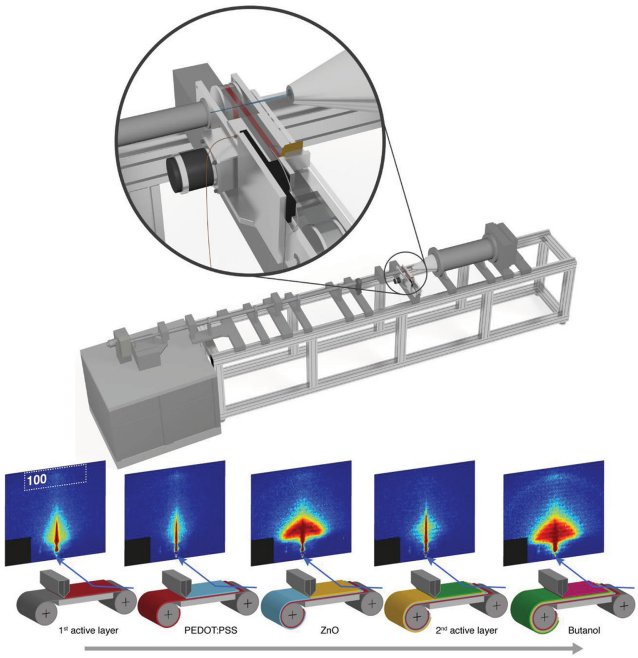

Figure 1. The R2R X-ray setup, about 6 m in overall length (top) with the small angle X-ray scattering data below, corresponding to coating of (from left to right): 1st active layer, PEDOT:PSS and ZnO intermediate layers, 2nd active layer and finally, a layer of butanol, testing the effect of a wet film that is not a solvent for the underlying layers. The position of the *100* reflection from P3HT corresponding to the lamellar stacking is marked in the scattering pattern of the 1st active layer.

resistance, allowing the fabrication of working tandem cells, while keeping the optical and electrical performance high. This intermediate layer, together with a range of other combinations were previously reported,[18] however with homo-cell tandem devices, illuminated from both front and bottom side, leading to the transparency of the recombination layer not being probed. Herein we demonstrate the performance which can be achieved with single sided illumination, where the true nature of the tandem cell is employed, with the high band gap front cell absorbing the high energy photons and the low band gap back cell absorbing the low energy photons, using only R2R compatible methods and materials. One of these cells was analyzed by high resolution X-ray phase contrast imaging, as discussed below.

2.2. Ptychographic X-Ray Imaging of a Multilayer Stack

Ptychography was developed for electron diffraction by Hoppe in 1969[21–23] as a method for improving spatial resolution beyond the limitations of probe size, and has subsequently been adapted for visible light[24] and X-ray microscopy.[25] The principle of ptychography is to collect the far-field diffraction patterns from the sample, illuminated by a localized coherent probe in a large number of overlapping steps, thus introducing a redundancy in the data set by oversampling, which is exploited to recover the phase information by iterative algorithms. Since the first theoretical work of Hoppe, the practical implementations awaited solutions to the computational problems of collecting, handling and analysing the large volumes of data that are required.[26,27] With this method, we obtain the complex-valued projections of phase shifts through an extended sample, i.e. the usual requirement of coherent diffractive imaging that the entire sample is illuminated by the coherent beam, is lifted. By combining phase projections from different angles, we obtain the 3D distribution of X-ray refractive indices which is directly related to electron density.[28] After the first practical demonstrations with hard X-rays, the development has been rapid and widespread and the technique is now available at many synchrotron beam lines. The penetration of hard X-rays allows a versatility of the technique that lends itself to material science while providing the capability for 3D imaging at very high spatial resolution[29] and the first applications in this field has recently appeared.[30,31]

Sample preparation is critical for the success of the approach and today it is possible to robustly make excerpts from a flexible organic film using FIB. Because of the small spatial extent (250 nm) of the highly coherent X-ray beam used for ptychographic illumination,[32] the sample must be relatively small to avoid exceedingly long data acquisition time for the many overlapping projections. The FIB technique allows the preparation of a sample prism, cut out from the actual completed solar cell, of a few microns in side length, ideal for 3D imaging. The sample can be manipulated in the FIB microscope and fixed to a macroscopic sample holder for tomography. The functional tandem solar cell devices were prepared on a previously reported mini roll coater.[33,34]

X-ray ptychographic tomography were performed on a sample of the tandem cell stack to resolve the many layers of the tandem cell stack and confirm the limited mixing between the individually coated layers. The use of the X-ray ptychography technique allowed a high spatial resolution of the layers, as seen by the reconstructed projection shown in **Figure 2**A. This powerful analytical tool combined with the in situ analysis of the film formation using GISAXS was thus used to develop the process of the full coated and printed organic tandem solar cells comprising 12 layers (Figure 2B). The good performance of the device, based on the Flextrode substrate[5] is remarkable, considering the highly porous structure of the silver front electrode (Figure 2C). The 3D analysis shows however, that the porous electrode structure is efficiently filled by rotary screen

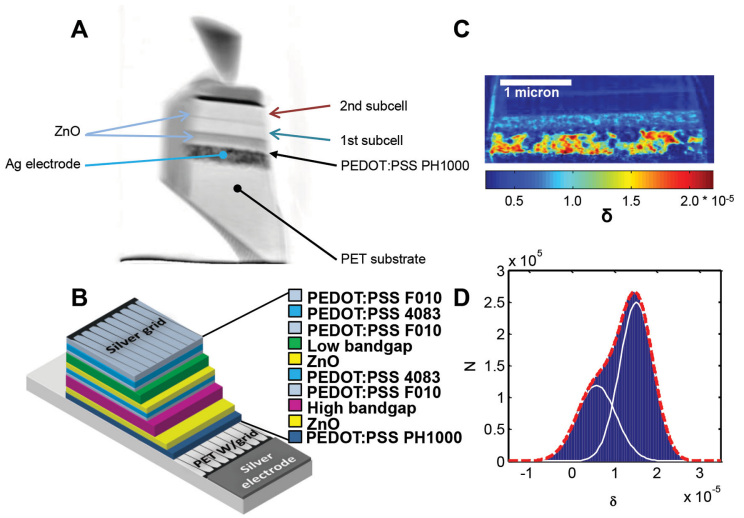

Figure 2. A) Ptychographic phase contrast projection of the polymer tandem solar cell stack. B) Schematic layout of the stack, showing the required layers for a full working cell. C) Vertical slice through the 3D reconstruction of the real part of the X-ray refractive index showing the highly porous structure of the bottom silver electrode, with the well-defined overlying polymer and ZnO layers. The thin, faint line through the top part of the cell, is the trace of the ZnO recombination layer, less than 40 nm thick, but clearly defined. D) Histogram of refractive indices in the reconstructed silver electrode volume fitted by two Gaussian functions corresponding to silver and PEDOT:PSS, showing the very high porosity with just 60% of the electrode volume occupied by solid silver. The void space is filled by matter with a refractive index that matches PEDOT:PSS.

printed PEDOT:PSS, forming a smooth surface for the coating of the subsequent layers (Figure 2C,D).

The materials used in these studies for tandem preparation and analysis (**Figure 3**A) are the high band gap polymer **P1** and the low band gap polymer **P2** together with the acceptor molecule PCBM. The polymers **P1** and **P2** have an optical band gap of 1.97 eV and 1.45 eV, respectively. Because the transmission of the Flextrode substrate is lower for the longer wavelength light (Figure 3C,D), the optimum band gap combination, as described by Ameri et al., is moved, requiring either a higher high band gap material or a tailoring of the high band gap subcell thickness.

2.3. Device Performance

The performance of the tandem cells presented herein (Figure 3B) shows a high efficiency when compared to the efficiency of the produced single junction reference cells based on the two polymers used as high and low band gap sub-cells. The efficiency may seem low compared to the present 11–12% records for the organic photovoltaic (OPV) field,[11] however taking into account the scalable fabrication methods used, the 2.67% efficiency of the tandem cell is indeed very satisfactory. Even more so, because the device is made on a flexible substrate, which as shown previously leads to a reduced light intensity reaching the active layer and thereby a reduced maximum efficiency.

Considering the performance parameters of the tandem cell, the combination of the two sub cells shows an open circuit voltage of 1.32 V, which compared to the sum of the reference cells of 1.44 V is a reduction of 8.3%. The maximum current output of the solar cell is reduced from 5.4 mA cm^{-2} and 4.9 mA cm^{-2} for the individual reference cells to 4.3 mA cm^{-2} for the tandem cell. This compares well with maximum theoretical current for a tandem cell being limited by current matching of the individual cells causing the tandem cell in this case to be limited by the low band gap cell, with a further small loss due to the overlapping between the absorption spectrum of the two polymers. The small drop in voltage and current is a confirmation of the electrical function of the intermediate layer, while all the cells tested showed a performance ranging from 2.4% to 2.67% indicating a strong reproducibility and solvent resistance quality in the coated stack. In total 60 cells were coated, with 10% of the cells tested. The tested cells were chosen evenly along the coated stripe to sample the performance within the full batch.

3. Conclusion

A fully roll coated tandem polymer solar cell has been shown, fabricated using only large scale compatible processes on flexible substrate and with a performance which surpasses the performance of the reference cells produced from the individual polymers. We showed with in situ X-ray structural characterization of the coating process that the exact formulation of the intermediate recombination layer is critical for preserving the structural integrity of the bottom sub cell and thus the

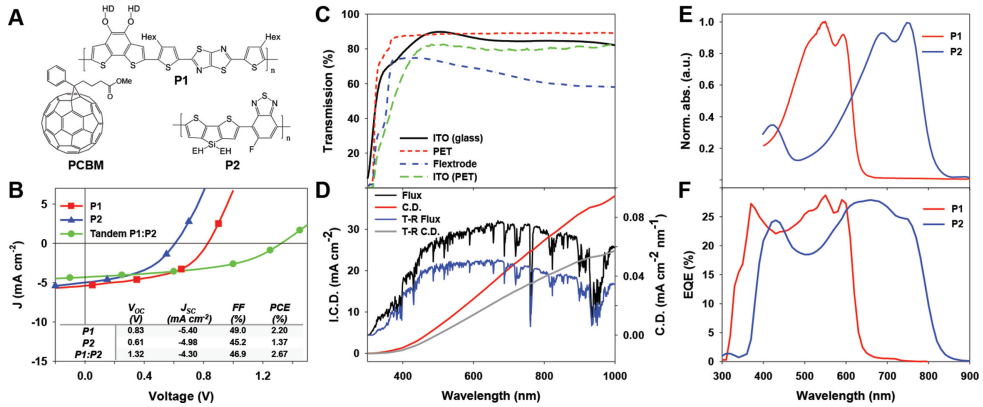

Figure 3. A) Structure of the high and low band gap polymers **P1** and **P2** and PCBM. B) *J–V* curves and performance numbers for reference cells of the two polymers and for the tandem cell produced from polymers **P1** and **P2**. C) Transmission measurements of different substrates, relative to air; ITO on glass, neat polyethylene terephthalate (PET) foil (Melinex), Flextrode on PET (Melinex) and ITO on PET, (Melinex). D) Solar spectrum at AM1.5G (Flux) and solar spectrum convoluted with the transmission of the Flextrode substrate (T-R Flux). The integrated current densities (I.C.D.) for the AM1.5G spectrum (C.D.) and the Flextrode transmission reduced spectrum (T-R C.D). E) Normalized absorption spectra of the polymers **P1** and **P2**. The absorption spectra show the complementarity of the two polymers, indicating their suitability for tandem cells. F) EQE measurement of devices prepared from **P1** or **P2** in a mixture with PCBM.

performance of the device. The successful formation of all the layers was documented with high resolution X-ray phase contrast imaging of the completed multilayer stack.

4. Experimental Section

Materials: P3HT and PCBM were purchased from Plextronic and Merck or Solenne BV., respectively. **P1** and **P2** were synthesized in house via Stille coupling by known routes of synthesis first reported by Hou et al.[35] and Carlé et al.[12] PEDOT:PSS Clevious P VP AL 4083 and PEDOT:PSS Clevious F010 were purchased from Heraeus Materials GmbH.

Inks: Inks for the polymer blends were made by mixing polymer and PCBM and adding solvents. **P1**:PCBM ink was made in a 5:10 mg mL^{-1} solution of chlorobenzene for tandem coating and 8:16 mg mL^{-1} for reference cells. **P2**:PCBM ink was made in a 8:12 mg mL^{-1} solution of chloroform for tandem coating and 16:24 mg mL^{-1} for reference cells. PEDOT:PSS 4083 was mixed with isopropanol in a 1:2 volume ratio. F010 used as compatibilizer for PEDOT:PSS 4083 was mixed with isopropanol in a 1:4 volume ratio (and referred to as F40 in the text) and F010 used as hole conducting electrode was mixed with isopropanol in a 2:1 volume ratio (referred to as F20). Zinc oxide (ZnO) ink was prepared as described in Hagemann et al.[36]

Device Fabrication: Tandem cell devices were fabricated on preprinted Flextrode substrate, with a series of coatings consisting of 1) front cell (high-bandgap) coated from **P1** ink at 13 µm wet layer thickness, 2) PEDOT:PSS F40 wetting layer ink at 8 µm wet layer thickness, 3) PEDOT:PSS 4083 hole selective layer at 23 µm wet layer thickness, 4) zinc oxide layer at 5 µm wet layer thickness, and 5) back cell (low-bandgap) **P2** ink at 15 µm wet layer thickness. The cells were completed with 6) PEDOT:PSS F40 wetting layer ink at 8 µm wet layer thickness, 7) PEDOT:PSS 4083 hole selective layer at 23 µm wet layer thickness, 8) PEDOT:PSS F20 top electrode with a wet thickness of 38 µm, and 9) silver top electrode flexographically printed with a web speed of 1.3 m min^{-1}. A full table of coating parameters and estimated dry thicknesses can be found in the Supporting Information, together with images of the cells from front and rear.

Reference single junction cells were fabricated using similar conditions, with the Flextrode substrate and a wet layer coating thickness of 14 µm and 12 µm for **P1** and **P2**, respectively. After coating of the active layer, the cell was finished with layers 6–9.

X-Ray Scattering Experiments: In situ small angle X-ray scattering (SAXS) experiments during coating of the device layers were carried out on a custom SAXS setup, using a rotating anode as source, operated at 40 kV, 40 mA in fine focus (200 µm source size), focused and monochromatized (wavelength 1.5418 Å) by a 2D multilayer, and collimated by 3 pinholes to a 1 mm beam diameter at the sample. The sample was illuminated at a position close to the drying front in a series of 100 s exposures while the substrate was moved from one roll to the other at a speed of 0.5 m min^{-1}, at 0.35° X-ray incidence angle. The SAXS data were acquired with a 2D delay line gas proportional detector.[37]

For the ptychographic imaging, experiments were conducted at the P06 beam line at PETRA III in Hamburg with an intensity of 8×10^6 photons s^{-1} in a 250 nm beam, focused by silicon nano-focusing lenses[38] with a 2.0 m sample-detector distance. Ptychography projections were taken at 90 projections over 180° projection angles with a 4.1 × 1.8 µm field of view and an approximately 22 min. accumulation period per projection with 560 overlapping illuminations. The ptychographic reconstruction software provided at the P06 beam line, implemented by Robert Hoppe, was used. The tomographic reconstruction was done with MATLAB code developed by Manuel Guizar-Sicairos.[28]

Supporting Information

Supporting Information is available from the Wiley Online Library or from the author.

Acknowledgements

H.F.D. and T.R.A. contributed equally to this work. This work received financial support from the European Commission as part of the Framework 7 ICT 2009 collaborative project ROTROT (grant no. 288565),

Eurotech Universities Alliance project "Interface science for photovoltaics (ISPV)", European Research Infrastructure (SOPHIA) and European Energy Research Alliance (EERA) are acknowledged for the support. This work was supported by Danish National Research Foundation, the Villum Foundation's Young Investigator Programme (2nd round, project: Materials for Energy Production) and The Danish Council for Strategic Research (project WAPART, j.no. 11–116380). Partial financial support was also received from the Danish Council for Independent Research, Technology and Production Sciences (project nr. 11–116864), the Danish Ministry of Science, Innovation and Higher Education under a Sapere Aude Top Scientist grant (no. DFF – 1335–00037A) and an Elite Scientist grant (no. 11–116028). Travel support for the synchrotron experiments was provided through the DANSCATT grant from the Danish Council for Independent Research | Natural Science (no. 12–130893). The authors gratefully acknowledge Torben Kjær for technical assistance with construction of the R2R X-ray coater, and Markus Hösel for assistance with preparation of graphics for the figures.

Received: May 2, 2014
Revised: August 4, 2014
Published online:

[1] T. R. Andersen, H. F. Dam, M. Hösel, M. Helgesen, J. E. Carlé, T. T. Larsen-Olsen, S. A. Gevorgyan, J. W. Andreasen, J. Adams, N. Li, F. Machui, G. D. Spyropoulos, T. Ameri, N. Lemaître, M. Legros, A. Scheel, D. Gaiser, K. Kreul, S. Berny, O. R. Lozman, S. Nordman, M. Välimäki, M. Vilkman, R. R. Søndergaard, M. Jørgensen, C. J. Brabec, F. C. Krebs, *Energy Environ. Sci.* **2014**, DOI: 10.1039/C4EE01223B.
[2] P. Sommer-Larsen, M. Jørgensen, R. R. Søndergaard, M. Hösel, F. C. Krebs, *Energy Technol.* **2013**, *1*, 15.
[3] F. C. Krebs, M. Hösel, M. Corazza, B. Roth, M. V. Madsen, S. A. Gevorgyan, R. R. Søndergaard, D. Karg, M. Jørgensen, *Energy Technol.* **2013**, *1*, 378.
[4] Plasticphotovoltaics, www.plasticphotovoltaics.com (accessed December 2013).
[5] M. Hösel, R. R. Søndergaard, M. Jørgensen, F. C. Krebs, *Energy Technol.* **2013**, *1*, 102.
[6] N. Espinosa, R. García-Valverde, A. Urbina, F. C. Krebs, *Sol. Energy Mater. Sol. Cells* **2011**, *95*, 1293.
[7] M. C. Scharber, N. S. Sariciftci, *Prog. Polym. Sci.* **2013**, *38*, 1929.
[8] Neuer Weltrekord für organische Solarzellen: Heliatek behauptet sich mit 12% Zelleffizienz als Technologieführer. http://www.heliatek.com/newscenter/latest_news/neuer-weltrekord-fur-organische-solarzellen-heliatek-behauptet-sich-mit-12-zelleffizienz-als-technologiefuhrer/ (accessed December 2013.)
[9] J. You, L. Dou, K. Yoshimura, T. Kato, K. Ohya, T. Moriarty, K. Emery, C.-C. Chen, J. Gao, G. Li, Y. Yang, *Nat. Commun.* **2013**, *4*, 1446.
[10] J. You, C.-C. Chen, Z. Hong, K. Yoshimura, K. Ohya, R. Xu, S. Ye, J. Gao, G. Li, Y. Yang, *Adv. Mater.* **2013**, *25*, 3973.
[11] M. A. Green, K. Emery, Y. Hishikawa, W. Warta, E. D. Dunlop, *Prog. Photovolt. Res. Appl.* **2014**, *22*, 1.
[12] J. E. Carlé, M. Helgesen, M. V. Madsen, E. Bundgaard, F. C. Krebs, *J. Mater. Chem. C* **2014**, *2*, 1290.
[13] A. Hadipour, B. de Boer, J. Wildeman, F. B. Kooistra, J. C. Hummelen, M. G. R. Turbiez, M. M. Wienk, R. A. J. Janssen, P. W. M. Blom, *Adv. Funct. Mater.* **2006**, *16*, 1897.
[14] G. Dennler, M. C. Scharber, T. Ameri, P. Denk, K. Forberich, C. Waldauf, C. J. Brabec, *Adv. Mater.* **2008**, *20*, 579.
[15] G. Dennler, M. C. Scharber, C. J. Brabec, *Adv. Mater.* **2009**, *21*, 1323.
[16] N. Li, T. Stubhan, D. Baran, J. Min, H. Wang, T. Ameri, C. J. Brabec, *Adv. Energy Mater.* **2013**, *3*, 301.
[17] T. T. Larsen-Olsen, T. R. Andersen, B. Andreasen, A. P. L. Böttiger, E. Bundgaard, K. Norrman, J. W. Andreasen, M. Jørgensen, F. C. Krebs, *Sol. Energy Mater. Sol. Cells* **2012**, *97*, 43.
[18] T. R. Andersen, H. F. Dam, B. Andreasen, M. Hösel, M. V. Madsen, S. A. Gevorgyan, R. R. Søndergaard, M. Jørgensen, F. C. Krebs, *Sol. Energy Mater. Sol. Cells.* **2014**, *120, Part B*, 735.
[19] N. Li, D. Baran, K. Forberich, F. Machui, T. Ameri, M. Turbiez, M. Carrasco-Orozco, M. Drees, A. Facchetti, F. C. Krebs, C. J. Brabec, *Energy Environ. Sci.* **2013**, *6*, 3407.
[20] A. P. L. Böttiger, M. Jørgensen, A. Menzel, F. C. Krebs, J. W. Andreasen, *J. Mater. Chem.* **2012**, *22*, 22501.
[21] W. Hoppe, *Acta Crystallogr. Sect. A* **1969**, *25*, 495.
[22] W. Hoppe, G. Strube, *Acta Crystallogr. Sect. A* **1969**, *25*, 502.
[23] W. Hoppe, *Acta Crystallogr. Sect. A* **1969**, *25*, 508.
[24] J. M. Rodenburg, A. C. Hurst, A. G. Cullis, *Ultramicroscopy* **2007**, *107*, 227.
[25] J. M. Rodenburg, A. C. Hurst, A. G. Cullis, B. R. Dobson, F. Pfeiffer, O. Bunk, C. David, K. Jefimovs, I. Johnson, *Phys. Rev. Lett.* **2007**, *98*, 034801.
[26] J. M. Rodenburg, H. M. L. Faulkner, *Appl. Phys. Lett.* **2004**, *85*, 4795.
[27] M. Guizar-Sicairos, J. R. Fienup, *Opt. Express* **2008**, *16*, 7264.
[28] M. Guizar-Sicairos, A. Diaz, M. Holler, M. S. Lucas, A. Menzel, R. A. Wepf, O. Bunk, *Opt. Express* **2011**, *19*, 21345.
[29] .M. Holler, A. Diaz, M. Guizar-Sicairos, P. Karvinen, E. Färm, E. Härkönen, M. Ritala, A. Menzel, J. Raabe, O. Bunk, *Sci. Rep.* **2014**, *4*, 3857.
[30] M. Esmaeili, J. B. Fløystad, A. Diaz, K. Høydalsvik, M. Guizar-Sicairos, J. W. Andreasen, D. W. Breiby, *Macromolecules* **2013**, *46*, 434.
[31] B. Chen, M. Guizar-Sicairos, G. Xiong, L. Shemilt, A. Diaz, J. Nutter, N. Burdet, S. Huo, J. Mancuso, A. Monteith, F. Vergeer, A. Burgess, I. Robinson, *Sci. Rep.* **2013**, *3*.
[32] A. Schropp, R. Hoppe, J. Patommel, D. Samberg, F. Seiboth, S. Stephan, G. Wellenreuther, G. Falkenberg, C. G. Schroer, *Appl. Phys. Lett.* **2012**, *100*, 253112.
[33] H. F. Dam, F. C. Krebs, *Sol. Energy Mater. Sol. Cells* **2012**, *97*, 191.
[34] J. E. Carlé, T. R. Andersen, M. Helgesen, E. Bundgaard, M. Jørgensen, F. C. Krebs, *Sol. Energy Mater. Sol. Cells* **2013**, *108*, 126.
[35] J. Hou, H. Y. Chen, S. Zhang, G. Li, Y. Yang, *J. Am. Chem. Soc.* **2008**, *130*, 16144.
[36] O. Hagemann, M. Bjerring, N. C. Nielsen, F. C. Krebs, *Sol. Energy Mater. Sol. Cells* **2008**, *92*, 1327.
[37] A.-M. Petrascu, M. H. J. Koch, A. Gabriel, *J. Macromol. Sci. Part B* **1998**, *37*, 463.
[38] C. G. Schroer, O. Kurapova, J. Patommel, P. Boye, J. Feldkamp, B. Lengeler, M. Burghammer, C. Riekel, L. Vincze, A. van der Hart, M. Küchler, *Appl. Phys. Lett.* **2005**, *87*, 124103.

Submitted to Energy and Environmental Science RSCPublishing

ARTICLE

Structure and crystallinity in water dispersible photoactive nanoparticles for organic solar cells

Cite this: DOI: 10.1039/x0xx00000x

E. B. L. Pedersen[a], M. C. Pedersen[b], S. B. Simonsen[a], R. G. Brandt[c], A. P. L. Böttiger[a], T. R. Andersen[a], W. Jiang[d], X. Zhiyuan[d], F. C. Krebs[a], L. Arleth[b] and J. W. Andreasen[a].

Received 00th January 2012,
Accepted 00th January 2012

DOI: 10.1039/x0xx00000x

www.rsc.org/

Water based inks would be a strong advantage for large scale production of organic photovoltaics. Formation of water dispersible nanoparticles produced by the Landfester method is a promising route to achieve such inks. We provide new insights into key ink properties for poly(3-hexylthiophene) (P3HT) and [6,6]-phenyl-C61-butyric acid methyl ester (PCBM) nanoparticles such as internal structure and crystallinity of the dispersed nanoparticles and the previously unreported drastic changes that occur when the ink is cast into a film. We observe through Transmission Electron Microscopy (TEM) and small angle X-ray scattering (SAXS) that the nanoparticles in dispersion are spherical with nano domains of P3HT – partly crystalline. When wet processed and dried into films the nanoparticles lose their spherical shape and become flattened to oblate shapes with a large aspect ratio. Most particles are observed to have a diameter 13 times of the particle height. After casting to a film the crystal domains adopt a preferred orientation with the majority of the nano crystals (68%) with face-on orientation to the substrate. We propose that low substrate surface energy is responsible for particle deformation and texturing.

Broader context

Polymer solar cells have demonstrated power conversion efficiencies comparable to what can be achieved with other thin-film technologies, but some issues with respect to environmental impact remain to be addressed. Photoactive nano-particles in aqueous dispersion have been envisioned as an effective way of dispensing with the use of toxic and environmental harmful solvents in the coating process of polymer solar cells. Preforming the donor/acceptor blend in nanoparticles that are dispersed in water allows for use of only aqueous or alcohol-based inks for coating, while at the same time providing a means of controlling the nano-structure of the heterojunction. We show that the nano-particles are very sensitive to the type of coating method and substrate surface energy, and that an otherwise optimal nano-structure may be compromised during coating by phase separation. Our results indicate that focusing the development effort on other types of stabilizing surfactants may provide the means to control phase separation and thus the formation of optimal nano-structure in roll-to-roll coated, environmental friendly polymer solar cells.

Introduction

Looking for alternative energy sources to reduce human dependence on fossil fuels and to promote a move towards societies powered by clean renewable energy, solar energy has by far the greatest potential[1,2]. Traditional silicon based solar technology is not competitive in energy price and face additional challenges in long energy payback time and recycling issues[3]. Organic PhotoVoltaics (OPV) is a promising group of solar technologies based on thin films of organic molecules, and has advantages of low energy payback time due to fast scalable roll-to-roll processing, use of small amounts of abundant materials in thin films and low temperature production[4,5]. Recently, the large scale deployment of organic solar cells has been demonstrated showing an advantage in scalability, but also highlighting the need for further research[6].

One of the areas of development is the active material itself. The active layer in OPV is typically cast from toxic chlorinated organic solvents. Production can be improved by switching to water based inks and thereby not having to deal with toxic and flammable fumes. Water based inks can also be coated simultaneously with interface layers like PEDOT:PSS as demonstrated through double slot dye coating[7].

There has been work on making water-soluble polymers which unfortunately have shown low energy conversion effeciency[8]. Another approach is to use a surfactant to preprocess the polymers into water dispersible nanoparticles with the Landfester method[9]. This method also causes a drop in energy conversion efficiency[10], indicating the challenge in taking proven materials and transforming them into water based inks. If successful, a Landfester method would

reduce the chloroform use to 45% of current solution based methods, and with the addition of a condenser, a closed loop system can be formed, where the chloroform is recycled and there is no ongoing consumption of chloroform.

Poly(3-hexylthiophene) (P3HT) and [6,6]-phenyl-C61-butyric acid methyl ester (PCBM) is a well-established active layer mixture. Surfactant free P3HT-PCBM nanoparticles have also been pursued[11] even with a high power conversion efficiency of 4%[12]. However, the high efficiency is not achieved by coating from water dispersion but with ethanol as the dispersion medium. The long term stability of these alcoholic nanoparticle dispersions has yet to be demonstrated but more importantly there is a need to understand the mechanism of film formation and morphology evolution from these nanoparticles to facilitate the development of water based inks that yield efficient performance when processed into solar cells. This calls for additional characterization of the nanoparticles themselves and the layers formed from them.

Dastoor et al. performed a number of studies on OPV relevant nanoparticles and found a number of interesting effects[11,13–16]. The ideal thickness of the film is quite thin (but comparable to bulk material), about 300 nm, and with careful annealing the surfactant appears to be removed from the connecting interfaces[15]. The internal structure of large Landfester particles (on the order of 150 nm diameter) has been found to be a core shell structure that grows upon annealing[13–16]. The large particles are a good model system but undesirable for application in OPV because they limit the active layer to only 1-2 particles in thickness, which yield very inhomogeneous layers, poor films and a high risk of electric short circuits when processed into complete final devices. In practice the particle size in water based inks used for fabricating devices are on the order of 20-50 nm in radius[15] and so far there only exist rough qualitative assessments regarding their internal structure[17].

Direct microscopy methods such as Scanning Transmission X-ray Microscopy have difficulties reaching resolutions of sub 10 nm even though development of soft X-ray ptychography has enabled 5 nm spatial resolution and 18 nm chemical resolution[18]. Scattering techniques such as Small Angle X-ray Scattering (SAXS) are capable of resolving smaller length scales but probes the entire illuminated population of nanoparticles. With such a technique no information of the individual particles is gained, but rather ensemble information. Furthermore, a suitable structural model must be formulated to extract information from the SAXS patterns. In the literature, there already exists a number of structural models for nanoparticles and their internal structure such as homogenous spheres and core-shell particles[19]. There has also been formulated general models to describe complex internal structures such as the Teubner-Strey description of microemulsions[20]. In conclusion, SAXS appears as an attractive method to quantify the average internal structure of Landfester nanoparticles relevant for OPV.

Another parameter which has so far not been touched upon in the analysis of OPV relevant nanoparticles is crystallinity. Compared to a bulk material the confinement of the polymer can reduce the crystallinity as seen in other systems[21], where also sonication[22] and surfactant parameters[23] affect crystallinity. This is particularly interesting in the context of OPV where materials crystallinity has been found to correlate with device current[24] – a parameter normally reduced in nanoparticle devices[16]. Crystallinity can easily be measured with X-ray diffraction. From X-ray diffraction structural information like the crystal domain size[25,26] and crystal orientation can be extracted. P3HT is in particular known to assume two orientations either face-on (side chains aligned parallel to the substrate) or edge-on (side chains aligned perpendicular to the substrate). With the crystal domains confined in the spherical nanoparticles one would expect random orientation of the crystal domains.

In this manuscript we use SAXS to characterize the internal structure of P3HT-PCBM Landfester particles with relevant diameters on the order of 20 nm for the first time. Furthermore, we investigate crystallinity of the particles in the aqueous dispersion and when cast into film and dried, supplemented by Atomic Force Microscopy (AFM) measurements to confirm drastic structural changes in the particles during casting and drying.

Results and discussion

In the following sections we first introduce the characterization of the nanoparticles in water dispersion. Afterwards we present the results for the film formation and link it to the characterization of internal particle structure.

Nanoparticles in dispersion

For the water based nanoparticle inks, the structural characterization falls into three categories, the particle size distribution, internal size distribution and crystal domain size. For the majority of these efforts we will study P3HT:PCBM 1:1 (mass ratio) Landfester particles. The particle size distribution is characterized with dynamic light scattering (DLS), transmission electron microscope (TEM) and SAXS using different models for internal structure as shown in figure 1. Both SAXS models and the TEM measurements agree on the size distribution as a log-normal distribution with the median around 8 nm. The samples contain a small fraction of aggregated nanoparticles in the dispersion, which complicates the DLS measurements. A traditional second order cumulant analysis fit to the correlation function gives a size distribution with an average hydrodynamic particle radius that is about 10 nm larger than observed through the other methods. However, a double exponential fit reveals two main populations: 97% volume fraction with a radius of 8.9 nm (in agreement with the SAXS and TEM measurements) and 3% volume fraction with a radius of around 40 nm. The two populations of the double exponential fit is consistent with the findings through a free form Contin analysis (results not shown). The DLS size distribution extracted with second order cumulant analysis try to accommodate both populations, which leads to an overestimation of particle size and poor fits to the correlation function. Landfester particle sizes reported only based on DLS using second order cumulant analysis should therefore be reconsidered as the true particle sizes might be smaller.

Crystallinity. In X-ray studies of the dispersed nanoparticles, we observe the P3HT 100 reflection, corresponding to lamellar packing[27] as shown in figure 2A. We tested the crystal behaviour in 3 kinds of nanoparticles and found a peak at 0.39 $Å^{-1}$ in particles of pure P3HT and 0.38 $Å^{-1}$ in particles containing P3HT:PCBM 1:1 by weight (figure 2). With P3HT:PCBM 1:7 particles (12.5 weight % P3HT) no crystal domains are formed. Similar observations have been reported for bulk mixtures with minimum P3HT fractions from 10 to 30% required for formation of crystalline P3HT domains[28,29]. From the width of the diffraction peak the average crystal domain size is determined by the Scherrer equation, as shown in **table 1**. With a P3HT 100 lattice spacing of 1.60 - 1.64 nm the number of molecules in the average crystalline domain is found to be about 3 molecules in the mixed particles and 5 molecules in the pure P3HT particles, along the 100 direction. The overall P3HT crystallinity decreases by a factor of 2.7 when mixed with PCBM (ratio between integrated diffraction signal when comparing P3HT:PCBM 1:1 to the pure P3HT particles).

The water dispersed nanoparticles already contain nanometer-sized crystal domains and are therefore to some degree already phase separated unlike the solution based inks. Optimal device morphology requires a high degree of intermixing of active layer materials, since the exciton diffusion length is only about 10 nm[30]. Phase separation in the water-based ink can be problematic, because annealing can increase the domain size significantly above the exciton diffusion length. Domain sizes in annealed Landfester nanoparticles have previously been shown to increase above the initial particle size[16]. Devices cast from solution based inks have also shown decreases in power conversion efficiency after long annealing times (60 min) due to phase separation of the active layer material[31].

Internal structure. To investigate the precise internal nanoparticle structure we employ a more detailed modelling of the full SAXS patterns for the particles shown in figure 2. For this purpose, we developed two scattering models of mixtures of P3HT:PCBM particles: A geometric core-shell model as previously reported[19] and a more abstract Teubner-Strey model which describe internal structure by a characteristic domain size and correlation length[20]. The fundamental mathematical expression is the form factor amplitude of a sphere (see e.g. Pedersen[32] for details on establishing geometric models of small-angle scattering). It is used to describe the scattering from the core and shell of the particles, the layer describing the hydrophobic SDS-tail, and an outer layer describing the hydrophilic SDS-headgroups.

In the model, we implement so-called molecular constraints in the model in order to minimise the number of refined parameters in the structural model. As an example, the scattering length density of the SDS-layers is kept consistent with the molecular properties of SDS rather than refining this quantity from the data.

We implemented a polydispersity of the particles in our model in order to accommodate the inherent dispersion in the particle size arising from the applied self-assembly procedure. This was done by numerical integration over a log-normal volume-weighted distribution of the radius of the core-shell-structure describing the P3HT:PCBM particles.

As shown in figure 2, the simple model for polydisperse core-shell-like particles fails to adequately reproduce the features of the data. For this reason, we instead use a homogenous sphere and included a contribution to the scattering arising from an emulsion-like domain structure as described by Teubner and Strey[20].

Furthermore, in order to fit the 100-peak of P3HT, a Gaussian was added to the final model in order to capture the crystalline diffraction from the P3HT.

Mathematically, we can write the final model as:

$$\begin{aligned} I(q) &= I(q)_{\text{Teubner-Strey}} + I(q)_{\text{Diffraction peak}} + I(q)_{\text{Particles}} \\ &= \frac{C_{\text{Teubner-Strey}}}{a_2 + c_1 q^2 + c_2 q^4} + C_{\text{Diffraction peak}} \cdot e^{-\frac{(\mu_D - q)^2}{2\sigma_D^2}} \\ &\quad + \int_0^\infty dR\ \Phi(\mu, \sigma, R) \cdot I(q, R)_{\text{Particle}} \end{aligned}$$

where a_2, c_1, and c_2 are the coefficients in the Teubner-Strey-model, μ_D and σ_D are the coefficients for the Gaussian describing the diffraction peak, $\Phi(\mu, \sigma, R)$ is the aforementioned size distribution, and I(q, R) is the four-shell form factor describing the scattering intensity from a P3HT:PCBM-particle described by the radius, R, as elaborated above. Finally, $C_{\text{Teubner-Strey}}$ and $C_{\text{Diffraction peak}}$ provide the relative scales for the different contributions. Note that we assume that the Teubner-Strey domains and the particle sizes are on different length scales and that we can therefor omit the crossterms, as the scattering contributions from these decouple.

The analysis was performed using the WillItFit-framework[33], and the source code for the presented models has been made available in the code repository of this software.

In the fits in figure 2, we have assumed that the polydispersity of the sample can be described as a lognormal-distribution. As part of this study, we also attempted to fit alternative distributions to the same data (e.g. a normal- and Schultz-distribution), and can report that this does not significantly change the fit or the overall refined structure.

As mentioned, the distribution from the final model shown in red in figure 1 is a log-normal distribution of the radii of the P3HT:PCBM-particles described by the median, m, and variance, s^2 :

$$m = 83.9\ Å \qquad s^2 = 0.21$$

We emphasise that the distribution describes the radii of the P3HT:PCBM-structure. In the model, the layer of SDS has a radius of 9.7 Å.

The inclusion of the Teubner-Strey-term describing the emulsion-like internal structure appears to be necessary in order to adequately describe the shoulder in the data around 0.09 $Å^{-1}$ and is consistent with the general view of the internal segregation of P3HT and

PCBM[17], which would indeed be a prerequisite for the crystallinity exhibited by Landfester-particles.

From the refined parameters describing the Teubner-Strey-emulsions, one can deduce the characteristic correlation length, ξ, and the characteristic domain size, d, respectively. From the parameters describing the fit shown in figure 2, we can calculate these quantities:

$$\xi = 31.3\ \text{Å} \qquad d = 83.0\ \text{Å}$$

These values correspond well to the length-scale of the P3HT-crystallites, which was established from the width of the peak in the high-q region of the data. It is possible that the shoulder around 0.09 $Å^{-1}$ can be attributed to the small-angle scattering signal from the P3HT-domains in the Landfester-particles or PCBM rich domains in a P3HT mixture.

Other work mainly employing energy resolved X-ray absorption have found core-shell structures inside Landfester nanoparticles[13,16,34]. For those experiments the investigated Landfester particles were about ten times the size (radius of $\geq$ 100 nm) compared to the particles investigated in this manuscript. It is therefore not unlikely that the internal structure could be different for those two cases. However, these big particles are less interesting for organic solar cell wherein the whole active layer is only hundreds of nanometer thick.

Experiments by Richards et al.[17] used neutron scattering to select between five models for internal structure. For particles with radius of about 65 nm they also found core-shell structure inspired by Ulum et al.[16]. Given the uncertainties in the data points it is unclear how strongly they exclude their other choices of models or more advanced models. With the Teubner-Strey model it is for instance entirely possible that the many nano domains are located primarily in the centre, where they are separated by 2-3 nanometers.

The mass fraction of SDS was estimated to be less than 20% and NMR experiments confirmed that the particles themselves contained no residues of chloroform (see supporting information). SDS will naturally be detrimental to the photoelectric performance of a device, but since even the state of the SDS molecules could be changed due to hydrolysis[35] it is difficult to estimate.

Nanoparticles cast as films

Our interest is to follow the precise nanoparticle morphology when the particles are cast into a wet film that is then dried and we therefore only work with single particles and particle monolayers. To investigate the spatial particle structure we employ Atomic Force Microscopy (AFM) and scan single particles spin cast on a mica substrate. The nanoparticles have a tendency to form small aggregates and connected snakelike structures on the substrate, so the particle concentration was reduced to 6 mg/L to achieve isolated particles.

The particle height and diameter were systematically extracted from the AFM images and are shown in figure 3. The particle diameter was found to be about 13 times the particle height indicating that particles are smeared out along the substrate as part of the coating process. Similar deformation were also observed for particles dropcast on mica. Our hypothesis is that the particles are soft enough to undergo a drastic deformation regardless of coating procedure (dropcast, spincast or roll-to-roll coating). We envision the transformation as spherical particles turning into deformed disk like structure upon contact with a substrate surface with sufficient low surface energy like mica or zinc oxide, but not deforming on surfaces with high surface energy such as carbon films on TEM grids.

In the experiments we were concerned that the AFM tip might contribute to the particle deformation. This effect was tested by successively scanning the same area, and verifying that reproducible particle dimensions were obtained. We also wanted to see how tip damage would appear and subjugated a single particle to constant tip scanning for prolonged time. The particle broke up into several isolated pieces suggesting the AFM tip damage would not manifest itself like the observed deformation and contributed little to the measured particle dimensions.

Crystallinity in nanoparticle films. The AFM scans contribute little to the understanding of internal particle structure after the drastic deformation. Grazing incidence wide angle X-ray scattering (GIWAXS) waw employed to investigate the crystalline texture of monolayers of P3HT:PCBM 1:1 nanoparticle cast on float glass substrate. If the structure of the nanoparticles were conserved the P3HT crystal domains would be orientated randomly, and we would expect crystallinity to be independent of substrate angle. However, we see a high degree of edge-on alignment with the substrate even before annealing at 140°C as shown in figure 4. In fact 68% of the P3HT crystal domains are oriented edge-on within ±10 degrees of the substrate normal and this number increase to 91% within ±30 degrees of the substrate normal. Annealing the film at 140°C has little effect on the overall crystal orientation.

The average crystal domain sizes are characterized by the Scherrer equation. A clear orientation dependence and annealing effects on the crystal domain size are observed. The edge-on crystals have about half the domain size of face-on crystals with unannealed sizes of 3 nm and 6 nm, respectively, whereas annealed sizes are 6 nm for the edge-on crystals and about 12 nm for face-on. Annealing causes in most cases approximately a doubling in crystal domain size e.g. from 3 to 6 nm. However, the edge-on crystals appear limited in crystal height to about 6 nm corresponding to the average particle height found in the AFM measurements (5.2 ±1.2 nm).

Compared to the nanoparticles in dispersion, the average crystal size is actually reduced from 5.1 nm to about 3 nm after coating. The shear forces in the particle deformation process actively reduce the average crystal domains size, but annealing at 140°C can restore it to about 6 nm.

Crystallinity in roll-to-roll coated nanoparticles. We have extended our analysis to include roll-to-roll coated films of nanoparticles. Scalable production of organic photovoltaics will use roll-to-roll coating instead of spin coating so our results are mainly interesting if our observation also holds for roll-to-roll coating. GIWAXS data from roll-to-roll coated samples are shown in figure 4. As seen even when coated in thick films the crystal domains of P3HT and PCBM in the nanoparticles have a high degree of texture i.e. non-random orientation. The substrate alignment of P3HT and PCBM crystals are likely due to similar mechanisms as investigated for spin coating where substrates with low surface energies cause particle deformation and rearrangement of the materials. Accelerated drying intermediate heating steps likely also contribute to the deformation.

Even in layers beyond the first, the materials in the nanoparticles align with the surface. The exact material distribution needs to be determined in the future but one could imagine the domains observed in the mono layers continue to grow when subsequent nanoparticles deform on top and increased by annealing. Since the deformation process is not fully understood it is not clear if the layer becomes a massive solid or if a porous structure is formed as the case would be for rigid spheres.

Spatial distribution of P3HT and PCBM in films roll-to-roll coated from Landfester particles. The particle deformation and crystal orientation indicates that the particles are no longer intact in the formed films. We measured the spatial distribution of P3HT and PCBM by scanning a roll-to-roll coated sample at different energies using scanning transmission X-ray microscopy (STXM) as shown in figure 5. The relative distribution of P3HT and PCBM is found by measuring STXM images at energies near the carbon k-absorption edge and fitting linear combinations of known reference spectra like previously described[36]. The relative thickness is found from the optical density above the absorption edge.

In the material distribution, we see that phase segregation domains are larger than the original particle size (~100 nm domains vs ~20 nm particle diameter). In general the PCBM domains also appear to be forming higher peaks than the P3HT. This can be deceiving for methods without chemical contrast since the PCBM domains resemble particles on their own. The overall structure after roll-to-roll coating is therefore not a true monolayer of particles but phase separated material forming a rough surface with islands of PCBM in a homogenous film of P3HT. The large phase separation before any annealing might be a product of early separation into domains within the particles. As the particles are coated, they deform upon contact with the substrate and in the accelerated drying process domains merge to larger domains. Given the observed material redistribution, it is also not surprising that P3HT crystal units decrease in size and show strong alignment with the surface substrate.

The deformation and phase separation are undesirable for OPV since the domain sizes become too large for optimal charge separation. This could be a contributing factor to the lower performance observed for nanoparticle based devices[15,16]. Schematic overviews of the structural changes that the nanoparticle undergo when coated are illustrated in **figure 6**.

As it was apparent that the Landfester particles already have phase separated during roll-coating, devices were prepared where additional phase segregation from annealing was minimized by using a low drying temperature as shown in **table 2**. However, longer drying times at lower temperatures are not feasible for large scale production. The future paths would either be to minimize the deformation using different surfactants and surface modifications or optimize the internal particle structure towards high degree of material mixing that becomes optimal when cast instead of optimizing towards an ideal internal structure that becomes suboptimal when coated.

Experimental

Nanoparticle preparation

The nanoparticles were produce by the Landfester method[9]. 400 mg of active material was dissolved in 30 mL chloroform and mixed with 90 mL 20 g/L SDS in demineralized water. The solution was placed in a water bath and sonicated for 5 min at 500 W with a Hielsher UIP1000hd unit. Chloroform was removed by evaporation at room temperature for 24 hours. Excess SDS was removed in cellulose dialysis tubes (14000 nominal molecular weight limit) with 90 mL nanoparticle dispersion in 3 L demineralized water reservoir for 72 hours with reservoir change every 24 hours. The final dispersion was concentrated by centrifugation in Amicon Ultra Centrifugal filter units (10000 nominal molecular weight limit).

TEM

TEM imaging was performed with a JEOL 3000F equipped with a 300kV FEG and a 4k CCD (Gatan MSC). For TEM imaging a droplet of the sample suspended in water (0.06g/L) was placed on a TEM copper grid with a holey carbon film. For imaging, a 60 µm objective aperture was used to enhance contrast, and the chosen magnification combined with a CCD binning of 2 resulted in a pixel resolution of 0.4 nm. From the acquired TEM images, particle sizes were measured by manually outlining the particle perimeters, using the software ImageJ and converting the measured projected particle areas to particle diameters using a circular approximation. The measured diameters are presented in the form of particle size distributions with an optimum bin size calculated according to reference[37].

STXM

The sample was prepared by roll to roll coating[7,10] nanoparticles on top of PEDOT:PSS, submerging the film in a solution of potassium hydroxide and scraping the films onto a TEM copper grid. STXM measurements were recorded at the synchrotron facility BESSY II in Berlin, Germany, at the beamline UE46-PGM2. The sample was observed in the MAXYMUS STXM end station under high vacuum at the carbon edge (282-320 eV). A step size of 20 nm was used and the X-rays were detected with a photo avalanche diode. The

absorption data was converted to optical density and by fitting linear combinations of reference spectra the relative material distribution maps were produced (see previous publication[36] for P3HT and PCBM reference spectra).

DLS

1 mL of nanoparticle dispersion (1 g/L) in water were measured with a DLS unit from Malvern Instruments Ltd, Zetasizer Nano Zs with a He-Ne laser 633nm max 4mW. The size distribution was automatically extracted by second order cumulant analysis. A subsequently DLS measurement was performed on 1 mL of nanoparticle dispersion (0.06 g/L) in water on a 200SM goniometer from Brookhaven Instruments that incorporate a 632.8 nm He–Ne laser. The instrument was operated at a fixed scattering angle of 90°. The standard analysis software of the instrument was used for analyzing the correlation function using double exponential fitting, free form Contin analysis and second order cumulant analysis. Both experiments were carried out at room temperature with 5 min calibration time of the sample.

SAXS

SAXS measurements on the dispersed nanoparticles (6 g/L) were carried out at the MAXLab beamline I911-SAXS[38]. 30 mL of sample were measured in a 1 mm capillary for 60 seconds under automatic sample movement to prevent beam damage. 2% Hellmanex and demineralized water were used to rinse the sample capillary between sample changes. The particles were kept in a buffer of 0.1 M Tris, 50 mM NaCl, pH 8. For each particle type a dilution series were measured and no concentration effects were observed in the SAXS data. For data analysis, see the main text. The experiments were carried out at room temperature.

GIWAXS

GIWAXS measurements were performed with a Rigaku RU-200 rotating Cu anode as source, operating at 50 kV, 200 mA. The X-ray beam point source was monochromatized and collimated (λ = 1.5418 Å) by a multilayer optic[39]. Spin coated samples were prepared on float glass substrate cleaned by sonication in isopropanol and 30 seconds plasma etching. 6 g/L P3HT:PCBM 1:1 nanoparticles were spin coated at 2800 rpm. Sample annealing was performed on a 140°C hotplate in ambient atmosphere. Roll to roll coated samples were fabricated by slot-die coating 60 g/L P3HT:PCBM 1:1 nanoparticles on a polyethylene glycol substrate as described previously[7,10].

AFM

AFM samples were prepared on mica substrates fastened to glass. The top layer mica was removed with tape prior to spin coating 6 mg/L P3HT:PCBM 1:1 nanoparticles at 2800 rpm. The AFM measurements were done as 5x5 micron micrographs with a 1024x1024 pixel resolution on a N8 Neos (Bruker Nano GmbH, Herzogenrath, Germany) using PPP-NCLR cantilevers (NANOSENSORS,Neuchatel, Switzerland). The AFM micrographs were post-processed with SPIP 6.2.6 software where particle height and diameter were extracted using an automated thresholding routine.

Device

A device structure of Glass/ITO/ZnO/Active layer/MoO_3/Al was used. Zinc oxide nanoparticle fabricated by the sol-gel method was spin coated at 1500 rpm onto an ITO substrate. The substrate was heated to 80°C and Landfester P3HT:PCBM 1:1 particles were spin coated at 800 rpm. The film was dried 60 min at 80°C in vacuum. About 10 nm of MoO_3 and 100 nm of Al was deposited on top of the active layer by thermal evaporation in a vacuum of 2×10^{-4} Pa. The device area was 12 mm^2. The photoelectric characterization was performed using a Keithley 236 source meter and a calibrated AM1.5G solar simulator.

Conclusions

We have characterized water based ink for organic photovoltaics fabricated as Landfester nanoparticles in dispersion. The size distribution is found to be smaller than normally reported in the literature (radii on the order of 10 nm) and in particular second order cumulant analysis of DLS data is found to overestimate the particle radius by at least 10 nm.

We have determined the internal particle structure of particles on the nanometer scale and found it is not a core-shell structure (previous found for larger particles) but a more complex intermixture of crystal P3HT or PCBM domains in a matrix of P3HT-PCBM. Crystal nano domains form within the particles given a sufficient fraction of P3HT is present. Presence of PCBM reduces the average crystal size from 8.7 nm in pure P3HT to 5 nm in a P3HT:PCBM 1:1 mix. The overall crystallinity also decreases by a factor of 2.7 in the P3HT:PCBM 1:1 particles compared to pure P3HT particles.

Upon spin and drop casting the nanoparticles deform and the average "particle" height becomes 5.2 ± 1.2 nm and the corresponding diameter about 13 times larger. The crystal domain size decreases from 5.1 nm to 3 nm and are highly textured with 91% crystals aligned edge-on (within ±30 degrees) of the substrate. Annealing at 140°C can restore the substrate aligned crystals to about 6 nm size. Face-on crystals are in general about a factor of 2 larger, which could indicate the edge-on crystals are limited by the overall particle height of 5.2 ± 1.2 nm.

After roll-to-roll coating the nanoparticles, aggregates of PCBM protrude in a homogeneous matrix of P3HT with domain sizes on approximate 100 nm. Without chemical information, such structure could easily be mistaken for intact nanoparticles. Crystal surface orientation is also observed in thicker roll coated nanoparticle layers. It is conjectured that phase segregation takes place to an extent that is harmful for the OPV power conversion efficiency.

For optimal OPV performance, crystallization and phase separation in the water-based ink presents a problem, because bulk layers traditionally are well mixed when cast and achieve optimal

performance upon annealing. This could also explain why nanoparticle based devices are not able to reach the performance of annealed bulk hetero junction devices – because the nanoparticle based layers might start out with large phase segregated domains.

For future experiments it would be very interesting to investigate the effect of solvent and surfactant on internal structure and crystallization – and whether the success of surfactant free nanoparticles may be explained by a higher degree of material mixing and smaller crystal domains.

Acknowledgements

We gratefully acknowledge financial support from The Danish Council for Strategic Research through the WAPART project, and from The Danish Council for Independent Research Natural Sciences, through the DANSCATT grant. We also express our gratitude to Michael Bechtel, for kind assistance during the experiments with the STXM at MAXYMUS, BESSY II, by the MPI for intelligent systems, department Schütz. The MAX-lab synchrotron is acknowledged for providing access, beam-time, and support at the I911-4 SAXS-beamline. Specifically, we thank Dr. Søren Kynde and beam-line scientist Dr. Christopher Söderberg for their assistance during the data acquisition.

Notes and references

[a] Department of Energy Conversion and Storage, DTU, Frederiksborgvej 399, 4000 Roskilde, Denmark.

[b] Structural Biophysics, Niels Bohr Institute, Faculty of Science, University of Copenhagen, Denmark.

[c] Department of Chemistry and Bioscience, Fredrik Bajers Vej 7H, 9220, Aalborg East, Denmark.

[d] Changchun Institute of Applied Chemistry, 5625 Renmin Street, Changchun, 130022,P. R. China

† See DOI: 10.1039/b000000x/

1. R. Perez and M. Perez, IEA SHC Sol. Updat., 2009, **50**, 2.

2. N. S. Lewis and D. G. Nocera, Proc. Natl. Acad. Sci. U. S. A., 2006, **103**, 15729–15735.

3. C. Sener and V. Fthenakis, Renew. Sustain. Energy Rev., 2014, **32**, 854–868.

4. S. B. Darling and F. You, RSC Adv., 2013, **3**, 17633.

5. N. Espinosa, F. O. Lenzmann, S. Ryley, D. Angmo, M. Hösel, R. R. Søndergaard, D. Huss, S. Dafinger, S. Gritsch, J. M. Kroon, M. Jørgensen, and F. C. Krebs, J. Mater. Chem. A, 2013, **1**, 7037.

6. F. C. Krebs, N. Espinosa, M. Hösel, R. R. Søndergaard, and M. Jørgensen, Adv. Mater., 2014, **26**, 29–39.

7. T. T. Larsen-Olsen, B. Andreasen, T. R. Andersen, A. P. L. Böttiger, E. Bundgaard, K. Norrman, J. W. Andreasen, M. Jørgensen, and F. C. Krebs, Sol. Energy Mater. Sol. Cells, 2012, **97**, 22–27.

8. R. Søndergaard, M. Helgesen, M. Jørgensen, and F. C. Krebs, Adv. Energy Mater., 2011, **1**, 68–71.

9. K. Landfester, Adv. Mater., 2001, **13**, 765–768.

10. T. R. Andersen, T. T. Larsen-Olsen, B. Andreasen, A. P. L. Böttiger, J. E. Carlé, M. Helgesen, E. Bundgaard, K. Norrman, J. W. Andreasen, M. Jørgensen, and F. C. Krebs, ACS Nano, 2011, **5**, 4188–96.

11. D. Darwis, D. Elkington, E. Sesa, N. Cooling, G. Bryant, X. Zhou, W. Belcher, and P. Dastoor, in AIP Conf. Proc., 2011, vol. 1415, pp. 120–123.

12. S. Gärtner, M. Christmann, S. Sankaran, H. Röhm, E.-M. Prinz, F. Penth, A. Pütz, A. E. Türeli, B. Penth, B. Baumstümmler, and A. Colsmann, Adv. Mater., 2014, **26**, 6653–6657.

13. K. B. Burke, A. J. Stapleton, B. Vaughan, X. Zhou, A. L. D. Kilcoyne, W. J. Belcher, and P. C. Dastoor, Nanotechnology, 2011, **22**, 265710.

14. D. M. DeLongchamp, R. J. Kline, and A. Herzing, Energy Environ. Sci., 2012, **5**, 5980.

15. A. Stapleton, B. Vaughan, B. Xue, E. Sesa, K. Burke, X. Zhou, G. Bryant, O. Werzer, A. Nelson, A. L. David Kilcoyne, L. Thomsen, E. Wanless, W. Belcher, and P. Dastoor, Sol. Energy Mater. Sol. Cells, 2012, **102**, 114–124.

16. S. Ulum, N. Holmes, D. Darwis, K. Burke, A. L. D. Kilcoyne, X. Zhou, W. Belcher, and P. Dastoor, Sol. Energy Mater. Sol. Cells, 2013, **110**, 43–48.

17. J. J. Richards, C. L. Whittle, G. Shao, and L. D. Pozzo, ACS Nano, 2014, **8**, 4313–4324.

18. D. a. Shapiro, Y.-S. Yu, T. Tyliszczak, J. Cabana, R. Celestre, W. Chao, K. Kaznatcheev, a. L. D. Kilcoyne, F. Maia, S. Marchesini, Y. S. Meng, T. Warwick, L. L. Yang, and H. a. Padmore, Nat. Photonics, 2014, **8**, 765–769.

19. D. Beyer, W. Lebek, W. D. Hergeth, and K. Schmutzler, Colloid Polym. Sci., 1990, **268**, 744–748.

20. M. Teubner and R. Strey, J. Chem. Phys., 1987, **87**, 3195.

21. B. Siekmann and K. Westesen, Colloids Surfaces B Biointerfaces, 1994, **3**, 159–175.

22. H.-Y. Kim, J.-A. Han, D.-K. Kweon, J.-D. Park, and S.-T. Lim, Carbohydr. Polym., 2013, **93**, 582–8.

23. B.-J. Kim, S.-G. Oh, M.-G. Han, and S.-S. Im, Synth. Met., 2001, **122**, 297–304.

24. E. D. Gormez, K. P. Barteau, H. Wang, M. F. Toney, and Y.-L. Loo, Chem. Commun., 2011, **47**, 436–438.

25. U. Holzwarth and N. Gibson, Nat. Nanotechnol., 2011, **6**, 21027.

26. P. Scherrer, Göttinger Nachrichten Math. Phys., 1918, **2**, 98–100.

27. M. J. Winokur, D. Spiegel, Y. Kim, A. J. Heeger, and S. Barbara, Synth. Met., 1989, **28**, 419–426.

28. J. Y. Kim and C. D. Frisbie, J. Phys. Chem. C, 2008, **112**, 17726–17736.

29. A. P. L. Böttiger, M. Jørgensen, A. Menzel, F. C. Krebs, and J. W. Andreasen, J. Mater. Chem., 2012, **22**, 22501.

30. P. E. Shaw, A. Ruseckas, and I. D. W. Samuel, Adv. Mater., 2008, **20**, 3516–3520.

31. Y. Huang, Y. Liao, S. Li, M. Wu, C. Chen, and W. Su, Sol. Energy Mater. Sol. Cells, 2009, **93**, 888–892.

32. J. S. Pedersen, Adv. Colloid Interface Sci., 1997, **70**, 171–210.

33. M. C. Pedersen, L. Arleth, and K. Mortensen, J. Appl. Crystallogr., 2013, **46**, 1894–1898.

34. N. P. Holmes, K. B. Burke, P. Sista, M. Barr, H. D. Magurudeniya, M. C. Stefan, a. L. D. Kilcoyne, X. Zhou, P. C. Dastoor, and W. J. Belcher, Sol. Energy Mater. Sol. Cells, 2013, **117**, 437–445.

35. M. Nakagaki and S. Yokoyama, J. Pharm. Sci., 1985, **74**, 1047–1052.

36. E. B. L. Pedersen, T. Tromholt, M. V. Madsen, A. P. L. Bottiger, M. Weigand, F. C. Krebs, and J. W. Andreasen, J. Mater. Chem. C, 2014, **2**, 5176.

37. D. Freedman and P. Diaconis, Zeitschrift für Wahrscheinlichkeitstheorie und Verwandte Gebiete, 1981, **57**, 453–476.

38. A. Labrador, Y. Cerenius, C. Svensson, K. Theodor, and T. Plivelic, J. Phys. Conf. Ser., 2013, **425**, 072019.

39. D. Apitz, R. P. Bertram, N. Benter, W. Hieringer, J. W. Andreasen, M. M. Nielsen, P. M. Johansen, and K. Buse, Phys. Rev. E - Stat. Nonlinear, Soft Matter Phys., 2005, **72**, 1–10.

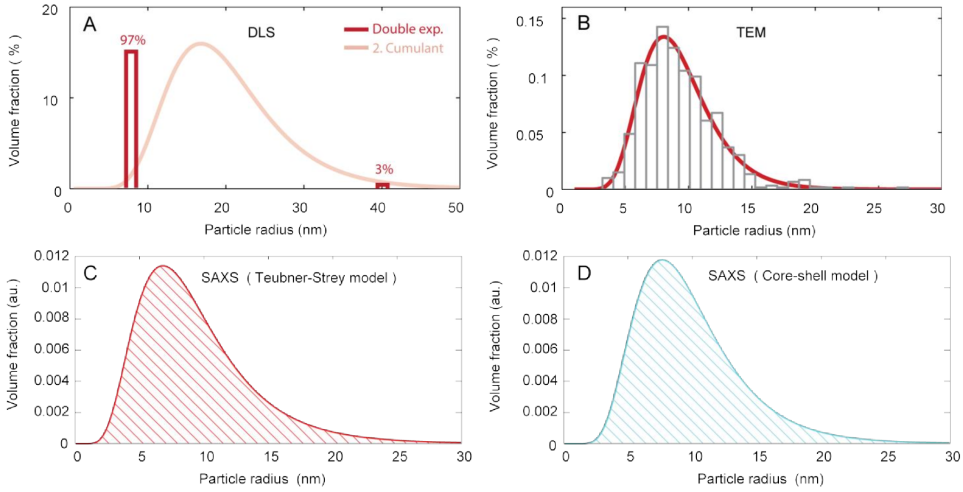

Figure 1, Size distribution of P3HT:PCBM 1:1 Landfester particles measured with different methods. A) Dynamic light scattering of particles dispersed in water. A double exponential fit to the correlation function yields 97% volume fraction of the particles have a radius of 8.9 nm in agreement with the other methods. A traditional second order cumulant analysis gives an impression of >10 nm larger particle sizes. B) Transmission Electron Microscopy of particles drop casted on a holey carbon copper grid. C-D) Small angle X-ray scattering results from particles dispersed in water using different models for internal structure showing results according to the Teubner-Strey model in C) and a core-shell model in D).

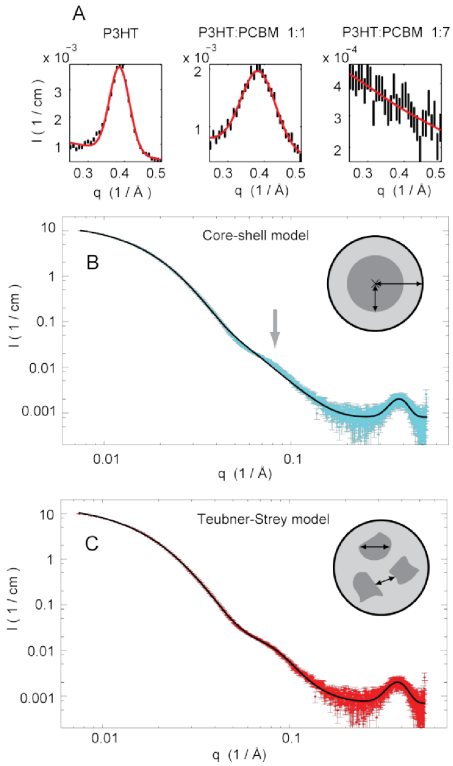

Figure 2, Small angle X-ray Scattering (SAXS) of nanoparticles dispersed in water. A) Scattering from the P3HT 100 peak for different compositions of P3HT and PCBM. B-C) Full SAXS spectrum for P3HT:PCBM 1:1 particles fitted to different internal models: B) Core-shell model (inner and outer radius) which does not fit the second shoulder around 0.08 $Å^{-1}$ marked with a grey arrow. C) Teubner-Strey model (domain size and distance) matching all features of the scattering curve.

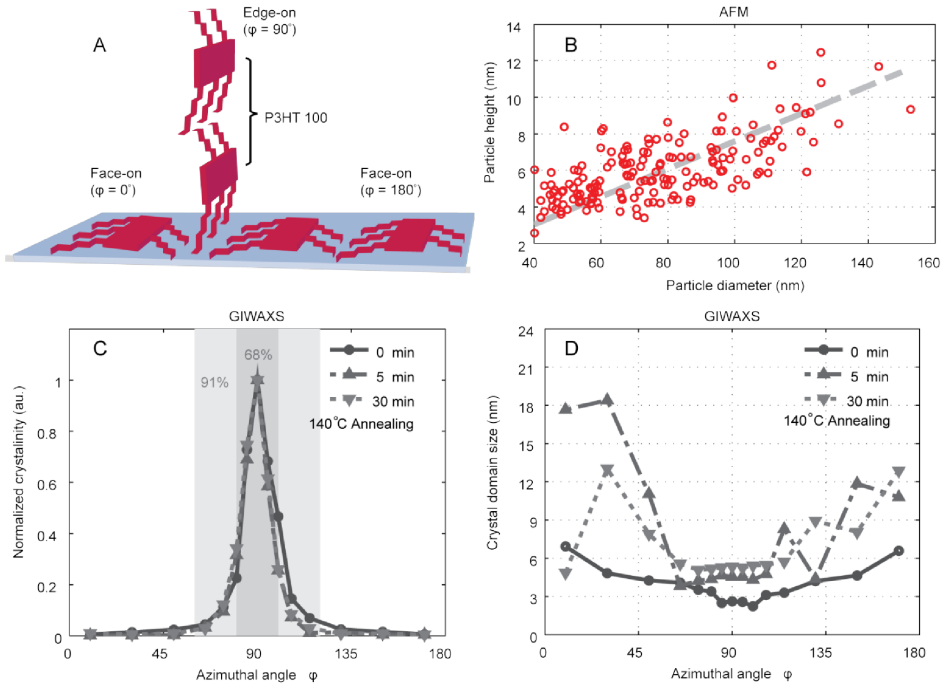

Figure 3, Particle deformation and reorientation of crystal domains. A) Schematic of face-on and edge-on orientation of P3HT. B) AFM measurements of individual P3HT:PCBM 1:1 nanoparticles spin cast on a mica substrate. The fitted trend line finds the particle diameter is about 13 times the particle height. C) Azimuthal distribution of P3HT 100 crystallinity normalized to the highest degree of crystallinity. The overall texture (angular distribution of integrated diffraction intensity) does not change as a function of annealing. Before annealing 68% of the crystallinity is aligned edge-on with the substrate (80-100 degrees azimuthal angle. D) P3HT 100 average domain size as function of azimuthal angle. The crystal domain size increases with annealing, and is generally larger for angles far from edge-on orientation. Edge-on crystals seems limited to about 6 nm average crystal size - about the same particle height found in AFM measurements.

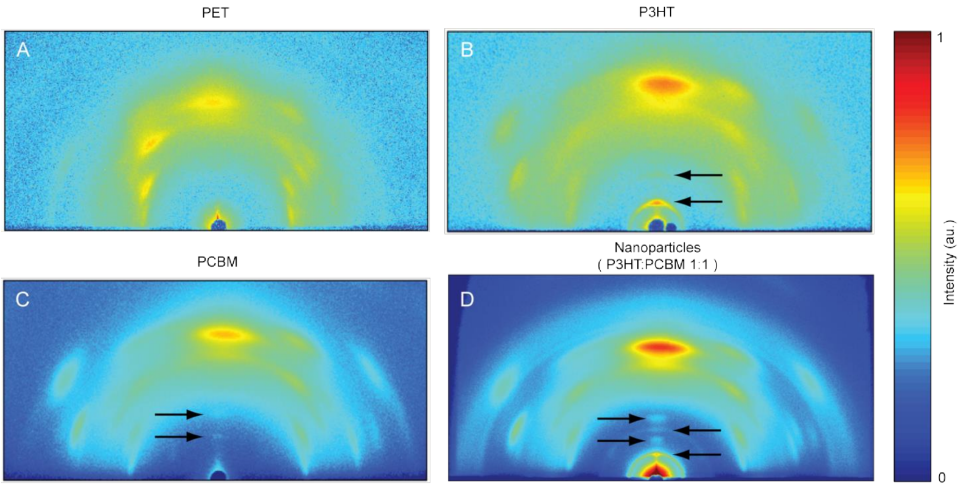

Figure 4, GIWAXS data as measured (q = 0.15 - 2.5 $Å^{-1}$) for A) PET foil used as substrate, B) roll coated P3HT, C) roll coated PCBM and D) roll coated nanoparticles. The left facing arrows in B, and D show textured P3HT with edge-on orientation (100) and (200). The right facing arrows in C) and D) show textured PCBM. The high degree of textured material in the roll coated nanoparticle layer indicates the particle shape is not conserved, but particle deformation and phase segregation are observed to take place in a fashion similar to spin coated particles.

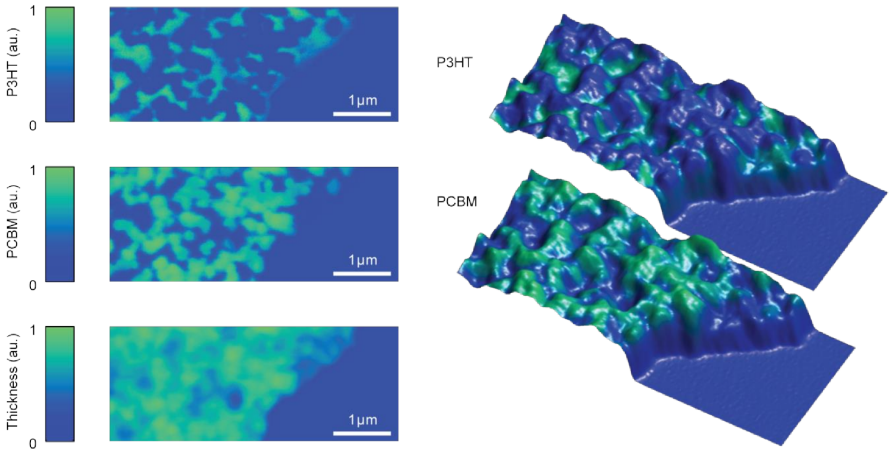

Figure 5, Spatially distibution of active material for a roll coated nanoparticle film dertermined using scaning X-ray transmission microcopy near the carbon K-edge. To the left graphs are shown with relative distribution of P3HT and PCBM as well as relative thickness found from optical density at 320 eV. Clear phase seperation is observed in domains >100 nm. To the right there are rendered thickness maps using coloring from the relative ditribution of P3HT (top) and PCBM (bottom). A clear tendency that the peak areas contain mainly PCBM appears.

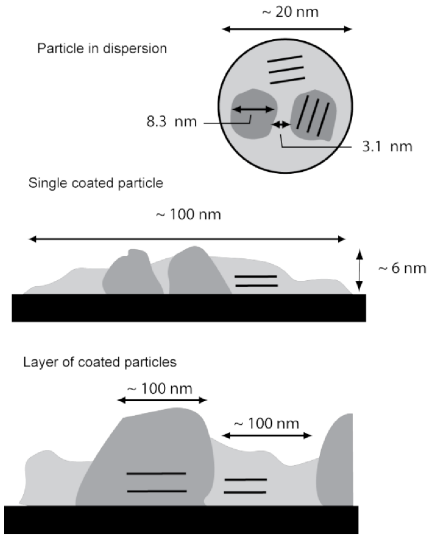

Figure 6, Schematic overview of structure and crystallinity in P3HT:PCBM 1:1 Landfester particles. They particles start out as a lognorm polydisperse size distribution ranging from 10-40 nm in diameter. The internal structure is accurately described by a Teubner-Strey model with domain sizes of about 8.3 nm separated by 3.1 nm. These domains could either be crystalline P3HT or PCBM rich areas. When an isolated particle is coated on a substrate it undergo drastic morphological changes as it is smeared out along the surface and the crystal domains decrease in size and align with the substrate. When roll-to-roll coating thicker layers the P3HT and PCBM phase separate further and aggregate to large +100 nm domains. The majority of the crystals units also remain aligned to the substrate in the roll-to-roll coated layer.

	Domain size (nm)	Molecules per domain	Normalized crystallinity
P3HT	8.7	5.2	100 %
P3HT:PCBM 1:1	5.1	3.0	37 %

Table 1: Average P3HT crystal domain sizes and corresponding number of P3HT molecules in the average crystal unit. The crystallinity is shown relative to the crystallinity of neat P3HT nanoparticles (normalized for concentration).

	J_{sc} (mA/cm^2)	V_{oc} (V)	FF (PCE)	PCE (%)	T_{drying} (°C)
Roll to roll coated[7]	1.95	0.45	33.1	0.29	140
Spin coated	4.89	0.47	50.5	1.16	80

Table 2: Photovoltaic performance of devices with P3HT:PCBM 1:1 Landfester nanoparticles as active layer. A lower drying temperature over longer time could be applied to the spin coated devices since they were not bound to the fixed processing speed imposed by roll to roll coating.

Table of Contents

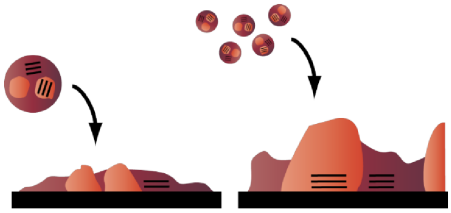

Studying water dispersible photoactive nanoparticles used for organic photovoltaics we provide new insights in the internal structure, crystallinity and the previously unreported drastic changes that occur when the particles are cast into a film.

Supporting information

Structure and crystallinity in water dispersible photoactive nanoparticles for organic solar cells

E. B. L. Pedersen, M. C. Pedersen, S. B. Simonsen, R. G. Brandt, A. P. L. Böttiger, T. R. Andersen, W. Jiang, X. Zhiyuan, F. C. Krebs, L. Arleth and J. W. Andreasen.

SDS estimate

The total volume, V, and area, A of the particles was found from TEM particle size distribution in the following way

$$A = \sum_i w_i \, 4 \, \pi \, r_i^2$$

$$V = \sum_i w_i \frac{4}{3} \, \pi \, r_i^3$$

where w_i was the relative fraction of particles with r_i.

The conversion to mass of SDS, m_{sds}, was done using the molar surface density, σ_{sds}, and the molar mass of SDS M_{sds}

$$m_{sds} = A \, \sigma_{sds} \, M_{sds}$$

An upper estimate of σ_{sds} was optained from σ_{sds} reported for latex particles (H. M. Vale and T. F. McKenna, *Colloids Surfaces A Physicochem. Eng. Asp.*, 2005, **268**, 68–72.).

The mass of P3HT:PCBM, m_{np}, was determined using the mass density of a 1:1 mixture of P3HT and PCBM, ρ_{np}

$$m_{np} = V \, \rho_{np}$$

The SDS mass fraction of the total mass was found to be 18 %.

NMR

The Landfester nanoparticles were scanned using ^{1}H NMR shown in figure 1. A clear water peak is observed but no chloroform signal is found.

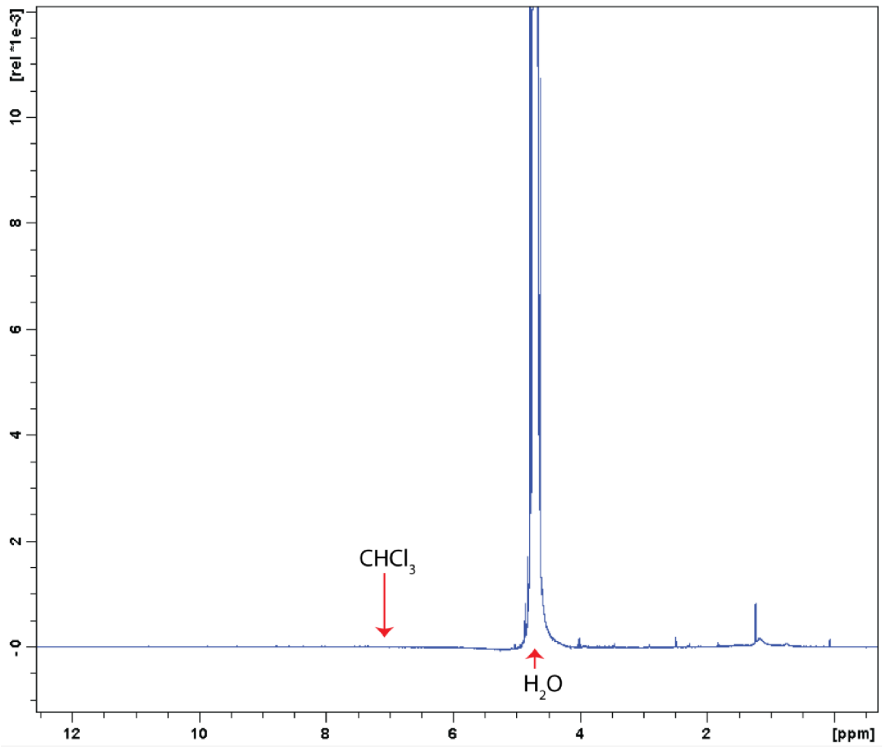

S1. NMR scan of P3HT:PCBM 1:1 Landfester particles dispersed in water.

Submitted to RSC Nanoscale

ARTICLE

Water-processed organic tandem solar cells improved by quantitative 3D nanoimaging

Received 00th January 20xx,
Accepted 00th January 20xx

DOI: 10.1039/x0xx00000x

www.rsc.org/

E. B. L. Pedersen,[a] D. Angmo,[a] H. F. Dam,[a] K. T. S. Thydén,[a] T. R. Andersen,[a] E. T. B. Skjønsfjell,[b] F. C. Krebs,[a] M. Holler,[c] A. Diaz,[c] M. Guizar-Sicairos,[c] D. W. Breiby[b] and J. W. Andreasen[a]

Organic solar cells have great potential for upscaling due to roll-to-roll processing and a low energy payback time, making them an attractive sustainable energy source for the future. Active layers coated from water-dispersible Landfester particles enable greater control of the layer formation and easier access to the printing industry, which has reduced the use of organic solvents since the 1980s. Through ptychographic X-ray computed tomography (PXCT) we image quantitatively a roll-to-roll coated photovoltaic tandem stack consisting of one bulk hetero junction active layer and one Landfester particle active layer. We extract the layered morphology with structural and density information including porosity present in the various layers and the silver electrode with high resolution in 3D. The Landfester particle layer is found to have an undesired morphology with negatively correlated top- and bottom interfaces, wide thickness distribution and only partial surface coverage causing electric short circuits through the layer. By top coating polymer material onto the Landfester nanoparticles we eliminate the structural defects of the layer such as porosity and roughness, and achieve the increased performance larger than 1V expected for a tandem cell. This study highlights that quantitative imaging of weakly scattering stacked layers of organic materials has become feasible by PXCT, as this information cannot be obtained by other methods. In the present study this technique specifically reveals the need to improve the coatability and layer formation of Landfester nanoparticles, thus allowing improved solar cells to be produced.

Introduction

In the pursuit of sustainable energy production only a few technologies have the potential to meet the world's energy demand and the one with the biggest potential is solar energy.[1] The most common photovoltaic technology is based on crystalline silicon, and is hampered by a long energy payback time between 1.7 and 2.7 years,[2] and therefore also by a high energy price. Organic photovoltaics is an emerging solar cell technology with a high upscaling potential and low energy payback time between 0.3 and 0.5 years[2] due to mass production methods of roll-to-roll coating of abundant elements.[3] It has been suggested that it will be possible to reach energy payback time of less than 1 day,[4] and large scale deployment of organic photovoltaic modules has already been demonstrated.[5]

Two of the challenges for consistent large scale production of multilayered organic electronics are solvents redissolving underlying layers and the control of molecular self-assembly within layers.[6] Packing surfactants around the organic molecules, thus turning them into water dispersible Landfester particles, offers an opportunity to both control the internal structure through the particle fabrication process[7] and to produce complex multilayer structures even with simultaneous coating of more than one layer at a time.[8] Furthermore, water based inks are non-toxic and ease large-scale production by removing the safety requirements associated with toxic and flammable organic solvents. Water based inks would also enable easier transition to large scale production by accessing the existing printing industry, which has made use of organic solvents since the 1980s,[9] and reduce the need to develop custom-built fabrication lines for organic photovoltaics.[10]

Water based inks are common for intermediate layers such as poly(3,4-ethylenedioxythiophene) polystyrene sulfonate (PEDOT:PSS) and ZnO, whereas water dispersible photoactive nanoparticles need further development to be applied widely. The major issue is that the power conversion efficiency is 1/3 compared to that achieved for bulk hetero junctions.[11] A recent improvement was made with surfactant free nanoparticles cast from alcohol based solvents with device power conversion efficiencies of 4%.[12] However, without particle stabilization such inks might be unstable and therefore difficult to upscale. The layer formation of active nanoparticles has mainly been studied by examining the surface properties using Atomic Force Microscopy (AFM) and the internal layer structure by using Transmission Electron Microscopy (TEM) or Scanning Transmission X-Ray Microscopy (STXM) on stand-alone nanoparticle layers.[11,13–15] To get a more complete image of the failure mechanisms it is desirable to image the full layer structure whilst embedded in a complete device stack, so that both the individual layers and the relevant interfaces can be examined.

[a] Department of Energy Conversion and Storage, Technical University of Denmark, Frederiksborgvej 399, 4000 Roskilde, Denmark
[b] Department of Physics, Norwegian University of Science and Technology, Høgskoleringen 5, 7491 Trondheim, Norway
[c] Paul Scherrer Institut, 5232 Villigen PSI, Switzerland

Electronic Supplementary Information (ESI) available: Determination of spatial resolution, simulations of partial volume effects, and comparison and explanation of threshold segmentation and Markov field segmentation. See DOI: 10.1039/x0xx00000x

Until recently, even though a multitude of techniques were applied to measure the morphology and structure of organic photovoltaic devices, none of them provided three-dimensional (3D) structural information of an entire device.[16] Ptychographic X-ray computed tomography (PXCT)[17] provides quantitative 3D images and has already been used to facilitate the development of an organic photovoltaic tandem device.[18] The technique is ideal for proving structural information for organic photovoltaics since it provides the nanometer resolution necessary to image thin layers in organic photovoltaics. PXCT at multi keV photon energies provides sufficient penetration power to image materials with thicknesses in the order of tens of microns, contrary to many high resolution X-ray and electron based techniques such as transmission electron microcopy and scanning transmission X-ray microscopy which are typically limited to about 100 nm thickness.[16] Experimentally PXCT has been demonstrated to reach 16 nm isotropic 3D resolution on a 6 micron thick for-purpose high-contrast object.[19]

Here we report 3D PXCT imaging of an organic photovoltaic tandem device, with one of the active layers being a conventional bulk hetero-junction and the other consisting of Landfester nanoparticles. This allows the direct comparison of the two kinds of active layers within the same dataset, and at the same time provides the opportunity to investigate the material interfaces and layer structures in the complete device. The quantitative nature of ptychographic tomography also allows investigation of mass density variations by extracting electron densities and comparing them to expected values of the known materials.

Results and discussion

We investigate the nanostructure of the organic tandem cell presented in **figure 1** using a sub tomogram of the central region of the sample to exclude artifacts from material redisposition at the sample sides originating from the sample preparation. The layered stack of materials was produced by slot-die coating material solutions and nanoparticle dispersions on a flextrode substrate[20] using a lab scale roll-coater[21]. The structure showed photo electric performance and a pillar of solar cell was cut and mounted on a sample holder using focused ion beam (FIB) milling. Since the PXCT electron densities were measured relative to air, all electron densities in the tomogram were corrected with the electron density of air, 10^{-3} Å^{-3}. We have obtained a ptychographic tomogram of the tandem structure with a spatial resolution of 20 nm, as estimated by Fourier shell correlation[22] (see supporting information for further details). Our prime target of investigation is the morphological differences between the active layer consisting of Landfester particles and the other active layer being a conventional bulk heterojunction based on PDTSBT-F:PCBM (see experimental for full name). The nearby PEDOT:PSS layers (used for charge transport) have little contrast to the active layers because both types of layers mainly consist of carbon. In our analysis, the photovoltaically active and PEDOT:PSS layers will therefore be analyzed as *one* layer referred to as organic layers: PDTSBT-F:PCBM and PEDOT:PSS as the organic bulk heterojunction layer, P3MHOCT:PCBM Landfester and PEDOT:PSS as the organic nanoparticle layer.

In the analysis of the tomogram, efforts were made to keep the physical significance of the segmentation by utilizing the electron density values and their spatial distribution with Markov field segmentation. The histograms of electron densities were fitted by two kinds of distributions: Gaussian peak shapes - corresponding to pure materials, and power functions with Gaussian cut-offs - corresponding to partial volumes i.e. interface voxels with more than one material present, see supporting information. This was done according to the shape of the electron density histogram and the prior knowledge of the distribution of layers within the solar cells. Nearest neighbor information was included in the segmentation by using a Markov field in order to accurately label materials with overlapping electron densities (see supporting information).

Nanoparticle and bulk heterojunction structure

The active Landfester nanoparticle layer is porous and contains small domains of air as seen in **figure 1**. From the electron densities it is apparent that the scale of the porosity is below the limit of 20 nm imposed by the resolution, since the electron densities arise from partial volume effects, i.e. voxels with both nanoparticles and air, and the air cannot originate from the sample surface since only an interior section of the sample is studied. The layers have been roll coated at 60°C and the final device was annealed at 100°C, so it is possible that further annealing before coating subsequent layers would remove or reduce porosity. The bulk heterojunction is homogeneous, as expected (see figure 1). The air between the nanoparticles reveals that the active layer only partially covers the surface. With only partial coverage the overlying PEDOT:PSS is most likely penetrating the active layer. The zinc oxide segment provides clear proof of a short circuit with instances of spikes penetrating the nanoparticle layer, as seen on figure 1D.

Short circuits through the nanoparticle layer are also visible in the electrical device characterization presented in **table 1**. The low open circuit voltage (V_{oc}) of the tandem device indicates a single junction device. It is comparable to the performance of single junction cells with only a bulk heterojunction layer, supporting the findings from ptychographic tomography of a non-functioning nanoparticle layer. The limited contact through the nanoparticle layer and the longer charge path also cause the short circuit current (J_{sc}) to decrease, compared to the single junction BHJ device. The failure of the device is therefore not primarily a result of poor photovoltaic performance of the nanoparticles, but a result of the nanoparticles only forming a partially covering layer. The decreased photoelectric performance of the nanoparticles due to the undesirable layer morphology highlights the need to consider the processing and layer formation of the nanoparticles as a key parameter to optimize in addition to optimization of the internal structure and photoelectric properties of the organic nanoparticles themselves.[7] Such optimization could consist of employing different surfactants or even mixtures of cat- and anionic surfactants.[15]

Electron density

Apart from high spatial resolution, ptychographic tomography also provides accurate quantitative information about the spatially resolved electron density, $\rho_e(\mathbf{r})$, obtained from tomographic reconstruction of phase contrast projections.[23,24] For the tandem cell, we find three layers of particular interest due to their electron density distributions: The two zinc oxide layers, the silver electrode and the organic layer containing nanoparticles. Based on the segmentation a slice containing only these layers along with histograms of their electron density distributions is presented in **figure 2**.

The zinc oxide layers have a reduced electron density, consistent with the fact that these layers are processed from ZnO nanoparticles. The normal electron density for bulk zinc oxide is 1.60 $Å^{-3}$, whereas the mean observed electron density is 0.96 $Å^{-3}$. In the analysis of this reduced electron density we have already considered partial volume effects between zinc oxide and organic materials, which have been classified into its own category as shown in figure 2B. The remaining pure zinc oxide phases have a Gaussian density distribution as expected due to experimental uncertainties. The reduction in electron density of 60% compared to the bulk material is therefore a real physical property which most likely arises from the nanoparticles that form the zinc oxide layers. The particulate structure could result in looser material packing or even nanometer scale porosity below our resolution limit.

The silver electrode also consists of nanoparticles, and we observe porosity in the silver electrode as opposed to our previous experiments.[18] In those experiments PEDOT:PSS infiltrated the whole electrode, whereas in the current study it only infiltrates the first 50-100 nm of a 1 micron thick electrode. This might be explained by a thicker PEDOT:PSS layer used in the previous experiment, which left sufficient material to penetrate the electrode.

For the organic materials we see little difference between the materials P3MHOCT:PCBM and PEDOT:PSS. They both mainly consist of carbon and exhibit a single Gaussian peak of the electron density. The porosity previously observed in the nanoparticle layers constitutes partially filled volumes with organic material and air. A small amount of the observed voxels (917 of 3.9×10^{6}) has electron densities equal to or below those of air (10^{-3} $Å^{3}$). The reason why we can identify all of the partial volumes as sub-resolution porosity is that air is the only constituent expected in the sample with lower electron density than carbon. Air is evidently present due to the observation of voxels with electron densities lower or equal to air beyond what can be expected from the Gaussian electron density distributions from organic material i.e. 917 voxels have electron density less or equal to 10^{-3} $Å^{3}$ whereas 6×10^{-13} voxels would be expected from the observed Gaussian distribution of the organic material. Thus, it is plausible that all the low density voxels have partial volumes of organic material and air, since no air voxels should be present as we are only looking at the interior of the sample.

Interfaces

Interfaces are particularly important in organic photovoltaics because they are critical for charge transport and successful device performance. PXCT provides nanometer scale information of the interfaces and as opposed to other methods, e.g. AFM, it can be used to investigate correlations between subsequent layers. A detailed quantitative analysis of the tandem interfaces and layers is presented in **figure 3**. The top-bottom correlation indicates how much a given layer is affected by the topology of the underlying layer. The 1 micron thick silver layer has low top-bottom interface correlation, likely due to the coarse structure caused by the nanoparticles in the layer. However, the resulting top surface roughness remains low. The observed characteristics of the silver electrode and subsequent PEDOT:PSS layer might also be due to the printing methods; the silver was flexographically printed and the PEDOT:PSS was rotary-screen printed.[20] Previously large scale variations have been found in the thickness of similar silver electrodes[25], but this and a previous ptychography experiment[18] find a rather flat silver layer. It might be explained by the subsequent rotary-screen printing altering the silver interface thus ensuring a more planar layer with low roughness. The remaining layers, with the exception of the organic area with nanoparticles, have a high degree of positive interface correlations and mostly narrow thickness distribution.

The organic layer with active nanoparticles has a negative interface correlation in addition to a high surface roughness of the top interface and a wide size distribution. Negative top-bottom interface correlation is undesirable since it results in a wide thickness distribution (thick and thin regions), and increases the risk of short circuits. A wide thickness distribution is undesirable for large-scale production because the optimal material thickness cannot be deployed and results in reduced photoelectric performance. The roughness of the organic nanoparticle layers also increases to three times the roughness of the underlying zinc oxide layer and is only gradually reduced in the subsequent layers.

The organic nanoparticle layer distinguishes itself by having overall characteristics that negatively affect the other layers, e.g. the tail in the size distribution of the top zinc oxide layer is caused by spikes through the active nanoparticles. Since the main difference between the two active layers is the structure (bulk versus nanoparticles), the undesired behavior of the active nanoparticle layer could easily be attributed solely to the layer consisting of nanoparticles. However, the remaining layers are all cast from particles that show good layer characteristics, including the inorganic zinc oxide nanoparticles, the organic PEDOT:PSS gel particles and the large silver particles. The surface energies and particle interactions appear to be undesirable only for the active layer nanoparticles.

The negative top-bottom interface correlation could suggest that the Landfester nanoparticles in the active layer initially locate themselves in topological minima and afterwards aggregate to form thick layers around these positions. The difficulties of proper nanoparticle layer formation have also been documented previously, where multiple castings have been necessary to produce sufficient layer thickness.[14] One of the main differences between the Landfester particles and the other materials is the charged surfactant necessary for proper particle stabilization in water. To increase the coatability of the nanoparticles a polar substrate or substrate modification could be applied, however it would both need to be water insoluble and to conserve the photovoltaic performance of the device. Another option is to reduce the net particle charge by applying a nonionic surfactant. Surfactant-free particles have also been dispersed in ethanol,[12,13] but without ionic surfaces, steric stabilization will likely be needed for long term ink stability.

Overcoming structural defects in the nanoparticle layer

The main structural fault of the roll coated nanoparticle layer was found to be the shorts circuits through the layer as a result of voids between the nanoparticles and its high surface roughness. It is thus critical to demonstrate that an improved nanoparticle layer will reach the performance expected of a tandem solar cell, as we have done in a follow-up experiment. By coating active layer materials on top of the nanoparticle layers, the voids can be filled up with material with lower conductivity than PEDOT:PSS, and ZnO and electric short circuits through the layer can be prevented. By partially redissolving the nanoparticle layer and filling up the rough

areas with new material, one will of course reduce the roughness of the layer (and subsequent layers). A schematic overview of the electric performance in a tandem structure and the visual appearance of smoothened layers are shown in **figure 4**. From the photograph it is clear that only minor redissolving of the nanoparticle layer takes place since the nanoparticle layer's edges and structures are visible through the P3MHOCT layer on top. In regards to the photovoltaic performance, clear tandem behavior can be seen by a V_{oc} higher than the single BHJ (0.6V). Only devices with top coated P3MHOCT reach those voltages with a V_{OC} of 0.96 V using front illumination, whereas double sided illumination[25] gives 1.06 V). It is not surprising that devices with top coated P3MHOCT have higher potential than devices with top coated PCBM, since P3MHOCT is a hole conductor and better matches the energy levels of the device structure. The devices were characterized with front illumination in which photons first pass through the nanoparticle active layer, and double sided illumination, as described by Andersen et al,[25] with photons incident from both sides with the use of mirrors. The greatest difference between the two illumination forms is found for pure NP devices. For these devices photo absorption in the NP layer will not contribute to the device performance due to the shorts through the NP layer. We also see that the V_{OC} does not change, and it should be noted that more than 50% of all devices had resistor behavior after switching. The experiments show that if coated nanoparticles films can achieve the same layer characteristics regarding porosity and roughness as solution cast active layers, they can form successful active layers in tandem devices. Future experiments should focus on optimizing the layer formation by choice of surfactant, polar surface modifications, intermediate heating steps and other means suitable for large-scale production.

Experimental

Full chemical names

Ag = Silver, PEDOT:PSS = poly(3,4-ethylenedioxythiophene):polystyrene sulfonate, ZnO = zinc oxide, PET = polyethylene terephthalate, Active - Bulk heterojunction = PDTSBT-F:PCBM, PDTSBT-F = poly[(4,4'-bis(2-ethylhexyl)dithieno[3,2-b:2',3'-d]silole)-2,6-diyl-alt-4,7-(5-fluoro-2,1,3-benzothiadiazole)] (previously reported as P2[18]), PCBM = phenyl-C61-butyric acid methyl ester, Active – nanoparticles = 1:1 P3MHOCT:PCBM Landfester particles, P3MHOCT = poly-(3-(2-methylhexyloxycarbonyl)dithiophene), Organic BHJ = PDTSBT-F:PCBM + PEDOT:PSS , Organic NP = P3MHOCT:PCBM Landfester particles + PEDOT:PSS.

Water dispersible Landfester nanoparticles

P3MHOCT and PCBM were mixed in a ratio of 1:1 in chloroform and processed into nanoparticles using the Landfester method[26] with Sodium Dodecyl Sulfate (SDS) as surfactant. The ink concentration was increased to 60 mg/mL by centrifugation.

Device fabrication

The device was made on a flextrode substrate[20] and the remaining layers were fabricated by slot-die coating on a lab scale roll-coater[21] as previously described[18] with the exception of the active nanoparticle layer. The Landfester nanoparticles, which replaced the high band gap polymer used in reference[18], were coated at 60°C with a speed of 1.3 m/min and a flow rate of 0.220 mL/min. The flextrode substrate used here differed from the one previously described[18] by having a thinner PEDOT:PSS layer. For coating PCBM or P3MHOCT on top of nanoparticles a 20 g/L chloroform solution was coated at 60°C with a speed of 1.0 m/min and a flow rate of 0.13 mL / min.

Sample preparation

A 6.2 micron × 5.5 micron prism of solar cell was cut with a focused ion beam (FIB) in an area with bottom electrode but without top electrode. The sample was protected by a sputtered gold layer, and a deposited platinum layer prior to FIB cutting. A wolfram tip was fastened to the sample by platinum deposition and used to move the solar cell prism onto the sample holder, where it was welded in place by platinum deposition.

Ptychographic X-ray tomography

The sample was imaged using ptychographic X-ray tomography at the cSAXS beamline at the Swiss Light Source, Paul Scherrer Institut in Villigen, Switzerland, using the setup described in reference.[19] A coherent beam with 6.2 keV photon energy was focused by a Fresnel zone plate (FZP) of 170 micron diameter made of Au structures of 1.2 micron height and with an outer-most zone width of 60 nm, having a focal distance of about 51 mm at this energy. A central stop of 40 micron diameter and a sorting order aperture of 30 micron diameter were used to block diffraction orders from the FZP not contributing to the focus. The total flux provided by the FZP illumination is estimated to be about $3.6 \cdot 10^8$ photons/s. The sample was placed at a distance of about 1 mm downstream of the focus, in such a way that the beam had a diameter of about 3.3 micron at the sample position. A flow of nitrogen protected the sample from oxygen to reduce beam damage during the experiment. Ptychographic scans covering an area of 10 × 5 micron^2 (horizontal × vertical) were performed on a grid of concentric circles with a radial step size of 0.8 micron. Coherent diffraction patterns were recorded with an exposure time of 0.1 s at each position of the scan with a Pilatus 2M detector[27] placed 7.389 m downstream the sample. Ptychographic scans were repeated at 470 angular positions of the sample with respect to the beam, covering a total range of 180°. To adequately constraint the reconstruction in the areas where no data is measured due to intermodule gaps, we acquired angular projections at alternating detector positions[19] and reconstructions of two consecutive scans were carried out jointly, enforcing the illumination probe to be the same, using the algorithm in reference,[28] with 200 iterations of an algorithm based on the difference map[29] followed by 100 iterations of maximum likelihood refinement.[30] For ptychographic reconstructions a region of 600 × 600 pixels centered around the diffraction intensity distributions on the detector was selected, yielding reconstructed images with a pixel size of 14.3 nm. The reconstructed phase images from all projections were used for tomographic reconstruction after post-processing and registration according to the procedure described in reference.[31] For registration in the horizontal direction we further used a method based on tomography.[32] The resolution of the 3D dataset was estimated to be about 20 nm by Fourier shell correlation as detailed in the supporting information.

To estimate the dose, d, imparted on the specimen we use the expression $d = \mu N_0 \varepsilon / \rho$,[33] where μ is the linear attenuation coefficient of the specimen, N_0 is the number of incident photons per unit area, ε is the photon energy and ρ is the mass density of the specimen. With N_0 about 3.7×10^7 photons/μm^2 in our ptychographic scans and 470 projections, we estimate a dose of about 8.0×10^7 Gy on the PEDOT:PSS material, and 7.1×10^8 Gy in the Ag. We note that here we estimate the surface dose which in this

sample overestimates the dose of Ag due to its thickness being about three times the attenuation length.

Data segmentation

The data was divided into subsets to ease segmentation. For each subset the voxel electron density distributions were fitted with Gaussians for pure materials and power functions for material mixtures (see supporting information). Due to overlapping data fits a Markov field with alpha-expansion was used to enhance segmentation. A graph-cut algorithm was used to minimize the energy of the Markov field.[34] The weights of the nearest neighbors were fitted on actual data to match the relative voxel distribution of the fits for all densities simultaneously using a 2-norm (see also supporting information).

Conclusions

Using ptychographic X-ray computed tomography (PXCT), we have investigated an organic tandem solar cell with two active layers: one consisting of a bulk heterojunction and one of Landfester nanoparticles. We have found that the primary failure mechanism of the device is short circuits connecting PEDOT:PSS and zinc oxide layers through the active Landfester nanoparticle layer. This is also evident in the photovoltaic performance where the open circuit voltage, V_{OC}, is similar to the single junction device consisting of a bulk heterojunction material only, and the short circuit current, J_{sc}, is reduced below the single junction device level.

The electron densities extracted from the PXCT reveal that layers cast from zinc oxide nanoparticles only have 60% of the expected density for the bulk materials, indicating a porous layer or less dense material packing due to the nanoparticle structure. The silver electrode is porous with large air cavities. Similarly, the organic layer containing active nanoparticles has sub-resolution porosity i.e. below 20 nm. A thorough and state-of-the-art interface analysis shows how all layers with the exception of the active nanoparticle layer have a positive top-bottom interface correlation. The active nanoparticle layer on the other hand has negatively correlated top- and bottom interfaces, which also implies a wide distribution in layer thickness and a high interface roughness. The surface roughness is gradually reduced in subsequent layers and it never decreases to the levels observed below the nanoparticle active layer. To make nanoparticle active layers a viable alternative to bulk heterojunctions, the coatability of the active nanoparticles will need to be improved. By top coating P3MHOCT on the nanoparticle layer we demonstrate that tandem potentials above 1V can be achieved when the nanoparticle layers structural flaws i.e. porosity and roughness, are reduced. We conjecture that the structure of the nanoparticle layer can be improved either through polar surface modifications, heating steps or by reduction of the net charge on the particles, for instance by use of nonionic surfactants. The otherwise unobtainable tomographic information makes PXCT a critical tool to face the nano-engineering challenges one must overcome to realize organic photovoltaics as a technology.

Acknowledgements

We gratefully acknowledge financial support from The Danish Council for Strategic Research through the WAPART project, from The Danish Council for Independent Research Natural Sciences, through the DANSCATT grant, and from the Danish National Research Foundation. E. T. B. Skjønsfjell and D. W. Breiby gratefully acknowledge the Norwegian Research Council for financial support.

References

1. R. Perez and M. Perez, *IEA SHC Sol. Updat.*, 2009, **50**, 2.
2. S. Lizin, S. Van Passel, E. De Schepper, W. Maes, L. Lutsen, J. Manca, and D. Vanderzande, *Energy Environ. Sci.*, 2013, **6**, 3136.
3. F. C. Krebs, *Sol. Energy Mater. Sol. Cells*, 2009, **93**, 394–412.
4. N. Espinosa, M. Hösel, D. Angmo, and F. C. Krebs, *Energy Environ. Sci.*, 2012, **5**, 5117.
5. F. C. Krebs, N. Espinosa, M. Hösel, R. R. Søndergaard, and M. Jørgensen, *Adv. Mater.*, 2014, **26**, 29–39.
6. C. Newby, J.-K. Lee, and C. K. Ober, *Macromol. Res.*, 2013, **21**, 248–256.
7. J. J. Richards, C. L. Whittle, G. Shao, and L. D. Pozzo, *ACS Nano*, 2014, **8**, 4313–4324.
8. T. T. Larsen-Olsen, B. Andreasen, T. R. Andersen, A. P. L. Böttiger, E. Bundgaard, K. Norrman, J. W. Andreasen, M. Jørgensen, and F. C. Krebs, *Sol. Energy Mater. Sol. Cells*, 2012, **97**, 22–27.
9. K. Svendsen and K. S. Rognes, *Ann. Occup. Hyg.*, 2000, **44**, 119–124.
10. J. E. Carlé and F. C. Krebs, *Sol. Energy Mater. Sol. Cells*, 2013, **119**, 309–310.
11. S. Ulum, N. Holmes, D. Darwis, K. Burke, A. L. D. Kilcoyne, X. Zhou, W. Belcher, and P. Dastoor, *Sol. Energy Mater. Sol. Cells*, 2013, **110**, 43–48.
12. S. Gärtner, M. Christmann, S. Sankaran, H. Röhm, E.-M. Prinz, F. Penth, A. Pütz, A. E. Türeli, B. Penth, B. Baumstümmler, and A. Colsmann, *Adv. Mater.*, 2014, **26**, 6653–6657.
13. D. Darwis, D. Elkington, E. Sesa, N. Cooling, G. Bryant, X. Zhou, W. Belcher, and P. Dastoor, in *AIP Conf. Proc.*, 2011, vol. 1415, pp. 120–123.
14. A. Stapleton, B. Vaughan, B. Xue, E. Sesa, K. Burke, X. Zhou, G. Bryant, O. Werzer, A. Nelson, A. L. David Kilcoyne, L. Thomsen, E. Wanless, W. Belcher, and P. Dastoor, *Sol. Energy Mater. Sol. Cells*, 2012, **102**, 114–124.

15. S. Satapathi, H. S. Gill, L. Li, L. Samuelson, J. Kumar, and R. Mosurkal, *Appl. Surf. Sci.*, 2014, **323**, 13–18.

16. W. Chen, P. Nikiforov, and S. B. Darling, *Energy Environ. Sci.*, 2012, 8045–8074.

17. M. Dierolf, A. Menzel, P. Thibault, P. Schneider, C. M. Kewish, R. Wepf, O. Bunk, and F. Pfeiffer, *Nature*, 2010, **467**, 436–9.

18. H. F. Dam, T. R. Andersen, E. B. L. Pedersen, K. T. S. Thydén, M. Helgesen, J. E. Carlé, P. S. Jørgensen, J. Reinhardt, R. R. Søndergaard, M. Jørgensen, E. Bundgaard, F. C. Krebs, and J. W. Andreasen, *Adv. Energy Mater.*, 2014.

19. M. Holler, A. Diaz, M. Guizar-Sicairos, P. Karvinen, E. Färm, E. Härkönen, M. Ritala, A. Menzel, J. Raabe, and O. Bunk, *Sci. Rep.*, 2014, **4**, 3857.

20. M. Hösel, R. R. Søndergaard, M. Jørgensen, and F. C. Krebs, *Energy Technol.*, 2013, **1**, 102–107.

21. H. F. Dam and F. C. Krebs, *Sol. Energy Mater. Sol. Cells*, 2012, **97**, 191–196.

22. M. Van Heel and M. Schatz, *J. Struct. Biol.*, 2005, **151**, 250–262.

23. A. Diaz, P. Trtik, M. Guizar-Sicairos, A. Menzel, P. Thibault, and O. Bunk, *Phys. Rev. B*, 2012, **85**, 1–4.

24. M. Esmaeili, J. B. Fløystad, A. Diaz, K. Høydalsvik, M. Guizar-Sicairos, J. W. Andreasen, and D. W. Breiby, *Macromolecules*, 2013, **46**, 434–439.

25. T. R. Andersen, H. F. Dam, B. Andreasen, M. Hösel, M. V. Madsen, S. A. Gevorgyan, R. R. Søndergaard, M. Jørgensen, and F. C. Krebs, *Sol. Energy Mater. Sol. Cells*, 2014, **120**, 735–743.

26. T. Kietzke, D. Neher, M. Kumke, R. Montenegro, K. Landfester, and U. Scherf, *Macromolecules*, 2004, **37**, 4882–4890.

27. P. Kraft, a. Bergamaschi, C. Bronnimann, R. Dinapoli, E. F. Eikenberry, H. Graafsma, B. Henrich, I. Johnson, M. Kobas, a. Mozzanica, C. M. Schleputz, and B. Schmitt, *IEEE Trans. Nucl. Sci.*, 2009, **56**, 758–764.

28. M. Guizar-Sicairos, I. Johnson, A. Diaz, M. Holler, P. Karvinen, H.-C. Stadler, R. Dinapoli, O. Bunk, and A. Menzel, *Opt. Express*, 2014, **22**, 14859.

29. P. Thibault, M. Dierolf, O. Bunk, A. Menzel, and F. Pfeiffer, *Ultramicroscopy*, 2009, **109**, 338–43.

30. P. Thibault and M. Guizar-Sicairos, *New J. Phys.*, 2012, **14**.

31. M. Guizar-Sicairos, A. Diaz, M. Holler, M. S. Lucas, A. Menzel, R. a Wepf, and O. Bunk, *Opt. Express*, 2011, **19**, 21345–57.

32. M. Guizar-Sicairos, J. J. Boon, K. Mader, A. Diaz, A. Menzel, and O. Bunk, *Optica*, 2015, **2**, 259–266.

33. M. R. Howells, T. Beetz, H. N. Chapman, C. Cui, J. M. Holton, C. J. Jacobsen, J. Kirz, E. Lima, S. Marchesini, H. Miao, D. Sayre, D. a. Shapiro, J. C. H. Spence, and D. Starodub, *J. Electron Spectros. Relat. Phenomena*, 2009, **170**, 4–12.

34. Y. Boykov and V. Kolmogorov, *IEEE Trans. Pattern Anal. Mach. Intell.*, 2004, **26**, 1124–37.

35. T. Tromholt, S. A. Gevorgyan, M. Jørgensen, F. C. Krebs, and K. O. Sylvester-Hvid, *ACS Appl. Mater. Interfaces*, 2009, **1**, 2768–2777.

Submitted to RSC Nanoscale

ARTICLE

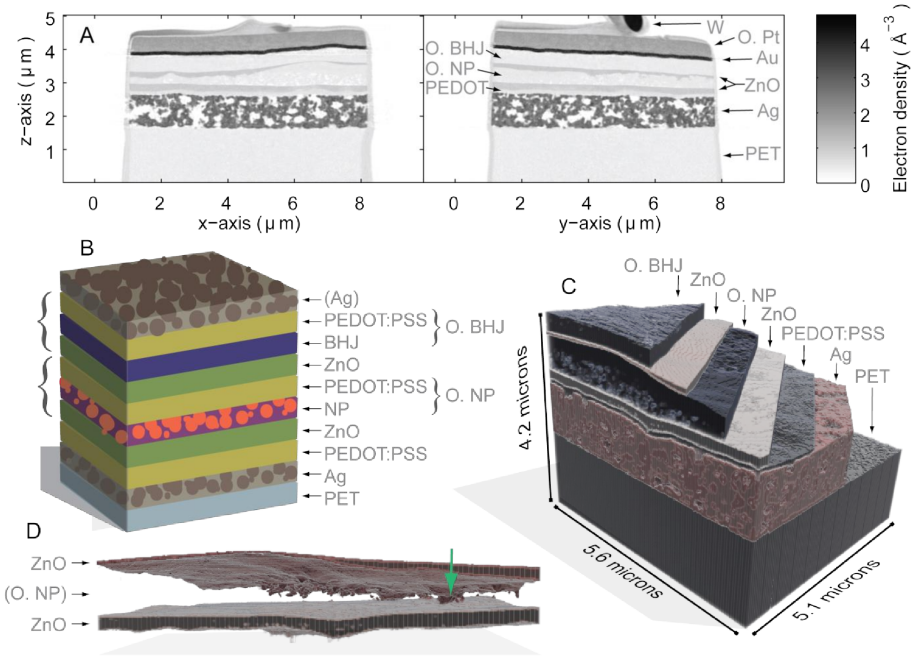

Figure 1. Ptychographic X-ray computed tomography of an organic tandem solar cell A) Tomogram slices showing the electron density of the layers that make up the tandem solar cell. The top consist of tungsten (W), platinum rich organic molecules (O. Pt) and gold (Au) all originating from the sample preparation, and therefore not part of the photovoltaic device. The device itself consists of PEDOT:PSS and a bulk hetero junction (O. BHJ), zinc oxide (ZnO), PEDOT:PSS and Landfester nanoparticles (O. NP), PEDOT:PSS (PEDOT) and silver nanoparticles (Ag) on PET foil (PET). B) Schematic drawing of device layers (for full names see materials and methods). There are two active layers: A bulk hetero junction (BHJ) cast from organic solvent and a Landfester nanoparticle layer (NP) cast from water. The sample was cut from an area without top silver electrode, which therefore is not present in the tomogram. C) Cutaway view of segmented layers annotated as in B. The active layer consisting of nanoparticles contains sub 20 nm pores whereas the bulk heterojunction is homogeneous. D) Zinc oxide layers surrounding the nanoparticle layers. The vertical arrow marks a short circuit that penetrates through the porous nanoparticle layer.

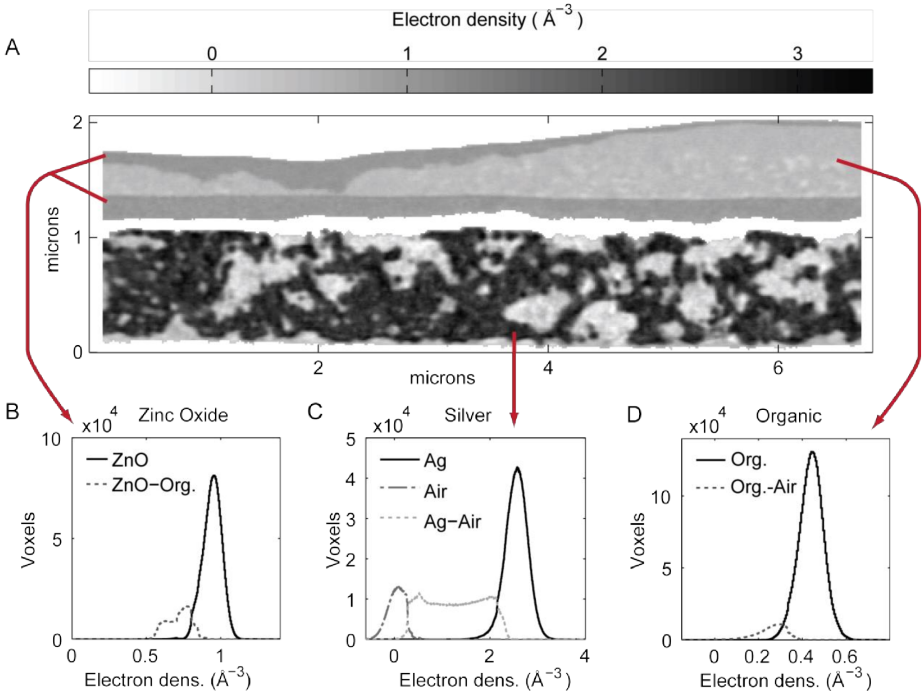

Figure 2. Electron density in the silver electrode and near the active layer consisting of nanoparticles. In A) we see a central tomography slice, near the short circuit of the nanoparticle layer only showing electron density for selected layers. The three histograms show electron density distribution based on segmentation. In B) we show the histogram of the two zinc oxide (ZnO) layers with a primary electron density of 0.96 Å^3 and partial volumes with nearby organic areas (ZnO-Org.). The electron density of the ZnO is only 60% of the expected bulk ZnO value (1.6 Å^{-3}), likely due to the ZnO layers being cast from nanoparticles. In C) we show the histogram of the silver layer, were silver (Ag), air and partial volumes with Ag-air mixture are distinguished. In D) we show the histogram corresponding to the organic layer, finding organic material (Org. = organic active nanoparticle and PEDOT:PSS) and sub-resolution porosity with nanoparticle materials and air (Org.-Air).

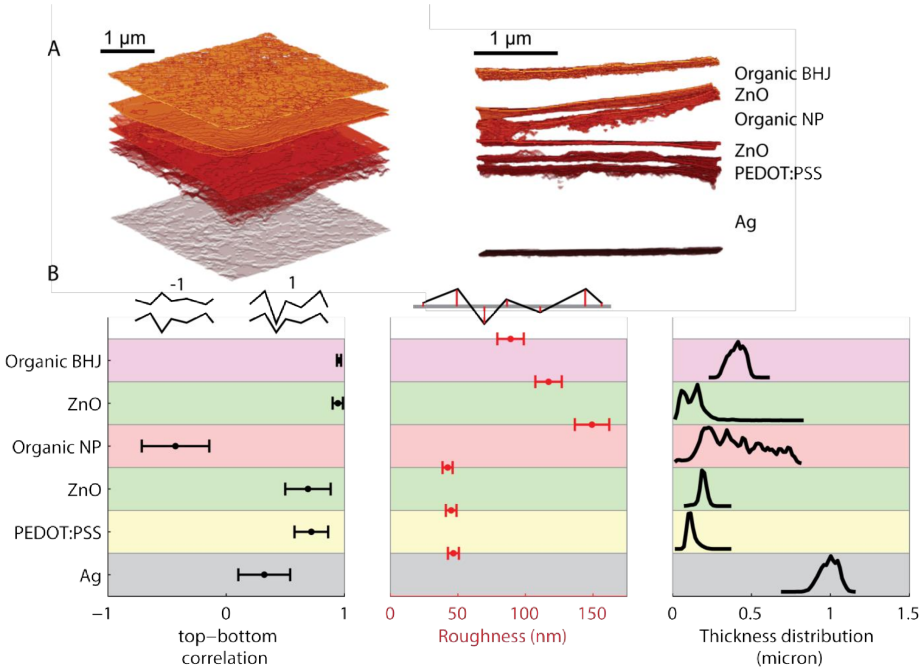

Figure 3. Interface analysis. A) Graphical representation of a part of the interfaces shown with top and side view with 1 micron scale bars. For full material names see materials and methods. B) Interface analysis of the different layers, from left to right: Correlation between the interface below and above the layer, roughness of interfaces and thickness distribution of the layers. The schematics above the graphs indicate the measured property i.e. top-bottom correlation is -1 for surfaces with opposite structure and 1 for identical structure disregarding scaling whereas roughness is defined as the average distance to a completely plane layer (red lines). The tail of the top ZnO thickness distribution is likely from spikes going through the organic NP layer.

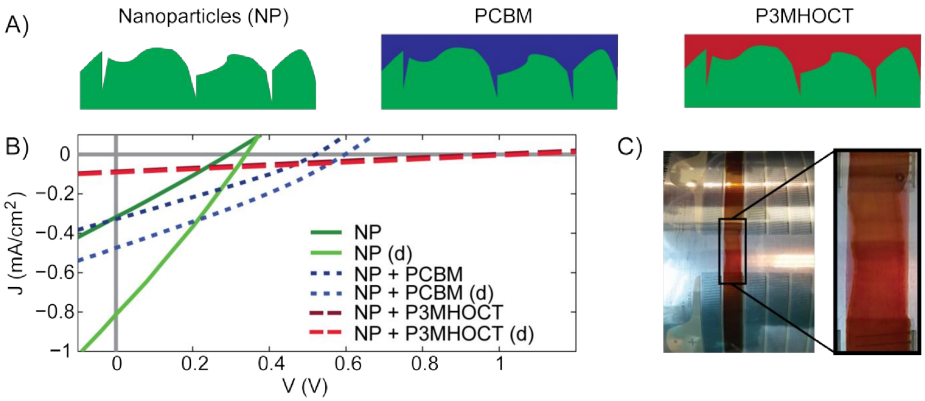

Figure 4. Measured tandem performance with alternative organic NP layers A) Schematics, from the left: Only nanoparticles, nanoparticles with solution cast PCBM on top, nanoparticles with solution cast P3MHOCT on top. B) The corresponding IV-curves for front illuminated devices, or double sided illuminated devices marked by (d). Devices with top coated P3MHOCT shown clear tandem voltage (> 1V) C) Photograph of coating of P3MHOCT on NPs. The NP layer remains visible below the P3MHOCT. It is clearest outside the zinc oxide areas where the NPs are dewetting more than P3MHOCT cast from solution.

Table 1. Device performance is shown for the studied tandem structure with both an active layer of nanoparticles (NP) and a bulk hetero junction (BHJ), and is further compared to a previously measured and published data.[18,35] BHJ_1 = PDTSBT-F:PCBM, BHJ_2 = P1:PCBM (P1 is a high bandgap polymer described in reference.[18]), BHJ_3 = P3MHOCT:PCBM and NP_3 = P3MHOCT:PCBM as Landfester particles. The structure in our experiment is similar to the previous successful tandem structure[18] except having P3MHOCT:PCBM nanoparticles instead of a high band gap BHJ. The low V_{oc} of our tandem device with an NP layer indicates it only functions as a single junction device, since the V_{oc} otherwise should exceed the V_{oc} of the single junction and approach the combined V_{oc} of the two single junctions of 1.2 V.

	V_{oc} (V)	J_{sc} (mA cm^{-2})	FF (%)	PCE (%)
Tandem BHJ_1 – NP_3	0.52	0.67	35.7	0.12
Tandem[18] BHJ_1 – BHJ_2	1.32	4.3	46.9	2.67
Single[18] BHJ_1	0.61	4.98	45.2	1.37
Single[35] BHJ_3	0.65	4.09	33.6	0.90

Ptychographic tomography provides 20 nm 3D resolution of a roll-to-roll coated organic tandem solar cell containing active layer cast from water-dispersible Landfester nanoparticles**.** Porosity is found in the silver electrode and active layer cast from nanoparticles. Interface characterization indicates structural defects in the nanoparticle layer such as roughness and shorts through the layer. When the defects are overcome by top coating polymer material, tandem performance with more than 1V is achieved. This highlights the need to improve intrinsic coatability of water dispersible nanoparticles to make them a viable alternative to bulk heterojunctions.

Keyword: tandem solar cells; multilayer materials; flexible materials; ptychography; organic nanoparticles

*Emil B. L. Pedersen, Dechan Angmo, Henrik F. Dam, Karl T. S. Thydén, Thomas R. Andersen, Eirik T. B. Skjønsfjell, Frederik C. Krebs, Mirko Holler, Ana Diaz, Manuel Guizar-Sicairos, Dag W. Breiby and Jens W. Andreasen**

ToC figure

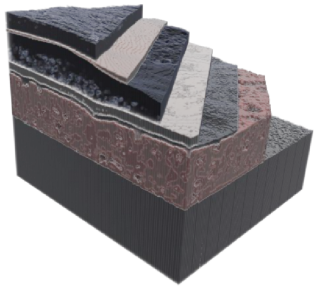

Supporting Information

Water-processed organic tandem solar cells improved by quantitative 3D nanoimaging

*Emil B. L. Pedersen, Dechan Angmo, Henrik F. Dam, Karl T. S. Thydén, Thomas R. Andersen, Eirik T. B. Skjønsfjell, Frederik C. Krebs, Mirko Holler, Ana Diaz, Manuel Guizar-Sicairos, Dag W. Breiby and Jens W. Andreasen**

S.1. Spatial resolution by Fourier shell correlation

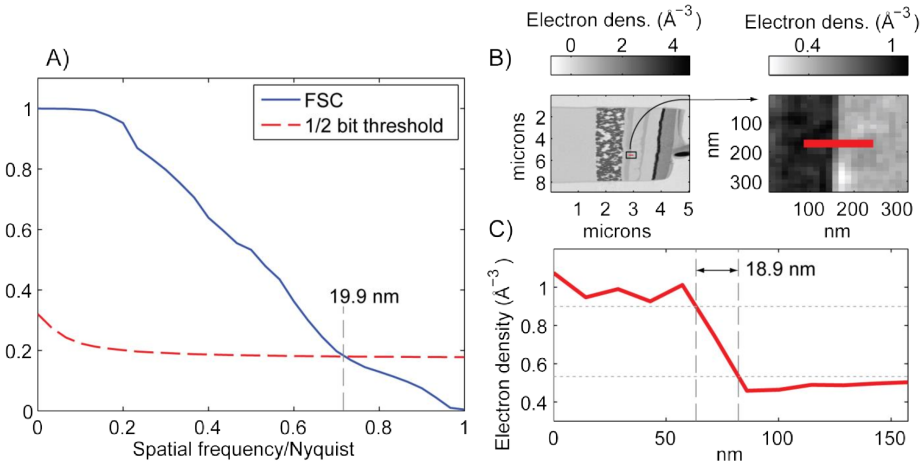

Figure S1: A) Fourier shell correlation (FSC) calculated for a central part of the tomographic data shown in the in main article. The 0.5 bit threshold intersects at 0.72 spatial frequency / Nyquist limit which with a Nyquist limit of 14.3 nm corresponding to 14.3 nm / 0.72 = 19.9 nm isotropic half period spatial resolution. B) Schematics of line scan shown in C) which yield 18.9 nm spatial resolution with the 10%-90% criterion.

The sample was measured at 470 projections that were reconstructed to a voxel side length at a half-period Nyquist limit of 14.3 nm. The resolution of the 3D dataset obtained by ptychographic tomography was estimated by Fourier shell correlation (FSC),[19,22] using two tomograms each computed from half of the projections. In Figure S1 we show in blue the computed FSC as a function of the spatial frequency on a Nyquist sampling scale. This curve can be compared with an analytically calculated threshold curve for a given signal-to-noise ratio, shown in Figure S1 with a dashed red line. The point at which the threshold curve intersects the FSC curve determines the

spatial resolution, which in this case is 0.72 spatial frequency / Nyquist limit and corresponds to 19.9 nm. We note that this resolution estimation could be pessimistic because the correlation is computed from tomograms with only half of the projections in each. The coarser angular sampling can reduce the FSC at high spatial frequencies and provide a low estimate of the resolution, and as seen on figure S1 the line scan yields a slightly better spatial resolution of 18.9 nm.

S.2. Partial volume simulations

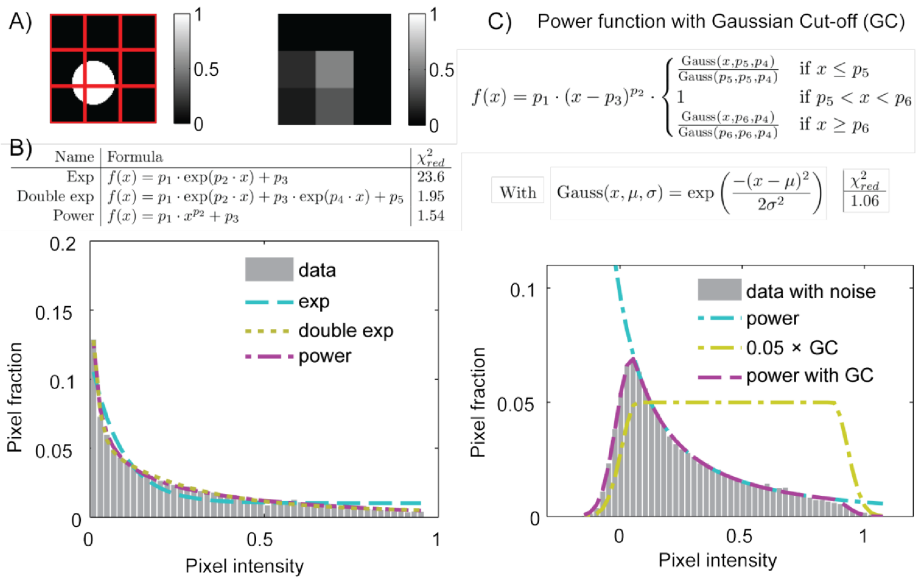

Figure S2: A) Illustration of simulation where sub-resolution cylinders (white =1, radius of 0.6 pixels) are randomly placed within a different medium (black = 0). The observed intensities due to partial volume effects are evaluated for 10^4 cylinders exemplified in the right figure. B) Resulting intensity histograms from the simulations described in A) are fitted with different functions. The goodness of fit is evaluated by reduced chi square assuming Poisson statistics and the power function is found to best match the distribution. C) The simulations are expanded to include Gaussian noise on the pixel intensities (σ = 0.05). To fit the new distribution the power function is multiplied with a step function with Gaussian Cut-offs (GC). The resulting fit yields a reduced χ^2 of about 1, and is shown along with two components of the fit: the power law function and the GC.

In a simulation carried out to calibrate the fit functions, a cylinder with diameter below the resolution was placed in a different medium, and the resulting partial volumes were calculated as shown in figure S2. 10^4 cylinders (r = 0.6 px) were randomly placed within the center pixel as illustrated in figure S2A using a uniform probability distribution without loss of generality due to the system symmetry. The resulting intensity distribution was fitted with different mathematical fit functions and found to be best described by a power law as shown in figure S2B. In real data sets the voxels will have noise due to experimental uncertainties, which is included in the simulation

as Gaussian perturbations of the pixel intensities (μ = 0, σ= 0.05). The new resulting distribution of the simulated noisy data is fitted with a product of a power function and a step function with Gaussian Cut-off (GC) as shown in figure S2C. The function is evaluated to be a good description of partial volumes effects like sub-resolution features based on the reduced χ^2 value near unity.

S.3 Markov field segmentation

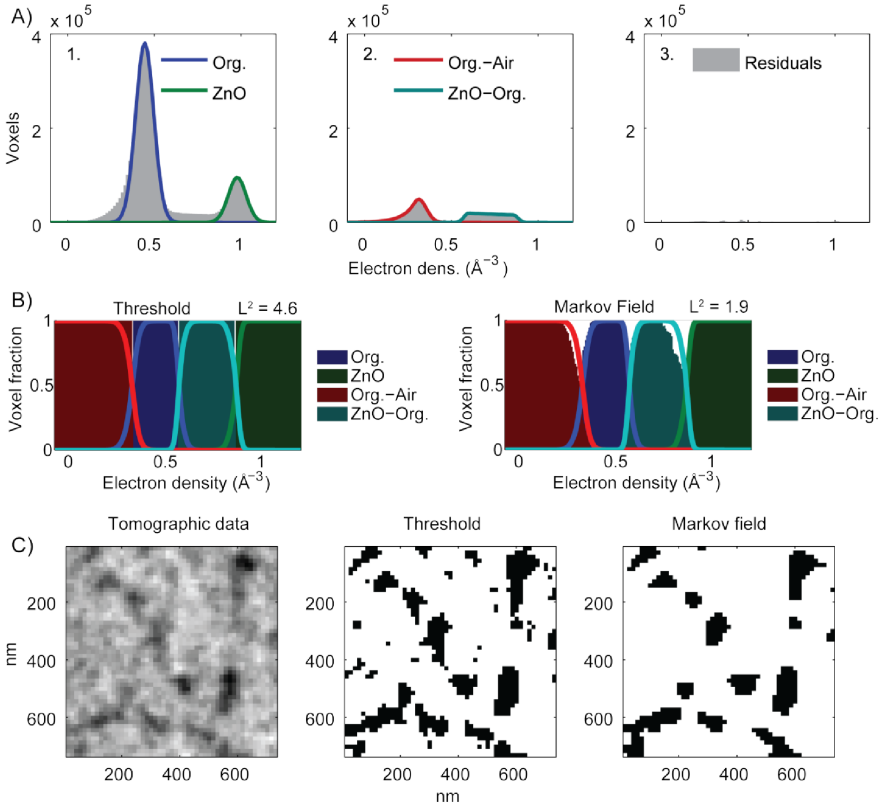

Figure S3: A) Electron density histograms from a subset of the tomogram are fitted with (1) Gaussian functions for pure materials and (2) power functions with Gaussian cut-offs for material mixtures as described in S2, after subtracting the Gaussian fits in (1) from the histogram. With insignificant residuals (3) the data are described solely by these 4 functions carrying strict physical meaning. B) The fitted functions from A) are converted to relative amount of voxels for each electron density. These functions are compared to the actual fraction of voxel being segmented into the given label at the given electron density. The lines represent the fits in A) and the colored areas the actual segmentation in the tomogram. Measured by the L^2 norm the distance of Markov fields segmentation in only 40% the distance of threshold segmentation, Markov fields segmentation thus getting closer to true physical functions in A). C) Organic material (Landfester particles) with volumes containing air. The tomographic data is illustrated to the left and the two types of segmentation are shown to the right. Note

the Markov field is implemented in 3D and uses all neighbors, therefore also taking voxels out of the shown plane into account. The Markov field greatly reduces the noise present in the threshold segmentation.

The nearest neighbors were included in the segmentation by an α-expanded Markov field since it improves the segmentation and thereby more easily justifies the physical interpretations as illustrated in figure S3. The energy function that the Markov function minimizes is

$$E(f) = -\sum_{i \in C_1} \alpha_i f_i - \sum_{(i,j) \in C_2} \beta_{ij} f_i f_j$$

Here C_x is the *x*-clique, *f* is the segmentation label, and α and β are weights for the 1- and 2- cliques, respectively. In practice the α parameters were set to 1, and the β parameters were optimized by performing full segmentation combined with a pattern search algorithm to minimize the distance to the describing functions presented for a sub section of the tomogram in figure S3. In this example the functions give: Org.-Air(0.35 $Å^{-3}$) ~ $3.4 \cdot 10^4$ voxels and Org.(0.35 $Å^{-3}$) ~ $7.5 \cdot 10^4$ voxels, so the expected voxel fraction at 0.35 $Å^{-3}$ electron density is ~0.3 for Org.-Air and ~0.7 for Org. material. The threshold segmentation gives Org.-Air(0.35 $Å^{-3}$) = 0 voxels and Org.(0.35 $Å^{-3}$) = $1.09 \cdot 10^5$ voxels thus reaching voxel fraction of 0 for Org.-Air and 1 for Org. material and residuals of 0.3 compared to their respective functions. The actual Markov segmentation was performed using a graph cut algorithm based on [Y. Boykov and V. Kolmogorov, *IEEE Trans. Pattern Anal. Mach. Intell.*, 2004, **26**, 1124–37].